Dedicated to

my Parents and Grandmother

PARAMETER ADAPTIVE VECTOR CONTROLLER FOR CSI-FED INDUCTION MOTOR DRIVE AND GENERALIZED APPROACHES FOR SIMULATION OF CSI-IM SYSTEM

A Thesis submitted to
Indian Institute of Technology, Kharagpur
for the award of the degree
of

Doctor of Philosophy

By
BASHUDEB CHANDRA GHOSH

DEPARTMENT OF ELECTRICAL ENGINEERING
INDIAN INSTITUTE OF TECHNOLOGY
KHARAGPUR - 721 302
1992

CERTIFICATE

This is to certify that the thesis entitled "**Parameter Adaptive Vector Controller for CSI-fed Induction Motor Drive and Generalized Approaches for Simulation of CSI-IM System**", submitted by Bashudeb Chandra Ghosh to the Indian Institute of Technology, Kharagpur, for the award of the degree of **Doctor of Philosophy in Engineering**, is a record of bonafide research work carried out by him under my supervision and guidance during the period from December 1987 to June 1992.

Kharagpur

July, 1992.

(Prof. S. N. Bhadra)
Department of Electrical Engineering
Indian Institute of Technology
Kharagpur, INDIA.

CONTENTS

ACKNOWLEDGEMENT

I would like to express my sincerest gratitude to my supervisor Prof. S. N. Bhadra for suggesting the subject of this dissertation and for his spontaneous guidance and cooperation in every respect of my research work until its completion.

I also express my deep appreciation and indebtedness to Prof. K. Venkataratnam, Head of the Department of Electrical Engineering for providing me with all possible facilities without which I could not think of the completion of my work.

I am grateful to Prof. K. B. Datta, Prof. A. K. Chattopadhyay and Prof. S. Sinha of Electrical Engineering Department and Prof. A. Mukherjee of Mechanical Engineering Department for their advice and interest related to my research work. I also acknowledge my gratitude to other faculty members who have always been willing to discuss and exchange ideas.

I am thankful to the staff members of workshop and laboratory of the department, especially Mr. L. B. Sharma, Mr. A. Williams, Mr. A. Sarkar and Mr. S. Chatterjee for their cooperation in fabrication and assembling my experimental set up.

Thanks are also due to my friends and research scholars of the Electrical Engineering Department of I.I.T. Kharagpur for their cooperation and encouragement. I also wish to thank Mr. Tapas K. Ghosh for his help in the preparation of this volume.

I wish to place on record my deep sense of gratitude to the I.C.C.R., Govt. of India for financial support and to the Director, B. I. T., Khulna, Bangladesh for granting me deputation to undertake the research work in India. He has been a constant source of encouragement to me.

Last but not the least, I am thankful to my wife Smt. Purnima Ghosh and children Rama and Manas for the troubles they have endured over the period of my work. Also, they have contributed in their own way to the completion of this dissertation.

I.I.T. Kharagpur
July , 1992.

(Bashudeb Chandra Ghosh)

BIODATA

Bashudeb Chandra Ghosh was born in Khulna, Bangladesh on September 22, 1955. He received the degrees of B. Sc. Engineering in Electrical Engineering from Khulna Engineering College under Rajshahi University of Bangladesh in 1976 and M. Sc. in Electrical Engineering from Bangladesh University of Engineering and Technology (BUET), Dhaka, in 1986. He joined the faculty of Khulna Engineering College (Now B.I.T. Khulna) in 1978 and is at present an Assistant Professor in the Department of Electrical Engineering. He joined the IIT Kharagpur in December 1987 as a research scholar of Electrical Engineering Department under Indo-Bangladesh Cultural Exchange Programme.

His main areas of interest are analysis of Electrical Machine, Power Electronics and Microprocessor-based control of electronic drives. He has a number of research paper to his credit.

ABSTRACT

The main subject matter of this dissertation is to develop parameter adaptive rotor flux oriented current fed induction motor drive systems for controlled speed operation. The parameter adaptive approaches do not require special test signals and softwares in a big way. Three easy-to-implement schemes are suggested. One scheme is based on airgap power estimation method and takes into account of the non-linear magnetic state while tracking the actual rotor resistance. The other two methods constitute model reference adaptive controllers. They are based on the inverter input voltage and torque producing component of the stator current. The effectiveness of these methods is examined by extensive simulation and experimentation with two laboratory type induction machines. The experimental set up makes use of two microcomputers (i-8006 with i-8007) and a PC/AT with Burr Brown's PCI system having multi-channel 12 bit data acquisition modules for implementing the control algorithms.

Prior to the description of parameter corrective algorithms, a control system suitable for a CSI-fed induction motor under rotor flux orientation is designed and tested by suitable simulation model. Then the influence of rotor resistance variation in the presence of magnetizing flux saturation has been extensively investigated. A two-parameter saturation model (two-term quintic non-linearity) is used in all these studies. It is further shown how the machine performances under field oriented condition are affected by inclusion of saturation

characteristics. Analytic expressions as well as digital simulation procedures are presented to study the performance of the drive system.

Robustness of the drive system has been studied applying the concept of Kharitonov's theorem and then justified from the simulation results of the system for both parametric and torque disturbances.

'Bond Graph' and 'Nodal method' provide an organised way to write equations for a dynamic system. Tedious way of writing equations and their arrangement and re-arrangement for framing state equations can be avoided in the proposed simulation techniques. Simulation studies based on systematic modelling and framing of the system equations using the above two methods for the operation of a speed controlled CSI-IM system under normal and abnormal conditions have also been provided.

KEY WORDS

Induction machine, CSI-fed, d-q-axis, Flux and current vectors, Saturation, Parameter estimation and adaptation, Modelling and simulation, Robustness, H_∞-norm, Bandwidth, Stability margin, Multi-microprocessor-based control, PCI system, Data acquisition, Resolution, Nodes, Corrector currents, Effort, Flow, Gyrator, Bonds.

LIST OF PRINCIPAL SYMBOLS
(All variables are having SI units)

a_1, a_5	constants of two-term quintic magnetising characteristic
B	friction coefficient
b_k	coefficients in the expression of L_m in terms of i_{mag}
e_k	error signal at k-th instant
e_i	error in current control loop
e_ω	error in speed control loop
g_{ds}	cosine of the torque angle(θ)
g_{qs}	sine of the torque angle(θ)
I_1, i_{dq}, i_R'	peak of the fundamental component of stator current
i_{dr}, i_{qr}	d- and q-axis instantaneous rotor current (syn. frame) referred to stator when d-axis aligns with the rotor-flux vector
i_{dr}', i_{qr}'	d- and q-axis instantaneous rotor current (syn. frame) referred to stator when d-axis aligns with stator mmf vector
i_{ds}, i_{qs}	d- and q-axis instantaneous stator current in syn. frame
i_{ds}^*	command value of flux component of stator current
i_{qs}^c	q-axis current in the slip calculator
$\hat{i}_{qs}$	estimated value of the q-axis stator current
i_R	instantaneous value of dc link current
I_R	average value of dc link current
i_R^*	reference dc link current
I_R'	normalized value of dc link current

i_{mag} magnetising current for air gap flux

k_{p1}, k_{i1} proportional and integral components of the 1st pi-controller

k_{p2}, k_{i2} proportional and integral components of the 2nd pi-controller

k_{p3}, k_{i3} proportional and integral components of 3rd pi-controller

L_f dc link filter inductance

L_m, L_m^* actual and nominal values of the magnetising inductance per phase referred to the stator

L_r, L_r^* actual and nominal values of the rotor self inductance per phase referred to stator

L_s stator self inductance per phase

$L_{\sigma s}$ leakage inductance ($L_s - L_m^2 / L_r$)

m_k output of pi-controller at k-th instant

p $\equiv \frac{d}{dt}$, differential operator

P_p pole pairs

P_{ag} air gap power

P_{st} power input to the stator of the machine

Q reactive power

R_f resistance of dc link filter

R_r rotor resistance per phase referred to stator

R_r^{ad} adapted rotor resistance in the controller(s)

S_{in} volt ampere input to the motor

T_{em} developed electromagnetic torque

$\hat{T}_{em}$ estimated value of electromagnetic torque

T^*_{em}	command torque generated in the controller
T_L	load torque
T_s	sampling time
$\underline{u}$	input vector in the state space simulation model
v_{ds}, v_{qs}	d-and q-axis instantaneous stator voltage in a frame synchronous with the rotor flux
v_I, V_I	instantaneous and average inverter input voltage
v_R, V_R	instantaneous and average converter output voltage
v_s, V_s	instantaneous and rms phase voltage for equivalent star
λ_m	air-gap flux linkage
λ_r	rotor flux linkage
λ^*_r	command rotor flux linkage
λ_{dr}	d-axis rotor linkage in stator terms
λ_{qr}	q-axis rotor linkage in stator terms
ω_e	speed of the reference frame relative to stator, el.rad/s
ω_m	motor speed mech.rad/sec
ω_{mf}	speed of the motor after filtering
ω_r	rotor speed, elec.rad/sec
ω_{ref}	reference speed of the motor mech.rad/sec
ω_{sl}	slip speed in elec.rad/sec relative to the rotor flux
ω_{sl}'	slip speed in elec.rad/sec relative to stator mmf vector
θ	space angle between the stator mmf vector and rotor flux vector (torque angle)
τ_f	time constant of filter, sec
τ_r	rotor time constant, sec

CHAPTER I

INTRODUCTION

1.1 BACKGROUND

The large majority of drives in Engineering and Industry today are electrical drives. High reliability, ease of control to meet the operating conditions, wide speed range and power ratings, low noise level, absence of hazardous influence on the environment, cleanliness, reduced overall size, etc. are the effective features that have resulted in their wide industrial applications when compared with other types (steam, hydraulic and diesel) of drives. Of course, non-electrical drives have their own field of applications (transportation, power generation etc.). The two typical classifications of electrical drives are the servo drive systems and the adjustable speed drive systems. The former is used in high dynamic performance domain, which requires fast response and high precision in torque and position control and immunity to load torque perturbation, while the latter refers to the speed control type applications over a wide range with high accuracy.

Until the early sixties, the dc motors owing to their low electric time constants and inherent physical decoupling of armature and field circuits were dominating the areas of servo drives and variable speed operation. Following the development of silicon controlled rectifiers

controlled static AC-to-DC and DC-to-DC power converter sets, dc motor further established itself as a superior servo as well as variable speed drive in contrast to its ac counter part inspite of having some inherent disadvantages arising from commutator and brushes such as frequent maintenance, inability to work in corrosive or explosive atmosphere, limited capability in high speed and high voltage operations. Infact, the control simplicity of the motor as well as of the static power converter contributed to its wide use. However, efforts were not lacking to develop suitable static power converters for adjustable frequency operation and appropriate control strategy for variable speed operation of ac motor, traditionally considered as a source of constant speed drive. Owing to simple and robust structure, least cost, high reliability and better maintainability and low inertia, induction motor, particularly the squirrel cage type, drew much attention. By the mid 1970's the industry saw the standard induction motors operate reliably from below 0.1 to 2.0 pu rated speed driven by solid state converter/inverter of varying configurations. However, with ordinary inverter drive system the dynamic characteristic are not so excellent because the power stage can control voltage or current with respective frequency but can not command the torque and flux independently. The problem arises from the complex and non-linear relationship of the machine primary currents to the generated torque. Current components responsible for independent control over the machine flux and torque are combined into a single variable, namely, the stator current, making the fast dynamic response difficult. However, the

vector (field orientation/co-ordinate) control strategy, introduced in the late sixties and early seventies [1, 2], of decoupling the flux and torque components of stator has changed the picture and made possible the precise control of torque, speed and position of ac motor for comparable, or even superior performances to those of dc motors. In the beginning, this control technique could not make much headway owing to the lack of implementation requirements. Recently introduced [3] Field Acceleration Method (FAM), which is convenient to apply in a voltage source inverter based system, has created a lot of interest in the field of controlling induction motor servo drives.

However, the interest in the vector control approach rapidly grew, and a number of strategies for vector control of induction machines appeared over the last two decades and the implementation schemes have achieved success. This has been possible due to rapid development of power electronic semi-conductor switches and high speed micro-computing systems with data acquisition facilities during the late seventies and early eighties. Incidentally, it may be said that vector control principle is also equally applicable to synchronous machines, and numerous reference in this regard are available in the literature.

1.2 BRIEF LITERATURE SURVEY

The vector control strategy has gained sufficient momentum to enter into the industrial application sector as a powerful tool for controlling robots, machine tool spindle drives, different types of servo drives, pinch roll drive of the continuous casting plant etc. Since through an induction motor stator both the torque and flux

producing currents flow, it is difficult for the general readers to grasp the principle of field orientation that decouples the torque and flux producing channels having no static axial configuration. In the literature are available a large number of papers [1, 4 - 5, 8 - 19], that discuss the basic principle of field orientation control, i.e., adjustment of the torque angle, or speed of the flux and torque vectors, with the variation of demanded load torque and set speed. Normally, the flux vector (rotor, stator or airgap) is kept constant for the operating speed lower than the base speed [15, 20] and magnitude and phase angle of stator mmf is controlled to generate the demanded torque, maintaining linear relationship between the torque component of stator current (generated in the controller) and the developed electromagnetic torque. Strictly speaking, all categories of electrical machines are generic in nature, and each machine is having a flux axis and an mmf perpendicular to that axis responsible for torque production. If the decoupling of these components could be ascertained through internal structure (compensated dc. machine) or external controller (FOC-IM), fast dynamic responses with improved stability could be achieved.

It has been indicated that the vector control schemes can be designed and implemented with reference to any of the three flux vectors stator, air-gap or rotor flux. Relative merits and demerits of the schemes based on different flux vector orientation, [18, 21, 25] indicate that easier and stable decoupling of torque and flux channels is possible with rotor flux orientation, while the other flux model

based schemes contain derivative terms of the stator current components and nonlinear torque slip characteristics with pull out condition. The compensation loop demands accurate measurement of leakage inductances [18, 25], that introduce stability problem in an airgap flux based orientation scheme. To avoid derivative term in the torque to slip-producing loop of the controller, the slip frequency is applied as a command input instead of the command torque in [18] for the stator and airgap flux orientation that makes the dynamic responses for torque disturbances slower than the rotor flux orientation scheme. In [26] a vector control scheme is presented that computes torque angle based on air gap flux orientation and presents a methodology to compute torque from terminal quantities. The scheme demands the decoupling criterion unaffected by rotor parameter deviation. Though most of the vector control schemes are based on rotor flux orientation, due to the above mentioned problems, still the stator and airgap flux orientation controllers are drawing increasing attention for easier measurement or computation of flux.

In the rotor flux oriented drive, instantaneous position of the stator mmf vector (making a desired torque angle with respect to rotor flux vector) is controlled either by knowing the position of the flux vector or by creating certain criteria that places the stator current vector in the desired position to satisfy decoupling criterion. The position of the rotor flux can be determined by direct measurement of the air-gap flux vector using search coils or sensors inside the machine [1, 21] or by making some modification in the machine

construction such as tapped stator windings [22] etc. or by the application of observers [23, 24] using the machine terminal voltages and currents.

The direct flux acquisition method is not very popular as it involves modifications to the commercially available machines, and the flux detectors detect the air gap flux. Apart from this, signals are noisy, particularly at low speeds, necessitating special filters that introduce delays in the direct measurement. Detection of flux by observer is a dynamic measurement approach and suffers from time-lag problems (integration troubles) and motor parameter deviations. Alternative to flux detection methods is the feed-forward slip-frequency method, proposed by Hasse [2] which avoids unwanted measurements inside the machine for flux feed-back and permits the use of commercially available machine without any modifications. The required signals are generally convenient and easy to measure. The strategy utilizes the motor velocity feed-back, feedforward slip-frequency command and the torque angle command to determine the position of the stator current vector. Velocity feed back signal is generally well defined and much less polluted by noise than the flux feed, and is easy to obtain. This is especially true at low speeds where the velocity signal does not suffer by ripples as does the flux feed-back signal in the direct method. However, this type of control strategy is highly dependent on key parameters of the induction motor and requires additional circuits and softwares for tracking these parameter changes and providing necessary corrections thereof.

Selection of the inverter type for implementing an indirect vector controller is motivated by the complexity of controller in contrast to the ruggedness of the inverter, cost effective switching of switching power devices, parameter sensitivity etc. Since the basic aspect of a vector controller is to generate the torque and flux producing current references for stator current and guide the actual currents in the machine to adjust accordingly, implementation becomes easier for current fed inverters [15, 18]. For voltage fed inverters the reference current components are used to generate reference phase voltages and requires compensation of cross coupled leakage reactance drop [3, 9, 14, 27]. Since the impedance drop is only a small percentage of the total voltage drop of the induction motor, the voltage fed based control schemes are almost insensitive to rotor parameter deviation where as in a current fed inverter the distribution of torque and flux producing currents are directly affected by the changes in rotor parameters in the machine from those used in the controller. A comparison between the well known V/F control with vector control criteria with voltage fed inverter scheme in [9] reveals that the vector control is an extension of constant volts/hertz control. Inclusion of load dependent voltage drop component makes the slip frequencies of the two schemes differ, as shown in [9].

The two forms of current fed drives are (i) current regulated PWM inverter (CRPWM) feeding sinusoidal currents in the machine phase windings and (ii) current fed six step inverter (CSI) injecting square wave currents in to the machine which has inductances and sluggishness

in performances of a CSI fed drive are [28].

* It injects prominent harmonic currents in the induction motor creating torque pulsations.
* The resultant mmf vector in the machine changes position in step
* Due to heavy filtering inductance in series with the stator windings of the IM quick response in current control is not possible.
* With small load torque stability problems arise that demands field weakening [10].

However, use of a current source inverter enjoys the following advantages :

* Complex coordinate transformations may be avoided to simplify the control system.
* A definite relation exists between the level dc link current and fundamental component of stator current.
* Comparatively easier control of inverter frequency.
* Low cost and inherent machine terminal short circuit protection facilities.

In application sectors where the sluggish performance of the current source inverters are negotiable with its comparable low cost, CSI-fed systems are the better choice [17] and a good number of vector control schemes based on CSI inverter have been proposed [10, 15, 17, 29 - 32]. For computation of slip speed, q- axis component of stator current derived from actual dc link current is proposed in [10, 15, 17] that avoids the inaccurate slip frequency estimation using its command

value [32, 33], due to the delay introduced by link inductance for instantaneous adjustment of the values. Inverter frequency is directly obtained from the addition of slip speed to rotor speed (electrical). Phase position of stator mmf vector is controlled in [10, 15, 17, 32, 33] by changing a delay (introduced in firing control of inverter thyristors) that is inversely related to the phase difference between the command values of torque and flux producing stator current components.

Controlling of the dc link current is done by adjusting the delay in firing converter thyristors to insert a variable voltage on the input side of the dc link [10, 32 -34]. In [15] nonlinear control of converter thyristor firing is introduced by inhibiting the gate pulses for the condition in which actual dc link current is higher than the reference value, otherwise, normal firing control is followed. A variable structure current controller acting on the firing sequence of converter thyristors is presented in [17]. The inverter input voltage and slip speed are both used as feedforward signals in [26]. The scheme utilizes torque angle based control of slip speed and adds a voltage component corresponding to current error with the inverter voltage (feed-forward) for controlling converter firing. The scheme in [16] uses flux calculations for flux feedback in excitation control circuit and firing of the inverter thyristors is done by coordinate transformation of the demanded values of the flux and torque components of the stator current vector. Converter firing is controlled by the dc link current comparator. A methodology is proposed in [34] to reduce

parasitic torque, based on adjustment of the duration of mmf vectors for the six step mmf vector of the CSI.

Current regulated PWM inverters enjoy the fast response in current control loop and injects sinusoidal currents in the stator phases to generate continuously rotating mmf vector and is the most favourable one for implementing field orientation control strategy as evidenced in the literature [13, 18, 35, 36]. To generate reference values of phase current, several coordinate transformations are required and the angle is computed from flux calculation [19, 35] or from slip and rotor speeds [13, 18]. One of the drawbacks of these control schemes is proper selection of initial conditions that affects transient responses at the starting of the control process. Modern control theories such as model reference adaptive control with decoupling of variables [37, 38], optimal state feedback for decoupled operation [39] and complete decoupling [40] are being introduced in vector control implementation.

Digital simulation of the drive and power circuits with the control strategies is a useful tool for predicting the system performances, selection of controller gains, study of robustness etc prior to practical realisation of the proposed control strategy. Digital simulation for a voltage source inverter-based scheme is presented in [42] and for a CRPWM inverter-fed system in [13]. In these, power semiconductor devices are considered as ideal switches. Simulation study for a CSI fed system under field orientation condition is presented in [33] and is based on a mathematical model that takes into account the rectifiers, inverter and induction motor dynamics.

The stability of a field oriented control system is enhanced due to decoupling of torque and flux channels [4, 37] and in most of the control schemes ordinary PI controllers are used. For better performances PID controller is proposed in [15] and variable structure controller in [17, 43, 44]. For a stable operation, model reference complementary controller has been used in [19] for velocity and position loop control in addition to vector control.

A lot of computation steps within a short sampling interval, is to be accomplished by a digital controller with utmost accuracy so that the controlling is superior to any highly accurate analog system. This view point is reflected in implementing a field oriented control scheme with slip frequency regulation or flux estimator. In seventies or early eighties Intel 8085 based microcomputing systems were used with multiprocessor [8] or along with some analog computing aids [13]. The 16 bit microprocessors and math-co-processing chips with complex functions are now the widely applied computing devices [10, 15, 17, 19, 27, 33, 37, 45] where most of the schemes uses i-8086 and i-8087 combination. The high speed digital signal processors with 12 bit data acquisition system and 32 bit floating point calculation facilities have been found to be used in implementing observer based schemes [23, 24]. Besides the microcomputing systems, PC's are also being used to observe the conditions of controller and power circuit variables and for passing on line commands/inputs to the microcomputers and above all for development of assembly language programs. The sampling times reported in the literature are 0.4 msec in [19], 2.178 m·sec. in [33].

Changes in parameters, specially in the case of slip regulated current fed rotor flux orientation system, severely affect the steady state and dynamic performances and these have been the subject matter of investigation in a large number of publications [46 - 52]. Temperature variation causes the change in resistance and degree of saturation affects the inductances. Most of the studies are concerned with the deviations of torque output and flux levels from their command values in the steady state [46, 47, 53 - 58]. Reduction of flux, one of particular importance in situations such as field weakening and optimal operation [20] where reduced excitation can cause the magnetizing inductance increase by more than 50%. Studies in respect of dynamic and transient responses of field oriented machines under nonlinear magnetic state are available in reference [48] and [52].

Magnetization curves are normally characterized in two ways either by approximate piece-wise linear hard limit saturation curve [59] or by a nonlinear mathematical model (Frohlich's equation or a two term polynomial [47, 50, 51]. In [49], a polynomial fit for magnetizing inductances is considered to study the effect of saturation and rotor resistance change in torque, flux, efficiency, power factor and stator current characteristics. Selection of the flux level for efficiency optimization in a field oriented induction motor is presented in [60]and for field weakening region in [50, 61].

Parameter adaptation schemes in vector control strategy has been carried out by direct measurement of the parameters [58, 62 - 65] or by estimating them from terminal quantities [46, 66, 67] or by generating

an error function from the comparison of a physical quantity and its generated reference (satisfying the field oriented condition) to correct the slip gain [33, 45, 53, 55, 69]. Relative merits and limitations of the various compensation schemes are presented in chapter IV.

1.3 MOTIVATION AND OBJECTIVES

The state of the art of vector control of induction motors is now almost in the matured state and perhaps no one is doubtful about the applicability of vector controlled induction motor in industrial servo drives and speed controlled system. New micro-electronic and high frequency switching devices are also coming out day by day and playing important role in implementing control systems involving huge computations. Some of the control strategies require complex computation circuits and are difficult to implement. Whatever may be the nature of control strategy, the basic question is, "Are these control strategies capable to maintain perfect decoupling of the torque and flux"? Physical control systems may not be capable to maintain field orientation perfectly due to computation delay, measurement errors, external noises, etc., and one must be contented with the performances closer to ideal condition as is permitted by the physical constraints of the drive in which the strategy is applied. Increasing complexity of control system may improve performances of the drive system but at the same time it may be cost prohibitive.

In current source inverter-fed systems the frequency of the inverter is controlled directly from the feedforward slip speed and

motor speed [15, 17, 26]. To make the response faster a feedforward signal representing the speed voltage is applied to the converter controller to generate the dc link voltage control signal [26 ,31]. This approach is particularly effective for obtaining fast response to speed changes. A current control system with high gain PI controllers (having large bandwidth) being effective for both torque and speed changes is considered in the present study. For controlling the inverter, besides its frequency, a phase angle control loop, based on d-q components of stator current, is provided in [15 , 17]. Since the q-axis reference current is generated from the speed error signal, noises in the speed channel will cause improper phase delays in the system. Also the slip speed computed from the commanded value of the torque component of current deviates from the desired slip speed, due to the delay introduced in the current loop by the dc link filter. The present study proposes correction to excitation frequency for inverter firing during the transient process. A simulation model developed on the basis of the above proposals for studying the drive performance under some justifiable assumptions is required to verify the effectiveness of the above considerations prior to the practical realization of the circuit configuration.

The influences of mismatch between the parameters of the machine and those used in the vector controller of a slip regulated rotor flux oriented system has been the focus of a large number of publications [46 - 52]. In these publications, excepting a very few, the investigation has generally centered round the study of the effects of

rotor resistance deviation on torque and flux. Saturation effect has seldom been treated simultaneously with rotor resistance variation. A systematic study is envisaged to visualize the effects of rotor resistance variation in the presence of magnetic nonlinearity. Results of simulation studies are given the support by approximate analytic expressions indicating the causes behind the effects. Besides the effect on torque and flux, considerations have also been extended to other variables like voltage and current. The effects of load torque on the internal and the external quantities of the machine during the detuned operation , caused by rotor resistance change, have been examined considering both the linear and non-linear magnetic states of the machine. To the author's knowledge, such aspects are not well documented. A study of the effects of parameter change on the transient response to step change in speed have been indicated in the present study.

A large number of schemes for detuning correction are available [33, 45, 46, 53, 55, 62 - 69]. They have their merits and limitations. Some of the compensation schemes are quite involved and some await physical realization. Though various control structures, with their merits and limitations, for detuning corrections are available, search for alternative and competitive adaptive controller, or endeavor for introducing innovation in the existing controllers, is still on, and this forms, even to date, an area of intense investigation. The present study proposes three compensation schemes which not only consider corrective measures for rotor resistance variation but also takes into

account the magnetic state of the machine. The first scheme, proposed in the present work, is the air-gap power based rotor resistance estimation method, and is considered to be an improvement over the algorithm proposed in [54]. The scheme considers the magnetic non-linearity and lays down an easy selection criterion of one solution out of the two for the rotor resistance. The other two methods use dc link voltage and torque producing component of stator current based adaptation algorithms for correction to the rotor resistance in the slip calculator.

Study of robustness of a vector controlled system due to parametric perturbations is not well documented in the literature. A study has been under taken in the present work to investigate in a systematic and easier way the stability of the system using the concept of Kharitonov's theorem [90]. Selection of the PI controller constants for robust operation of the system is given a support by Kharitonov's theorem.

A number of papers is available on the simulation of CSI-fed systems [70 - 76] and vector controlled systems [10, 42, 51] considering different aspects of operations. In almost all cases, certain simplifying assumptions have been made that do not always reflect the reality of the exact problems involving converter and inverter. Quest for an improved model to simulate a system complying with the reality as far as possible can not be overemphasized. Simulation of the vector controlled CSI-IM system using a simplified model of the drive system under some justifiable assumptions for both

linear and nonlinear magnetic circuits is proposed. This is to study the transient response and performances of the parameter compensation schemes of the drive system.

The bond graph technique which has been related mostly to the field of mechanics, finds very limited applications to electrical power engineering. The concept uses power and energy as input-output variable and thus provides a very general basis for simulation involving mixed components (mechanical electrical and electronics) [77 - 80]. ' Bond Graph ' approach is applied in this dissertation to simulate a CSI-IM system, dispensing with many simplifying assumptions and the necessity of considering the changing circuit topologies which are quite often the requirements in many studies. A realistic picture emerges. For this study diodes of the CSI are represented by their V-I characteristics and induction motor in two phase representation.

The 'Nodal Method' is another generalized approach for simulation of a system on a digital computer. The three-phase input to the induction motor is retained, and modulated resistance values (low and high) are used to represent ON and OFF states of the semiconductor switches. This very much facilitates the simulation of CSI-IM system under normal and abnormal conditions.

Summarizing, the salient features of present research work are:

1. In the case of CSI-IM drive systems, the dc link current and voltage have definite relations with the fundamental components of motor current and voltage in the synchronously rotating reference frame. If

the dc link quantities are made use of, variable coordinate transformations are avoided [15, 31]. This has been innovatively used in the implementation of vector control strategy simplifying steps in the hardware and software.

2. Influences of saturation have been outlined in details both for tuned and detuned conditions of the drive. The effect of rotor resistance variation has been accounted simultaneously with the corresponding changes in the magnetizing inductance. Fundamental component of motor terminal voltage, dc link power and current, and the saturation characteristic (expressed in the form of $i = a_1\lambda + a_5\lambda^5$) have been used to evaluate the magnetizing inductance for use in the general analysis to study the effects of parameter change and also for simulation of the drive system.
3. All the three compensation schemes take care of both rotor resistance and magnetizing inductance variation. The schemes being basically dependent on dc link data require less hardware and program steps for signal processing.
4. Robustness of the drive system has been studied applying the concept of Kharitonov's theorem [94] and then justified from the simulation results of the system for both parametric and torque disturbances.
5. Implementation of the proposed vector control strategy with the parameter compensation schemes has been carried out with two microcomputers and one PC/AT with data acquisition systems. Two microprocessor-based speed estimation methods are developed with optical encoders for use with control schemes for two induction motors (one squirrel cage and the other slip ring type).

6. 'Bond Graph' and 'Nodal method' provide an organised way to write equations for a dynamic system. Tedious way of writing equations and their arrangement and rearrangement for framing state equations can be avoided in the proposed simulation techniques. Many of the restrictive assumptions in respect of the inverter and motor behaviour in simulation study of CSI-IM system are not required when the system is modelled by 'Bond Graph' and 'Nodal Method'.

1.4 DISSERTATION OUTLINE

Chapter I begins with a general discussion on drive systems, inverters, field oriented control pertaining to induction motor, controllers etc. This is followed by an overview of a few selected contributions to indicate, in brief, the various studies that have been made over the past two decades in the area of vector controlled induction motor. The chapter concludes with the objectives of the study presented in the dissertation.

Chapter II commences with the two-axis model of the induction machine in a rotating reference frame and proceeds, under justifiable assumptions, to obtain a general model involving the dc link and the induction motor. Then the principle of field orientation control is introduced and key equations relating various parameters and currents and voltages of both dc link and machines are derived. An equivalent circuit model, valid under rotor-flux orientation scheme, is also developed. In the next step, vector control circuit configuration is presented and the control sequence is explained. This chapter ends with

a digital simulation procedure in which a continuous model is adopted for the rectifier-inverter and induction motor combination in synchronous reference frame and linear difference equations for controllers.

Chapter III discusses at length the effects of parameters variation on the steady state and dynamic performances of the speed controlled system originally set to work under field oriented condition. Analytic expressions are presented for qualitative explanations of the deviation of key quantities such as torque, flux level, current components terminal and inverter input voltages etc. Unlike in many publications simultaneous effects of saturation and rotor resistance variations are considered.

Chapter IV proposes three schemes for detuning correction by updating the control gains appropriately after identifying the rotor parameter deviations. In one scheme, the rotor resistance is evaluated from air gap power while the inductance from reactive power. Other two schemes make use of the dc link voltage and torque component of stator current to compensate for parameter deviations. Simulation results are furnished to verify the feasibility of the adaptation algorithm.

Chapter V presents controller design and robust stability study of an induction motor with field orientation control. A possible minimum value of $\|H\|_\infty$ for the transfer function is ascertained in the selection of a particular set of PI-controller constants with a prescribed bandwidth. Robustness of the drive system is studied by

testing the segments of the interval plant resulting out of parametric variations.

Chapter VI presents the implementation of the indirect vector control scheme, inclusive of the adaptation algorithms, with two microcomputers (8086 with i-8087) and a PC/AT, using minimal hardware. The two microcomputers were used to control the converter and inverter, and the PC/AT was to indicate the controller and the drive conditions as well as to estimate the rotor parameters and execute the algorithms required for the adaptation processes. The programs for the PC/AT were in Turbo-Pascal. One of the microcomputer was equipped with 12-bit data acquisition system and the PC/AT with Burr Brown's PCI system having 12-bit data acquisition module. This chapter also details innovative methods to estimate instantaneous speed with optical encoders. The system was tested on a squirrel cage motor (3.75 kw) as well as on a slip ring machine (0.75 kw) both coupled with dc generators. The chapter furnishes extensive test results for various operating conditions with and without compensation schemes. The operating conditions studied were start-up transients, step change in torque and speed, step change in rotor resistance (for slip ring machine) etc. Corresponding predicted results are also furnished.

Chapter VII presents development of transient models, based on 'Bond graph' approach and 'Nodal' method, for simulation of CSI-IM systems and furnishes simulation results for different operating conditions, viz. normal, abnormal and transient conditions. In

conclusion it compares some of the results with those obtained by other methods to establish the acceptability of the models for simulation.

Finally, general conclusions are drawn in chapter VIII with a few proposals for further research work related to the present work.

CHAPTER II

MATHEMATICAL MODEL AND SIMULATION

2.1 BASIC EQUATIONS OF INDUCTION MACHINE

The study of inverter driven induction motor requires a suitable mathematical model that could easily be coupled with the dc system on the inverter input side. According to two-axis machine theory, when a symmetrical induction motor is described in a reference frame that rotates in synchronism with the stator mmf, all the ac phase-variable sets get transformed into equivalent dc variables and can readily be combined with the variables on the input side of the inverter. Under the usual assumptions of no hysteresis, eddy currents, space harmonics, etc, the basic system equation of an induction motor in terms of a 2-phase model (d-q variables) in an arbitrary synchronous reference frame is

$$\begin{bmatrix} v_{ds} \\ v_{qs} \\ 0 \\ 0 \end{bmatrix} = \begin{bmatrix} R_s+pL_s & -L_s\omega_e & pL_m & -L_m\omega_e \\ \omega_e L_s & R_s+pL_s & L_m\omega_e & pL_m \\ pL_m & -\omega_{sl}L_m & R_r+pL_r & -L_r\omega_{sl} \\ L_m\omega_{sl} & pL_m & L_r\omega_{sl} & R_r+pL_r \end{bmatrix} \begin{bmatrix} i_{ds} \\ i_{qs} \\ i_{dr} \\ i_{qr} \end{bmatrix} \qquad (2.1)$$

Fig.2.1 shows the spatial relationship between the axes of different frames of reference viz., stator-fixed, rotor-fixed, and synchronously rotating d-q reference frames.

The electromagnetic torque is

$$T_{em} = \frac{3}{2} P_p (\lambda_{qr} i_{dr} - \lambda_{dr} i_{qr}) \quad (2.2)$$

where

$$\lambda_{dr} = L_r i_{dr} + L_m i_{ds} \quad (2.3a)$$

$$\lambda_{qr} = L_r i_{qr} + L_m i_{qs} \quad (2.3b)$$

The variables λ_{dr} and λ_{qr} imply linkages with the rotor circuits along the synchronously rotating d- and q-axis respectively.

Substitution of (2.3a) and (2.3b) in (2.2) yields

$$T_{em} = \frac{3}{2} P_p L_m (i_{qs} i_{dr} - i_{ds} i_{qr}) \quad (2.4)$$

With reference to Fig.2.1, if i_{dq} is the magnitude of the vector current $\bar{I}_{dq}$, the corresponding d- and q-axis currents in the synchronous reference frame are

$$\left.\begin{aligned} i_{ds} &= i_{dq} g_{ds} \\ i_{qs} &= i_{dq} g_{qs} \end{aligned}\right\} \quad (2.5)$$

where

$$\left.\begin{aligned} g_{ds} &= \cos\theta \\ g_{qs} &= \sin\theta \end{aligned}\right\} \quad (2.6a)$$

which imply that $\tan\theta = \dfrac{i_{qs}}{i_{ds}}$ (2.6b)

For the current-fed induction motor drive system in Fig.2.2, the power-balance equation, with no loss in the inverter, is

$$v_I i_R = \frac{3}{2} (v_{ds} i_{ds} + v_{qs} i_{qs}) \quad (2.7)$$

Use of (2.5) in (2.7) yields

$$v_I i_R = \frac{3}{2} i_{dq} (v_{ds} g_{ds} + v_{qs} g_{qs}) \quad (2.8)$$

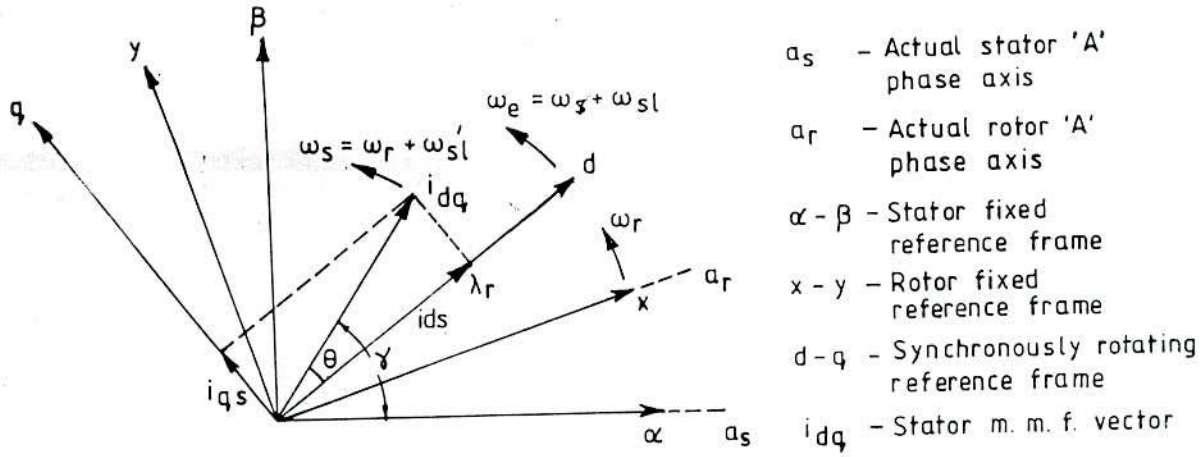

Fig. 2.1 Relation between various co-ordinate systems and principle of field orientation

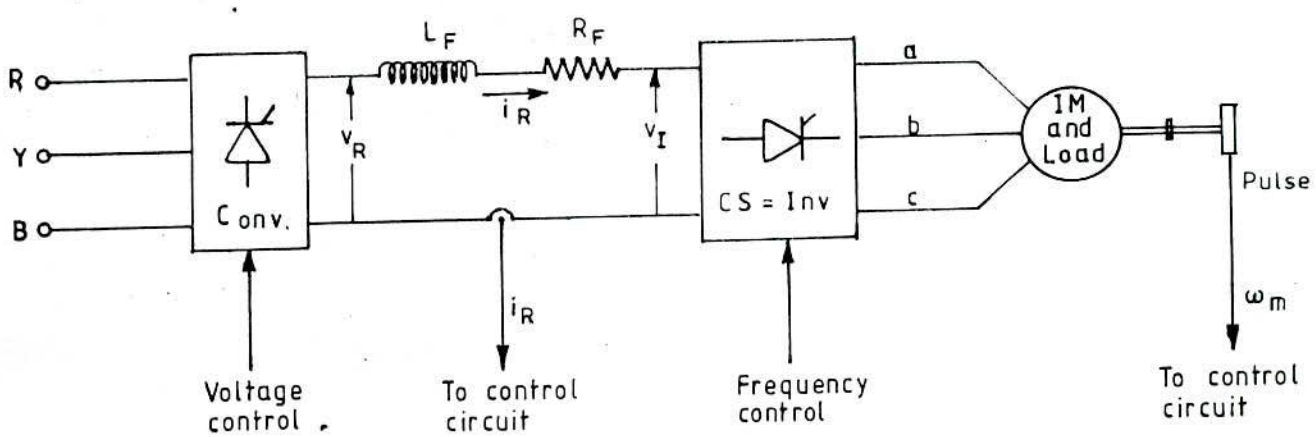

Fig. 2.2 CSI-IM drive system

If the commutation effect is ignored, the stator current of the induction motor, supplied by a current source inverter, is a 120^0 wide square wave of magnitude i_R in each half cycle. Other than causing ohmic losses, the harmonic currents have no significant contribution to the generation of net torque [75]. Neglecting the harmonics, the fundamental component of vector current magnitude i_{dq} in (2.8) is related to the dc link current i_R by

$$i_{dq} = \frac{2\sqrt{3}}{\pi} \; i_R \text{ (fundamental component)} \qquad (2.9)$$

$$= i_R'$$

Substitution of (2.9) in (2.8) gives

$$v_I = \frac{3\sqrt{3}}{\pi} (v_{ds} \, g_{ds} + v_{qs} \, g_{qs})$$

or, $$v_I' = v_{ds} \, g_{ds} + v_{qs} \, g_{qs} \qquad (2.10)$$

where

$$v_I' = \frac{\pi}{3\sqrt{3}} \, v_I \qquad (2.10a)$$

Although the steady state operation of controlled current induction motor drives does neither involve the stator input voltage nor the rectifier output voltage responsible for maintaining the dc link current at the required level, but the transient behaviour of the dc link current significantly affects the dynamic behaviour of the CSIM drives. Hence, it would be in order to develop dynamic equations relating the dc link circuit with system parameters and other variables.

For the dc link circuit (Fig.2.2) the voltage equation is

$$v_R = v_I + (R_f + p \, L_f) \, i_R \qquad (2.11)$$

Combining (2.10a) and (2.11), and using the relation in (2.9), yields

$$v_R' = v_I' + (R_f' + pL_f')\, i_R' \tag{2.12}$$

where

$$v_R' = \frac{\pi\, v_R}{3\sqrt{3}}$$

$$R_f' = \frac{\pi^2}{18} R_f$$

$$L_f' = \frac{\pi^2}{18} L_f$$

Rectifier output power and inverter input are given by (2.13) and (2.14) respectively

$$P_R = v_R\, i_R = \frac{3}{2} v_R'\, i_R' \tag{2.13}$$

$$P_I = v_I\, i_R = \frac{3}{2} v_I'\, i_R' \tag{2.14}$$

From the relations in (2.5) and (2.9) it is noted that

$$i_R' = i_{ds}\, g_{ds} + i_{qs}\, g_{qs} \tag{2.15}$$

Substituting the expression for v_{ds} and v_{qs} from (2.1) in (2.10) and using (2.5) and (2.9), one obtains

$$v_I' = (R_s+pL_s)\, i_R' + L_m\, (g_{ds}\, pi_{dr}+g_{qs}\, pi_{qr}) + L_m\, \omega_e\, (g_{qs}\, i_{dr}-g_{ds}\, i_{qr}) \tag{2.16}$$

using (2.16) in (2.12) gives

$$v_R' = [(R_s+R_f')+(L_s+L_f')p]\, i_R' + L_m(g_{ds}\, pi_{dr}+g_{qs}\, pi_{qr}) + L_m\, \omega_e(g_{qs} i_{dr}-g_{ds} i_{qr}) \tag{2.17}$$

2.2 FIELD ORIENTATION

2.2.1 Principle and basic equations of a field-oriented induction motor

In one approach for framing the relevant mathematical relations to understand and explain the vector control of induction motor, the synchronous reference frame is so aligned that its one axis, say the d-axis, coincides at every instant with a defined flux-vector in the machine. As discussed earlier, the flux-vector may correspond to stator flux, air-gap flux or the rotor flux. Derivations and the study to follow are for the orientation scheme in which the rotor flux-linkage vector remains in space phase with the d-axis of the synchronous reference frame. For such constraints

$$\lambda_{dr} \triangleq L_m i_{ds} + L_r i_{dr} = \lambda_r \tag{2.18a}$$

$$\lambda_{qr} \triangleq L_m i_{qs} + L_r i_{qr} = 0 \tag{2.18b}$$

which by (2.5) and (2.9) becomes

$$L_m i'_R g_{ds} + L_r i_{dr} = \lambda_r \tag{2.19a}$$

$$L_m i'_R g_{qs} + L_r i_{qr} = 0 \tag{2.19b}$$

Elimination of i_{dr} and i_{qr} in (2.17) by (2.19) gives

$$v'_R = [(R_s + R'_f) + (L_{\sigma s} + L'_f)p]i'_R + \frac{L_m \omega_e g_{qs}}{L_r} \lambda_r + \frac{L_m g_{ds}}{L_r} p\lambda_r \tag{2.20}$$

where $L_{\sigma s} (= L_s - \frac{L_m^2}{L_r})$ is the leakage inductance.

Eqn. 2.20 is similar to the voltage equation of a dc machine except the last term. Even if the field excitation changes, the armature voltage equation of a dc machine does not contain any transformer emf, but (2.20) indicates that the dc voltage applied to the inverter must contain a component to counteract the transformer emf in the event of the variation of rotor flux linkage.

Applying the conditions in (2.18) to the rotor circuit emf equations, the third and fourth rows of (2.1) can be written as

$$R_r\, i_{dr} + p\lambda_r = 0 \tag{2.21a}$$

$$\omega_{sl}\, \lambda_r + R_r i_{qr} = 0 \tag{2.21b}$$

Eliminating i_{dr} and i_{qr} by (2.19),

$$p\, \lambda_r = \frac{R_r}{L_r}\, (L_m\, i'_R\, g_{ds} - \lambda_r) \tag{2.22a}$$

$$\omega_{sl}\, \lambda_r = \frac{R_r}{L_r}\, L_m\, i'_R\, g_{qs} \tag{2.22b}$$

which can be re-written as

$$\lambda_r = \frac{L_m\, i_{ds}}{(1+\tau_r p)} \tag{2.23}$$

and

$$\omega_{sl} = \frac{L_m\, i_{qs}}{\tau_r\, \lambda_r} \tag{2.24}$$

By the definition of slip-speed, as implied in (2.1), the angular speed of the rotor flux vector, i.e.,of the rotating reference frame is given by

$$\omega_e = \omega_r + \frac{L_m\, i_{qs}}{\tau_r\, \lambda_r} \tag{2.25}$$

For constant rotor flux operation,

$$\omega_e = \omega_r + \frac{R_r\ i_{qs}}{L_r\ i_{ds}} \qquad (2.26)$$

It is to be noted that ω_{sl} is the slip speed of the rotor with respect to the rotating d-axis (Fig.2.1), i.e., the rotor flux vector. Torque angle changes with the change in the operating condition of the machine, hence during the transitional state stator mmf vector must move at a speed different from that of the rotor flux vector. Slip speed ω'_{sl} of the rotor with respect to the stator current vector must be given by

$$\omega'_{sl} = \omega_{sl} + \frac{d\theta}{dt} \qquad (2.27)$$

Angular speed of stator mmf vector is then

$$\omega_s = \omega_r + \omega'_{sl} \qquad (2.28)$$

$\frac{d\theta}{dt}$ should be made available in terms of measurable, i.e., transduced, and/or estimated quantities. Two methods are suggested for calculating the value of $\frac{d\theta}{dt}$.

Method 1

For the field oriented condition the torque angle θ can be expressed as

$$\cos\theta = \frac{i_{ds}}{i_{dq}} \qquad (2.29)$$

and

$$\sin\theta = \frac{i_{qs}}{i_{dq}} \qquad (2.29)$$

For constant rotor flux operation, implying constancy of i_{ds}, differentiation of (2.29) and use of (2.30) gives

$$\frac{d\theta}{dt} = \frac{i_{ds}}{i_{qs}} \frac{1}{i'_R} \frac{di'_R}{dt} \qquad (2.31)$$

It may be noted that $i_{dq} = i'_R$ (cf 2.9)

Use of (2.12) in (2.31) leads to

$$\frac{d\theta}{dt} = \frac{i_{ds}}{i_{qs}} \frac{1}{i'_R} \left(\frac{v'_R - v'_I - R'_f i'_R}{L'_f} \right) \qquad (2.32)$$

Method 2

Under constant rotor flux operation, elimination of the stator currents from (2.23), (2.24), (2.29) and (2.30) gives

$$\tan \theta = \frac{\omega_{sl} L_r}{R_r} \qquad (2.33)$$

Differentiation of (2.33) with respect to time and use of (2.29) then yields

$$\frac{d\theta}{dt} = \frac{L_r}{R_r} \frac{i_{ds}^2}{i'^2_R} \frac{d\omega_{sl}}{dt} \qquad (2.34)$$

Eliminating $\frac{L_r}{R_r}$ from (2.33) and (2.34) and writing $\tan\theta$ for i_{qs}/i_{ds} yields

$$\frac{d\theta}{dt} = \frac{i_{qs}\, i_{ds}}{i'^2_R} \frac{1}{\omega_{sl}} \frac{d\omega_{sl}}{dt} \qquad (2.35)$$

Expression for $\frac{d\theta}{dt}$ in (2.32) and (2.35) can conveniently be evaluated by digital processors. These issues are dealt with in a

latter section. v_I' in (2.32) needs be transduced while $\frac{d\omega_{sl}}{dt}$ in (2.35) requires computation. Depending upon the control circuitry and the strategies adopted, estimated or measured values are used for the remaining quantities.

By combining (2.2) and (2.18) the expression for the electromagnetic torque becomes

$$T_{em} = \frac{3}{2} p_p \frac{L_m}{L_r} \lambda_r i_{qs} \qquad (2.36)$$

Alternatively, it is evident from the voltage eqn.2.20 of the rotor-flux oriented induction machine that the electro-mechanical power P_{em} (cf. eqn.2.13) is

$$P_{em} = \frac{3}{2} \frac{L_m \omega_e g_{qs} \lambda_r}{L_r} i_R' \qquad (2.37)$$

The speed of the reference frame being ω_e/p_p mechanical radians per sec, the developed torque is obviously

$$T_{em} = \frac{P_P}{\omega_e} P_{em} = \frac{3}{2} p_p \frac{L_m}{L_r} \lambda_r i_R' g_{qs}$$

i.e., $$T_{em} = \frac{3}{2} p_p \frac{L_m}{L_r} \lambda_r i_{qs} \qquad (2.38)$$

which is the eqn.2.36.

Irrespective of the transient or steady state condition the torque function in (2.38) always holds for field oriented condition. Use of (2.5), (2.9) and (2.23) in (2.38) yields the following two widely used expressions for steady state torque

$$T_{em} = \frac{3}{2} P_p \frac{L_m^2}{L_r} i_{ds} i_{qs} \qquad (2.39a)$$

or, $$T_{em} = \frac{3}{2} P_p \frac{L_m^2}{L_r} i_R^{,2} \sin\theta \cos\theta \qquad (2.39b)$$

2.2.2 Block diagrams

Eqns. 2.23, 2.24, and 2.36 define rotor-flux oriented induction machine, and essentially reduce the control dynamics of an induction motor to those of a separately excited compensated dc motor. Controlling the magnitude of i_{ds} adjusts the rotor flux level through a first order time delay equal to the rotor circuit time constant, and for constant flux operation, generated torque becomes linearly related with i_{qs}. From equations 2.23 and 2.24 and 2.36 the decoupled condition of an induction motor from the view point of rotor flux field orientation can be represented by the block diagram in Fig. 2.3. The block diagram representation of a field oriented induction motor, arising from eqns. 2.20, 2.23 and 2.38 is illustrated in Fig. 2.4. For constant flux operation the block diagram in Fig. 2.4 reduces to the compact form as shown in Fig. 2.5, which will be found later to be more useful in determining the PI controller constants and/or in the study of the stability problems. Block diagrams in Figs. 2.4 and 2.5 represent the dynamic behaviour of the induction motor in the rotor flux reference frame.

Block diagram representations in Figs. 2.4 and 2.5 always hold for a current-fed induction motor. Though unknown, there exists inside the machine rotor flux linkage, and stator current vector can always be

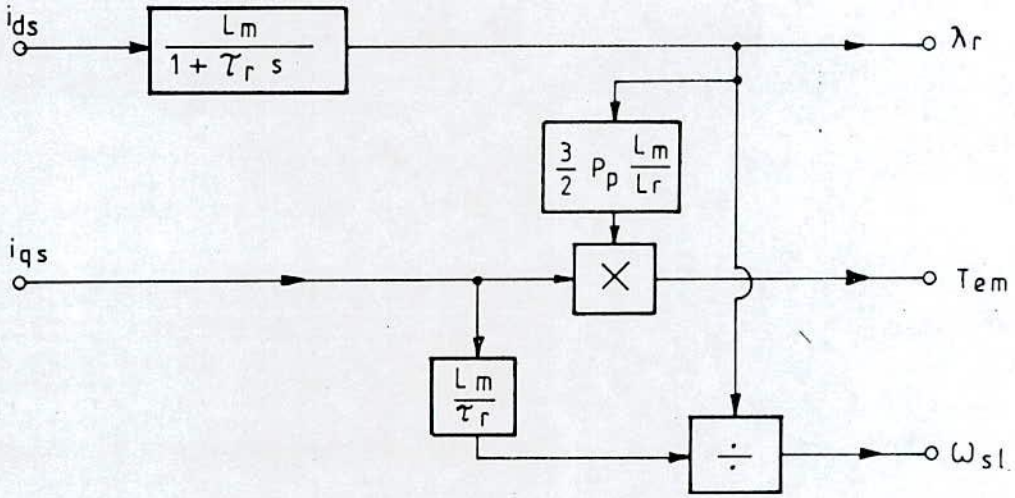

Fig. 2.3 Block diagram of induction motor model in rotor flux reference frame

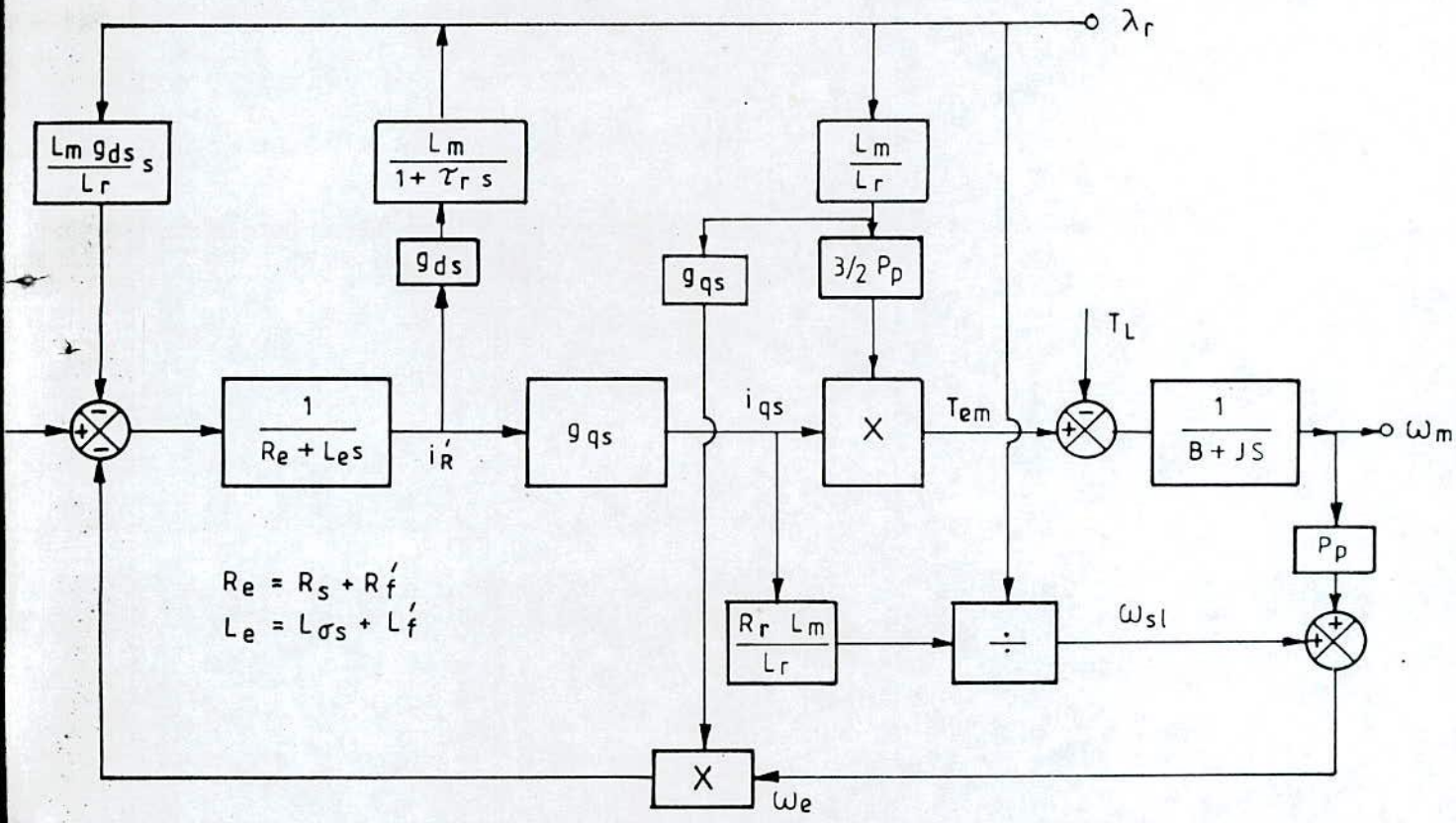

Fig. 2.4 Block diagram representation of rotor-flux oriented induction motor

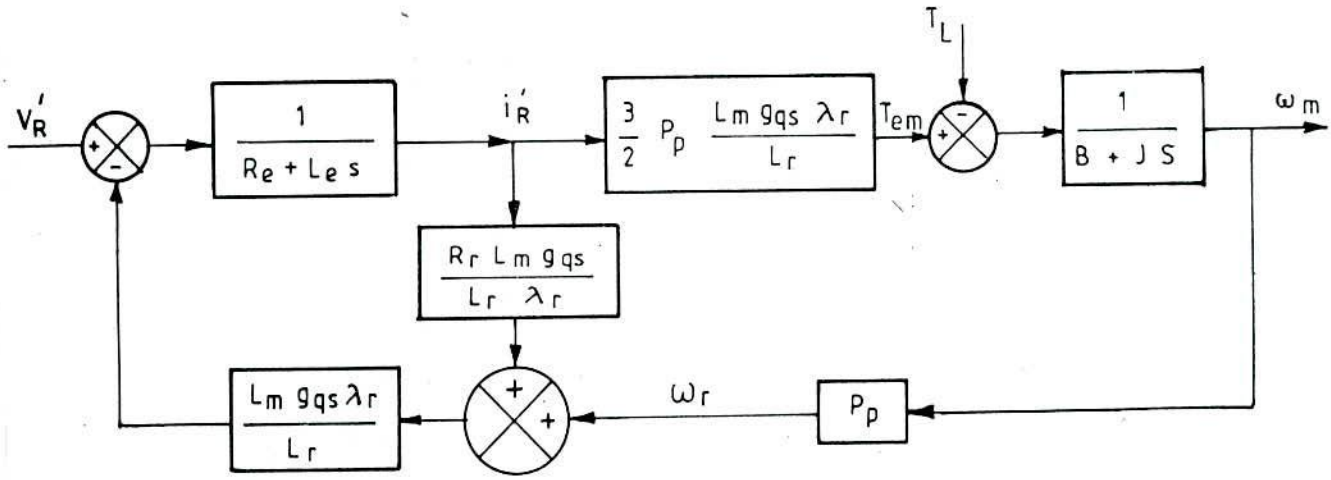

Fig. 2.5 Reduced from the block diagram representation in Fig. 2.4

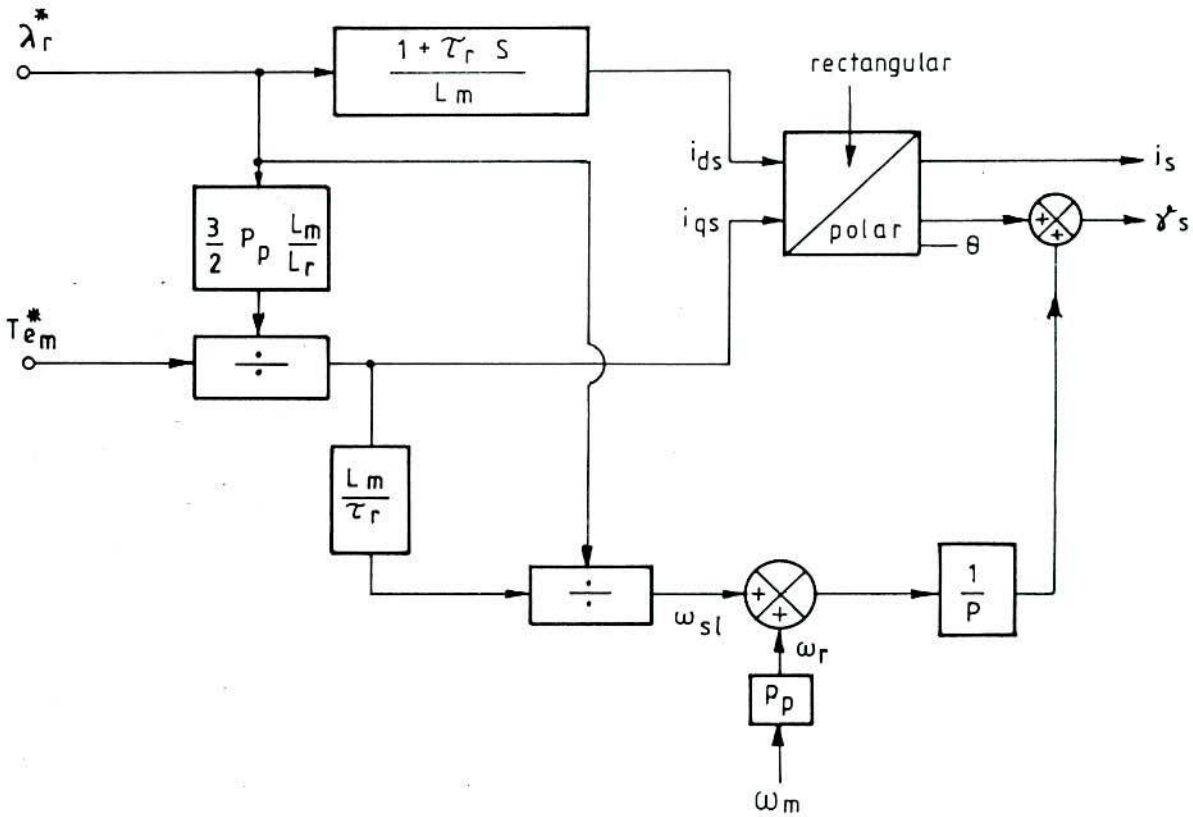

Fig.2.6 Decoupling controller for rotor flux orientation diagram and stator current vector orientation , rotor flux reference frame.

resolved along and perpendicular to the direction of rotor-flux vector. However, arbitrary change of the position of stator current vector does not lead to decoupled condition, i.e., independent control of flux and electromagnetic torque. With the field orientation control strategy, provision should exist for independent control of torque and flux components of the stator current vector i.e., i_{qs} and i_{ds} in the same way as used to control armature and field currents of a dc motor, and their generation from the command values of torque and flux respectively. These components decide the magnitude as well as the position of the stator current vector relative to the rotor-flux vector. This is achieved by taking the inverse of the model in Fig.2.3 to form the decoupling controller shown in Fig.2.6 for realization of field orientation of a current-fed induction motor.

2.3 METHOD OF IMPLEMENTATION

Based on the preceding analysis a control scheme has been formulated. The block schematic for a variable speed CSI-fed induction motor, using the field oriented control is shown in Fig. 2.7. The scheme uses (2.24) and (2.32) or (2.35) for orienting the stator current vector for complete decoupled control. The control strategy assumes that there is no variation of flux level and that the nominal machine parameters in the controllers and those of the actual machine are in agreement. In practice, flux level and its orientation change and parameter variation occurs necessitating corrective measures in the control strategy. Compensation schemes for parameter mismatch and flux deviation are considered in Chapter IV. In the control scheme,

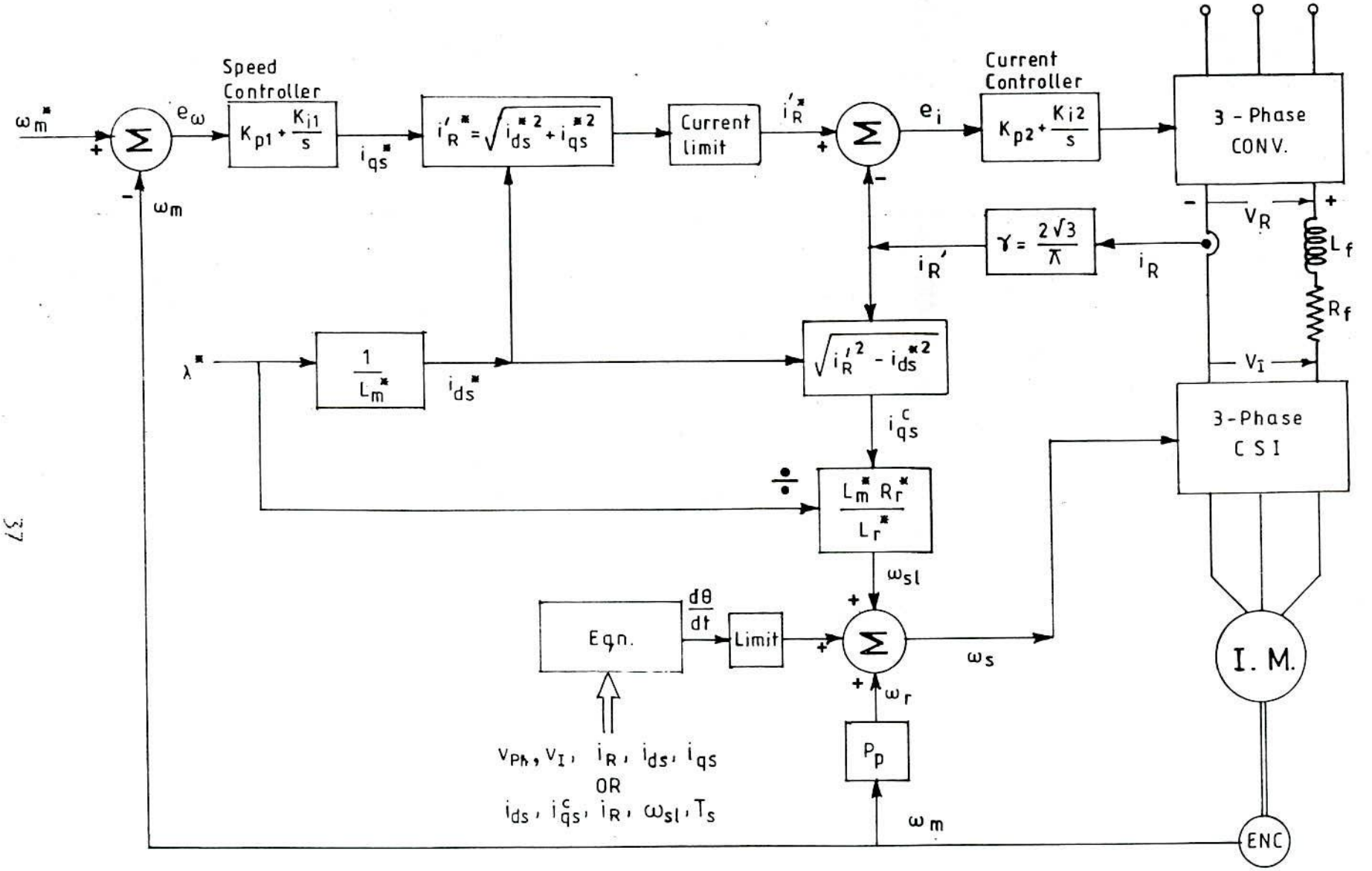

Fig. 2.7 Basic structure of a rotor flux oriented controller for adjustable speed CSI-fed induction motor drive

illustrated in Fig.2.7, the speed controller (PI type) generates the demanded stator torque current i^*_{qs} and the magnetizing current calculator furnishes the reference for the stator flux current, i.e., i^*_{ds}. As the dc link current of the CSI-IM drive bears a definite ratio with the stator current amplitude (fundamental component), the voltage reference for the rectifier is produced by comparing the commanded value of the fundamental stator current amplitude with the dc link current passing through the ratio block, indicated with r in Fig.2.7. This strategy of adjusting the stator current equal to its commanded value through the dc link current avoids the matrix coordinate transformation. The current error is processed through a PI controller to obtain the required output voltage from the converter.

Under field orientation condition, the rotor flux vector and the flux component of the stator current vector are supposed to remain in space phase and for constant flux operation i_{ds} in the machine ideally must remain equal to i^*_{ds}. This is assumed in the scheme. By reference to Fig.2.7, the stator torque current i_{qs} in the machine must then be

$$i_{qs} = i^c_{qs} \tag{2.40a}$$

where

$$i^c_{qs} = \sqrt{i'^2_R - i^{*2}_{ds}} \tag{2.40b}$$

Since a definite time will elapse before the actual stator current attains its commanded value, the slip frequency should correspond to actual stator current components i_{qs} and i_{ds} ($=i^*_{ds}$, by the scheme) rather than correspond to i^*_{qs} and i^*_{ds}. This may lead to excessive or

inadequate estimate of the slip frequency, particularly, during the initial period of the transient. Secondly, during the transient period stator mmf vector must move at a speed different from that of the d-q reference frame i.e., of i_{ds} vector. Then the slip speed of the rotor with respect to the stator mmf vector is obtained by adding a corrective term given by (2.32) or (2.35) to determine the frequency for proper alignment of the stator current vector. Limits for $d\theta/dt$ is incorporated for both the sides as a safe guard against the situations of highly changing current or any abnormal condition of the drive operation. It is noted from simulation study and later from experimental observation, that computation for slip frequency angle (integral of ω_{sl}), rotor position angle and knowledge of command torque angle may be dispensed with if an appropriate frequency is imparted to stator current.

2.4 DIGITAL SIMULATION

2.4.1 Motivation

Successful operation of a field oriented induction motor can not be achieved without feedback and/or feedforward control circuits. In fact, whatever may be the control strategies for controlling the motion of CSI-fed induction motor drives, control loops must be added for stabilization and to realize a desired operating condition. Such importance of feedback control calls for a detailed simulation study to understand the steady state behaviour as well as the dynamics of the drive system before embarking on the hardware realization. This is especially valuable to eliminate trial and error exercises on the

experimental set up, and also to assess the appropriateness of the control strategy and the various gain constants in the control loops that are supposed to produce desirable drive dynamics.

2.4.2 Mathematical model - induction machine and dc link

A mathematical model for the rectifier, inverter and induction motor combination has been established earlier in terms of two-axis equations in a rotating reference frame synchronous with the rotor flux. For simulation of the induction motor coupled to the dc link it is found convenient to model the induction motor in a reference frame synchronous with the stator excitation frequency and with the d-axis aligned along the stator current vector. For such realignment of the reference axis, the induction motor model, coupled with dc link quantities becomes

$$v_R' = [(R_s+R_f')+(L_s+L_f')p]\, i_R' + L_m\, pi_{dr}' - L_m\, \omega_s\, i_{qr}' \qquad (2.41a)$$

$$0 = L_m\, pi_R' + (R_r + pL_r)\, i_{dr}' - L_r\, \omega_{sl}'\, i_{qr}' \qquad (2.41b)$$

$$0 = L_m \omega_{sl}' i_R' + L_r\, \omega_{sl}'\, i_{dr}' + (R_r + L_r p)\, i_{qr}' \qquad (2.41c)$$

It may be noted that the d-axis being aligned along the stator mmf-vector eqns. (2.41) are obtained from eqn. 2.17 and last two rows of eqn. 2.1 by setting g_{ds} =1, g_{qs} = 0, i_{qs} = 0 and replacing i_{ds} by i_R', i_{dr} by i_{dr}' and i_{qr} by i_{qr}'. By eqn. 2.4 the electromagnetic torque then becomes

$$T_{em} = -\frac{3}{2}\, P_p\, L_m\, i_R'\, i_{qr}' \qquad (2.42)$$

The torque balance equation is written as

$$J \frac{d\omega_m}{dt} = -\frac{3}{2} P_p L_m i'_R i'_{qr} - B \omega_m - T_L \tag{2.43}$$

Equations (2.41) through (2.43) in state variable form becomes

$$p\underline{x} = L^{-1} [R\underline{x} + \underline{u}] \tag{2.44}$$

where

$$\underline{x}^T = [i'_R \; i'_{dr} \; i'_{qr} \; \omega_m] \tag{2.44a}$$

$$\underline{u}^T = [v'_R \; 0 \; 0 \; -T_L] \tag{2.44b}$$

$$R = \begin{bmatrix} -(R_s+R'_f) & 0 & \omega_s L_m & 0 \\ 0 & -R_r & \omega'_{sl} L_r & 0 \\ -\omega'_{sl} L_m & -\omega'_{sl} L_r & -R_r & 0 \\ 0 & 0 & -\frac{3}{2} P_p L_m i'_R & -B \end{bmatrix} \tag{2.44c}$$

$$L = \begin{bmatrix} L_s+L'_f & L_m & 0 & 0 \\ L_m & L_r & 0 & 0 \\ 0 & 0 & L_r & 0 \\ 0 & 0 & 0 & J \end{bmatrix} \tag{2.44d}$$

The magnitude of the rotor flux vector in the machine at any instant is given by

$$\lambda_r = \sqrt{(L_m i'_R + L_r i'_{dr})^2 + (L_r i'_{qr})^2} \tag{2.45}$$

Differential equations in (2.44) are solved by Runge-Kutta-Gill method for a time increment δt giving the value of $\underline{x}$ at the instant

$t_{k+1} = t_k + \delta t$. Such a method of computation tacitly assumes that v_R' in $\underline{u}$ and ω_{s1}' and ω_s in [R] are known. They are taken to be the values at $t_k = kT$ remaining constant over the interval $kT \leq t \leq (k+1)T$ where, T is the sampling time. New values are assigned to them at $t_{k+1} = (k+1)T$ for subsequent computation for $\underline{x}$ over the interval $(k+1)T < t < (k+2)T$ with the usual time-increment δt till $t = (k+2)T$ is arrived at. Computation for v_R', ω_{s1}' and ω_s are furnished in (2.53) (2.27) and (2.28) respectively.

2.4.3 Mathematical model - controllers

The control strategy is formulated for implementation through digital processors. Linear difference equations are used for various controller sections, and are formed from discrete transfer function (Z-transforms) of the controllers.

A PI controller (Fig.2.7) in frequency domain is represented as

$$\frac{M(s)}{E(s)} = K_p + \frac{k_1}{s} \qquad (2.46)$$

Applying the bilinear transformation $s = \frac{2}{T}\left(\frac{z-1}{z+1}\right)$ with T as the sampling time and then taking the inverse z-transform gives

$$m(kT) = m(\overline{k-1}\ T) + (k_p + \frac{k_1 T}{2}) e(kT) - (k_p - \frac{k_1 T}{2}) e(\overline{k-1}\ T) \qquad (2.47)$$

where e(kT) and m(kT) are the respective values at the kT-th instant.

If the rotor speed is passed through a first order filter (Fig.2.8) one can obtain

$$\omega_{mf}(s) = \frac{k_f}{1+\tau_f s}\ \omega_m(s) \qquad (2.48)$$

where k_f is the gain of the filter and τ_f is the time constant of the filter. The difference equation to determine the input to the speed

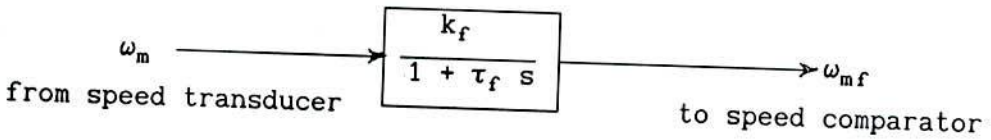

Fig. 2.8 First order filter in speed feedback loop

comparator is obtained by applying the above bilinear transformation and taking the inverse z-transform.

$$\omega_{mf}(kT) = \frac{T\,k_f}{1+2\tau_f}\,[\omega_m(kT) + \omega_m(\overline{k-1}\ T)] - \frac{T-2\tau_f}{T+2\tau_f}\,\omega_{mf}\ (\overline{k-1}\ T) \qquad (2.49)$$

2.4.4 Set values

In order to obtain the reference value for the torque component of the stator current difference equation (2.47) is applied to the PI controller 1 (Fig.2.7).

$$i^*_{qs}(k) = i^*_{qs}(k-1) + (k_{p1} + \frac{k_{i1}T}{2})\,e_\omega(k) - (k_{p1} - \frac{k_{i1}T}{2})e_\omega(k-1) \qquad (2.50)$$

where $e_\omega = \omega^*_m - \omega_{mf}$

Magnitude of the commanded current vector is given by

$$i'^*_R = \sqrt{i^{*2}_{qs} + i^{*2}_{ds}} \qquad (2.51)$$

Application of the difference eqn.2.47 to the controller 2

(Fig.2.7) yields the control voltage $v_c(k)$ for the converter at the kT-th instant.

$$v_c(k) = v_c(k-1) + (k_{p2} + \frac{k_{i2}\, T}{2})\, e_1(k) - (k_{p2} - \frac{k_{i2} T}{2})\, e_1(k-1) \qquad (2.52)$$

where $e_1 = i_R'^{*} - i_R'$

converter output voltage v_R' is given by

$$v_R'(k) = k_c\, v_c(k)\, \frac{\pi}{3\sqrt{3}} \qquad (2.53)$$

The required angular velocity of the rotor-flux vector at any instant to attain the desired position with respect to the rotor is calculated from (2.54) which, in the discrete time system, is expressed as follows

$$\omega_e(k) = P_p\, \omega_{mf}(k) + \frac{R_r}{L_r} \frac{i_{qs}(k)}{i_{ds}^{*}} \qquad (2.54)$$

The adjusted angular speed of the stator mmf vector at the instant t = kT to maintain the required space phase angle, i.e., the torque angle, from the rotor flux-vector is given by

$$\omega_s(k) = \omega_e(k) + \frac{i_{qs}(k)\, i_{ds}^{*}\, [\omega_{s1}(k) - \omega_{s1}(k-1)}{T[i_R'^{2}(k)\ \ \omega_{s1}(k)\ ]} \qquad (2.55)$$

2.4.5 Flow chart - simulation algorithm

The sequence of computation for the complete simulation of the CSI-IM drive system, based on the above continuous model of the dc link-IM system and the discrete-time equations for the controller sections, is summarised in the form of a flow-chart in Fig.2.9. The flow chart has the provision of starting the machine from rest.

2.5 SIMULATION RESULTS

The performance evaluation of the control scheme was made by simulation on a digital computer (HP1000). Parameters of the squirrel cage motor (Machine I) and the dc link filter as well as the PI controller gains used in the tests are listed in Appendix I. Sampling time for the speed and the current controllers was 2ms. Rotor flux command was set at its rated value and the stator magnetizing current (i^*_{ds}) was obtained from the nominal magnetising inductance. Series of digital simulation tests were carried out and some typical results are demonstrated in Figs.2.10 through 2.12 that present the behaviour of some important control variables following the start up and step changes in torque and speed.

Fig. 2.10 shows the starting of motor from rest with set speed 105 rad(mech) per sec and load torque 6.5 Nm (including friction). The drive attains its set speed quite fast with little overshoot (8%) over a short duration and the flux level shows minor ripples around its set value during the transient period. The identical profiles of ω_{sl}, T_{em} and i_{qs} and the almost linear relation between the curves indicate the capability of the drive system to work in a decoupled manner. In spite

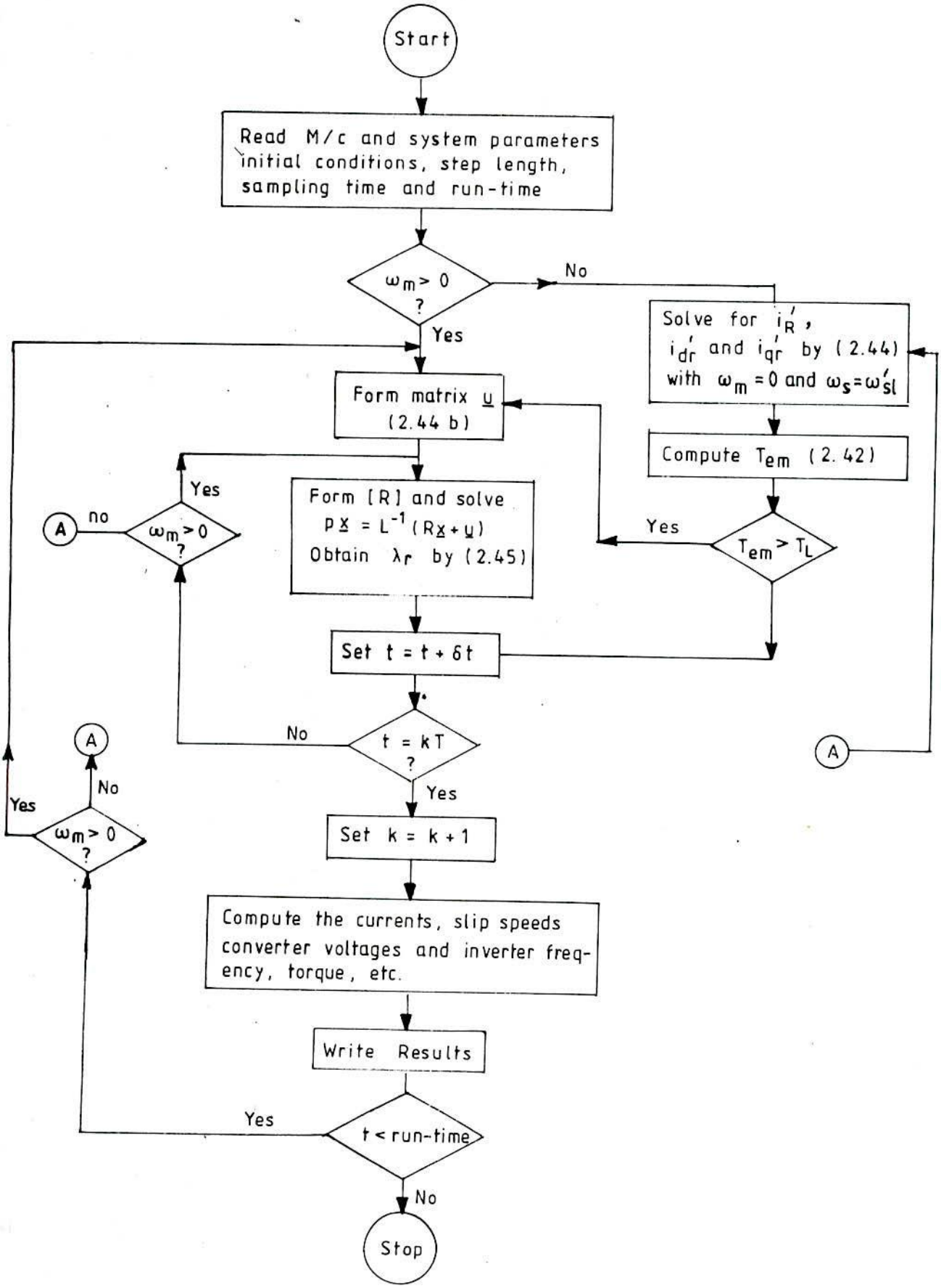

Fig. 2.9 Computational sequence for simulation

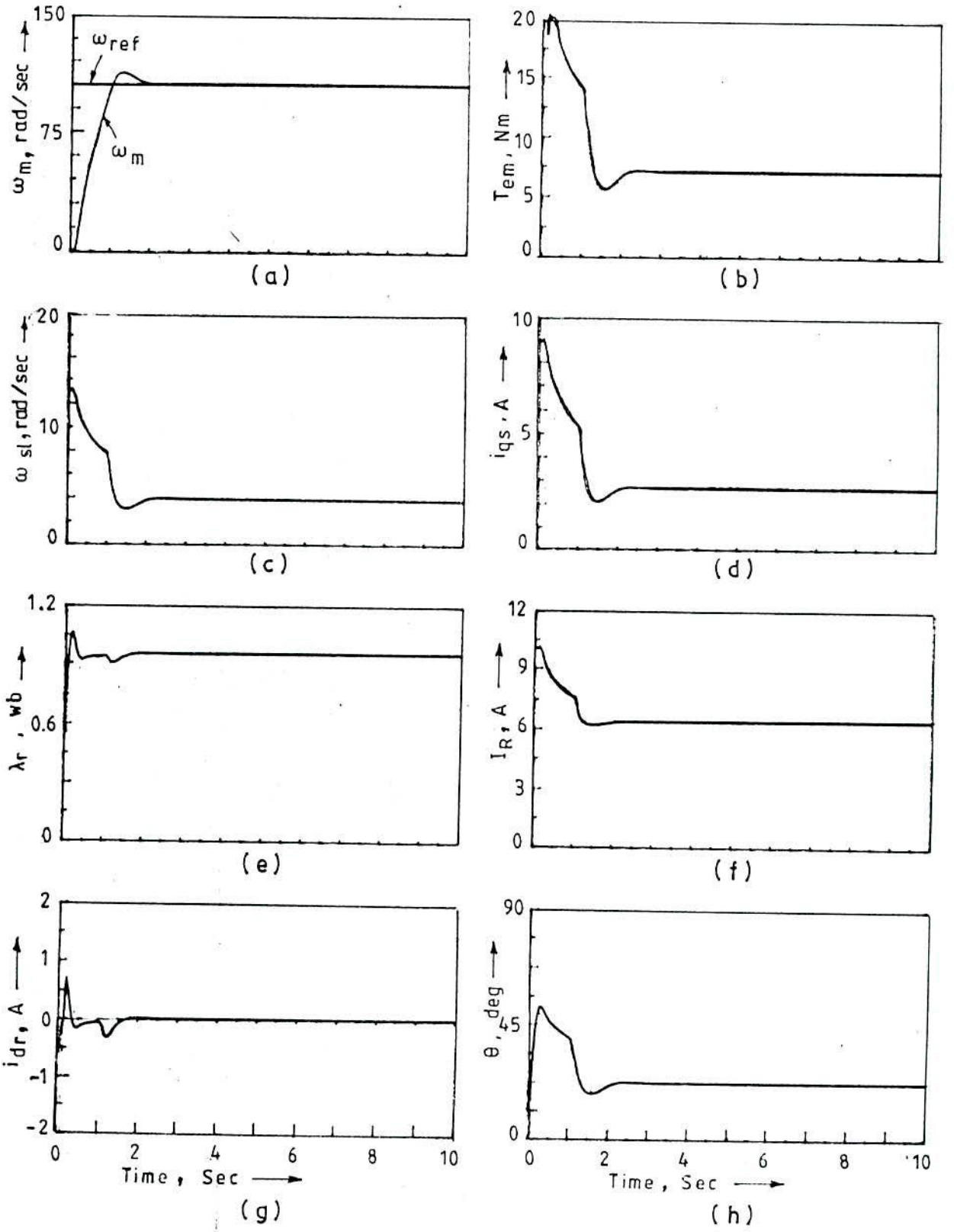

Fig. 2.10 Simulation results for starting transients in Fig. 2.7 for step change in reference speed with load torque 7.0 Nm (Machine-I)

of the absence of flux feedback the results of the start from rest are indicative of the effectiveness of the control scheme.

Fig.2.11 presents the behaviour for sudden change in the set speed from 105 rad/sec to 130 rad/sec. As before, simulation results confirm decoupled operation. This is evident from Fig.2.11(e). Minor deviation of the rotor flux from its set value is noted during the settling period, and i_{dr} (Fig.2.11g) too departs very little from the zero value to which it settles in the steady state. The drive responds to the new set speed quite fast with little overshoot.

Lastly, Fig. 2.12 demonstrates the response produced by a step change in the load torque from 6.5 to 9.0 Nm. The response to the changed torque shows negligible deviation in speed and minor oscillations in the rotor flux during the transient period. In the figure ω_{sl}, T_{em} and i_{qs} (Figs.2.12c,2.12b,2.12d) maintain near linear relations and display the similar variations in their plots. Deviation of T_{em} from T_L (Fig.2.12b) in the steady state is due to viscous torque.

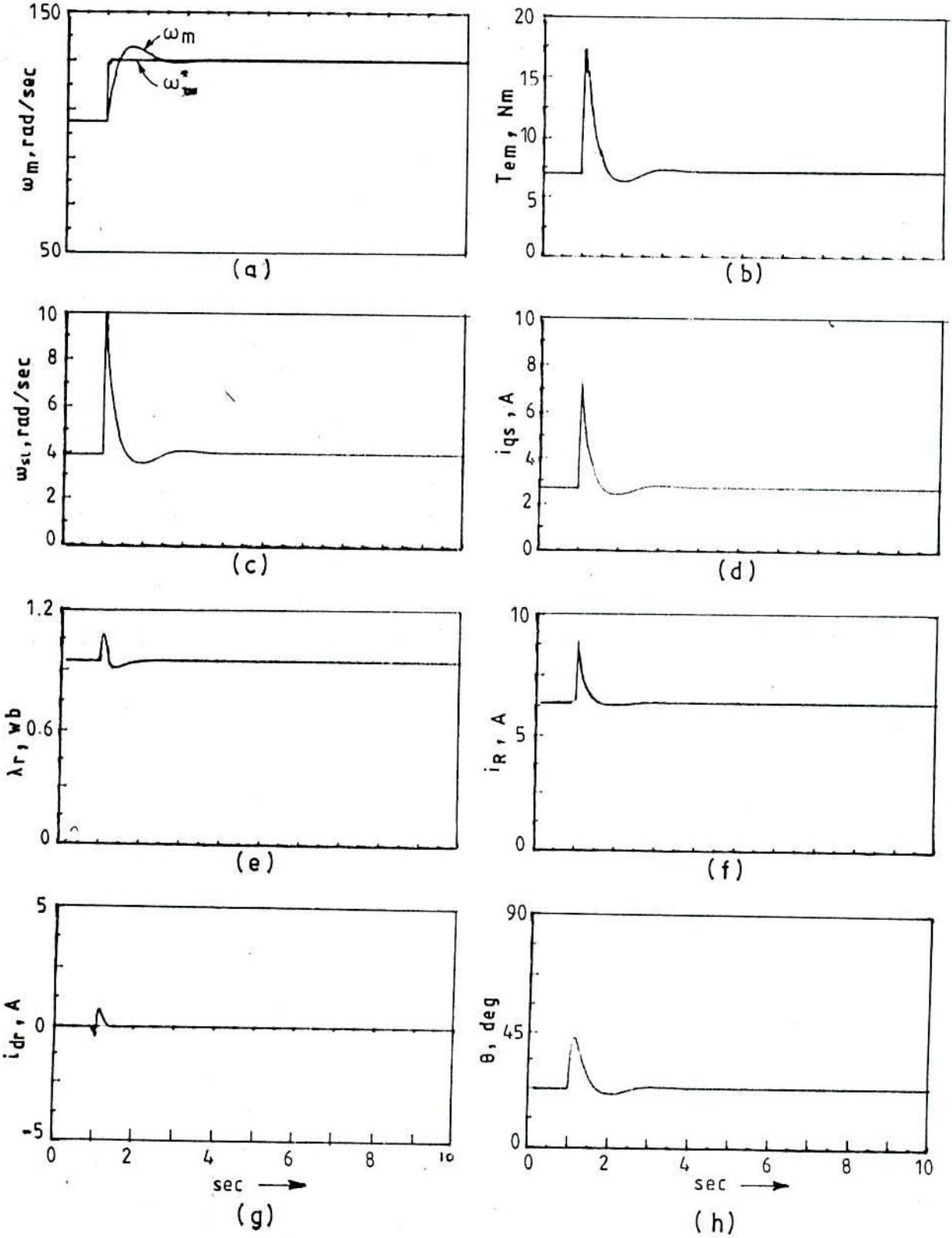

Fig. 2.11 Simulation results for responses of system in Fig. 2.7 to step change in reference speed (105 to 130 rad/sec) with load torque 7.0 Nm

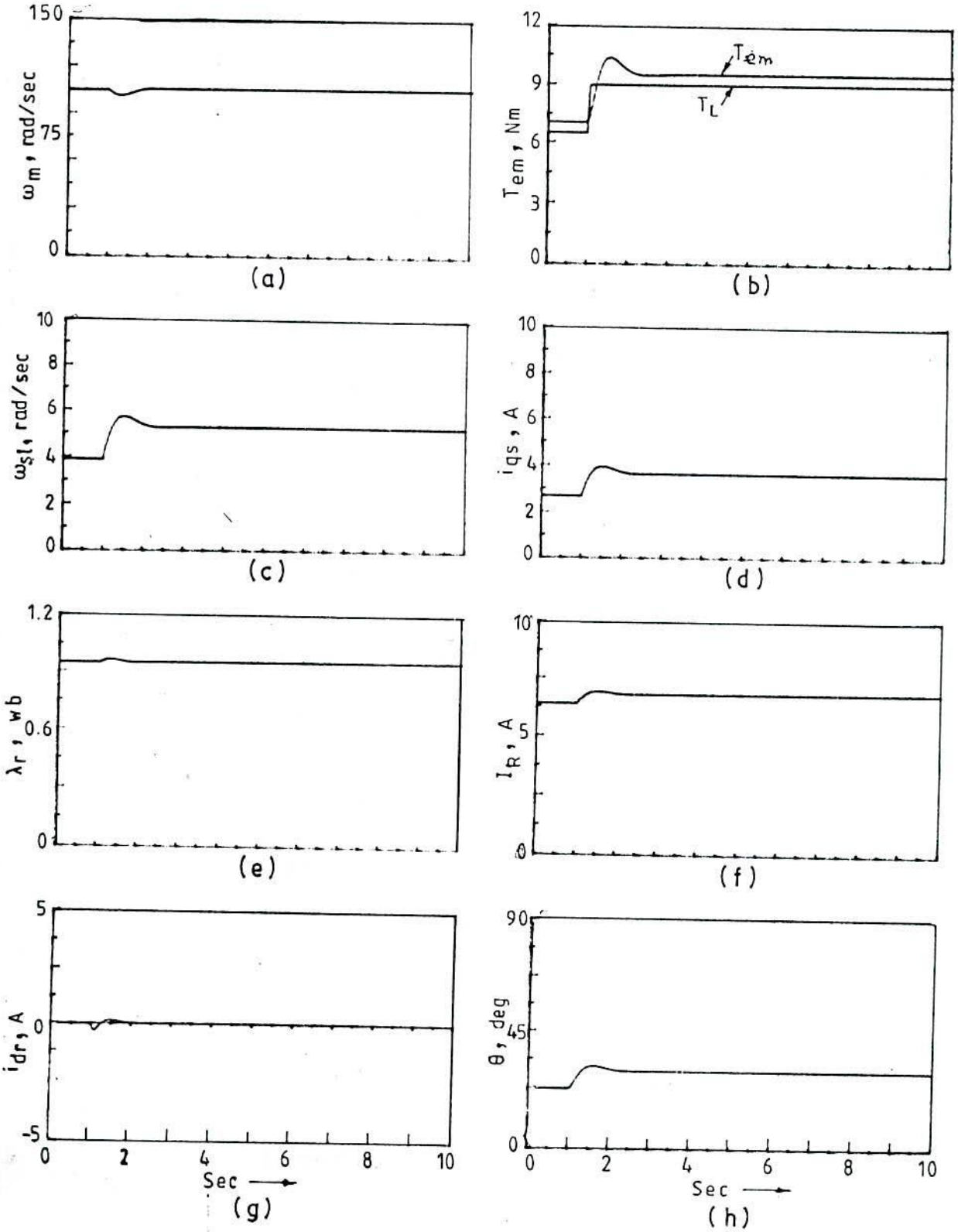

Fig. 2.12 Simulation results for responses of system in Fig. 2.7 to step change in load torque (6.5 to 9.0 Nm) with the reference speed set at 105 rad/sec

CHAPTER III

EFFECTS OF PARAMETER DEVIATION

3.1 INTRODUCTION

Precise decoupling torque and flux channels requires information regarding instantaneous rotor flux position and its magnitude, and the appropriate orientation of the stator current vector in relation to the rotor flux vector. In the direct method of field orientation control (DFOC) the rotor flux vector is ascertained from direct measurement of air-gap flux vector using sensing devices in the machine. In the indirect method of field orientation control (IFOC) rotor flux-vector is estimated either (i) through flux observer using motor line voltages, phase currents and machine parameters or (ii) from the commanded values of flux and torque (speed error) and the estimated slip-angle and rotor angle. For correct tuning, the torque and the flux components of stator current-vector and slip value inside the machine must agree with the reference values (i^*_{qs}, i^*_{ds} and ω^*_{sl}) generated outside by the controllers from the reference values of torque (speed error) and flux. (cf. eqns. 2.23, 2.36, 2.24 and 2.28). The key relations involving the commanded values and the nominal parameters of the machine are (cf. eqns. 2.23, 2.36, 2.24 and 2.28)

$$i^*_{ds} = \frac{1}{L^*_m}\left(1+\frac{L^*_r}{R^*_r}p\right)\lambda^*_r \qquad (3.1a)$$

$$i_{qs}^{*} = \frac{2}{3\,P_p}\;\frac{L_r^{*}}{L_m^{*}}\;\frac{T_{em}^{*}}{\lambda_r^{*}} \qquad (3.1b)$$

$$\omega_{sl}^{*} = \frac{L_m^{*}}{L_r^{*}}\;\frac{R_r^{*}}{\lambda_r^{*}}\;i_{qs}^{*} \qquad (3.1c)$$

$$\omega_s^{*} = \omega_r + \omega_{sl}^{*} + \frac{d\theta}{dt} \qquad (3.1d)$$

The above equations indicate the dependence of indirect field orientation control strategy heavily on the machine parameters used in the feedforward control algorithm. Any mismatch between the parameters used in the controllers and those of the motor results in detuning. Rotor resistance of the machine changes with temperature and may exceed its nominal value by 50% for a temperature rise of 130^{o} above the ambient value, and the inductance values depend on flux levels. In certain cases flux levels either need be varied to get better performance [78] or be weakened [82] for operation at speed above the base speed. The inductances may vary from 80 to 120 percent of their nominal values (at rated flux level) for the change in the magnetic state of the machine over a wide range [46].

The influence of parameter deviations on the performances of indirect rotor-flux oriented induction motor drive has been the subject of study in many references [46-58, 83, 84]. Any disagreement between the actual parameters of the motor and those used in the controllers has pronounced effects on the steady state and dynamic performances of the drive. Detuned settings of the controller gains of slip calculator

make the flux level differ from the commanded value. Over-excitation or under excitation results in the loss of linear input-output torque relation making the drive unsuitable for torque control applications. In general, detuning leads to increased losses owing to over flux and/or over current condition resulting in a detrimental effect on the thermal rating of the motor. In the dynamic operation, the fast torque response to change in torque command is adversely affected because of the change in flux level that is associated with large rotor time constant, and the transient response to torque command exhibits oscillations in torque and flux response [47]. However, in speed controlled drive, the oscillations in transient response are taken care of by the outer speed loop controller but the delay and the non-linearity remain.

This chapter presents analytical approach in respect of the effects of magnetic flux saturation and rotor resistance variation on the performance of field-oriented speed controlled induction motor drive shown in Fig.2.7. Unlike studies in many publications, the analysis considers simultaneously the influences of these two changes. Saturation level is not only influenced by the excitation component of the stator current and torque level but also indirectly affected by rotor resistance deviation. Rotor resistance variations, if not accounted for in the controllers, not only causes detuning but may aggravate the situation by affecting the saturation level.

The presentation in the succeeding sections is organized as follows:

(a) Representation of saturation characteristics and accounting for the variation of magnetizing inductance through nonlinear analytic expressions; (b) study of the effects of detuning on steady state performances caused by rotor resistance deviation taking into account of both linear and nonlinear magnetic models; (c) effects of magnetic saturation on steady state characteristics with rotor resistance unchanged for both oriented and non-oriented condition; (d) parameter variation effect on transient performances.

3.2 MAGNETIC NON-LINEARITY AND MAGNETIZING INDUCTANCE

Magnetic state in the stator and the rotor iron depends respectively on the total stator and rotor flux linkage which in turn depend on the radially directed air gap flux and circumferentially directed leakage fluxes. Strictly speaking, leakage inductances are not independent of operating conditions, and are influenced by the degrees of tooth saturation. With normally designed machines, the teeth are usually under saturation until air gap flux falls well below its nominal value. Thus in the region of interest, leakage inductances can be treated as constant when flux level does not show wide variations and the stator and rotor currents do not attain very high values. By such considerations, the effect of iron saturation can be accounted for by appropriate adjustment of the value of the magnetizing inductance L_m, based on the saturation curve of the machine, considering leakage inductances as constant.

The magnetizing current in terms of d-q variables can be expressed as

$$i_{mag} = \sqrt{(i_{ds} + i_{dr})^2 + (i_{qs} + i_{qr})^2} \qquad (3.2)$$

The variable magnetizing inductance is a function of magnetizing current. Let

$$L_m = f(i_{mag}) \qquad (3.3)$$

To obtain information on (3.3) for the experimental motors, whose nominal parameters are furnished in Appendix I, the machine under test was driven at synchronous speed by an auxiliary motor and the stator was supplied from a constant frequency variable voltage source. The rms saturation curve in Fig. 3.1. (for Machine I) was plotted from the recorded ammeter, voltmeter and wattmeter data after subtracting the stator resistance and leakage-reactance drops. Then, following the procedure outlined in [118], the true saturation characteristic in the following two-term quintic form was then evaluated from the rms saturation,curve

$$i_{mag} = a_1 \lambda_m + a_5 \lambda_m^5 \qquad (3.4a)$$

The following alternative form of (3.4a) in terms of magnetizing energy is found sometimes to be of convenience to study the saturation effect

$$\lambda_m \, i_{mag} = a_1 \lambda_m^2 + a_5 \lambda_m^6 \qquad (3.4b)$$

The derived true-saturation curve for the experimental motor (SC) is shown in Fig.3.2a and the variation of L_m with i_{mag} in Fig.3.2b. L_m-i_{mag} curve was divided in three segments each of which was given a

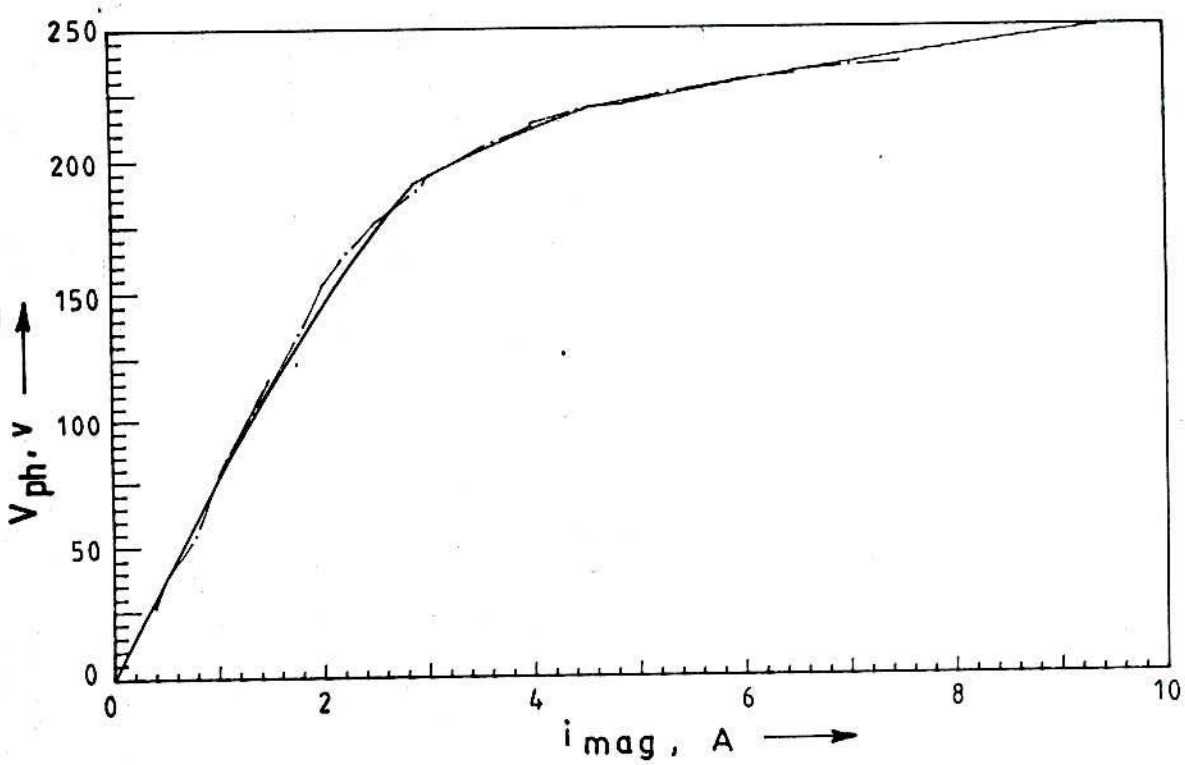

Fig. 3.1 RMS saturation curve (Machine I)

—·—·— measured

——— deduced from $i_{mag} = a_1 \lambda + a_5 \lambda^5$
(ref. Appendix I for a_1 & a_5)

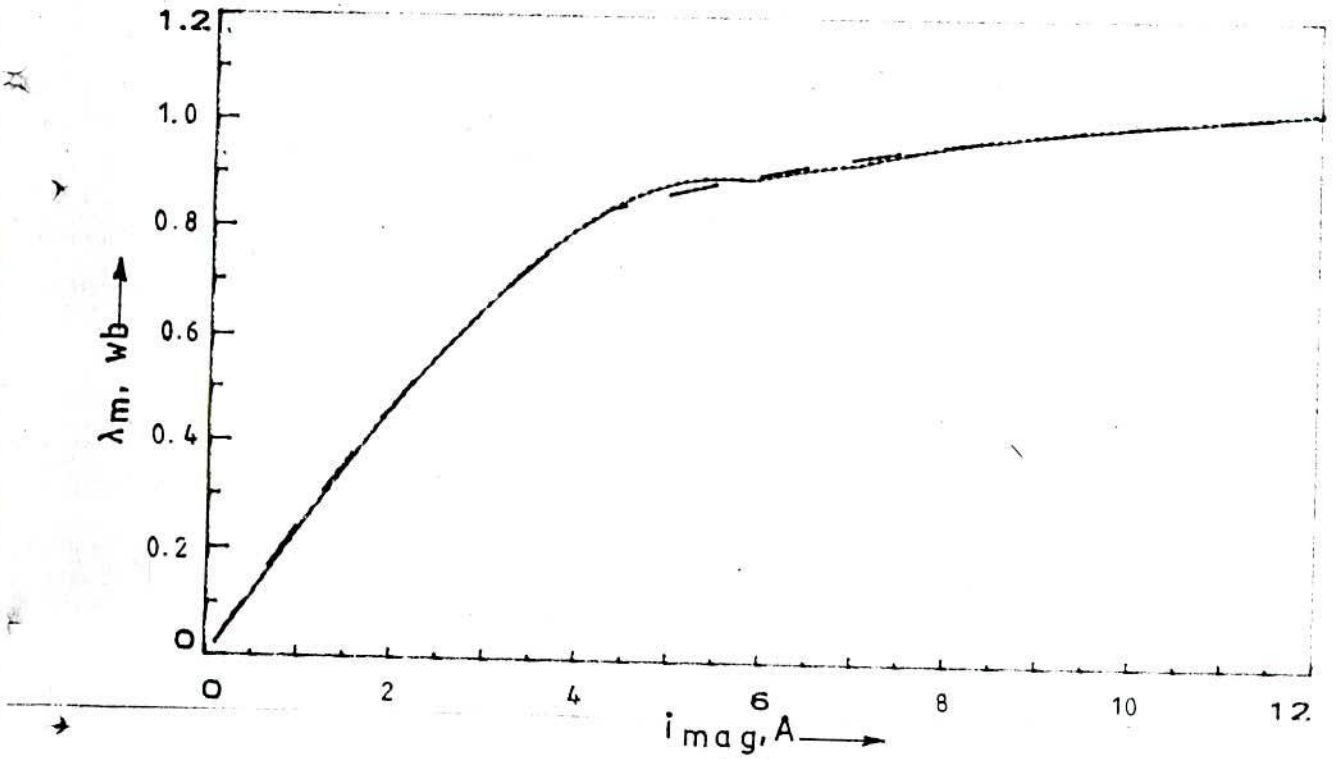

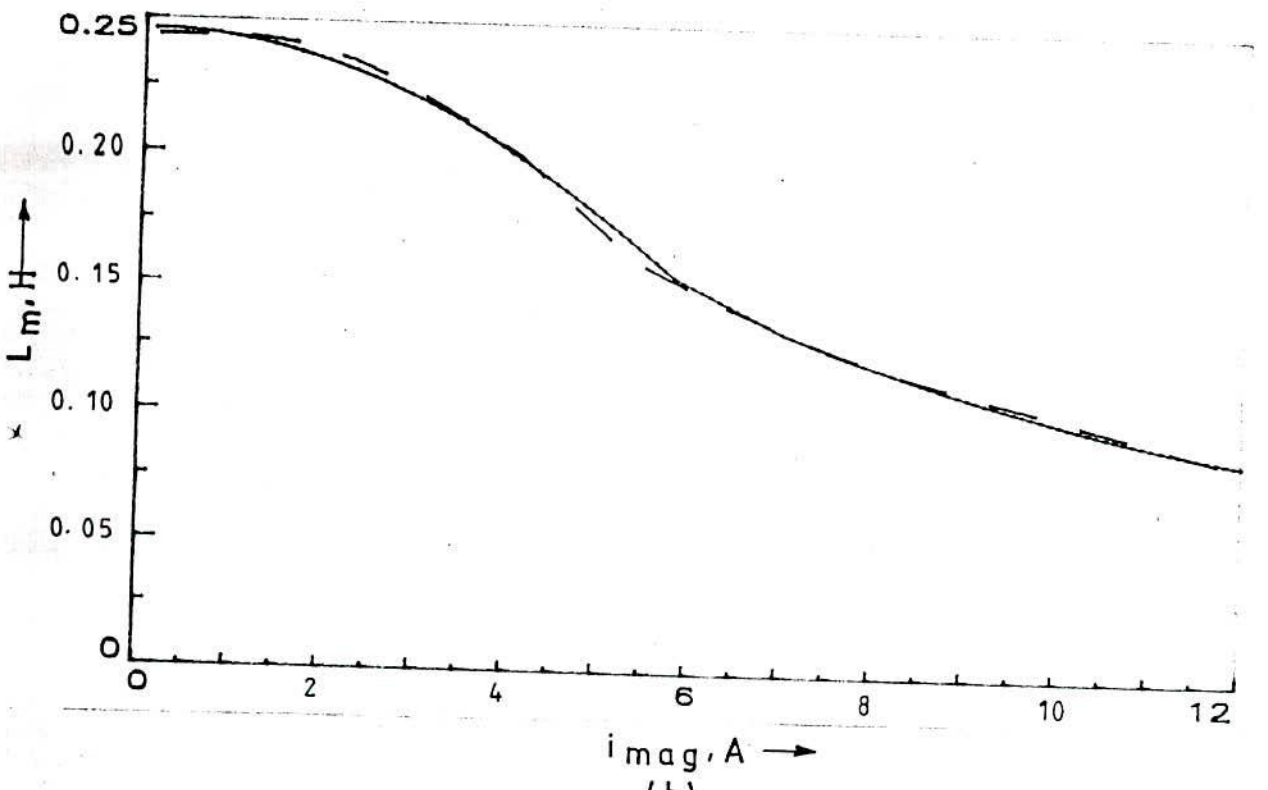

Fig. 3.2 (a) True saturation characteristics

——— $i_{mag} = a_1 \lambda + a_5 \lambda^5$

---------- using $L_m = b_0 + b_1 i_{mag} + b_2 i_{mag}^2$

(b) Magnetizing inductance

——— deduced from $i_{mag} = a_1 \lambda + a_5 \lambda^5$

---------- polynomial ($L_m = b_0 + b_1 i_{mag} + b_2 i_{mag}^2$)

polynomial fit of the form

$$L_m = b_o + b_1\, i_{mag} + b_2\, i_{mag}^2 \qquad (3.5)$$

Plots based on the model in (3.5) are shown in Fig.3.2b for comparison. Similarly, for machine II, the constants a_1 and a_5 for the magnetization curve and b_0, b_1, b_2 and b_3 for the polynomial fit (cubic) describing $L_m - i_{mag}$ curve was obtained. The constants for both the machines are listed in Appendix - I.

3.3 ANALYSIS FOR PARAMETER VARIATION EFFECTS FOR SPEED CONTROLLED DRIVE

With reference to the last two equations in (2.1) the following two equations in synchronous reference frame can be written for the rotor circuit under steady state operation.

$$-\omega_{sl}\, L_m\, i_{qs} + R_r\, i_{dr} - \omega_{sl}\, L_r\, i_{qr} = 0 \qquad (3.6)$$

$$\omega_{sl}\, L_m\, i_{ds} + \omega_{sl}\, L_r\, i_{dr} + R_r\, i_{qr} = 0 \qquad (3.7)$$

Solution to above for i_{dr} and i_{qr} yields

$$i_{dr} = \frac{R_r\, \omega_{sl}\, L_m}{R_r^2 + \omega_{sl}^2\, L_r^2} \left(i_{qs} - \frac{\omega_{sl}\, L_r}{R_r}\, i_{ds} \right) \qquad (3.8)$$

$$i_{qr} = - \frac{R_r\, \omega_{sl}\, L_m}{R_r^2 + \omega_{sl}^2\, L_r^2} \left(i_{ds} + \frac{\omega_{sl}\, L_r}{R_r}\, i_{qs} \right) \qquad (3.9)$$

Eqns. 3.8 and 3.9 are useful in determining detuning effect corresponding to any d-q reference frame defined by i_{ds}, i_{qs} and ω_{sl}.

The electromagnetic torque in terms of orthogonal current components

$$T_{em} = \frac{3}{2} P_p L_m (i_{qs} i_{dr} - i_{ds} i_{qr}) \quad (3.10)$$

Use of (3.8) and (3.9) in (3.10) gives

$$T_{em} = \frac{3}{2} P_p \frac{R_r \omega_{sl} L_m^2}{R_r^2 + \omega_{sl}^2 L_r^2} (i_{qs}^2 + i_{ds}^2) \quad (3.11)$$

For closed loop speed controlled system command torque gets adjusted until the developed torque by the machine equals the load torque, i.e.,

$$T_{em} = T_L \quad (3.12)$$

From (3.11) and (3.12) and since $i_R^{'2} = i_{qs}^2 + i_{ds}^2$

$$i_R^{'2} = \frac{2}{3} \frac{T_L}{P_p} \frac{R_r^2 + \omega_{sl}^2 L_r^2}{R_r \omega_{sl} L_m^2} \quad (3.13)$$

Denoting the parameter or variables in the controllers with superscript of asterisk (like x^*), the commanded slip by the proposed control scheme in Fig.2.7 is

$$\omega_{sl}^* = \sqrt{i_R^{'2} - i_{ds}^{*2}} \left(\frac{R_r^* L_m^*}{\lambda_r^* L_r^*} \right) \quad (3.14)$$

Equating the expression for $i_R^{'2}$ in (3.13) and (3.14)

$$\left(\frac{2}{3} \frac{T_L}{P_p} \frac{R_r^2 + \omega_{sl}^2 L_r^2}{R_r \omega_{sl} L_m^2} \right) - \left(\frac{\omega_{sl}^* \lambda_r^* L_r^*}{R_r^* L_m^*} \right)^2 - i_{ds}^{*2} = 0 \quad (3.15)$$

As the angular slip frequency is directly transmitted to the motor

$$\omega_{sl} = \omega_{sl}^* \quad (3.16)$$

Under this condition

$$\left(\frac{2}{3} \frac{T_L}{P_p} \frac{R_r^2 + \omega_{sl}^{*2} L_r^2}{L_m^2 R_r \omega_{sl}^*} \right) - \left(\frac{\omega_{sl}^* \lambda_r^* L_r^*}{R_r^* L_m^*} \right)^2 - i_{ds}^{*2} = 0 \qquad (3.17)$$

Actual rotor flux in the machine under the constraints (3.12) is given by

$$\lambda_r^2 = \frac{2}{3} \frac{T_L}{P_p} \frac{R_r}{\omega_{sl}} \qquad (3.18)$$

Command torque is given by

$$T_{em}^* = \frac{3}{2} P_p \frac{L_m^{*2}}{R_r^*} \omega_{sl}^* i_{ds}^{*2} \qquad (3.19)$$

under the constraint (3.12) T_L/T_{em}^* is the ratio of actual developed electromagnetic torque to command torque.

Furthermore, for the control algorithm in Fig. 2.7 steady state operation yields

$$i_R = i_R^* \qquad (3.20a)$$

$$i_{qs}^c = i_{qs}^* \qquad (3.20b)$$

Equation (3.17) is the key equation to start with. Non-linear equations derived above require numerical solution. Equations (3.17), (3.14), (3.8), (3.9), (3.2) and (3.3) are taken up in sequence for their numerical solution to study the influence of parameter variation on the performances of an induction motor under the field orientation control strategy in Fig.2.7. Fig.3.3 outlines the sequence of computations following a change in the rotor resistance for controlled

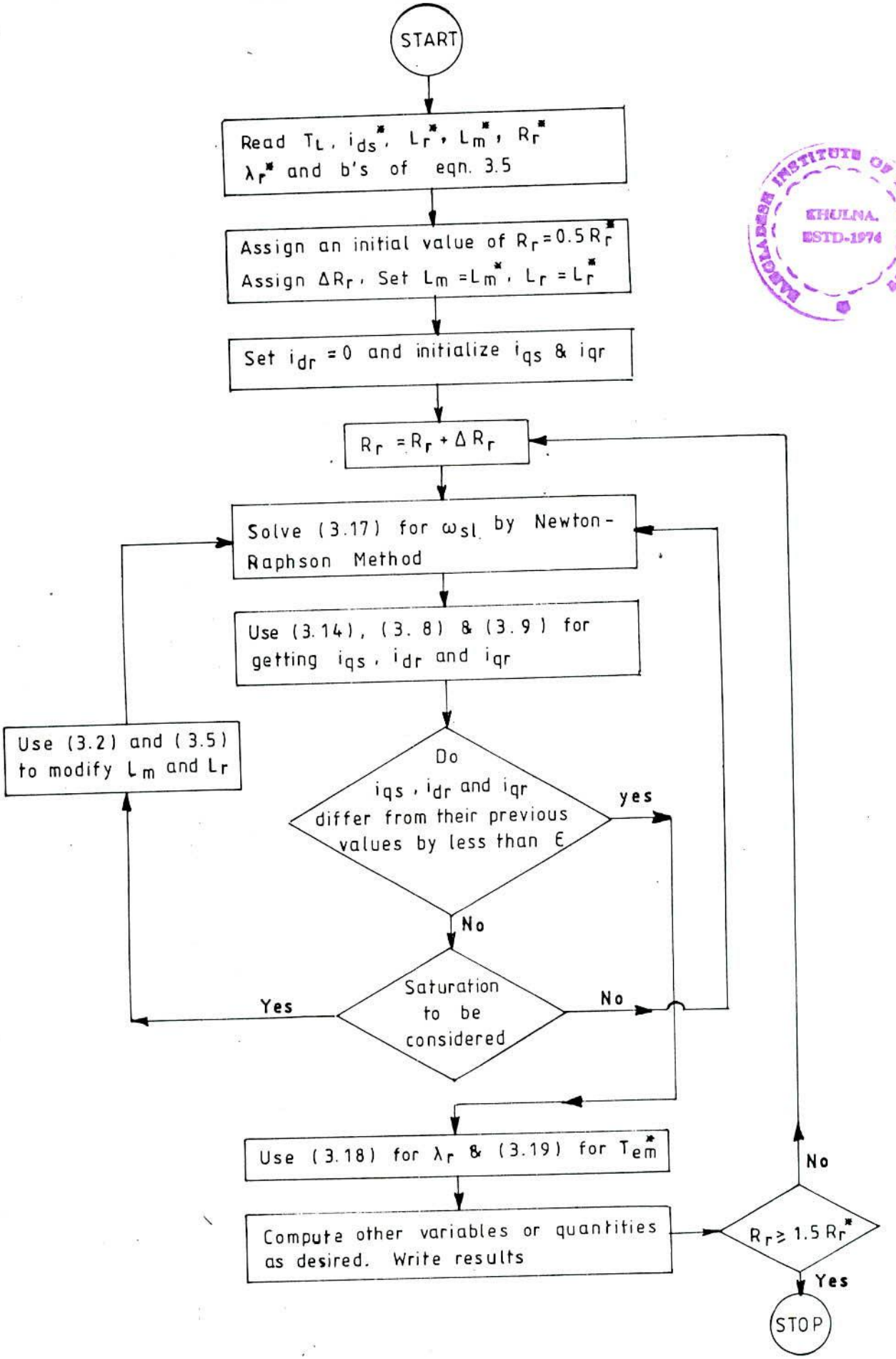

Fig 3.3 Computational sequence to study the effect of rotor resistance variation inclusive of magnetic non-linearity

speed operation driving a given torque load. The program also accommodates variation in the values of L_m and L_r to take into account of the saturation effect.

3.4 STEADY STATE SIMULATION RESULTS UNDER DETUNED CONDITION FOR ROTOR RESISTANCE DEVIATION

Based on the procedure outlined above, the steady state performances of the field oriented CSI-IM drive system under closed loop operation, were studied for rotor resistance variation using both linear (constant inductance) and non-linear (saturation) models of the magnetic flux paths.

Mismatch between the rotor resistance in the slip calculator and that of the machine model gives rise to incorrect slip-frequency estimation which in turn affects the rotor flux as is evident from (3.18). This change in the flux level inside the machine alters the value of the rotor inductance making it differ from that used in the slip calculator, which may further adversely affect the gain of the slip calculator.

To study the influence of load torque on the extent of detuning caused by rotor resistance change, Machine I and II of Appendix I were examined for three different load torques (for machine I: 5 Nm, 12.5 Nm and 25 Nm; for machine II: 1 Nm, 2.5 Nm and 5 Nm).

3.4.1 Effect on mutual inductance

The effect of change in the rotor resistance on the values of mutual inductance for the speed control strategy without adaptation is

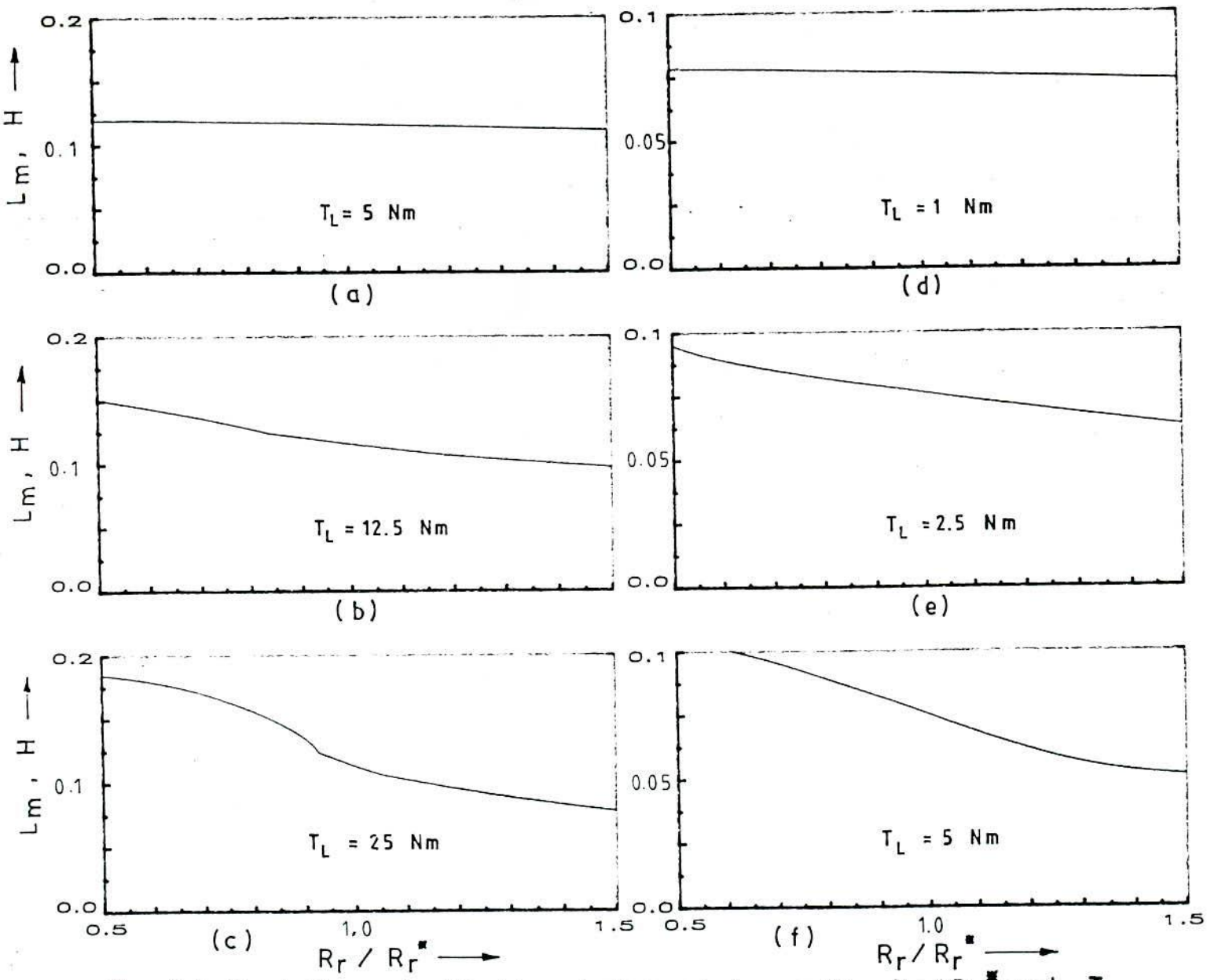

Fig. 3.4 Variation of effective value of L_m with R_r / R_r^* and T_L.
a, b, c : Machine-I & d, e, f : Machine II

shown in Fig. 3.4. The increasing influence of load torque on the effective value of mutual inductance is distinctly noted for both the machines.

3.4.2 Effect on torque output

The variation of the ratio of developed torque (load torque) to command torque with the ratio of actual to nominal values of rotor resistance are shown in Fig. 3.5.

For constant inductance (saturation neglected) model, the variation of T_{em}/T^*_{em} for low developed torque is found to be inverse to that for high developed torque. For low load torque the torque ratio curves for saturation and linear models show similar trend in their variations (Figs. 3.5a and 3.5d). For high load torque (Fig. 3.5c and 3.5f) the saturation effect makes torque curve droop beyond $R_r/R^*_r = 1$ while the constant inductance model indicates an upward trend though at a slower rate above $R_r/R^*_r = 1$. For an intermediate torque load the torque curve, considering saturation effect, droops steadily while that for an unsaturation model indicates a rising trend initially and then droops.

An insight into the nature of the torque ratio (T_{em}/T^*_{em}) profile as a function of (R_r/R^*_r), presented above, can be made in a generalized way for steady state conditions as follows.

As the command angular slip-frequency ω^*_{sl} is directly transmitted to the motor, i.e., $\omega_{sl} = \omega^*_{sl}$, substitution of the expression for ω^*_{sl} (3.1c) in (3.11) and rearrangement of terms give

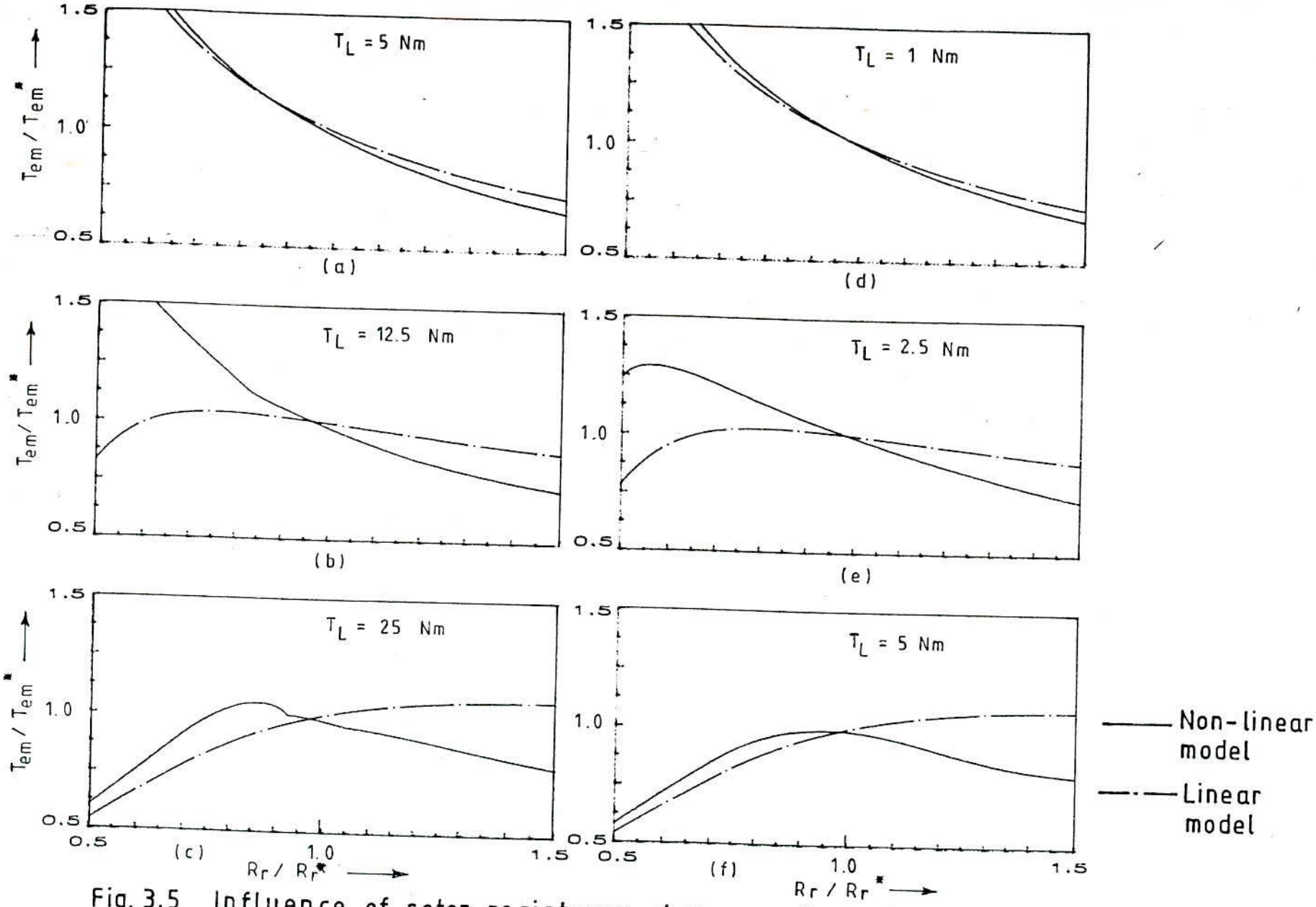

Fig. 3.5 Influence of rotor resistance change on the output-input torque ratio. a, b, c - Machine I & d, e, f - Machine II

$$T_{em} = \frac{3}{2} P_p \frac{\frac{L_m^2}{L_r^*} \frac{R_r^*}{R_r} i_{qs}^* i_{ds}^*}{i_{ds}^{*2} + \left(\frac{L_r}{L_r^*} \frac{R_r^*}{R_r} \right)^2 i_{qs}^{*2}} (i_{qs}^2 + i_{ds}^2) \qquad (3.21)$$

The expression for the commanded value of torque under steady state can be expressed as (cf eqns. 2.23 and 2.36)

$$T_{em}^* = \frac{3}{2} P_p \frac{L_m^{*2}}{L_r^*} i_{ds}^* i_{qs}^* \qquad (3.22)$$

Application of (3.22) in (3.21) yields

$$\frac{T_{em}}{T_{em}^*} = f_1 \times f_2 \qquad (3.23)$$

where,

$$f_1 = \frac{L_m^2}{L_m^{*2}} \frac{R_r^*}{R_r} \qquad (3.24a)$$

$$\text{and} \quad f_2 = \frac{1 + \frac{i_{qs}^{*2}}{i_{ds}^{*2}}}{1 + \left(\frac{L_r}{L_r^*} \frac{R_r^*}{R_r} \right)^2 \frac{i_{qs}^{*2}}{i_{ds}^{*2}}} \qquad (3.24b)$$

As leakage flux is a small percentage of the total flux-linkage with the rotor circuit, we may reasonably write

$$\frac{L_m}{L_m^*} \approx \frac{L_r}{L_r^*} \qquad (3.25)$$

Expressions for f_1 and f_2 in (3.24) can then be re-written as

$$f_1 = \frac{L_m}{L_m^*} x \qquad (3.26a)$$

$$f_2 = \frac{(1 + \frac{i_{qs}^{*2}}{i_{ds}^{*2}})}{1 + x^2 (\frac{i_{qs}^*}{i_{ds}^*})^2} \qquad (3.26b)$$

where $$x = \frac{L_r}{L_r^*} \frac{R_r^*}{R_r}$$

Fig.3.6(a) shows the linear variation of f_1 as a function of x with L_m/L_m^* as parameter to consider the influence of saturation, while Fig. 3.6(b) shows the variation of the factor f_2 as a function of x with i_{qs}^*/i_{ds}^* as parameter indicating the extent of the influence of load torque. For linear model $L_m/L_m^* = 1$. The following general trend can be inferred from the plots of Figs.3.6 which are indicative of the likely pattern of variation of T_{em}/T_{em}^*, with R_r/R_r^* in Figs.3.5 for induction motor under detuned condition.

i) For low torque, i.e., $i_{qs}^* < i_{ds}^*$, the factor f_1 affects the torque ratio (T_{em}/T_{em}^*) as f_2 departs not much from 1. Hence for $R_r^* < R_r$ (i.e., $x < 1$) $T_{em}/T_{em}^* < 1$. Reverse will be the case for $R_r^* > R_r$. This holds for both saturated and unsaturated model. These are noted in Fig.3.5a and 3.5d.

ii) For linear magnetic circuit and $i_{qs}^* > i_{ds}^*$ (high torque), when $R_r^* > R_r$ (i.e., $x > 1$) the torque ratio $T_{em}/T_{em}^* < 1$, f_2 being the overriding

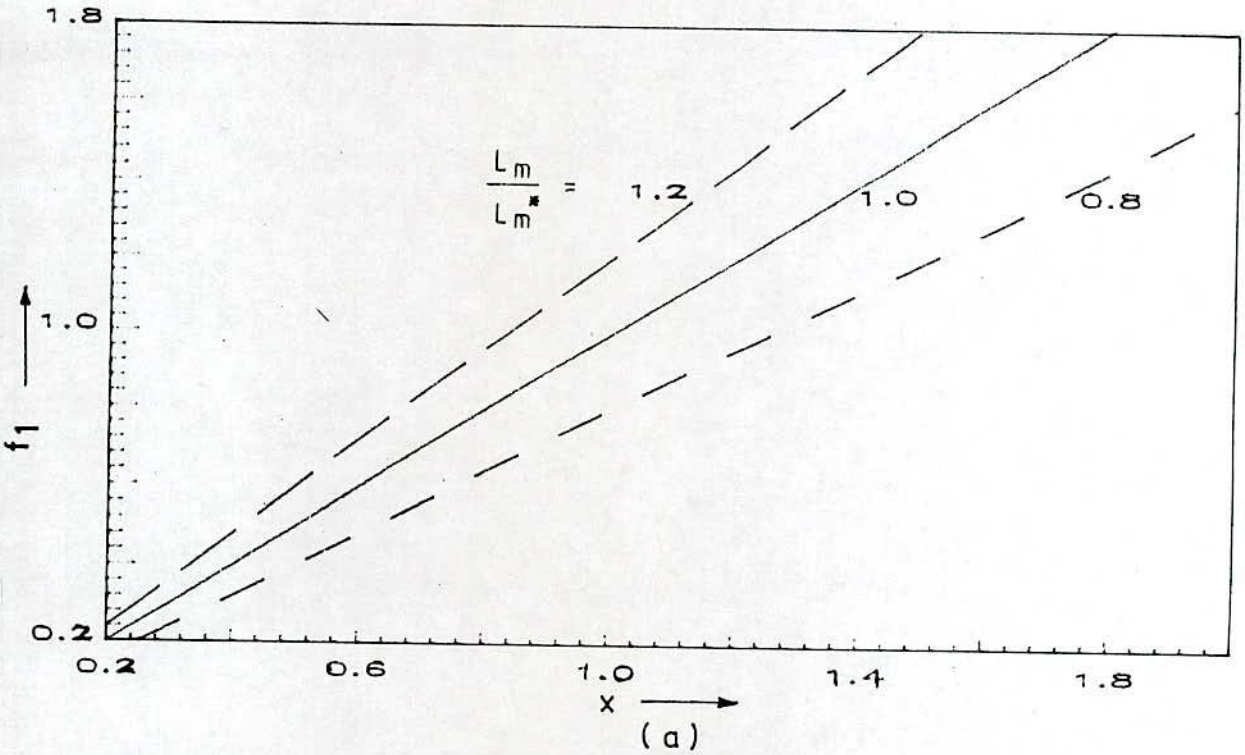

(a)

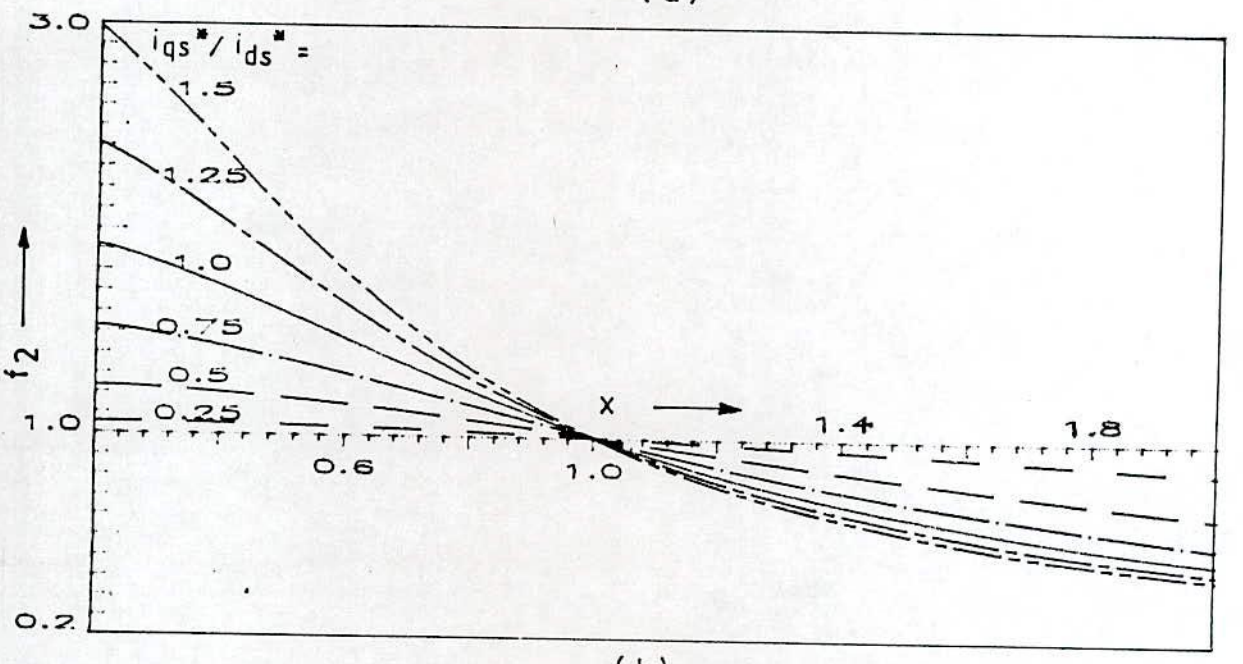

(b)

Fig. 3.6 Variation of f_1 and f_2 with x (eqn. 3.26)

(a) f_1 vs. x

(b) f_2 vs. x

factor. On the other hand as R_r^* becomes less than R_r (i.e. $x < 1$), torque ratio T_{em}/T_{em}^* initially exceeds 1, but not going far above 1, and afterwards exhibits a downward trend as f_1 predominates.

iii) In the case of linear magnetic model $f_1 = x = R_r^*/R_r$ but in the case of non-linear magnetic model $f_1 < x < R_r^*/R_r$ for $R_r^*/R_r < 1$, and $f_1 > x > R_r^*/R_r$ for $R_r^*/R_r > 1$. As a result for $i_{qs}^* > i_{ds}^*$, $f_1 < 1$ is the overriding factor when $R_r^*/R_r < 1$, thus making the torque ratio $T_{em}/T_{em}^* < 1$. On the other hand for $R_r^*/R_r > 1$ the product $f_1 f_2$, i.e., T_{em}/T_{em}^*, first exceeds unity and then goes below unity.

3.4.3 Flux linkage variation

Variation in the rotor flux linkage, under detuned condition, for the same load torques are shown in Fig.3.7.

It is noted that for low load torque rotor flux linkage remains constant except for a minor steady variation with the linear magnetic model. In the case of medium load torque, linear magnetic model shows significant change in the rotor flux linkage moving from below the set flux to above the set flux as the ratio R_r/R_r^* changes from less than 1.0 to greater than 1.0. On the other hand, saturated model depicts practically no significant change in the rotor flux linkage except at low (R_r/R_r^*). For high load torque, both the magnetic models indicate significant variation in the rotor flux linkage but the variation is less with the non-linear model than with the linear model, particularly this is evident with the increased value of the rotor resistance.

In order to comprehend the logistic behind the different trends in the rotor flux linkage profiles with linear and non-linear magnetic

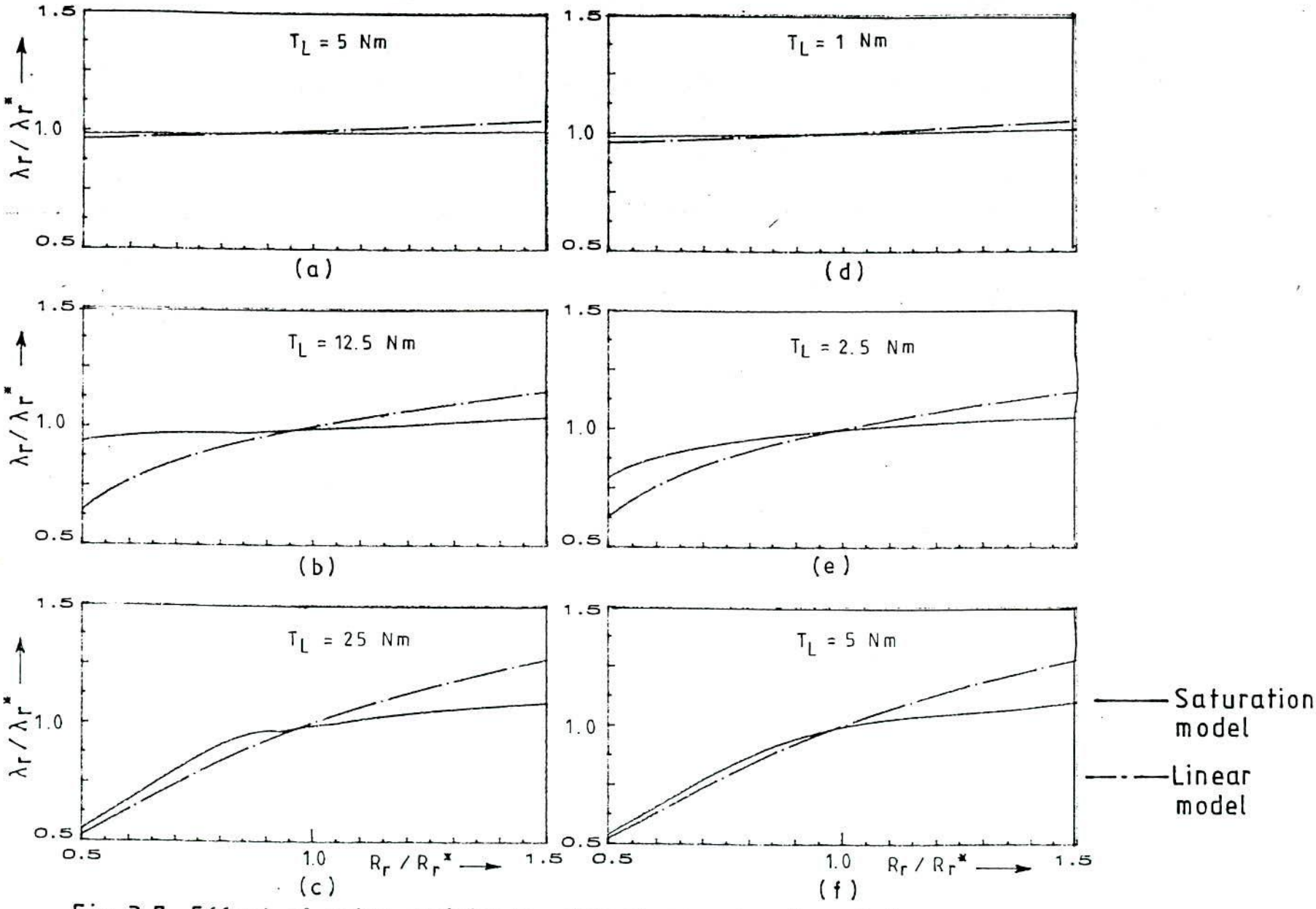

Fig. 3.7 Effect of rotor resistance change on rotor flux linkage
a, b, c - Machine I & d, e, f - Machine II

models an approximate analysis for a qualitative explanation can be made. The ratio λ_r/λ_r^* deviates from unity as λ_r changes from its set value during detuned operation. Even under detuned operation λ_{dr} is the dominant component of the rotor flux linkage.

So, the change in this direct axis component of the flux due to variation in R_r of the machine from its nominal value will be indicative of the profile of the variation of the flux linkage ratio. The variation of the d-axis component of the flux linkage due to change in the ratio R_r/R_r^* is presented in Fig. 3.8 (for both the machine). Identical nature of changes of λ_{dr} in Fig. 3.8 for the two machines under different loading conditions with those of λ_r/λ_r^* in Fig. 3.7 proves the above proposition. The d-axis component of the rotor flux linkage under steady state detuned condition can be expressed, using (3.8) in (2.3a), as

$$\lambda_{dr} = L_m \, i_{ds}^* + \frac{Lm \, \omega_{sl} \, L_r}{R_r^2 + (L_r \, \omega_{sl})^2} (R_r \, i_{qs}^* - L_r \, \omega_{sl} \, i_{ds}^*) \qquad (3.27)$$

As ω_{sl} is equal to its command value, eqn. 3.27 can be re-written in the form

$$\lambda_{dr} = \frac{L_m}{L_m^*} \lambda_r^* + L_m \frac{x \frac{i_{qs}^*}{i_{ds}^*}}{1 + x^2 \left(\frac{i_{qs}^*}{i_{ds}^*}\right)^2} (1 - x) \, i_{qs}^* \qquad (3.28)$$

where x, as before is

$$x = \frac{R_r^*}{R_r} \frac{L_r}{L_r^*}$$

Expression in (3.28) indicates explicitly that i_{qs}^*, i.e., the commanded torque has direct influence on λ_{dr} for $R_r \neq R_r^*$. For linear model, the first term remains constant and the magnitude of the second term is influenced by the deviation in R_r from its nominal value. For the non-linear magnetic model the first term is not a constant and the magnitude of the second term is governed by the factor x and the two terms have compensating effect. That is why much deviation in λ_r from λ_r^* is observed with the linear model than with the non-linear model. This is evident in Figs.3.7 and 3.8.. But the actual picture for deviation in λ_r/λ_r^* transpires by considering the effect of quadrature component of flux linkage in conjunction with (3.28).

Under field orientation condition the quadrature axis component of rotor flux linkage is zero. Under steady state detuned condition the following expression for λ_{qr} is obtained by substituting (3.9) in (2.3b).

$$\lambda_{qr} = L_m\, i_{qs}^* - L_r \frac{\omega_{sl}^2\, L_m\, L_r\, i_{qs}^* + R_r\, \omega_{sl}\, L_m\, i_{ds}^*}{R_r^2 + (\omega_{sl}\, L_r)^2} \qquad (3.29)$$

Replacing ω_{sl} by its command value, given by (3.1c) and re-arrangement of the terms yields

$$\lambda_{qr} = f_3 \left[1 - \frac{L_r}{L_r^*} \frac{R_r^*}{R_r}\right] i_{qs}^* \qquad (3.30)$$

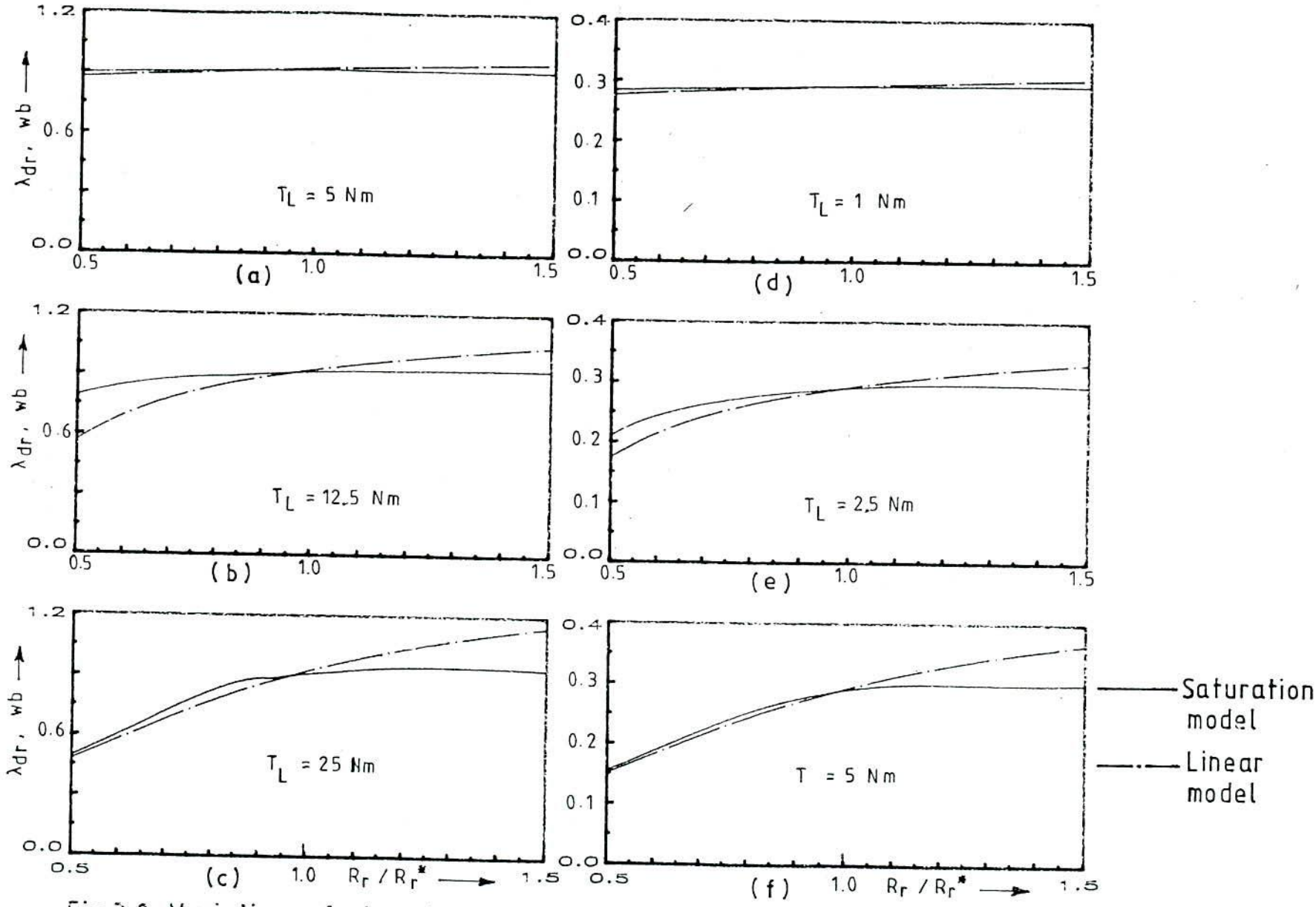

Fig.3.8 Variation of d-axis rotor flux linkage with changes in R_r and load torque a, b, c - Machine I & d, e, f - Machine II

where,

$$f_3 = \frac{L_m}{1 + \left\{\frac{R_r^*}{R_r} \quad \frac{L_r}{L_r^*}\right\} \left\{\frac{i_{qs}^*}{i_{ds}^*}\right\}^2}$$

For very low values of torque, i.e., $i_{qs}^* << i_{ds}^*$, f_3 has negligible effect on λ_{qr} and so with linear model λ_{qr} varies almost linearly with respect to R_r^*/R_r. It can be visualized from (3.30) that for $R_r > R_r^*$ λ_{qr} is positive, while for $R_r < R_r^*$, λ_{qr} is negative. This is distinctly evident in Fig.3.9. Under the non-linear magnetic model, the ratio L_r/L_r^* deteriorates the factor x further in the same direction of R_r^*/R_r, and that is why q-axis rotor flux linkage under non-linear condition is larger in magnitude than that found with linear magnetic model. The effect is pronounced with increasing value of i_{qs}^* (i.e. torque). Furthermore, it is noted from (3.30) that for a given value of i_{qs}^*/i_{ds}^* the factor f_3 assumes a higher value with $R_r > R_r^*$ than that with $R_r < R_r^*$. It makes the λ_{qr} value more for $R_r/R_r^* > 1.0$ than for $R_r/R_r^* < 1.0$. Plots of λ_{qr} as a function R_r/R_r^* in Fig. 3.9 with different load torques reveal these aspects.

3.4.4 Effects on dc link and machine voltages

The influence of motor parameter deviations on dc link voltages are shown in Figs.3.10 (a-f) in terms of the ratio of actual inverter input voltage to the ideal voltage under field orientation condition. Close correlation of the nature of variation with those of torque ratios (Figs.3.5 (a-f) indicate that for current regulated systems developed torque bear almost direct relation with the dc link voltage. Such correlation is evident from certain relations derived earlier.

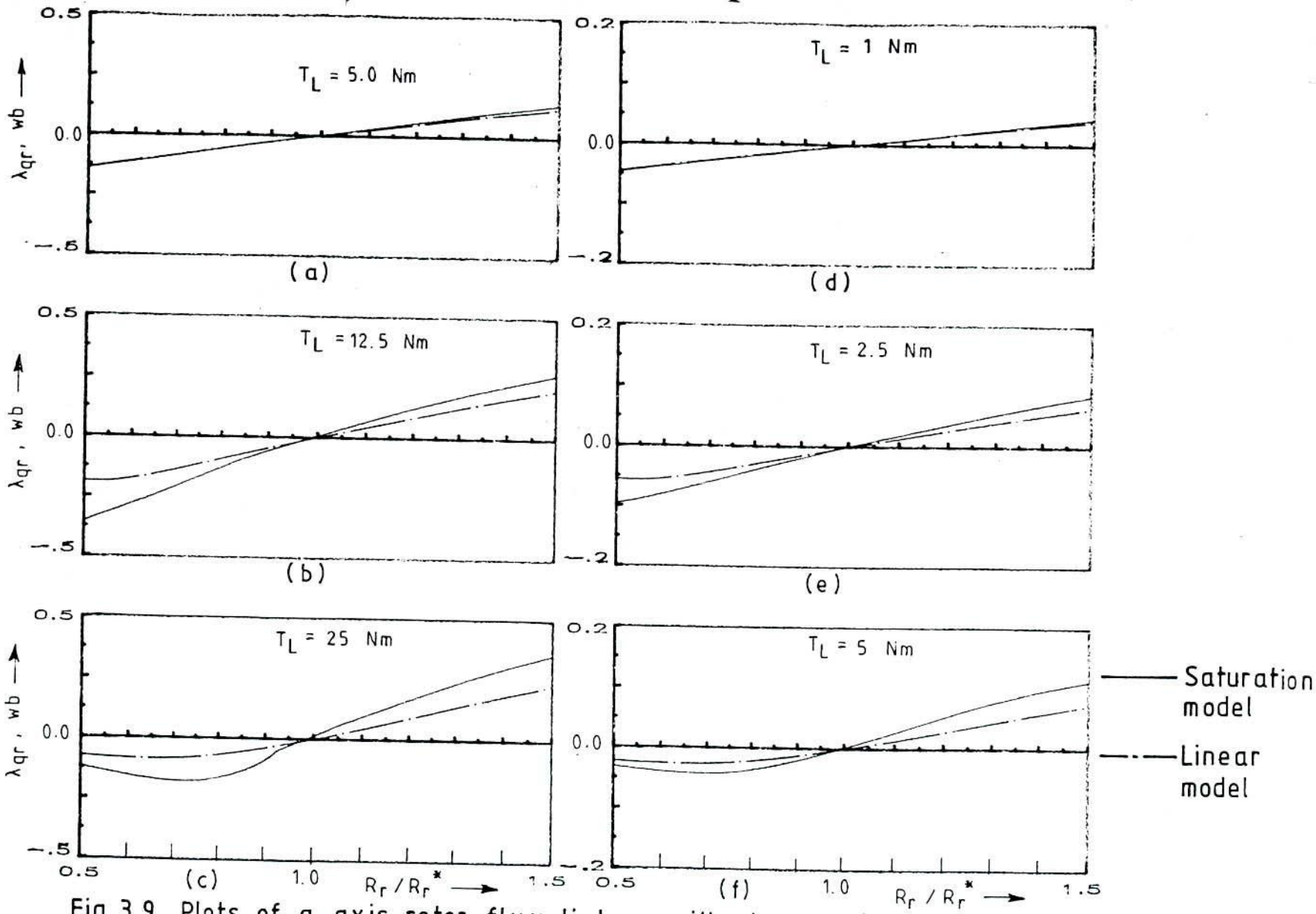

Fig. 3.9 Plots of q-axis rotor flux linkage with changes in Rr and load torque a, b, c, - Machine I & d, e, f, - Machine II

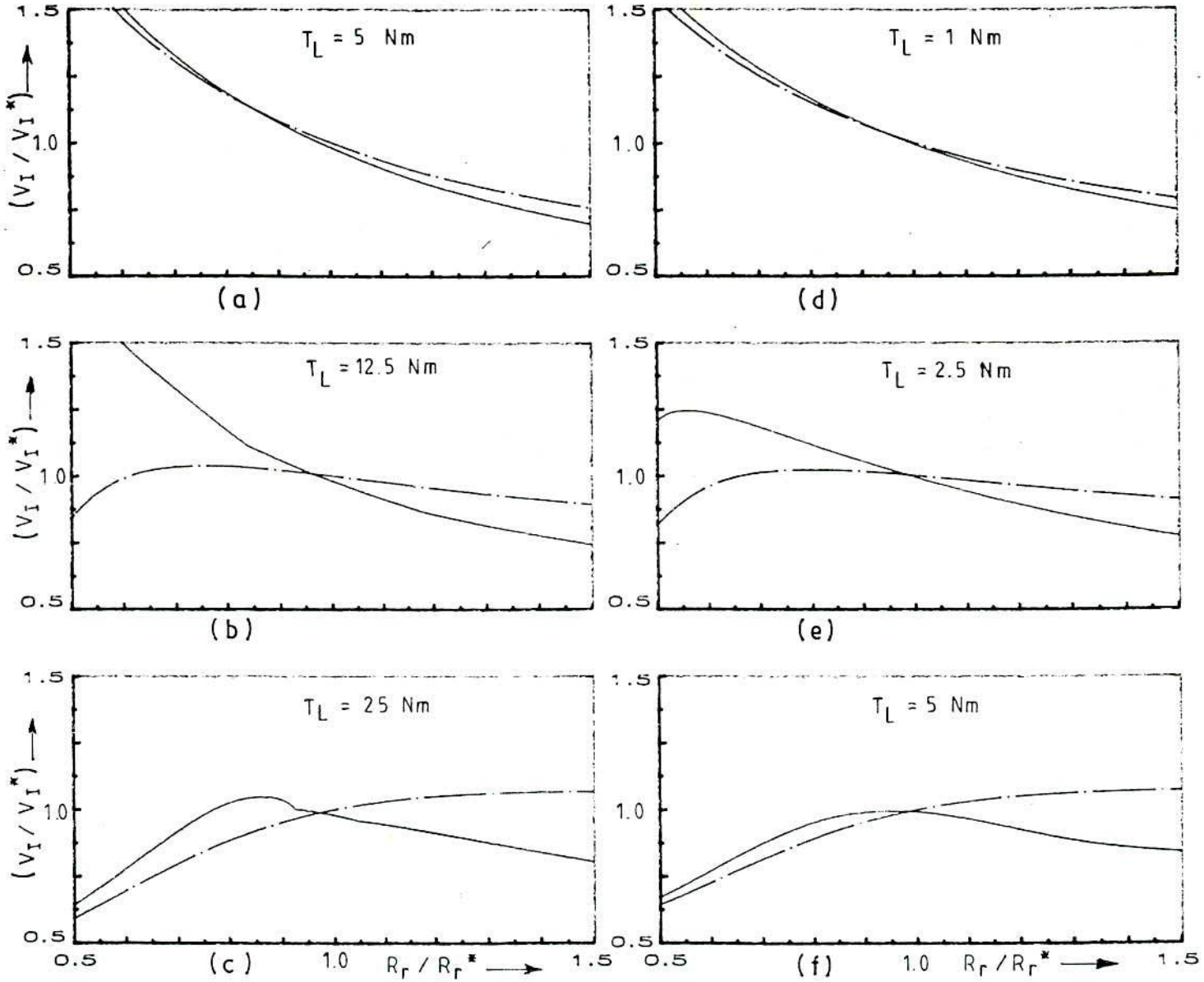

Fig. 3.10 Plots showing the effect of R_r and T_L on inverter input voltage a, b, c : Machine I ; d, e, f : Machine II

——— Saturation model ; —·—·— Linear model

If dc link and stator resistance drops can be considered negligible when the speed is not low enough, the converter output voltage ratio (actual to field oriented condition) can be approximately expressed as (cf. eqn.2.20).

$$\frac{v_I'}{v_I'^*} = \frac{L_m}{L_m^*}\,\frac{i_{qs}}{i_{qs}^*}\,\frac{i_R'^*}{i_R'}\,\frac{\lambda_r}{\lambda_r^*}\,\frac{L_r^*}{L_r} \tag{3.31}$$

The torque ratio (actual to command) by the expression in (2.38) is expressed as

$$\frac{T_{em}}{T_{em}^*} = \frac{L_m}{L_m^*}\,\frac{L_r^*}{L_r}\,\frac{\lambda_r}{\lambda_r^*}\,\frac{i_{qs}}{i_{qs}^*} \tag{3.32}$$

The constraints in-force are

$$i_R' = i_R'^* \tag{3.34}$$

In such a case, the ratios in (3.31) and (3.32) must assume the same values. This is reflected in Figs. 3.5 and 3.10 for both constant inductances and variable inductances caused by saturation effect.

Figs.3.11 show the variation of the ratio of actual machine terminal voltage to the terminal voltage under field orientation as a function of rotor resistance. The nature of variation is the same as those of flux ratio variation in Fig. 3.7. This is the natural expectation. The expressions for the components of stator voltage can be written from (2.1) after some simplifications as

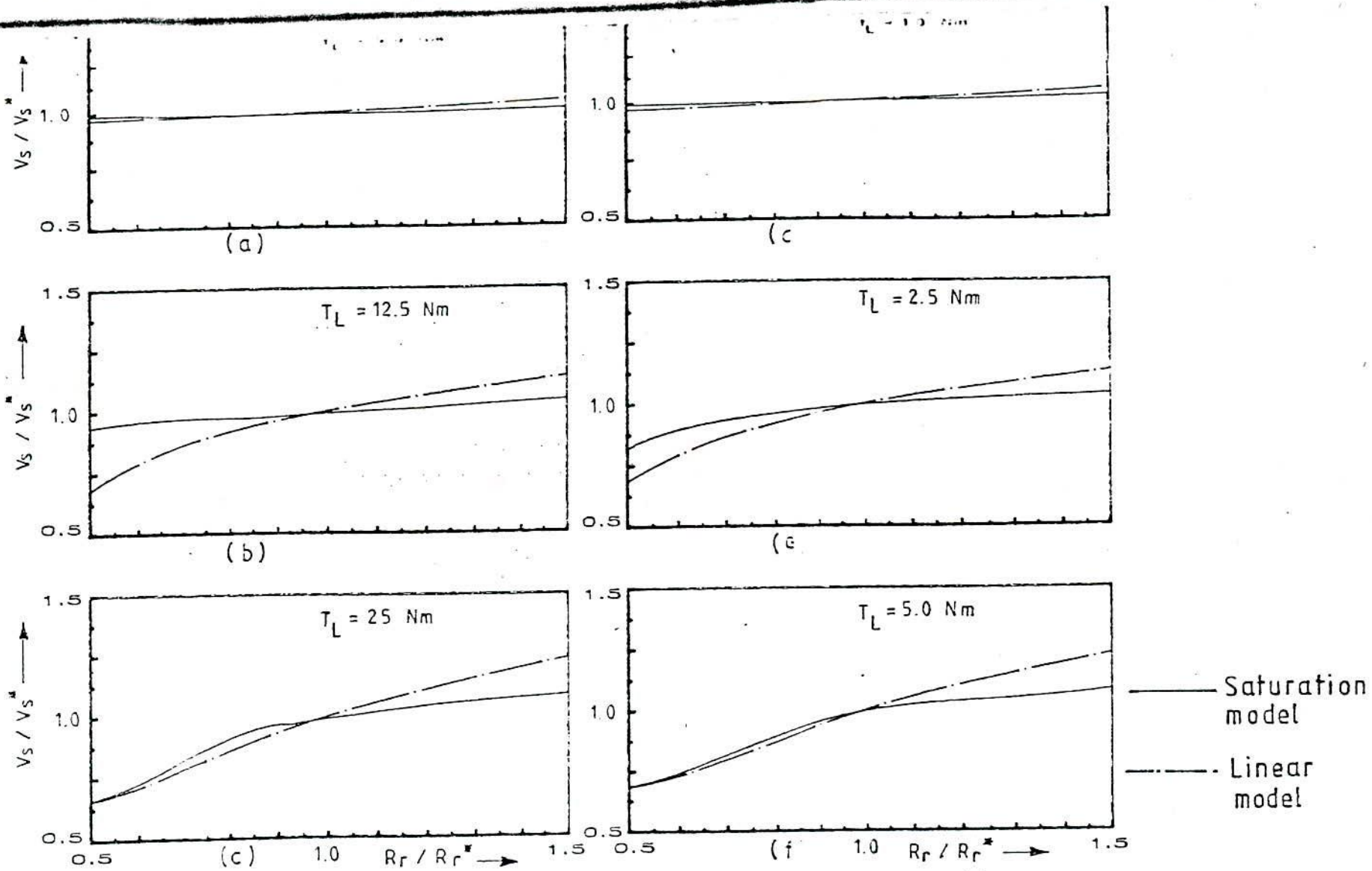

Fig. 3.11 Effect of rotor resistance and load torque on machine terminal voltage (fundamental) a, b, c - Machine I; d, e, f - Machine II

$$v_{ds} = R_s\, i_{qs} + \omega_e \left(L_s - \frac{L_m^2}{L_r}\right) i_{ds} + \omega_e \left(\frac{L_m}{L_r}\right) \lambda_{dr}$$

$$v_{qs} = R_s\, i_{ds} - \omega_e \left(L_s - \frac{L_m^2}{L_r}\right) i_{qs} - \omega_e \left(\frac{L_m}{L_r}\right) \lambda_{qr} \qquad (3.34)$$

If leakage inductance and resistance drops are considered negligible, the relationship between the machine terminal voltage and the flux-linkage becomes

$$V_s = \frac{1}{\sqrt{2}} \sqrt{v_{qs}^2 + v_{ds}^2} \approx \frac{1}{\sqrt{2}}\, \omega_e \left(\frac{L_m}{L_r}\right) \sqrt{\lambda_{dr}^2 + \lambda_{qr}^2}$$

$$\text{i.e. } V_s \approx \frac{1}{\sqrt{2}} \left(\frac{L_m}{L_r}\right) \omega_e\, \lambda_r \qquad (3.35)$$

The approximate expression for V_s in (3.35) explains the similarity in the profiles of machine terminal voltage ratios and the flux-ratios in Figs. 3.11 and 3.7 respectively.

3.4.5 Effects on dc link current

The effect of changing rotor parameter on the dc link current under controlled speed operation is shown in Fig. 3.12 for the same three specific load torques on the machines. For low torque operation dc link current is seen to be practically insensitive to rotor parameter deviations (Fig. 3.12a & 3.12d). With high load torque and $R_r < R_r^*$, the link current decreases for both linear and non-linear magnetic models as R_r approaches R_r^*, but, for $R_r > R_r^*$ the link current gradually increases under non-linear magnetic state, while it droops slowly if the magnetic state of the machines remains unaltered.

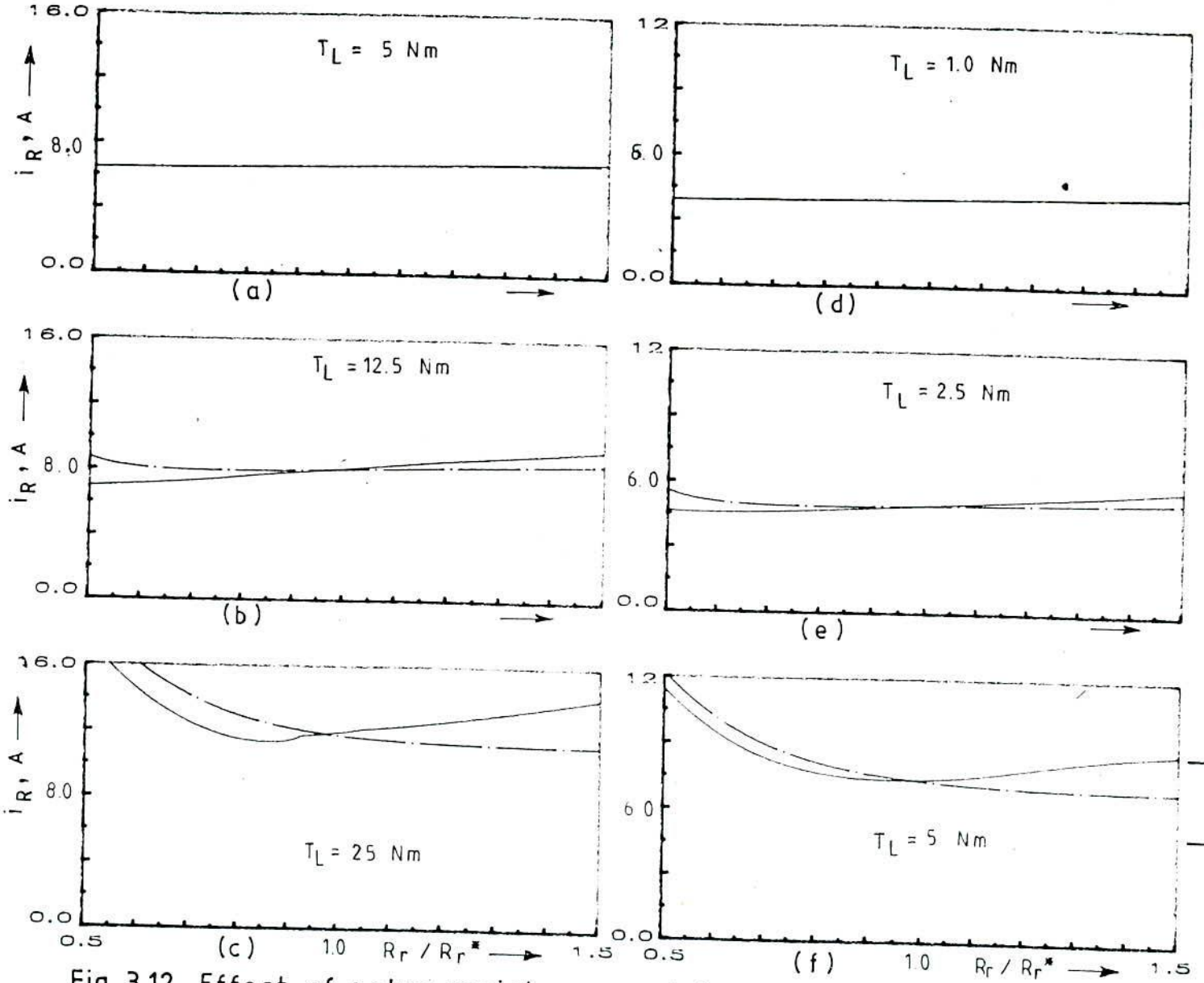

Fig. 3.12 Effect of rotor resistance and load torque on dc link current
a, b, c, - Machine I ; d, e, f, - Machine II

The above pattern of link current variations can easily be visualized from the flux-ratio change, shown in Figs. 3.7 and the expression for electro-magnetic torque. Under the constraint that the load torque is equal to electromagnetic torque for controlled speed operation

$$T_L = \frac{3}{2} P_p \frac{L_m}{L_r} \lambda_r i_{qs} \qquad (3.36)$$

L_m to L_r ratio does not change significantly with the change in the magnetic state of the machine as the leakage inductance is usually a small percentage of the magnetizing inductance. Hence, for constant torque load operation, i_{qs} will vary inversely as λ_r, and so will be approximately the current vector magnitude. This explains the reverse pattern of variation in Fig. 3.12 when compared with those in Fig. 3.7.

3.5 EFFECT OF MAGNETIZING FLUX SATURATION

3.5.1 Field Orientation Maintained

The torque production in a CSI-fed induction motor is highly dependent on the degree of saturation even under field oriented condition. Besides affecting the maximum torque production and the maximum torque per ampere squared the saturation level affects the linearity of the torque response of field oriented machine by making the actual machine inductances differ from those used in the controllers. Degree of saturation, i.e., the magnetic state, in the machine is decided by the rotor flux which in turn, as can be seen from (3.18), depends basically on the electromagnetic torque and the

feedforward slip forcing the current vector to a position that changes the excitation component of stator current. Thus in an indirect field oriented induction motor inappropriate transmission of angular slip speed may result in overfluxing or underfluxing in the machine. This is illustrated in Fig. 3.13 for machine-I (Table A.I of Appendix I) for three different values of developed torque. In a normally designed machine, flux levels well above the rated value are unacceptable from the operational point of view as the corresponding large magnetizing current will reduce severely the torque producing component of current.

Fig. 3.14 demonstrates the nature of the effect of saturation on the torque characteristics of a CSI-Fed induction motor. Steady state torques under field oriented condition for three specific values of stator current are plotted as a function of the ratio of the torque component to flux component of the stator current with and without saturation. The effect of flux saturation that are apparent from the field oriented plots are:

i) The torque characteristics under the influence of saturation effect are more flat than those corresponding to linear models.

ii) The magnitude of peak torque/ampere squared with saturation considered, decreases for high and medium link currents but increases for low values of link current when compared with the non-saturated machine. However, for increased slip speed values saturation effect yields better torque/ampere square.

iii) The peaks of developed torque, under nonlinear magnetic state, occur at a ratio of i_{qs} to i_{ds} which is larger than unity and going

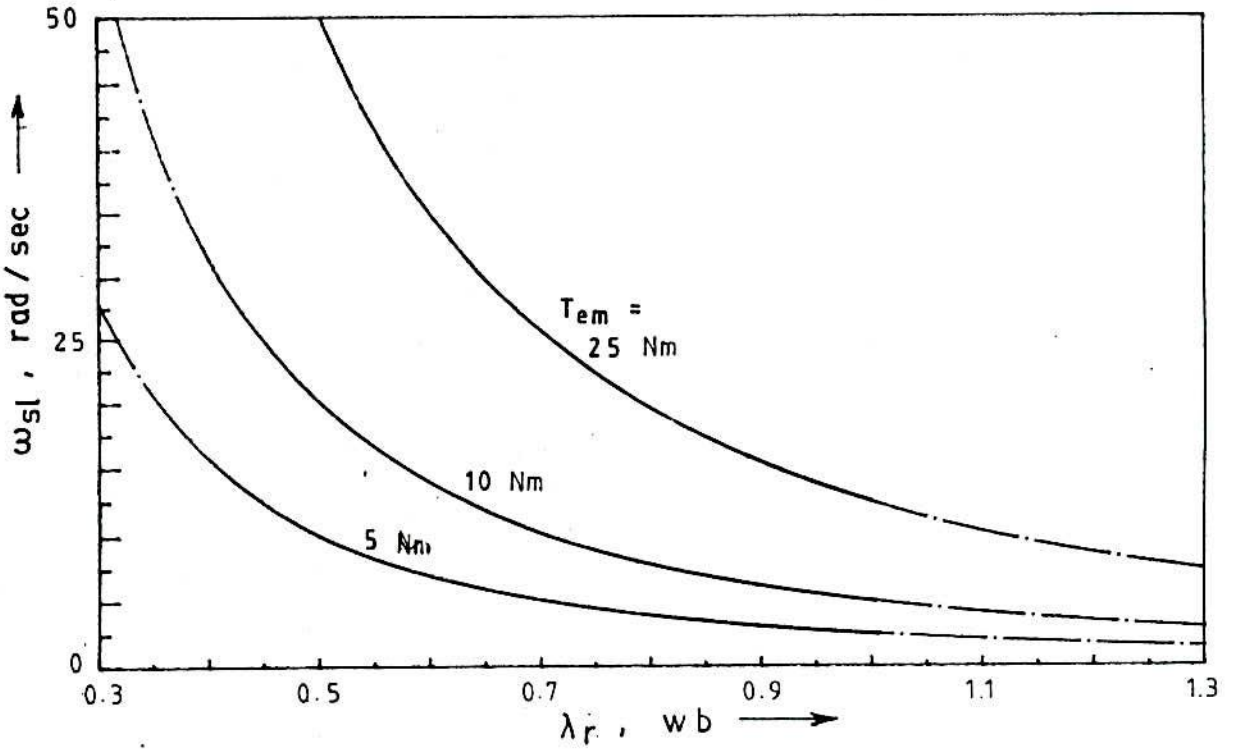

Fig 3.13 Effect of slip speed and load torque on flux level (eqn. 3.18) of machine-I

higher for increased values of link current. As expected from the torque function in (2.38) and noted in Fig.3.14 the peak torque for unsaturated machine occurs at $i_{qs}/i_{ds} = 1.0$, i.e., when i_{qs} and i_{ds} each equals 70.70% of the magnitude of the stator current vector. The reason for the shift towards higher values of i_{qs}/i_{ds} for the peak torque to appear in the case of saturated machine can be found in the torque producing function in (2.38) when viewed along with level flux saturation characteristic in Fig. 3.15 . Because of the slow rate of increase of the rotor flux with magnetizing current beyond the knee point, two segment linear level-flux saturation model in Fig.3.15 in place of the exact saturation model of Fig.3.2a can be considered to be sufficient for qualitative examination and reasonably good approximate quantitative assessment of the influence of saturation on the field orientation characteristics.

For rotor flux-based vector control the torque equation is

$$T_{em} = \frac{3}{2} P_p \frac{L_m}{L_r} \lambda_r i_{qs} \tag{3.37}$$

The L_m to L_r ratio will show slow change with degree of saturation if the leakage reactance is small and magnetizing current is not too large. So for a given stator current i'_R, T_{em} will take on maximum value $T_{em,max}$ when the product of λ_r and i_{qs} attains maximum value. Maximum value of λ_r is given by $\lambda_{r,max} = L_{mo}\ i_{do}$ (Fig.3.15) . As magnetizing current greater than i_{do} is ineffective in raising the flux level further, best effect for given i'_R will be produced when

$$i_{qs} = \sqrt{i'^2_R - i^2_{do}} \tag{3.38}$$

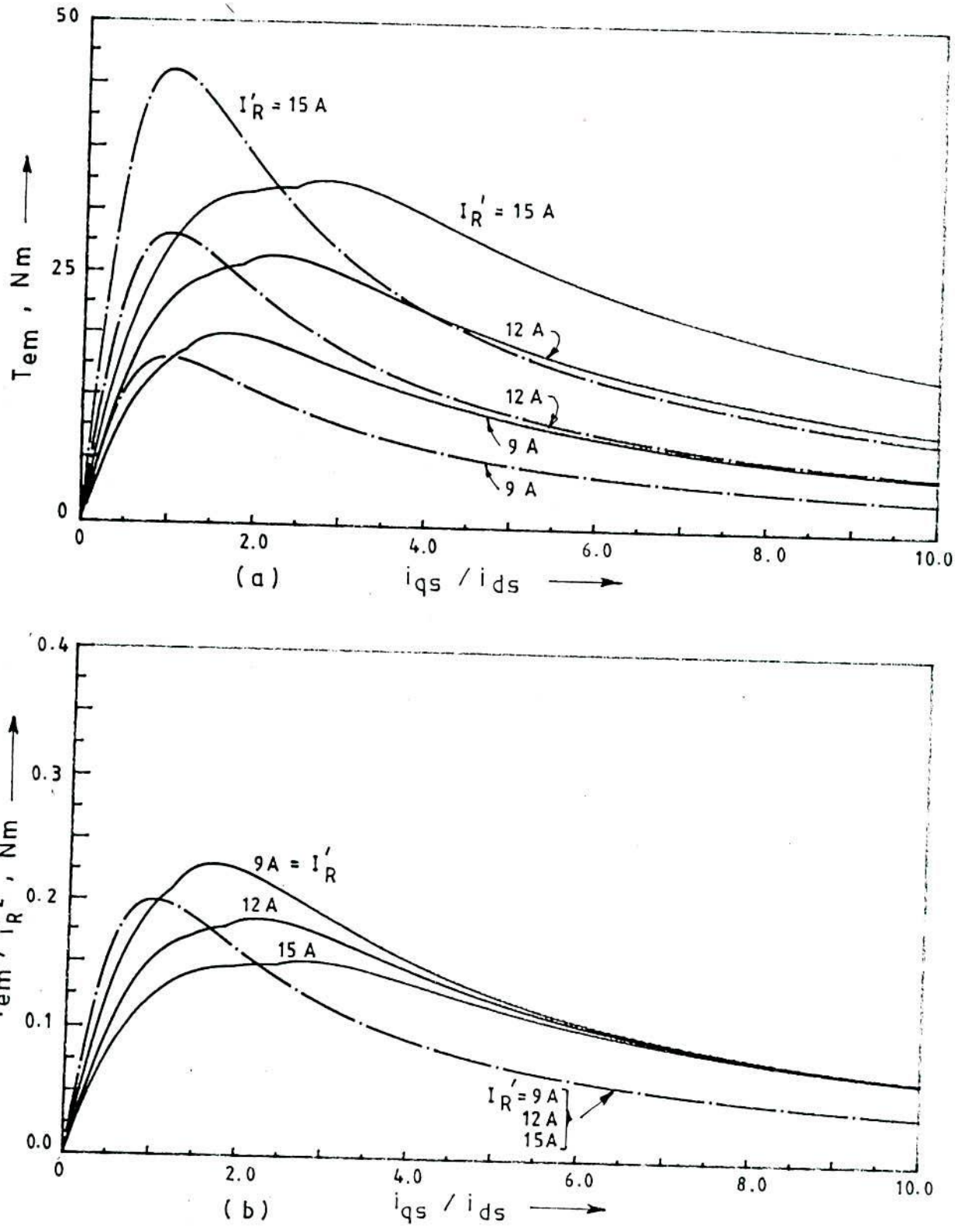

Fig. 3.14 Effect of the ratio of torque to flux components of stator current for constant dc link current under field orientation (a) torque, (b) torque/amp^2
——— Saturation model; —·—·— Linear model

Hence $T_{em,max}$ will be

$$T_{em,max} = \frac{3}{2} P_p \frac{L_{mo}^2}{L_{ro}} i_{do} \sqrt{i_R'^2 - i_{do}^2} \qquad (3.39)$$

and in the T_{em} - i_{qs}/i_{ds} plane, will lie on a straight line whose slope by (3.38) and (3.39) is given by

$$\frac{T_{em,max}}{\left(\frac{i_{qs}}{i_{ds}}\right)} = \frac{3}{2} P_p \frac{L_{mo}^2}{L_{ro}} i_{do}^2 \qquad (3.40)$$

indicating a shift in the $T_{em,max}$ position unlike in non-saturating induction machine.

By taking the derivative of $\left(\frac{T_{em,max}}{i_R'^2}\right)$ with respect to $\left(\frac{i_{do}}{i_R'}\right)$, Eqn. (3.39) indicates that maximum value of torque per ampere squared will be produced for the stator current

$$i_R' = \sqrt{2}\ i_{do} \qquad (3.41)$$

Table 3.1 compares the values of $T_{em,max}$ and (i_{qs}/i_{ds}) at which $T_{em,max}$ occurs using the saturation curves of Fig. 3.2a and Fig. 3.15. Discrepancy may be attributed to very approximate fit of the level flux saturation curve on the exact magnetization characteristic. However, such limit flux saturation curve brings out the salient aspects of the effects of saturation on the torque characteristics of CSI-fed field oriented induction machine.

The effect of excitation on developed torque under field oriented

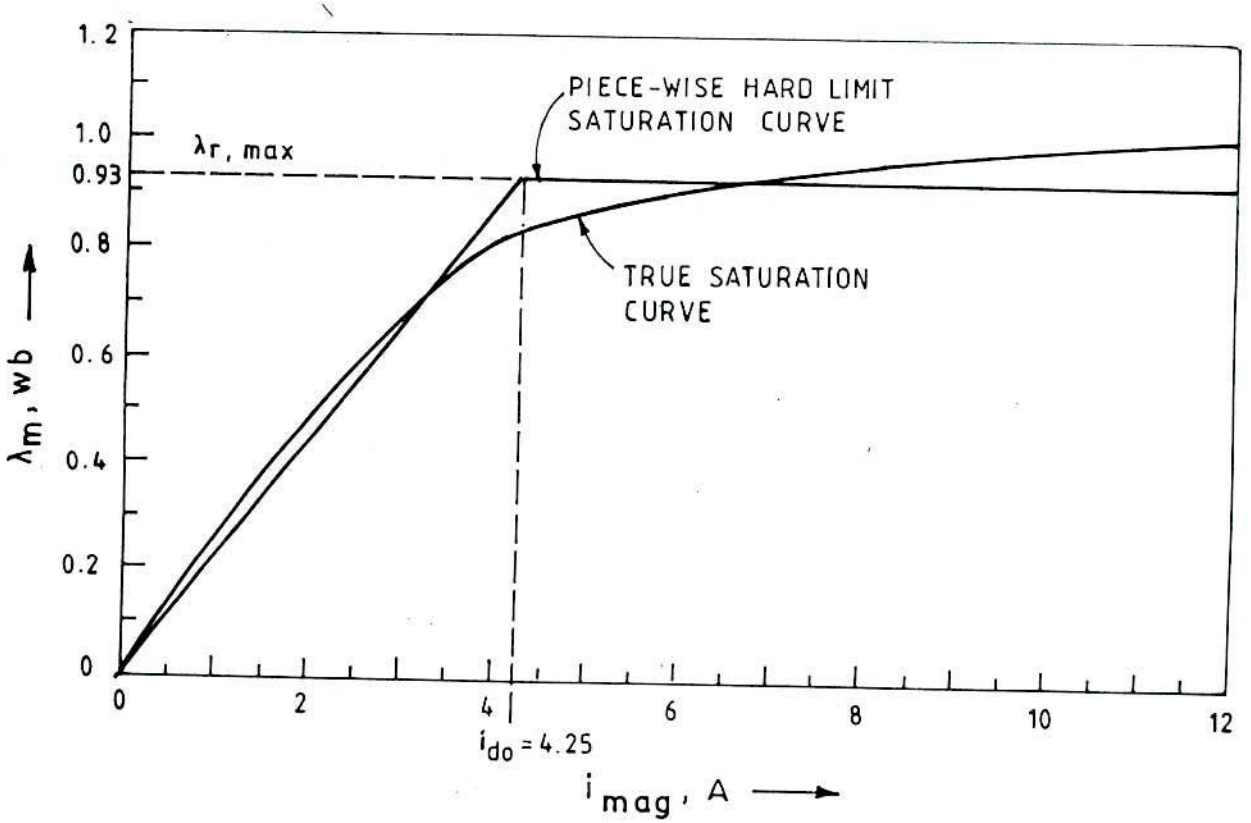

Fig. 3.15 Approximation of saturation characteristics by piece-wise linear hard limit saturation curve of machine-I

TABLE 3.1

L_{ro} = 0.2323H, L_{mo} = 0.2188H, $\lambda_{r,max}$ = 0.93Wb at i_{do}= 4.25A

Stator current A	Sat. curve	$\frac{i_{qs}}{i_{ds}}$	$T_{em,max}$ Nm
15	(1)	2.75	34.38
	(2)	3.38	37.79
	(3)	1.00	45.00
12	(1)	2.18	26.56
	(2)	2.64	29.48
	(3)	1.00	28.82
9	(1)	1.60	19.75
	(2)	1.86	20.84
	(3)	1.00	16.21

In the table

(1) Based on actual saturation curve (Fig 3.2a)

(2) Based on level flux saturation curve (Fig. 3.15) and eqns. 3.37 & 3.39.

(3) Based on constant parameter model (Fig. 3.14a)

condition was studied by varying i_{ds} for both saturated and constant parameter models. Saturated model uses (3.5) to accommodate the variable inductance. Results of simulation studies are shown in Fig. 3.16(a). In both the cases (saturation and unsaturation) peak value of torque/amp^2 occurs at increasing values of i_{ds} with increase in load torque. However, the values of i_{ds} required for saturation model are lower than those corresponding to constant parameter model. The slip frequency characteristics in Fig. 3.16(b) indicate that for saturation model the characteristics are flat for high values of i_{ds} and slip values increase linearly with torque. This is expected as indicated by (3.18). Owing to the decreased ability of the magnetizing current to

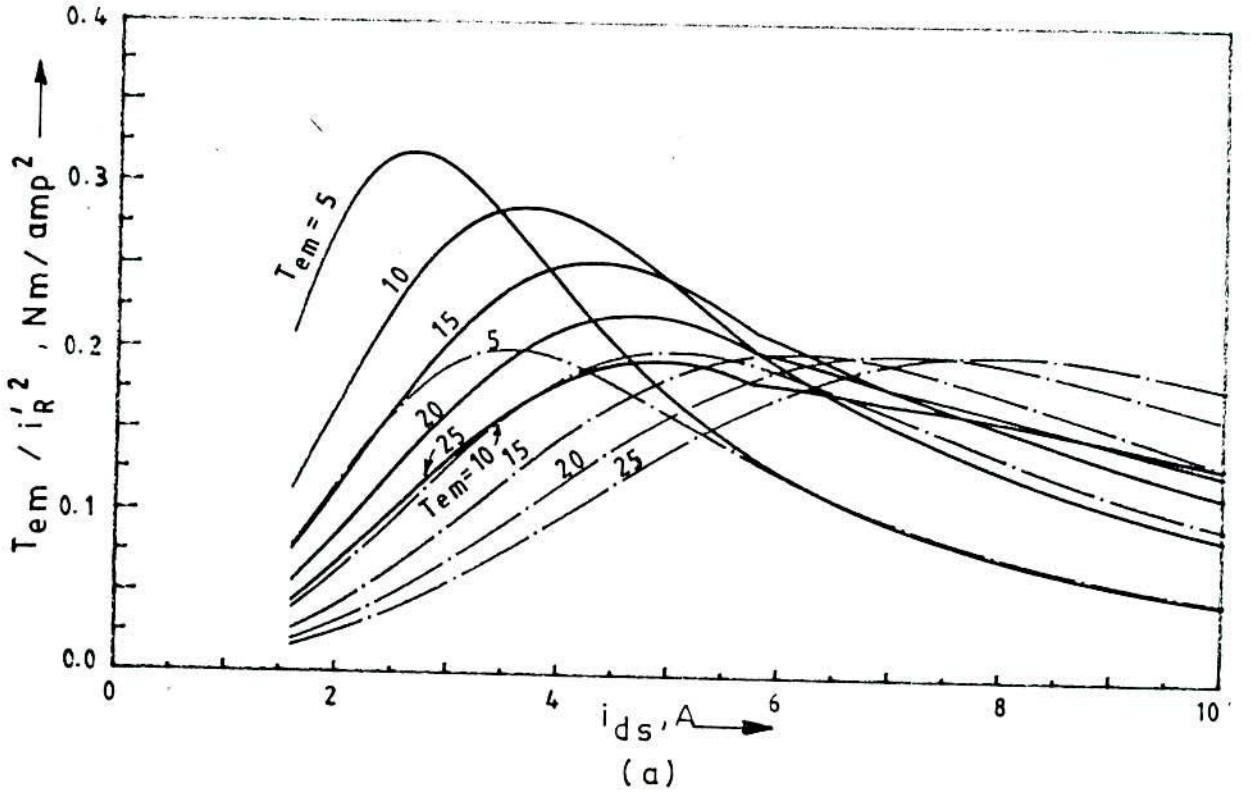

(a)

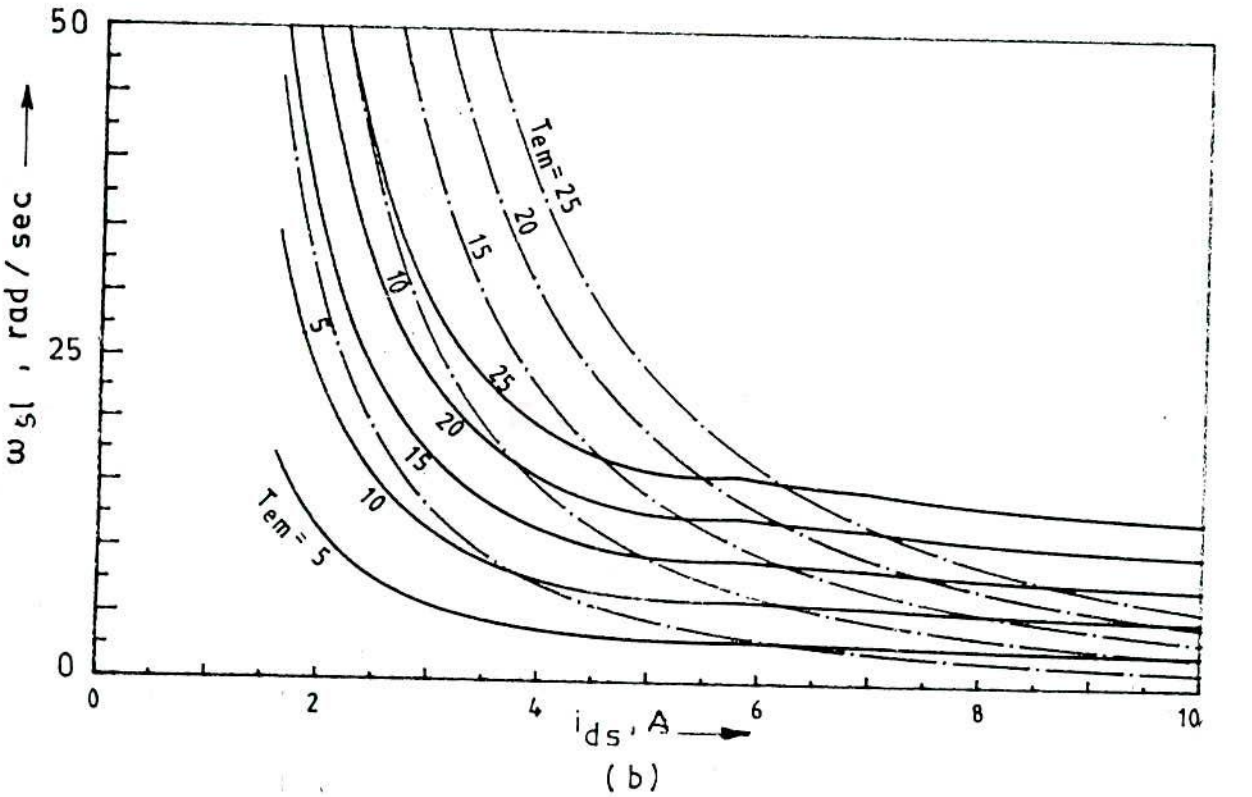

(b)

Fig. 3.16 Effect of excitation on (a) torque / amp^2 and (b) slip-speed for constant developed torques under field oriented condition ——— Saturation model —·—·— Constant parameter model

increase the rotor flux under saturation condition torque producing component of stator current must, therefore, increase linearly with the torque and with it the slip. At decreased level of i_{ds} actual magnetic state demands less value of slip speed for field orientation than those indicated by constant parameter model.

3.5.2 Non-oriented condition

The inductances of the induction motor change with the saturation level which in turn depends on i_{ds}. Effects resulting from the mismatch between the inductances used (nominal value) in the slip calculator and the actual machine inductances are shown in Fig. 3.17 which presents the plots of total rotor flux linkage, link current and quadrature axis rotor flux as a function of i_{ds} with rotor resistance unchanged. For comparison, characteristics with unchanged inductances are shown in Fig. 3.18. Though expressions in (3.2) and (3.3) suggest adjustment in the values of L_m, and hence of L_r, with changes in torque load torque for the same i_{ds} but the typical simulation results, as applied to machine-I (SC type), in Fig. 3.17 indicate that tuning will be practically maintained for all load torques if the inductance values in the slip calculator correspond to the command value of $i_{ds}(i^*_{ds})$. However, the changing of i_{ds} will lead to detuned condition as are noted in Fig. 3.17, where inductances are not adjusted in the calculation of slip gain.

3.6 EFFECT ON SPEED RESPONSE DUE TO ROTOR RESISTANCE DEVIATION

The effect of change in rotor resistance on the transient performance was examined by simulating the drive system in Fig.2.7 for

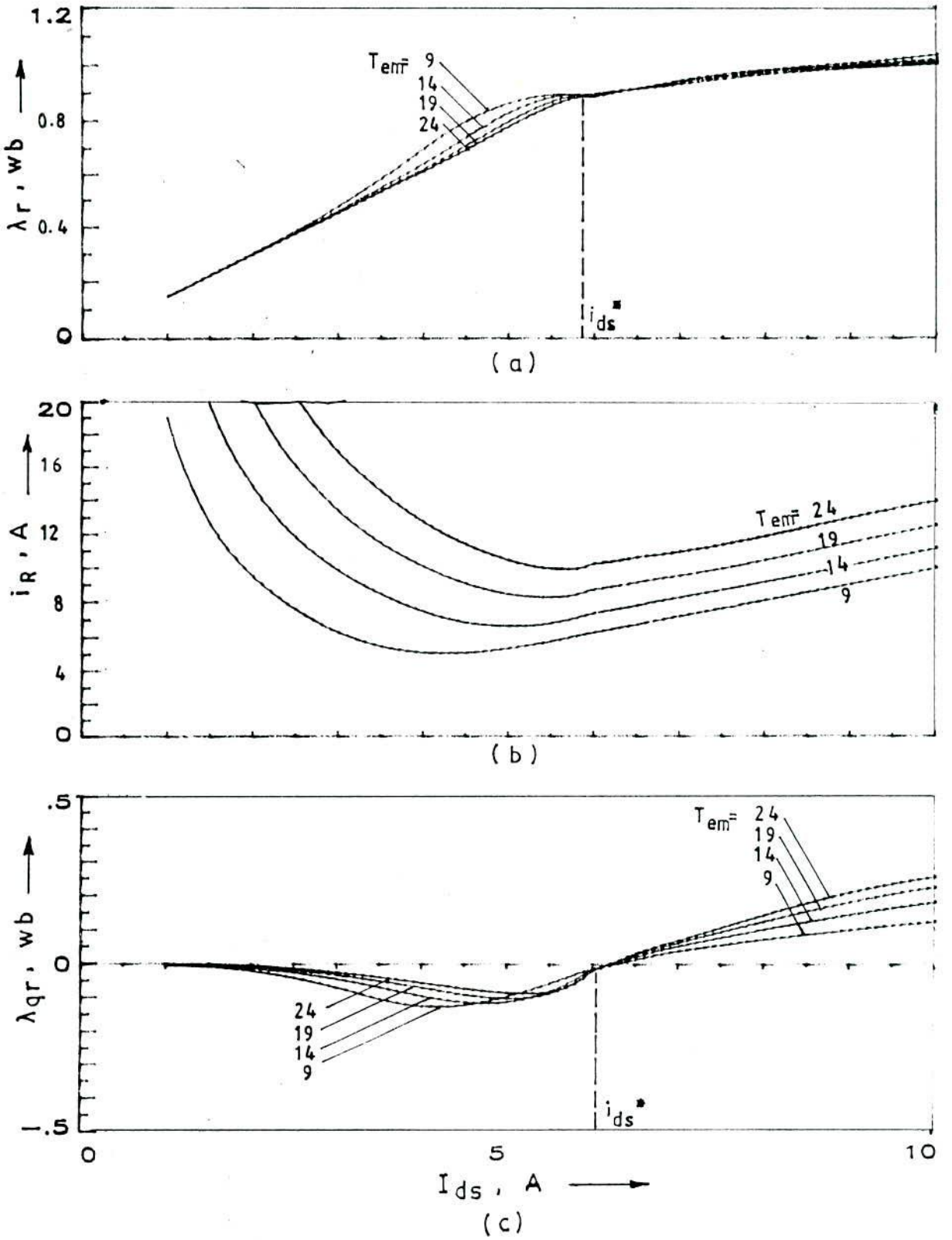

Fig. 3.17 Effect of exciation and load torque on (a) rotor flux (b) dc link current and (c) q-axis flux; saturation model

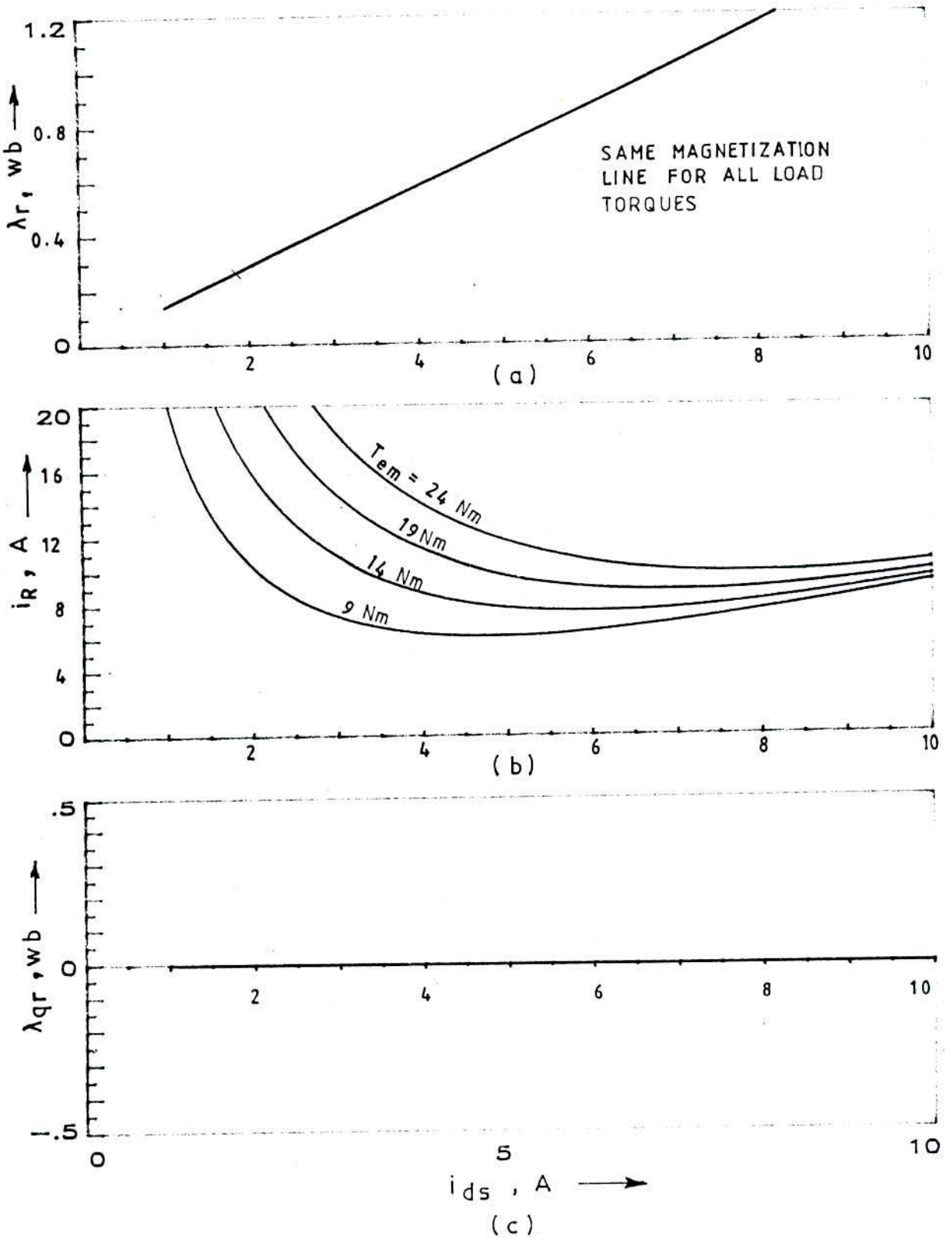

Fig. 3.18 Effect of excitation and load torque on (a) rotor-flux (b) dc link current and (c) q-axis flux; Linear model

a step change in speed command from 1000 rpm to 1400 rpm with 16Nm load torque for the conditions mentioned below. Simulation results are shown in Fig. 3.19.

1. The rotor resistance in the machine model is increased by 20% of the nominal value and saturation not incorporated, while nominal parameters are retained in the controller.

2. The rotor resistance in the machine model is increased by 20% of the nominal value and saturation effect included but nominal parameters are retained in the controller.

3. Rotor resistance in the machine model and in the controller are enhanced by 20% of the nominal value but saturation is considered only with the machine model.

It is noted from Fig. 3.19(c) that the instantaneous torque overshoot for condition 2 due to change in speed reference is less than those arising in the cases of conditions 1 and 3, which is reflected in the corresponding speed responses (Fig. 3.19a). It is indicated that the speed response suffers if no parameter adaptations are considered in the controllers for parameter deviations in the machine. From Figs. 3.19(b) and 3.19(c) it is evident that overshoot in i_{qs}^{c} for the three conditions are almost similar and for condition 2, i_{qs}^{c} has higher value than the others but due to coupling effect it fails to develop the same torque overshoot as in condition 3. This can be attributed to insufficient increase in λ_r owing to enhanced magnetizing

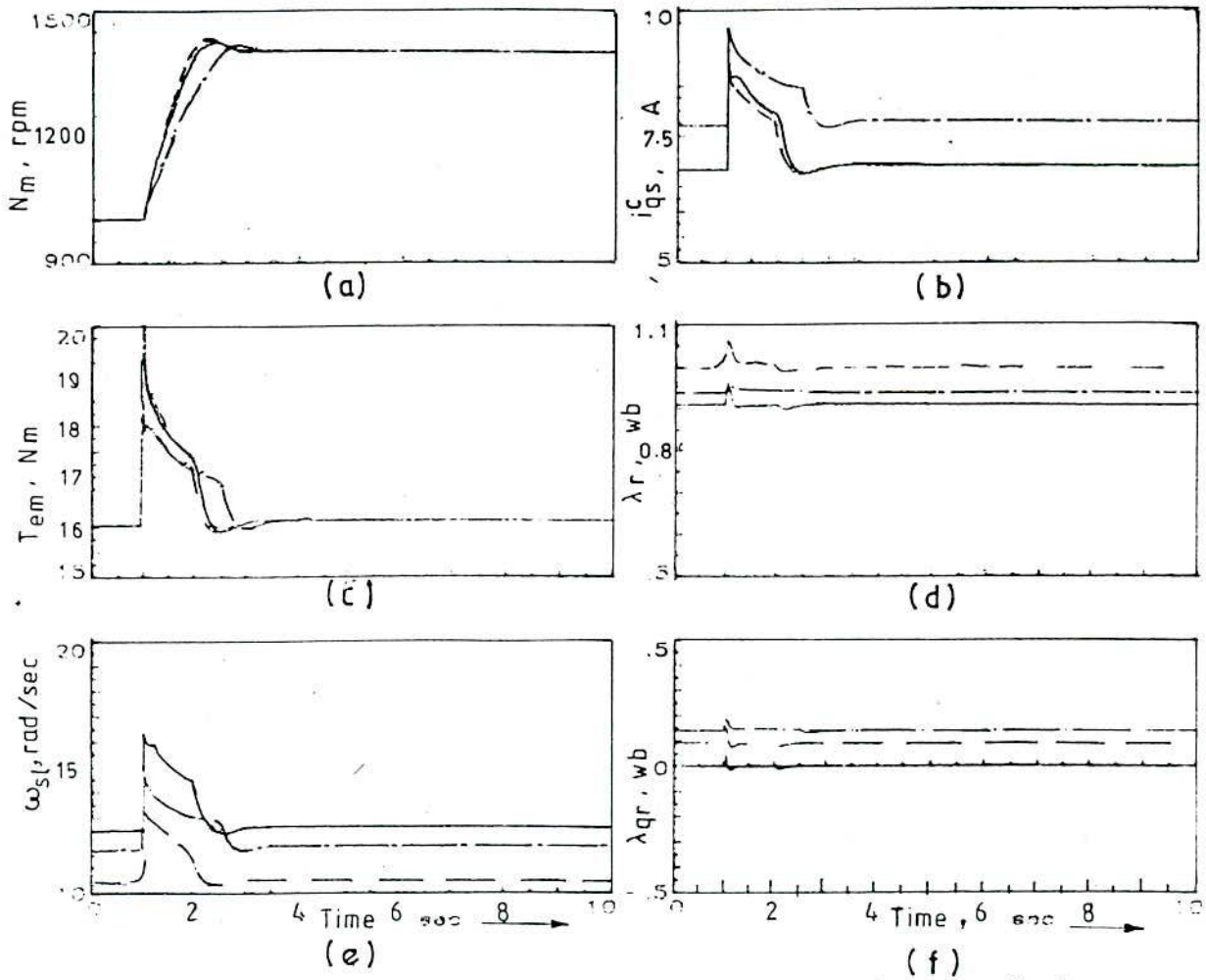

Fig. 3.19 Dynamic responses for step change in speed from 1000 rpm to 1400 rpm with 16 Nm torque load for

(I) $R_r = 1.2\, R_r^*$ for machine, R_r^* in controller, Linear model ——— —

(II) $R_r = 1.2\, R_r^*$ for machine, R_r^* in controller, Saturation model —·—·—

(III) $R_r = 1.2\, R_r^*$ for machine & Controller, saturation model ————

current (than the tuned condition) and the speed response is slower due to reduced developed torque. In the detuned condition 1 almost similar torque overshoot occurs as in the tuned condition 3. This is due to linear increase in flux (Fig.3.19d) with increased magnetization current (linear model). The traces of λ_{qr} for the three conditions indicate the relative detuning for the three conditions of operation.

CHAPTER - IV

PARAMETER ADAPTATION

4.1 INTRODUCTION

A slip frequency controlled field oriented induction motor drive system works satisfactorily if the feed forward slip frequency is evaluated correctly. This requires either an on-line tuning or estimation of the correct slip gain by other means [84]. For perfect tuning all the parameters of the induction motor used in the controllers need be updated as they change during operation. But identification of all the parameters makes the control system very much complex and cost prohibitive. For general applications, this is not feasible as well as desirable. It is found to be sufficient to focus attention on such key parameters whose deviations seriously affect the performance of an indirect field oriented induction motor. These key parameters are rotor resistance and rotor inductance in rotor flux orientation scheme.

Relevant literature reveals two broad categories of parameter adaptation schemes based on the following fundamental approaches:

(i) Direct or indirect measurement or identification of rotor parameters [62 - 67].

(ii) Creating an error function related to the deviation of certain physical variables from their ideal values satisfying field orientation criterion [45, 53, 68, 69]. This error function is used to

correct the slip gain in the manner as to bring the error to zero. This is generally known as model reference adaptive control [MRAC].

The relative merits and demerits of parameter corrective schemes are related to speed of computation, complexities of implementation, ease of sensing, sensitivity of the variation to parameters and parameter dependence of the created reference values.

A detailed classification of parameter compensation schemes are available in [84]. The direct measurement of key parameters requires signal injection and call for a very careful processing of the output signals for determining the parameters [58, 62 - 65]. Some of them [53] require additional circuitry for measurement. On line implementation of these schemes increases complexity of the control system. M.V.Reyes et al [66] propose parameter estimation algorithm for the machine parameters that call for program stepping up in a big way and is difficult to implement. Scheme in [64] is stator resistance dependent and heavily computation based. It requires flux estimation from terminal quantities in the determination of rotor parameters. In this method nonlinear differential equations are solved with initial conditions for each step of integration. The scheme proposed by Ohm et al, [54] computes rotor resistance from dc link power measurement and is stator resistance dependent. C. Wang et.al. [58] have described a method of evaluating rotor time constant by injecting single phase and dc currents to the induction motor and observing certain criteria that relate the nature of transient currents (ac and dc) with rotor time constant. For fine tuning linearity in T_{em} vs. i_{qs} characteristic is utilized in this scheme.

Model reference adaptive systems may use torque [55, 68], air gap power [69], reactive power [45, 53, 55], stator voltage components [55], etc, to generate error for updating the gains of the slip frequency controller. In [33] error in torque is generated by determining the changes in quadrature axis stator current reference and rotor flux components from steady state operating condition. The error function produces a compensating slip speed which is added to the nominal slip speed for tuning the control scheme. Scheme in [55] estimates the developed torque from the measured stator voltages and currents and the reference torque from the d- and q-axis components of stator current with quadrature-axis rotor flux set at zero. The scheme requires extra transducers and evaluation of initial conditions. The tuning procedure described in [68] uses coherent power of model reference error generated from torque. In this case slip gain of the feedforward path is modified according to the error. One of the earlier contributions [53], using reactive power as the variable, is dependent on stator leakage inductance for computation of error function. The detuning corrective measure in [45] uses modified reactive power which is also stator leakage inductance dependent. The voltage regulator schemes in [55] are dependent on stator leakage inductance and correct slip gain for tuning. A line voltage sensing scheme in [117] proposes to compute line voltage from the switching conditions of the inverter. The voltages are to be used to compute the reactive power. The tuning method based on observing the linearity in speed response following the application of square wave reference torque input is presented in [68].

This chapter endeavours to present three methods of adaptation schemes for tuning the indirect vector control system. The first method estimates the rotor resistance from the air gap power following almost the procedure outlined in [54] but with certain modifications. The proposed method uses updated values of inductances evaluated from the magnetic energy. Neglecting the effects of inductance deviation leads to incorrect estimate for the rotor resistance. The estimated resistance is directly fed to the slip speed calculator for maintaining the decoupled operation. The second method uses dc link voltage to generate an error function while the third method uses torque component of stator current. In the latter two schemes (MRAC) only one variable requires to be computed and the other one is obtained directly from power or control circuit. The adaptability of the MRAC schemes is also discussed. The schemes use only dc quantities which are easy to transduce so that hardware requirement is minimal.

4.2 AIR GAP POWER BASED ROTOR RESISTANCE ESTIMATION

4.2.1 Basic equations

Use of air gap power for the development of adaptation algorithm to update the rotor parameters (rotor resistance or time-constant) in the controllers offers certain obvious advantages when compared with compensation schemes that utilize instantaneous voltage and current signals from the drive motor. Measurement and processing of dc link power and current require less hardware in the control circuit implementation and uses simple program steps in the signal processing. Two earlier papers [54, 69] have forwarded adaptation algorithms to

correct the detuning for the rotor resistance change based on the measurement of air gap power. In [69] air gap power equivalence, computed from the dc link side, is matched against reference synchronous watt for slip regulator tuning of a vector controlled induction motor servo drive. But generation of reference air gap power in the case of speed controlled system is a problem. Secondly, suggested equivalent rotor resistance change to take care of the changing rotor inductance may not lead to decoupled torque and flux, particularly for a speed controlled system. This is because even under non-oriented condition an induction motor at a suitably adjusted slip can develop the same air gap power as that of the reference making the error between the commanded and the actual values of the air gap power zero. In [54] rotor time constant is calculated by solving a quadratic equation constructed from air gap power measurement. But the adaptation routine to select the appropriate one, out of two time-constant values, requires prior detailed experimentation, other than routine tests, in respect of the temperature characteristic of the individual motor. Secondly, rotor inductances, if not duly corrected for saturation effect, would lead to incorrect estimates for rotor resistance (time constant) and may even make the roots of the quadratic equation in R_r (eqn. 4.3) complex leading to the failure of adaptation routine. The paper does not lay down the approach to include the saturation effect which is needed for the updating procedure to work well. The following sections present rotor parameter adaptation scheme, which uses air gap power on the lines in [54] to track the changing rotor resistance, includes saturation effect in the calculation and selects the

appropriate solution for the resistance out of two values from the motor terminal voltage observation.

From (3.11) steady state torque of an induction motor under balanced operation is

$$T_{em} = \frac{3}{2} P_p \, I_R^{',2} \, \frac{s \, \omega_e \, R_r \, L_m^2}{R_r^2 + s^2 \omega_e^2 \, L_r^2} \tag{4.1}$$

Air-gap power is

$$P_{ag} = \frac{T_{em} \, \omega_e}{P_P} \tag{4.2}$$

Combining (4.1) and (4.2) leads to the following quadratic equation in R_r

$$R_r^2 - \frac{3}{2} \frac{I_R^{',2}}{P_{ag}} s \, \omega_e^2 \, L_m^2 \, R_r + s^2 \, \omega_e^2 \, L_r^{\,2} = 0 \tag{4.3}$$

Solution to which gives the actual value of R_r provided all the other variables inclusive of rotor inductances are available. Eqn. 4.3 requires a proper estimate of the value of P_{ag} from quantities that are directly accessible. Subtraction of stator copper and inverter losses from the time average value of the instantaneous inverter input power gives us an estimate of the actual air gap power as follows

$$P_{ag} = P_{inv} - p_{st,loss} - p_{i,loss} \tag{4.4}$$

where,

P_{inv} = inverter input power

$p_{st,loss}$ = stator copper loss

$p_{i,loss}$ = inverter loss

Assuming quasi-square wave motor currents of 120^0 width, the above losses can be estimated using the following expressions

$$p_{st,loss} = (2\ I_R^2\ R_s) \tag{4.5a}$$

$$p_{i,loss} = 2(V_{th} + V_d)\ I_R \tag{4.5b}$$

in which V_{th} (= 1.1 to 1.4 V) and V_d (= 0.7 V) are the thyristor and diode drops respectively.

4.2.2 Selection of R_r

Solution to (4.3) gives two values of R_r one of which is only related to the operating state of the machine. By virtue of the framing of eqn. 4.3 on the basis of (4.1) and (4.2) both the solutions satisfy the developed torque and input current conditions for the chosen values of other parameters and quantities in eqn. 4.3. However, out of the two solutions that will be the required value of R_r which will satisfy other conditions of operation such as terminal voltage, slip value, degree of saturation giving rise to the value L_m used in eqn. 4.3 etc. Under detuned operation, command values for the d-q axis currents, namely, i_{ds}^* and i_{qs}^* do not match the actual values of the flux- and torque- producing current components i_{ds} and i_{qs} existing inside the machine. For the selected value of the rotor resistance, say $R_{r,s}$, the values of i_{ds} and i_{qs} are given by

$$i_{ds} = I_R' \frac{R_{r,s}}{\sqrt{R_{r,s}^2 + s^2\ \omega_e^2\ L_r^2}} \tag{4.6}$$

$$i_{qs} = I_R' \frac{s\ \omega_e\ L_r}{\sqrt{R_{r,s}^2 + s^2\ \omega_e^2\ L_r^2}} \tag{4.7}$$

The following two conditions must be satisfied simultaneously for the selection of the correct solution.

Condition I:

As the commanded value of slip is directly transmitted to the motor.

$$R_{r,s} = \omega^{*}_{sl} L_r \frac{i_{ds}}{i_{qs}} \tag{4.8}$$

The product of two solutions for R_r being $s^2 \omega_e^2 L_r^2$, the higher value is selected if $i_{ds} > i_{qs}$, otherwise the lower value.

Condition II:

When the selected value of R_r is used in (4.6) i_{ds} must produce that level of saturation for which the value of L_m must match the value used in (4.3) to calculate R_r.

Alternatively, the measured motor terminal voltage must agree with the computed motor terminal voltage (fundamental component) based on the selected solution to eqn. 4.3. and which corresponds to the magnetic state prevailing in the machine and used in (4.3).

4.2.3 Saturation level and selection of L_m and L_r

The variables I_R, s and ω_e are transmitted to the motor from outside. A very sensitive as well as a decision making parameter in (4.3) is the value to be assigned to L_m and this requires careful consideration.

With reference to the equivalent circuit in Fig.A.2 (Appendix II) the reactive volt-amp input to the motor under steady state condition is

$$Q = \frac{3}{2} \left(L_{\sigma s} \, I_R^{\prime 2} + \frac{L_m^2}{L_r} \, i_{ds}^2 \right) \omega_e \qquad (4.9)$$

If V is the rms value of the fundamental component of the motor line-to-line terminal voltages, the volt-amp input to the motor is

$$S_{in} = \sqrt{3} \, \frac{V \, I_R^{\prime}}{\sqrt{2}} \qquad (4.10)$$

where $I_R^{\prime}$, by definition, is the peak of the fundamental component of the stator current wave form. From (4.4) power input to the motor

$$P_{st} = P_{inv} - p_{i,loss} \qquad (4.11)$$

From (4.10) and (4.11) an estimate for steady state reactive volt-amp input Q to the stator is

$$Q = \sqrt{S_{in}^2 - P_{st}^2} \qquad (4.12)$$

Equating the expression for Q in (4.9) and (4.12), and re-arrangement of the terms give

$$\lambda_r \, i_{ds} = \frac{L_r}{L_m} \left(\frac{2}{3\omega_e} \sqrt{S_{in}^2 - P_{st}^2} - L_{\sigma s} \, I_R^{\prime 2} \right) \qquad (4.13)$$

where, by definition, under steady state condition

$$\lambda_r = L_m \, i_{ds} \qquad (4.14)$$

Although dependent on machine inductances, expression in (4.13) obtains us an estimate for steady state value of $\lambda_r\ i_{ds}$ with reasonable accuracy since $L_{\sigma s}$ and the ratio $\frac{L_r}{L_m}$ do not show significant variation with the saturation level over the usual operating range of flux. Circuit transducers directly provide us with the quantities on the right-hand side. Use of the calculated value of $\lambda_r\ i_{ds}$ by (4.13) in the saturation function, defined by (3.4b) enables us to separate out the values of i_{ds} and λ_r. This tacitly assumes that i_{ds} very closely equals i_{mag} (vide eqn. 3.2b). Then the operating values of L_m and L_r or the values close to the operating point are obtained. The extent of the validity of this assumption is examined in section 4.2.4.

4.2.4 Summary of air-gap power based parameter estimation algorithm and an observation

As indicated in the above sections, the air-gap power and the reactive volt-ampere input to the stator can be used to estimate the actual rotor parameters for tuning the slip calculator. For a reasonably good dynamic responses correction should be applied to the controller at an interval which should be short compared to the rotor time constant. The sequence of computational steps for parameter adaptation algorithm should be as follows:

I. Following the acquisition of data pertaining to dc link current and voltages to the inverter and the stator terminal voltage (fundamental component) estimate P_{st}, P_{ag} and S_{in} using (4.11) and (4.4) and (4.10) respectively.

II. Use (4.13) to obtain $\lambda_r\ i_{ds}$ and then saturation function (3.4b) to separate λ_r and i_{ds}. Obtain L_m and L_r.

III. Solve (4.3) for R_r. Two values of R_r are obtained as solutions.

IV. Calculate i_{ds} and i_{qs} by (4.6) and (4.7) respectively for both solutions.

V. Select that solution which yields same i_{ds} as that under step II.

VI. Check further the condition I under section 4.2.2 i.e., whether i_{ds} is greater than the corresponding i_{qs} (step IV) in case the selected solution is higher. For lower value it will be otherwise.

Alternatives to steps IV to VI (based on phase or line voltage comparison)

IV. Using the estimated values of L_m and L_r calculate machine terminal voltage for each solution of R_r for the given stator current, slip and inverter frequency.

V. Select that solution for R_r for which the calculated terminal voltage is close to the measured terminal voltage.

Results of rotor parameter estimation for machine II (Appendix I), using the aforesaid algorithm, with nominal parameters in the slip calculator and step wise change of actual rotor resistance in machine model are shown in Fig. 4.1. Rotor parameters were estimated 1 sec. after the change in the actual rotor resistance was effected in order to obtain the steady state operation. Results show that the estimated value of R_r and τ_r agree well with the actual values if the rotor parameters do not deviate significantly from those used in the slip calculator. Larger deviations undermine the assumptions made in the end of section 4.2.3. However, if the parameters in the slip calculator are

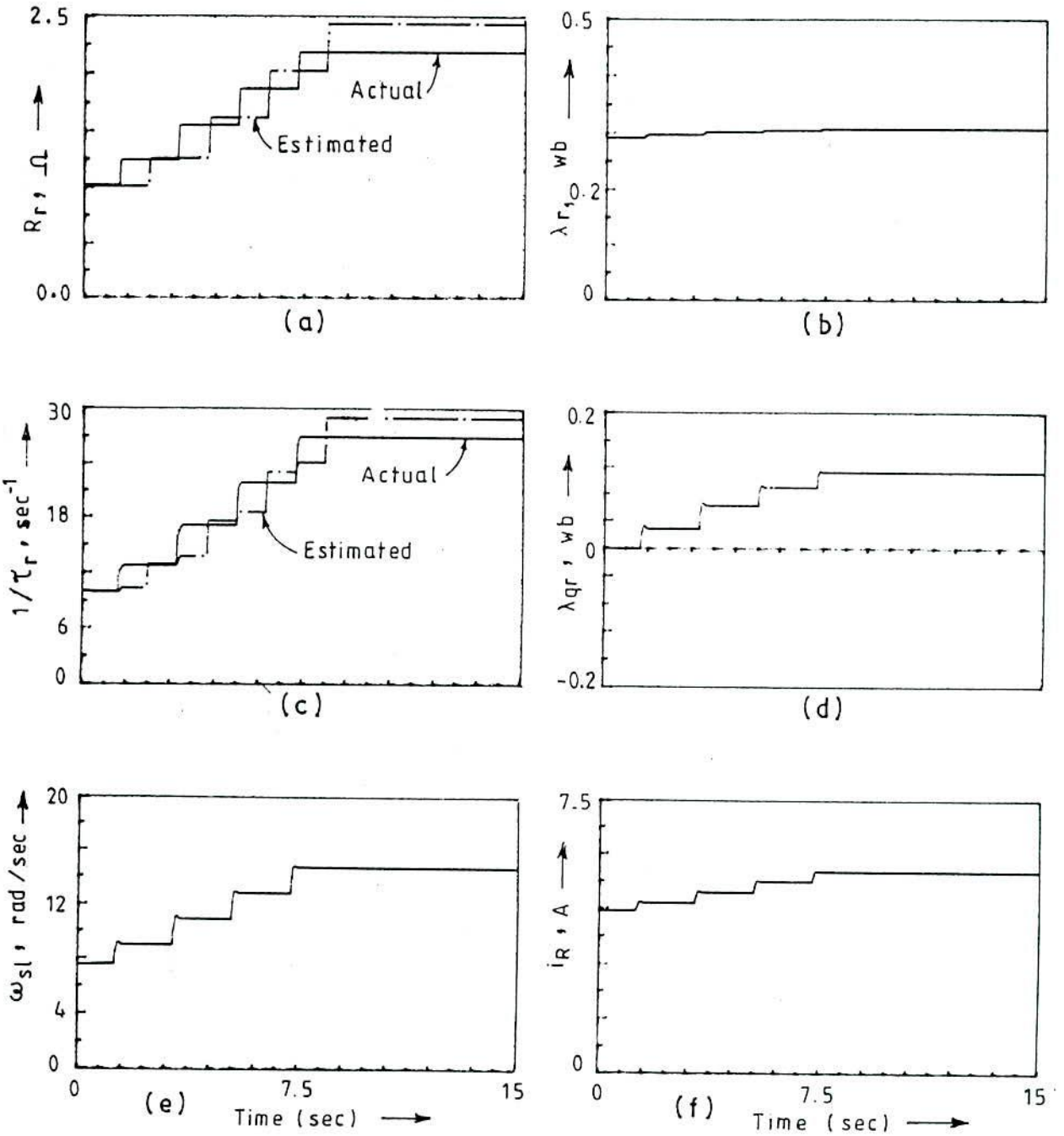

Fig. 4.1 Estimation of rotor resistance by air-gap power method updating the inductance

updated each time with the estimated parameters, the tracking of actual rotor parameters would be possible inspite of significant change in the rotor resistance.

4.3 INDIRECT ADAPTIVE CONTROLLER FOR DETUNING CORRECTION

Detuned condition of an indirectly controlled field oriented induction motor results in the deviation of certain physical variables from the values that would exist under properly tuned condition. These idealised values under field oriented condition are generally referred to as model reference. Two adaptive controllers based on (i) DC link voltage model reference and (ii) quadrature-axis current reference model are addressed in the following subsections. In these schemes discrepancy between specific model reference quantity and the corresponding estimated or the measured variable is passed through PI controller(s) to continuously modify the gain of the slip calculator until the error is driven to zero.

4.3.1 DC link voltage based rotor resistance adaptation scheme

4.3.1.1 Principle of the adaptation scheme

This section presents an easy-to-implement adaptation method for rotor resistance change, and the strategy makes use of the dc link voltage for sensing detuned condition of the controllers with respect to field orientation condition and takes necessary steps for subsequent correction in the slip gain to restore the decoupled state in the machine. The proposed adaptive controller makes provisions for generating a dc link voltage reference model from the set value of

flux, nominal values of inductances and dc link current satisfying the field-oriented condition. Subtraction of the dc link voltage drop from (2.20) and setting $p(\equiv \frac{d}{dt}) = 0$ result in the following field oriented inverter input dc link voltage model reference under steady state operation

$$V_I'^{Ref} = R_s\, I_R' + \frac{L_m^{*2}}{L_r^*}\,\frac{R_r^*\, L_r^*\, \omega_{sl}^*}{R_r^{*2}+(\omega_{sl}^*\, L_r^*)^2}\,\omega_e^*\, I_R' \qquad (4.15)$$

where,

$$V_I'^{Ref} = \frac{\pi}{3\sqrt{3}}\, V_I^{Ref}$$

ω_e : rotor flux-vector speed (elect-rad/sec).

R_r^*, L_m^* and L_r^* refer to parameters, nominal or adjusted as the case may be, used in the controllers.

Rotor slip speed relative to the rotor flux vector is given by (cf.2.24)

$$\omega_{sl}^* = \frac{i_{qs}^c\, R_r^*}{L_r^*\, i_{ds}^*} \qquad (4.16)$$

$$i_{qs}^c = \sqrt{I_R'^2 - i_{ds}^{*2}}$$

In (4.15) actual dc link current I_R' is retained in place of $I_R'^*$ because if flux orientation really exists in the machine with λ_r^*, eqn.4.15 must be the controller reference model.

The complete block diagram for the control strategy with parameter adaptation scheme obtained from the comparison of actual dc link voltage V_I with its reference V_I^{Ref} (4.15) is shown in Fig. 4.2. The

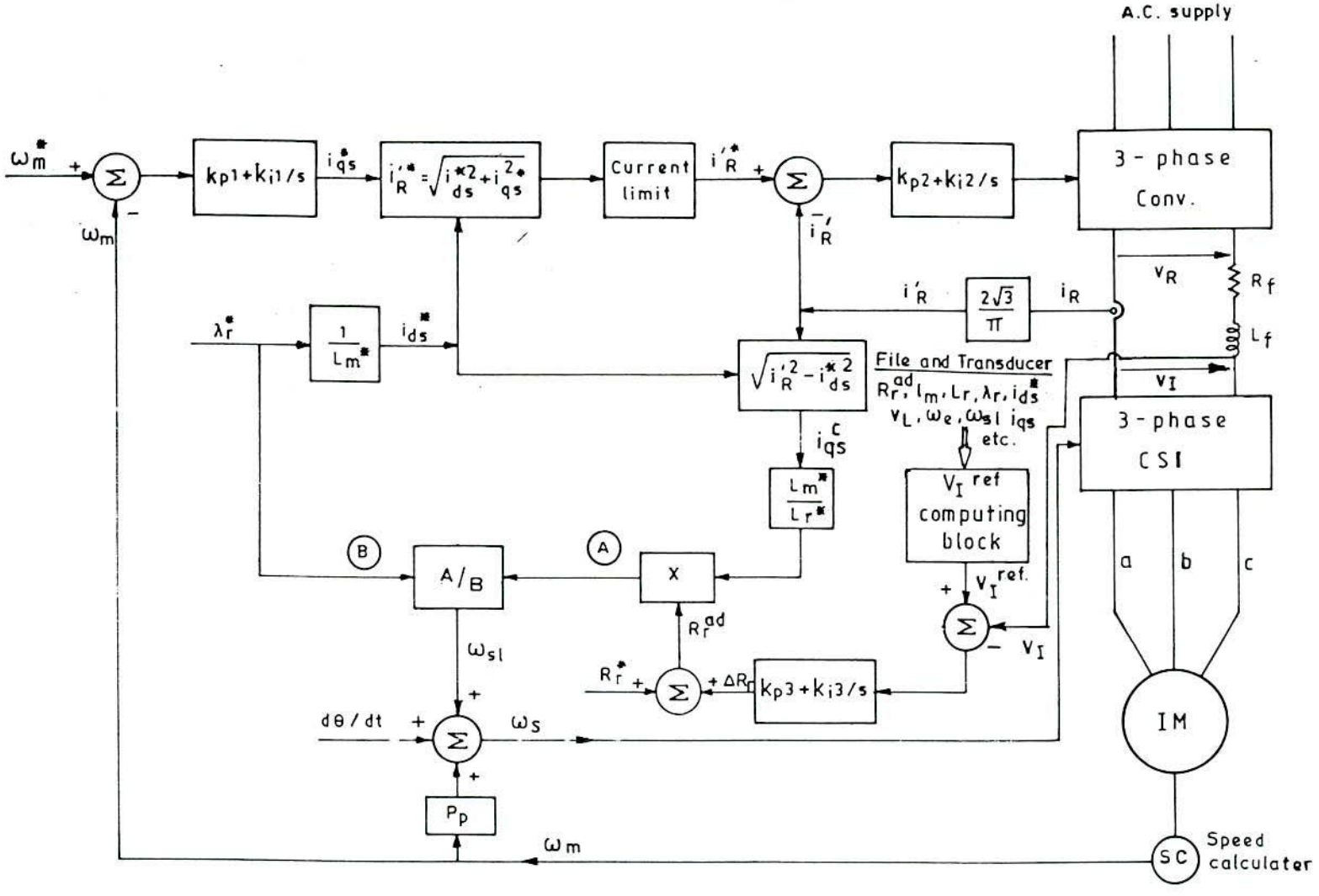

Fig. 4.2 Implementation of dc link voltage based rotor resistance compensation scheme

error so generated from the difference is processed through a PI controller to provide the slip calculator with a rotor resistance correction term. The adaptation process may be continued for an interval and be made operative observing the mismatch in the two voltages or setting some other criteria to invoke it. The other control loops are similar to those in Fig.2.7. The realization of the generation of rotor resistance correction signal is achieved by using high performance microcomputers for which suitable digital algorithms must be derived.

An alternative expression for generating $V_I^{'ref}$ using eqn. 2.20 and eqn 4.26 (derived latter under the section 4.3.2) is

$$v_I^{'ref} = (R_s + L_{\sigma s}p)i_R^{'} + \left\{ \frac{2}{3}\sqrt{S_{in}^2 - P_{st}^2} - L_{\sigma s}\,\omega_e\, i_R^{',2} \right\} \frac{i_{qs}^c}{i_{ds}^{*}\, i_R^{'}} \qquad (4.17)$$

4.3.1.2 Adaptation ability of the proposed system

Does the equality of the two voltages (model reference and actual voltage) ensure parameter adaptation? Correct tuning of the slip calculator will be achieved if at the zero error signal the parameters in the controllers agree with those of the actual machine. This aspect requires investigation. Actual scaled dc link voltage is given by an expression similar to (4.15) with actual parameters and variables. As the reference current and the frequencies are directly transmitted to the machine, we can make

$$I_R^{'} = I_R^{'*} \qquad (4.18a)$$

$$\omega_{sl} = \omega_{sl}^{*} \qquad (4.18b)$$

$$\omega_e = \omega_e^{*} \qquad (4.18c)$$

Indicating the adapted rotor resistance in the slip calculator as $R_r^{ad}(=R_r^*)$, the error function can be expressed as

$$\varepsilon_v = V_I^{'Ref} - V_I^{'}$$

$$= \frac{L_m^{*2}\, R_r^{ad}\, \omega_{sl}^*}{R_r^{ad\,2} + (\omega_{sl}^*\, L_r^*)^2}\, \omega_e^*\, I_R^{'*} - \frac{L_m^2\, R_r\, \omega_{sl}}{R_r^2 + (\omega_{sl}\, L_r)^2}\, \omega_e\, I_R^{'} \qquad (4.19)$$

For a normally designed motor leakage inductance is a small percentage of magnetizing reactance. In such a case

$$\frac{L_r}{L_r^*} \approx \frac{L_m}{L_m^*} = \beta \text{ (say)} \qquad (4.20)$$

Use of (4.16), (4.18) and (4.20) in (4.19) and subsequent simplification gives:

$$\varepsilon_v = \frac{i_{qs}^c}{i_{ds}^{*3}} \frac{\left\{\alpha\beta^2\left(i_{ds}^{*2} + i_{qs}^{c2}\right) - i_{ds}^{*2} - i_{qs}^{c2}\,\alpha^2\beta^2\right\}}{\left\{1+\alpha^2\beta^2\left(\frac{i_{qs}^c}{i_{ds}^*}\right)^2\right\}\left\{1+\left(\frac{i_{qs}^c}{i_{ds}^*}\right)^2\right\}}\, \omega_e\, I_R^{'} \qquad (4.21)$$

in which α is R_r^{ad}/R_r.

If the saturation level could be communicated to the slip calculator, or if the saturation level could be maintained corresponding to nominal inductances, β takes the value 1.0. Then for zero error function, factorising the numerator and equating it to zero, we have

$$(i_{ds}^{*2} - i_{qs}^{c2}\,\alpha)\,(\alpha - 1) = 0 \qquad (4.22)$$

That is, either

$$R^{ad} = R_r \tag{4.23a}$$

or, $$R^{ad} = \frac{i_{ds}^{*2}}{i_{qs}^{c2}} R_r \tag{4.23b}$$

Actual rotor resistance, as indicated by (4.23a) will be generated by the rotor resistance adaptive controller if the level of saturation corresponding to L_m^* could be maintained.

4.3.2 Quadrature-axis current model

The indirect vector control structure, proposed in chapter II uses the commanded value of flux producing stator current, viz., i_{ds}^* in the slip calculator. Under field orientation condition the actual flux and torque producing components of stator current vector inside the machine must agree with those in the vector controller. This particular criterion points out that the q-axis component of stator current in the slip regulator may be taken as reference in the model reference adaptive control strategy. The other variable necessary to generate the error function by comparison with the model reference should be the actual quadrature axis component of stator current in the machine.

By reference to the vector diagram of stator current components in Fig. 4.3 when field orientation is restored the vector current component ab, used in the slip calculator, becomes equal to oc, the torque component of stator current vector existing in the machine. The model reference (=ab) is

$$i_{qs,ref}(= i_{qs}^{c}) = \sqrt{i_R^{',2} - i_{ds}^{*2}} \qquad (4.24)$$

Since the actual torque component of stator current vector, i.e., oc is not available, it can be estimated from the developed torque as follows: (cf. 2.38)

$$\hat{i}_{qs} = \frac{2}{3} \frac{\hat{T}_{em} L_r}{P_p \lambda_r L_m} \qquad (4.25)$$

where, $\hat{T}_{em}$ is the estimated or the measured developed electromagnetic torque. $\hat{T}_{em}$ can be estimated from the dc link power outlined in section 4.2.

By (4.13) for the condition prevailing inside the machine

$$\frac{L_m \lambda_r}{L_r} i_{ds} = \frac{2}{3} \frac{1}{\omega_e} \sqrt{S_{in}^2 - P_{st}^2} - L_{\sigma s} i_R^{',2} = F_m \text{ (say)} \qquad (4.26)$$

Combining (4.25) and (4.26) and using $i_R^{',2} = (i_{ds}^2 + i_{qs}^2)$, we have

$$\hat{i}_{qs} = \frac{i_R'}{\sqrt{1 + \left(\frac{3P_p F_m}{2 \hat{T}_{em}}\right)^2}} \qquad (4.27)$$

The estimated value of $i_{qs}(= \hat{i}_{qs})$ is compared with the field oriented reference for the q-axis current $i_{qs,ref}$ and the difference $(=i_{qs,ref} - \hat{i}_{qs})$ is processed through a PI controller to provide a corrective term to the nominal rotor resistance used in the slip calculator. As in the previous scheme the improvement on this corrective term will cease when the error signal is driven to zero. The schematic for the rotor resistance adaptation implementing q-axis

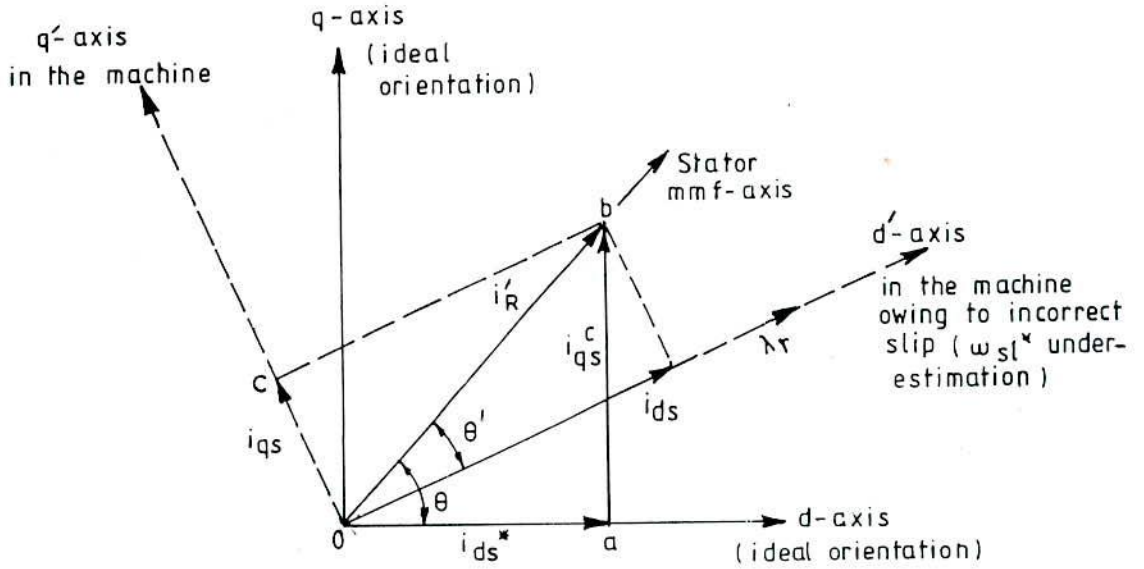

Fig. 4.3 Vector diagram of stator current components for the controller and inside the machine

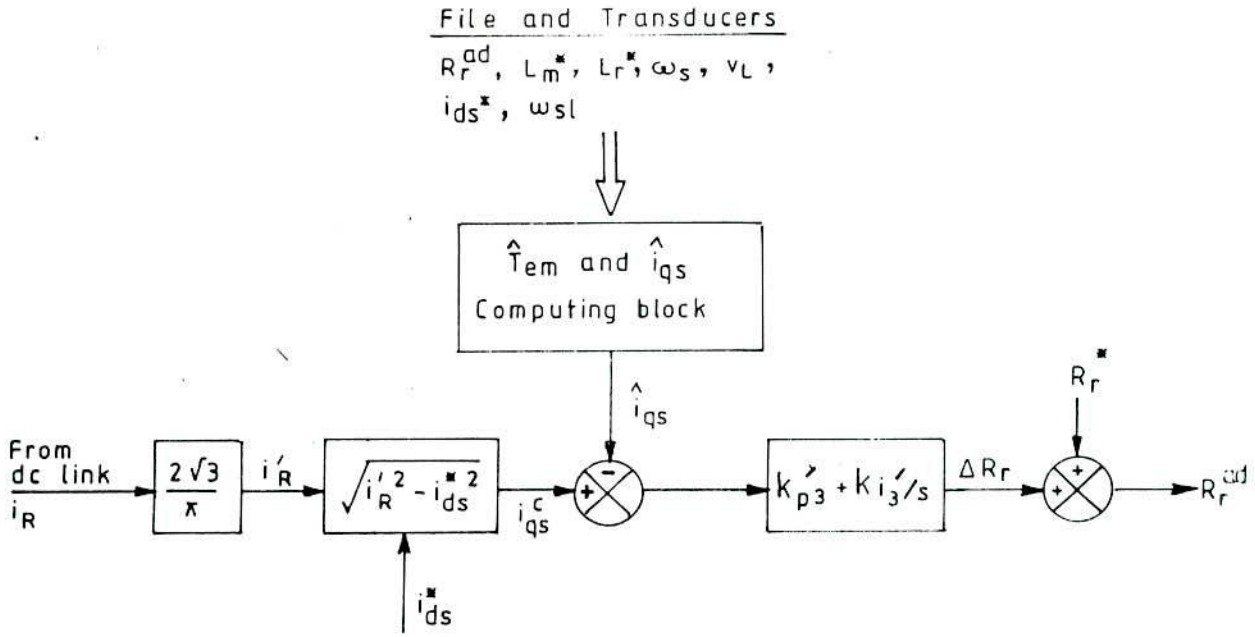

Fig. 4.4 Schematic diagram for i_{qs} based R_r adaptation scheme

current reference model is shown in Fig. 4.4. The complete block diagram of the drive system is similar to that in Fig. 4.2. except the rotor resistance corrective block which is replaced by the scheme in Fig. 4.4.

4.4. SIMULATION STUDIES

4.4.1. Studies envisaged

In order to establish the feasibility and credibility of the proposed parameter adaptation schemes digital simulation of the vector controlled induction motor drive system, using its transient model, was carried out, and adaptive ability of different schemes was evaluated for certain operating conditions. Parameters of two motors (squirrel cage and slip ring), used in the simulation test, as well as various controller gains are furnished in Appendix I. Details of the simulation of the vector controllers and motor for a speed-controlled drive system have been dealt with in Chapter II. Transient model of the machine contains the actual parameters which the motor is supposed to have during its operation. On the other hand the slip calculator works either with the nominal parameters or with the updated parameters that are transmitted from the parameter adjustment blocks or calculators. The effectiveness of the schemes was tested by introducing changes in the rotor resistance in the transient model of the induction machine and then observing how the updated resistance from the controller tracked the new changed resistance. Further observations were noted in respect of rotor flux, rotor slip speed, rotor currents in field co-ordinates etc. to see whether the scheme could restore field

orientation. Changes in the rotor resistance were made from nominal value (i) in step and (ii) in ramp. The simulation traces of various drive quantities, obtained on the application of the proposed parameter adaptation schemes to speed controlled system, are presented in Fig. 4.5 through Fig. 4.15. The dc link voltage based scheme was tested using both the reference voltage models represented by (4.15) and (4.17). The simulation results are furnished corresponding to the voltage model in (4.17).

4.4.2 Tuning by R_r estimation from airgap power

Fig. 4.5 presents the variation in λ_r, λ_{qr}, ω_{sl}, etc., when a ramp change in rotor resistance of the slip ring machine is allowed and adaptation is invoked at every 2 seconds. It is noted from the plots in Fig. 4.5(b) and Fig. 4.5(d) how λ_r attains its nominal value and λ_{qr} reduces to zero as the slip calculator is provided with updated estimate of the rotor resistance. T_{em}/i_{qs} as observed from Fig. 4.5(c) tends to restore its value set for field orientation condition, and slip speed (Fig. 4.5(e)) is found to increases in proportion to the adapted resistance operation. Fig. 4.6 shows the step wise change in rotor resistance of the slip ring machine, and in each step adaptation is delayed by 1.5 sec. Here too it is noted from the variation of λ_r and λ_{qr} how effectively field orientation is restored.

Fig. 4.7 depicts the slip speed and rotor flux linkage variation in machine I (SC) for ramp change in rotor resistance with adaptation set in every 2 sec for two different load torques (6.5 Nm and 16.5 Nm).

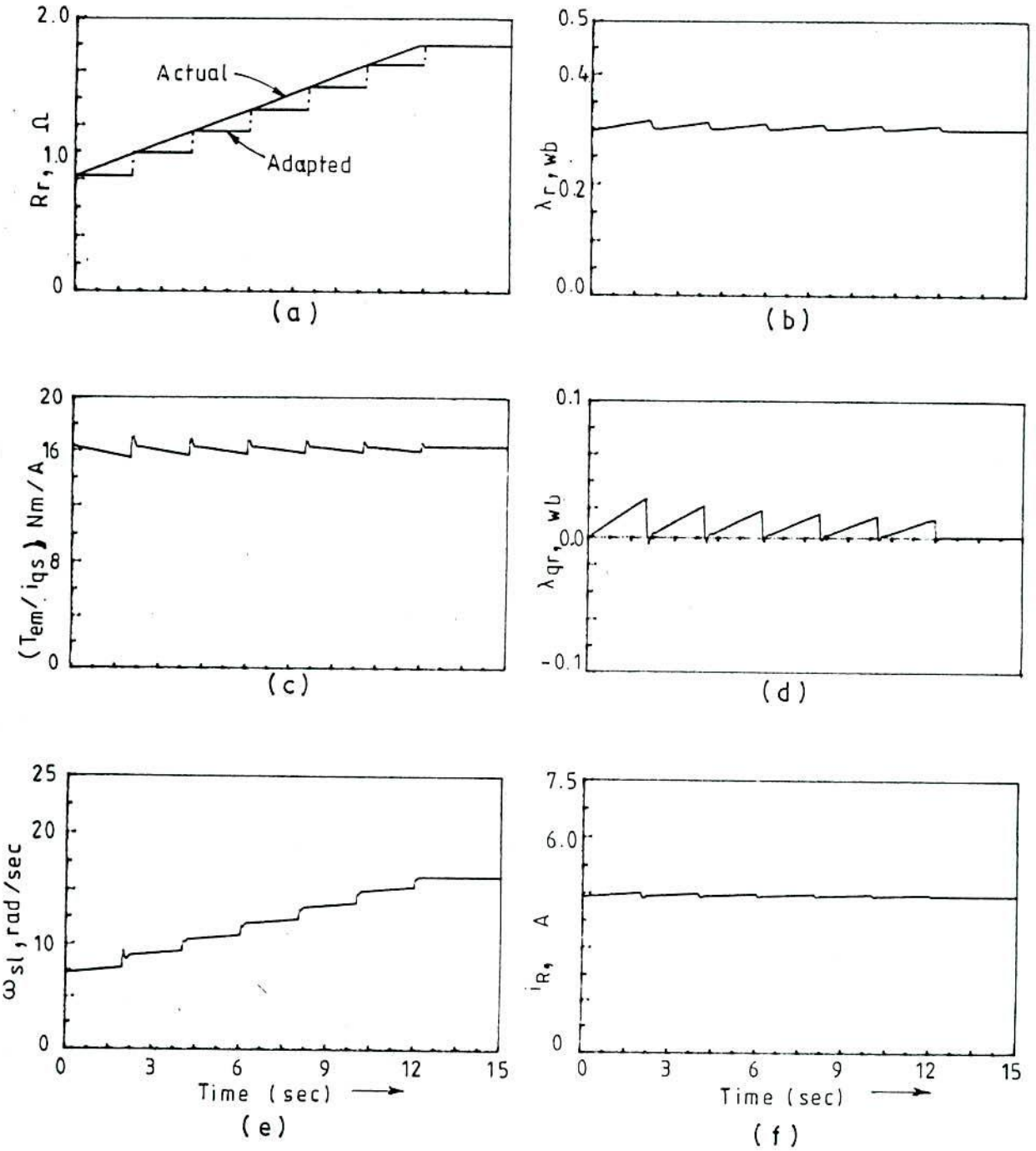

Fig. 4.5 Simulation traces for air gap power-based parameter estimation and compensation for linear variation of rotor resistance of machine II

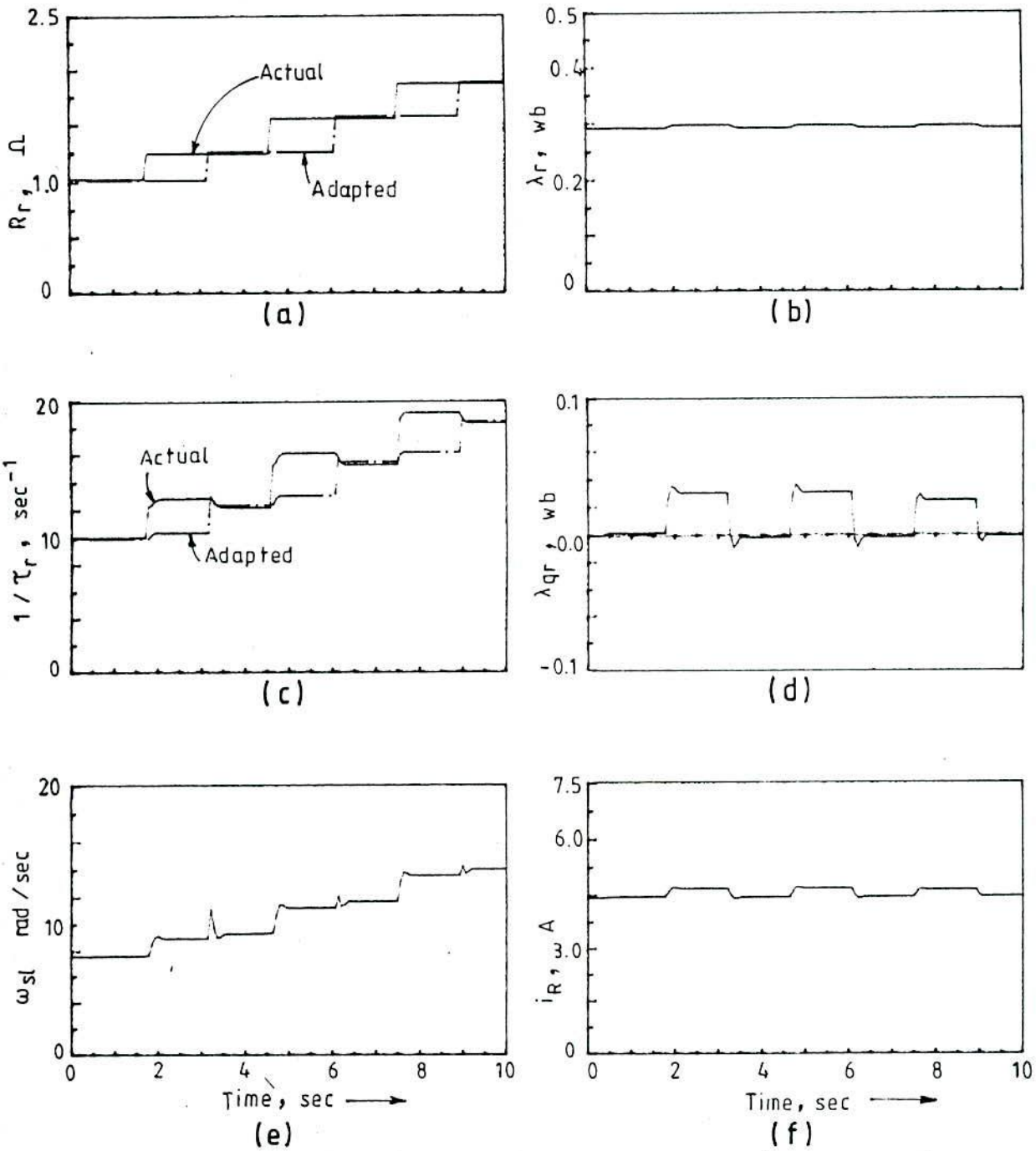

Fig. 4.6 Simulation traces for parameter estimation and compensation for machine II for stepwise increase in R_r

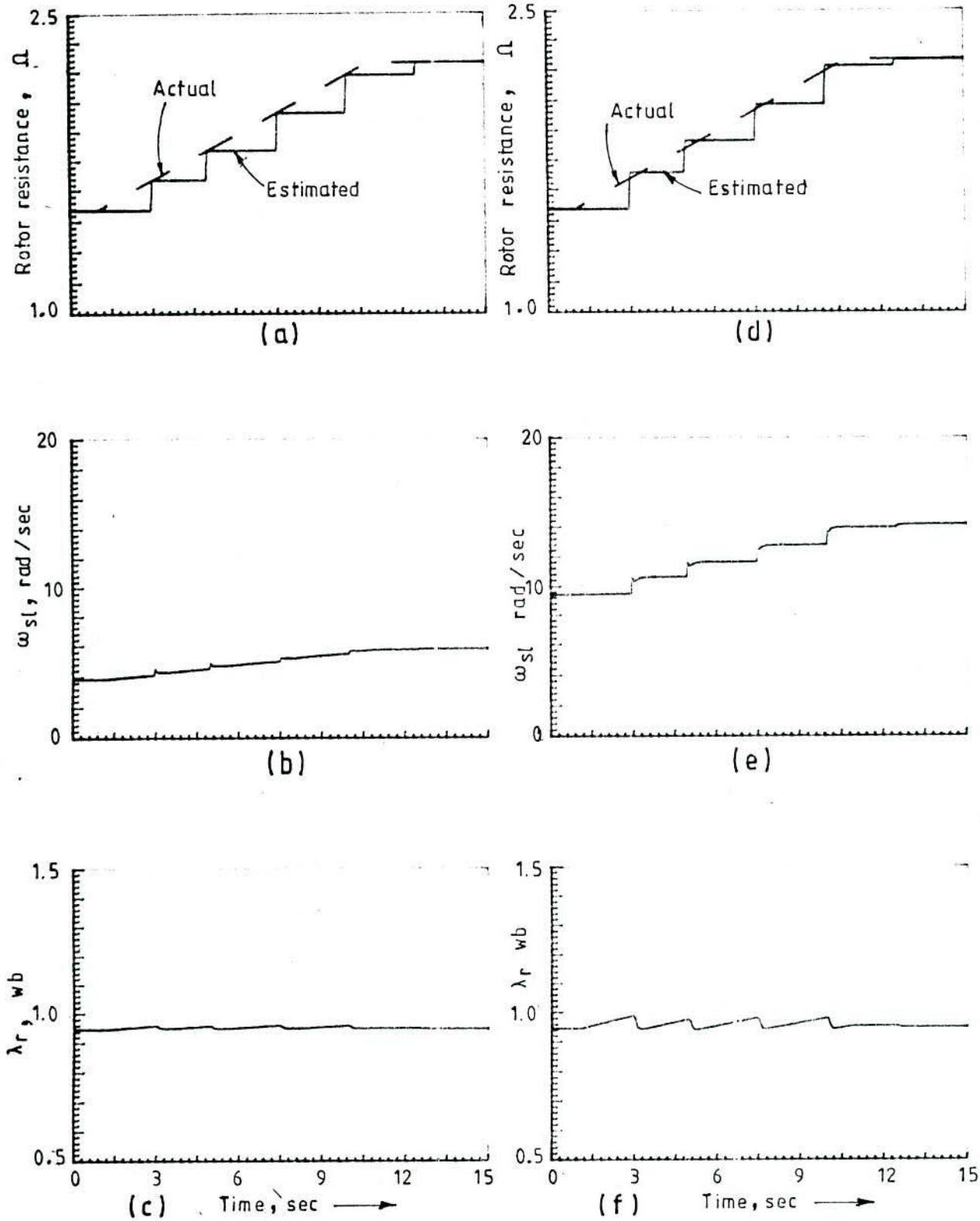

Fig. 4.7 Simulation traces for parameter estimation and compensation using air gap power method for machine I for step-wise change in rotor resistance with two load torques for a, b, c : T = 6.5 Nm; for d, e, f : T = 16.5 Nm

4.4.3 DC link voltage-based scheme

Fig. 4.8 presents simulation results for both uncompensated and dc link voltage based compensated system when R_r of Machine I increases linearly from 1.5087Ω to 2.25Ω. Fig. 4.8a shows the adapted rotor resistance in the controller corresponding to actual value in the machine. Plots in Figs. 4.8(c) and 4.8(d) illustrate the loss of field orientation in an uncompensated system and the restoration of it due to adaptation mechanism. The restoration of field orientation is evident from the traces of λ_{qr} which gradually reduces to zero as the controller progressively adapts the value of resistance approaching to that of the rotor. From Fig. 4.8b ω_{sl} is found to change linearly as the adaptation mechanism proceeds. In the speed controlled system motor speed is not affected (Fig. 4.8(e)) and the dc link current shows no significant change (Fig. 4.8f).

Results shown in Figs. 4.9 and 4.10 are in respect of the slip ring machine when the rotor resistance changes in step and in linear fashion respectively. Here are also noted fairly satisfactory working of the compensation schemes as small deviations in λ_r and λ_{qr} from their idealised condition. In the simulation study 2.0 ms was taken as the sampling time.

Fig. 4.11 illustrates the simulation results for dc link voltage based rotor resistance adaptation scheme for which linear variation in rotor resistance and step increase in speed during the adaptation process. The plots in Fig. 4.11 shows no significant effects of the transient condition on the adaptation process.

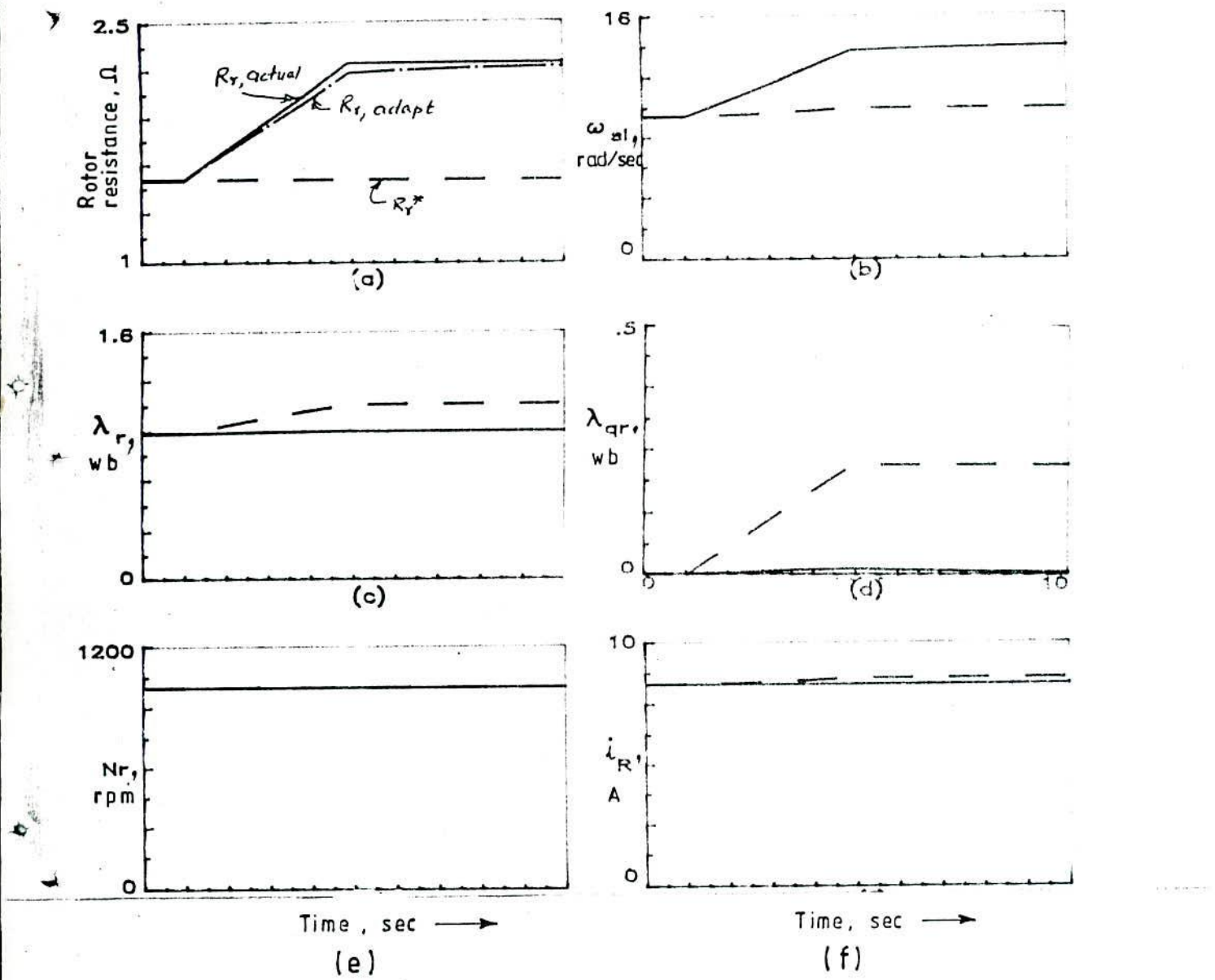

Fig. 4.8 Simulation results for dc link voltage based rotor resistance adaptation scheme for machine I with ramp change in R_r, T_L = 6.5 Nm

——— with compensation

— — — without compensation

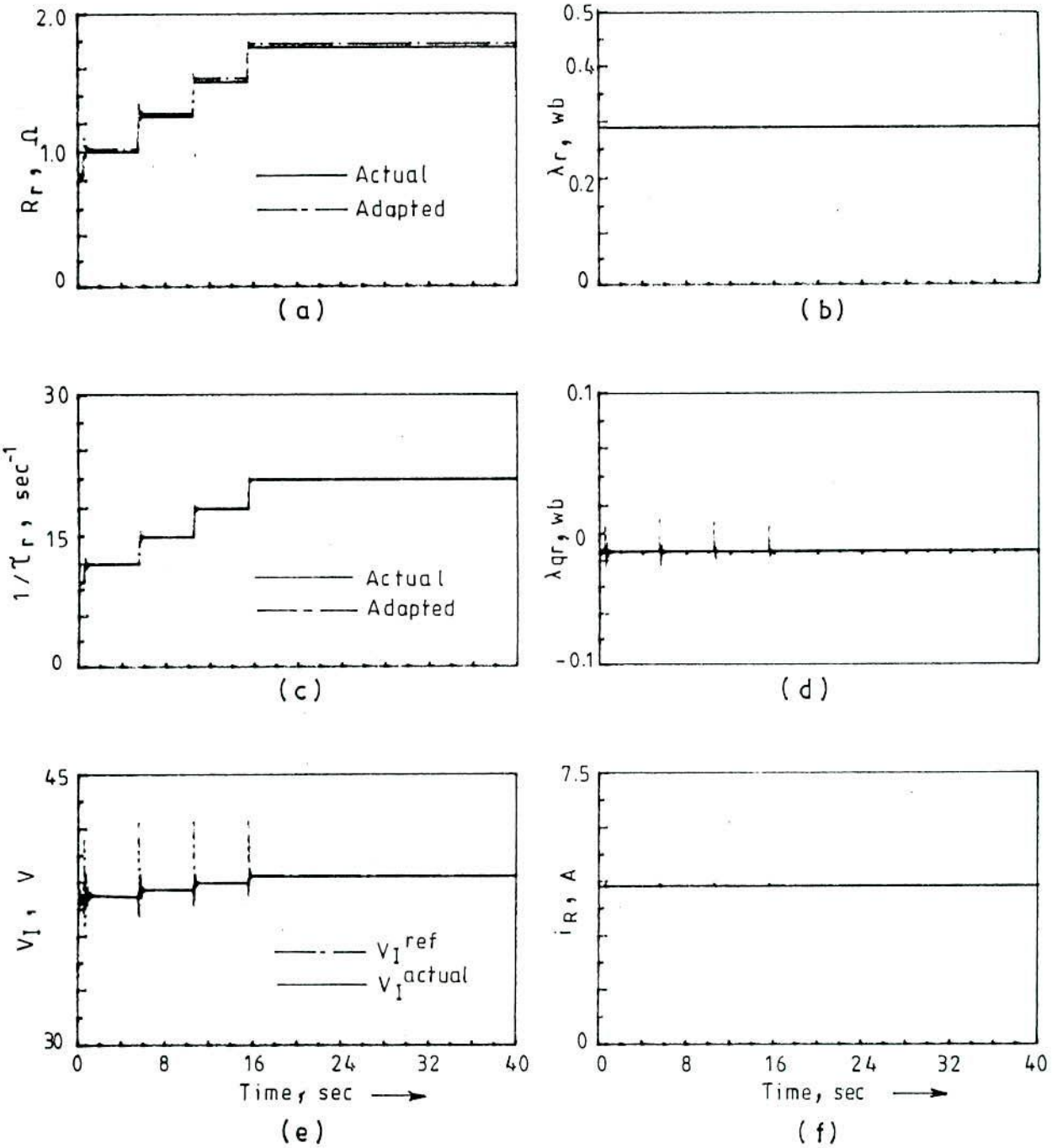

Fig. 4.9 Simulation traces for dc link voltage-based rotor resistance adaptation scheme for machine II with step-wise change in R_r, T_L = 2.0 Nm

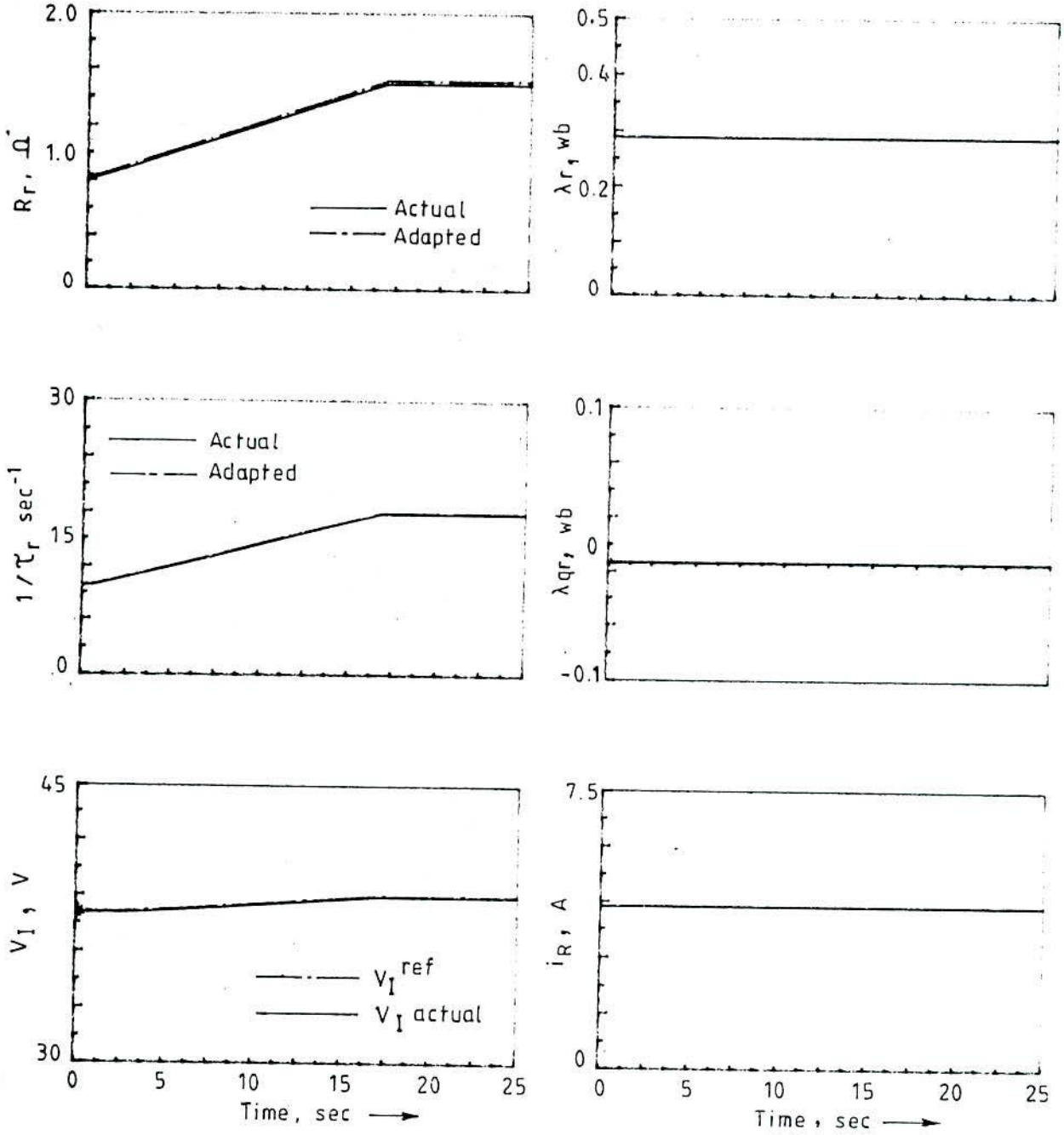

Fig. 4.10 Simulation traces for dc link voltage-based rotor resistance adaptation scheme for machine II with ramp change in R_r, $T_L = 2.0$

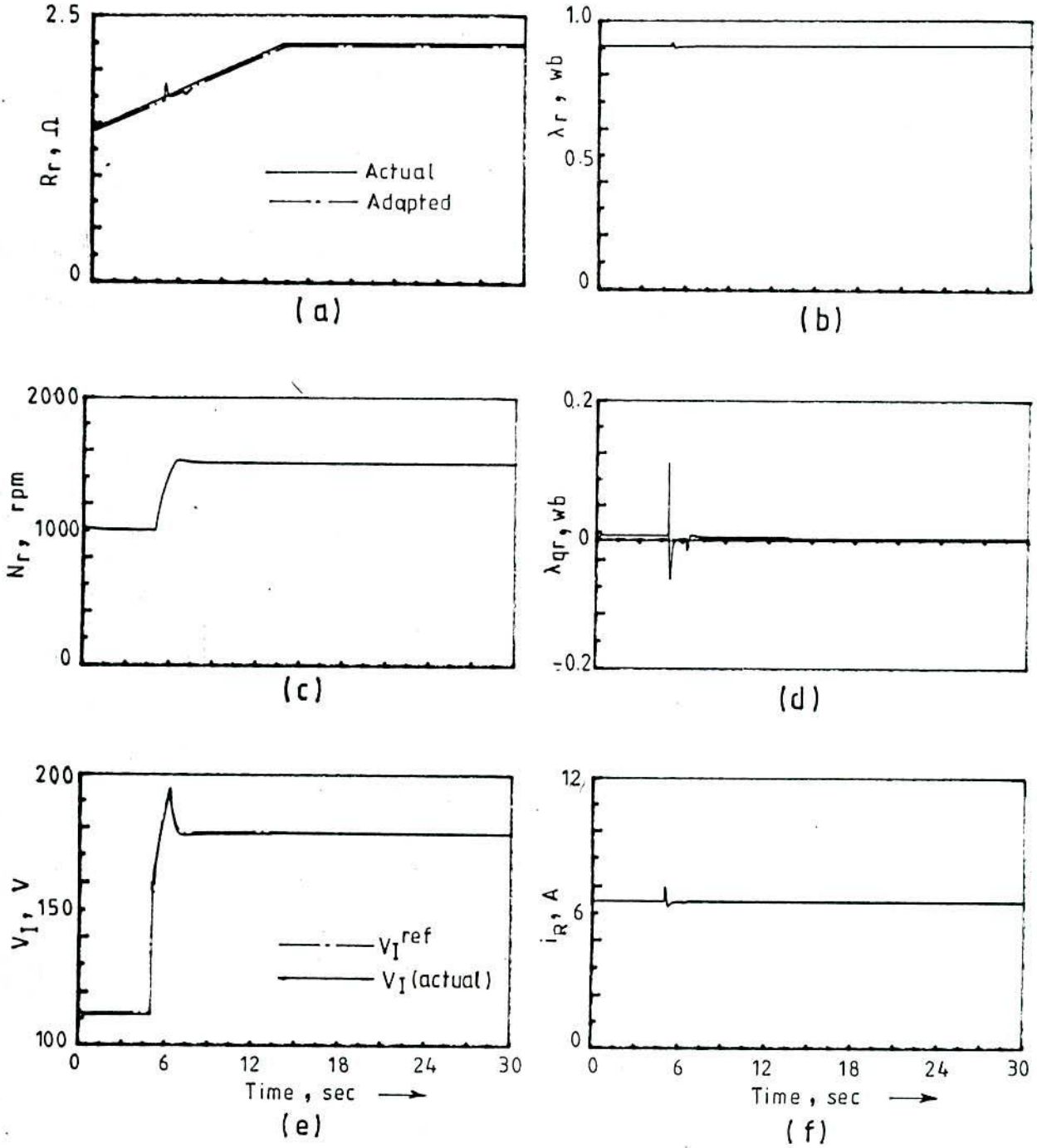

Fig. 4.11 Simulation results showing the responses and adapted resistance value in the v_I adaptation scheme for step increase in speed [1000 -1500 rpm] during the linear increase in the rotor resistance of machine I

4.4.4 Quadrature-axis component of stator current based adaptation of R_r

Simulation study depicted in Fig. 4.12(a) shows how the resistance in the slip calculator tracks the actual machine resistance. Fig. 4.12(c) compares the ratio R_r to L_r adapted in the slip calculator to that actually prevailing in the machine. A slight depression in the ratio (R_r/L_r) in the beginning is due to increased value of the transmitted slip causing a decrease in the saturation level (increase in L_r). Though in the steady state condition a deviation (very small) is noted between the parameters used in the controller and those actually existing in the machine model, field orientation is restored for all practical purposes as are evident from Figs. 4.12(b) and 4.12(d). Results in Fig. 4.13 and 4.14 are in respect of linear variation in rotor resistance of Machine-I and step wise changes for slip ring machine (Machine-II) respectively. Here also the effective working of the adaptation mechanism can be noted.

Fig. 4.15 indicates the insensitiveness of step change in torque when adaptation process based on q-axis stator current was in progress for ramp change in R_r.

4.5 CONCLUSIONS

Three parameter adaptive schemes have been proposed to update the gain of the slip calculator to offset the effects arising out of rotor parameter deviation. Simulation results for the steady state and dynamic conditions show the effectiveness of the compensation schemes that do not require complex control operations.

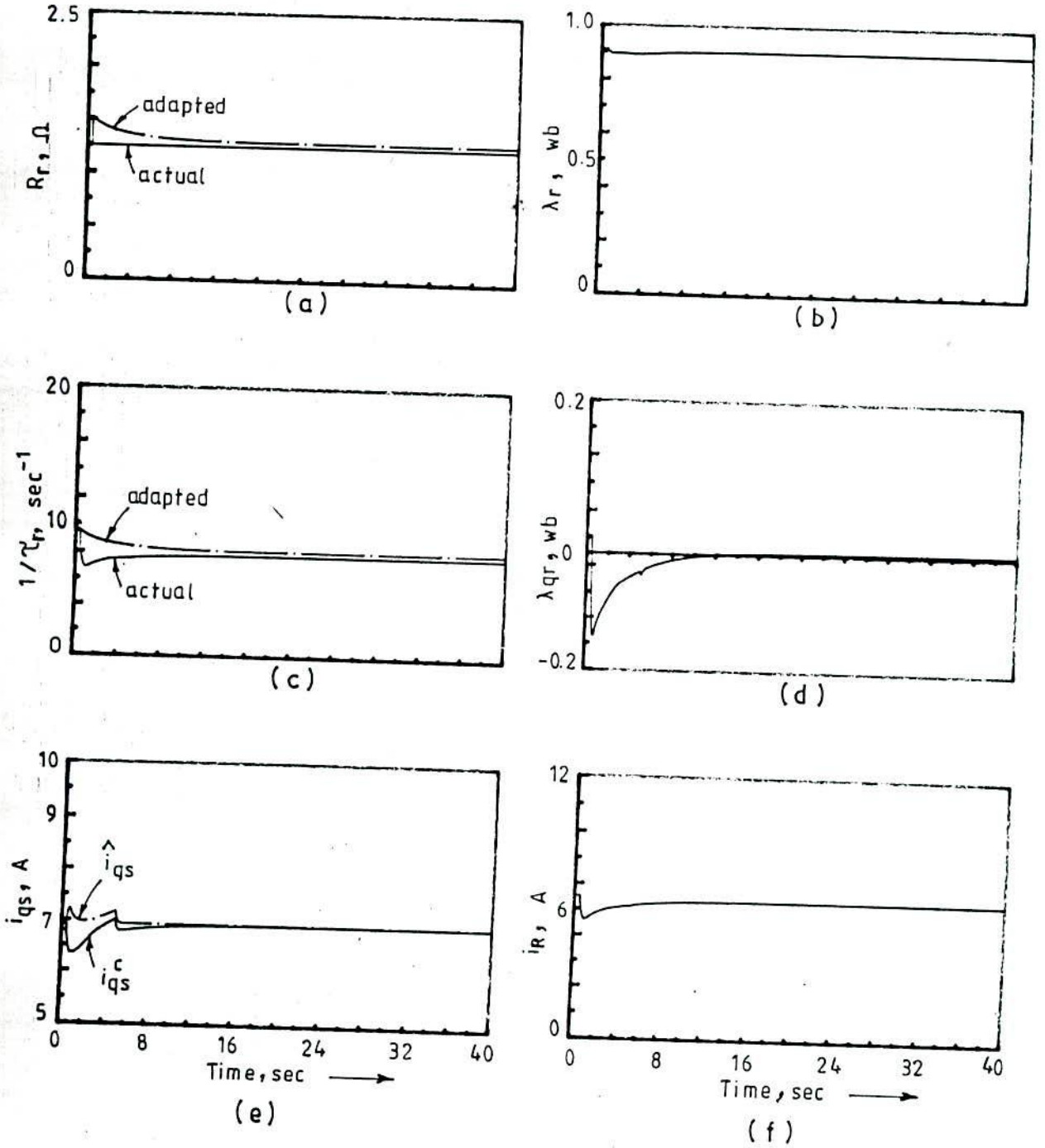

Fig. 4.12 Simulation traces showing the responses and adapted rotor resistance and time constant for step decrease in actual rotor resistance of machine I
Quadrature axis stator current based adaptation scheme for $T_L = 2.0$ Nm

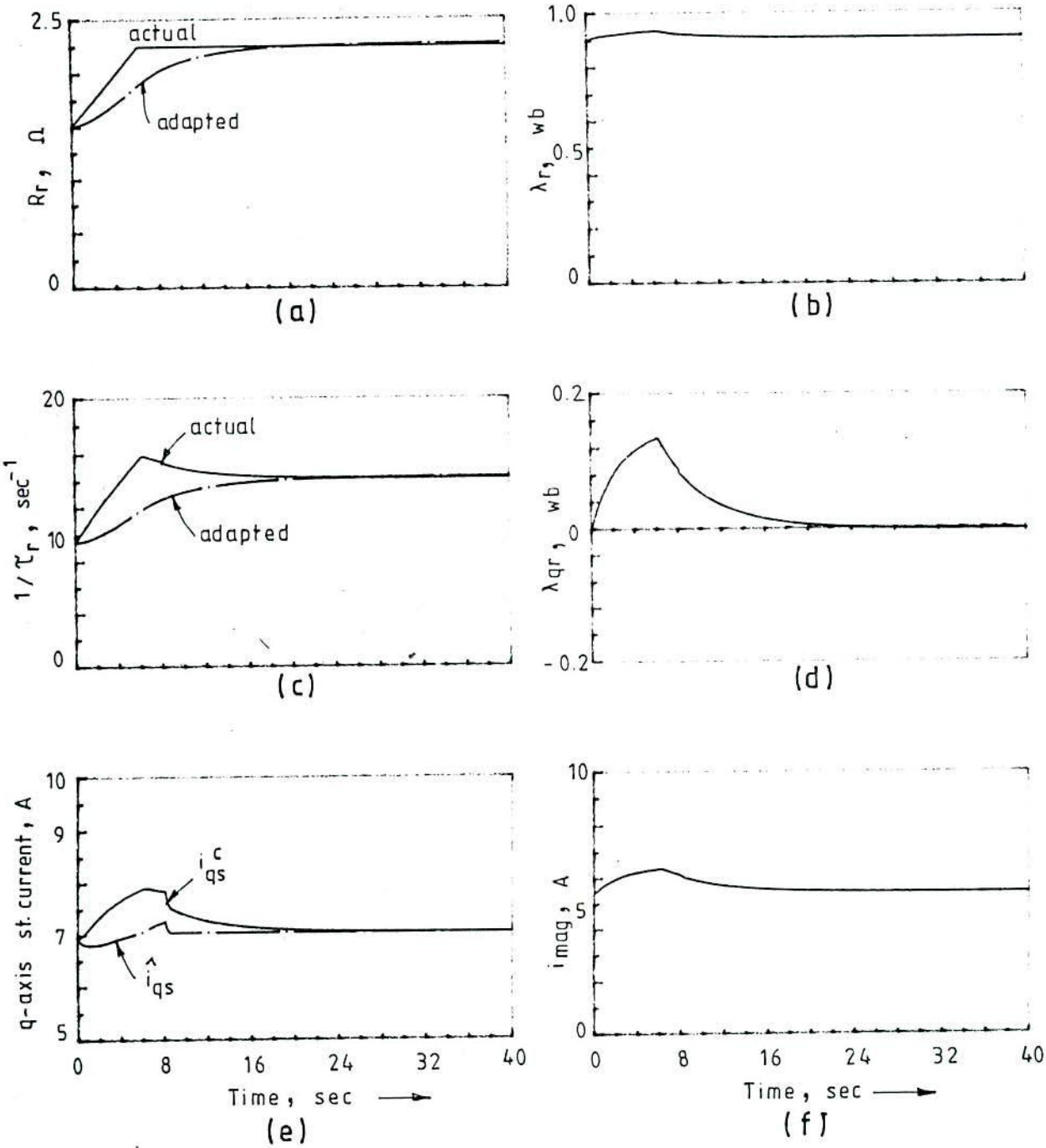

Fig. 4.13 Simulation traces showing the responses and adapted rotor resistance and time constant for linear increase in actual rotor resistance of machine-I on the q-axis stator current based adaptation scheme. T_L = 15 Nm

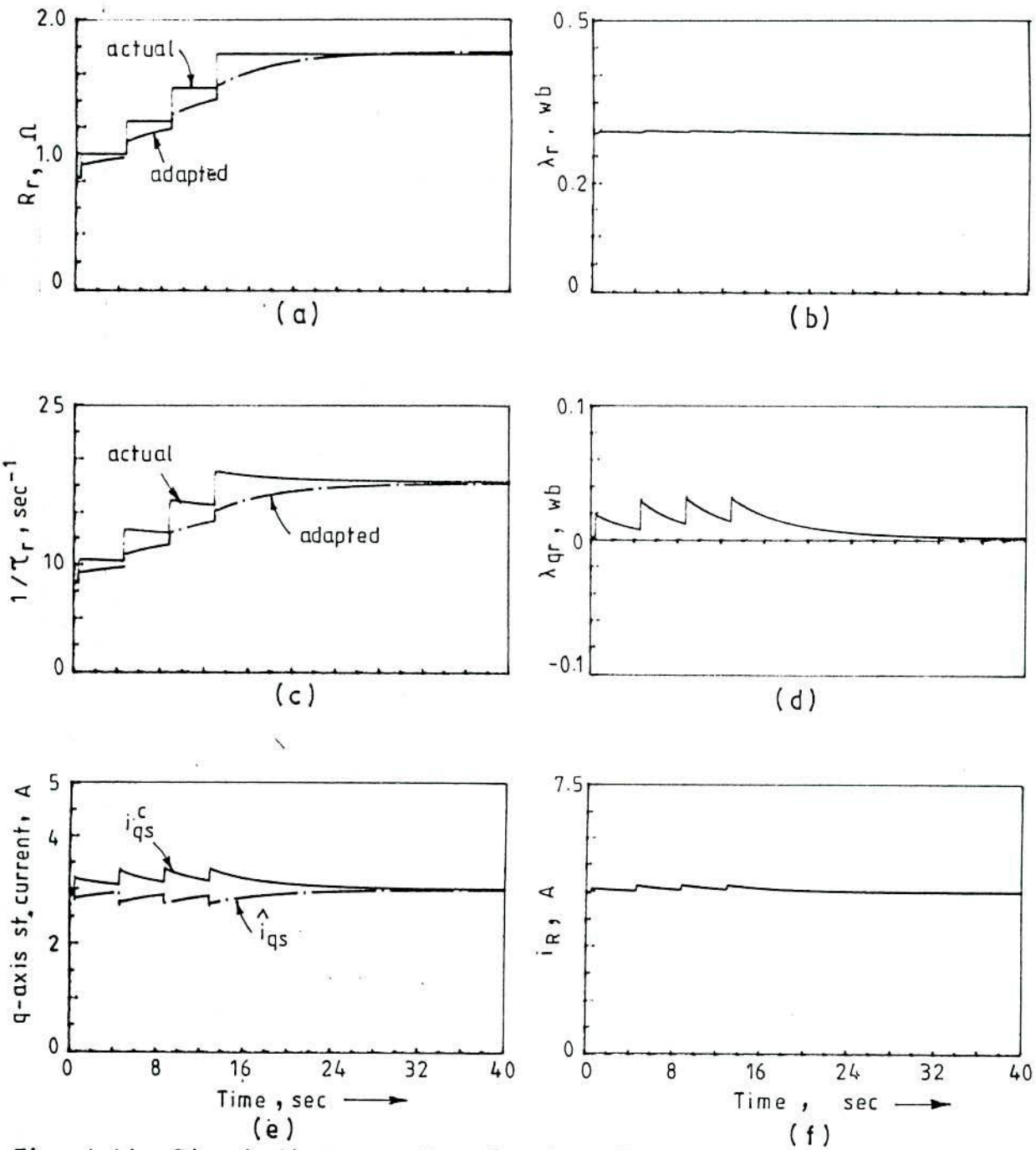

Fig. 4.14 Simulation results showing the responses and adapted rotor resistance and time constant for step-wise changes in actual rotor resistance of machine-II. Q-axis stator current-based adaptation scheme T_L = 2.0 Nm

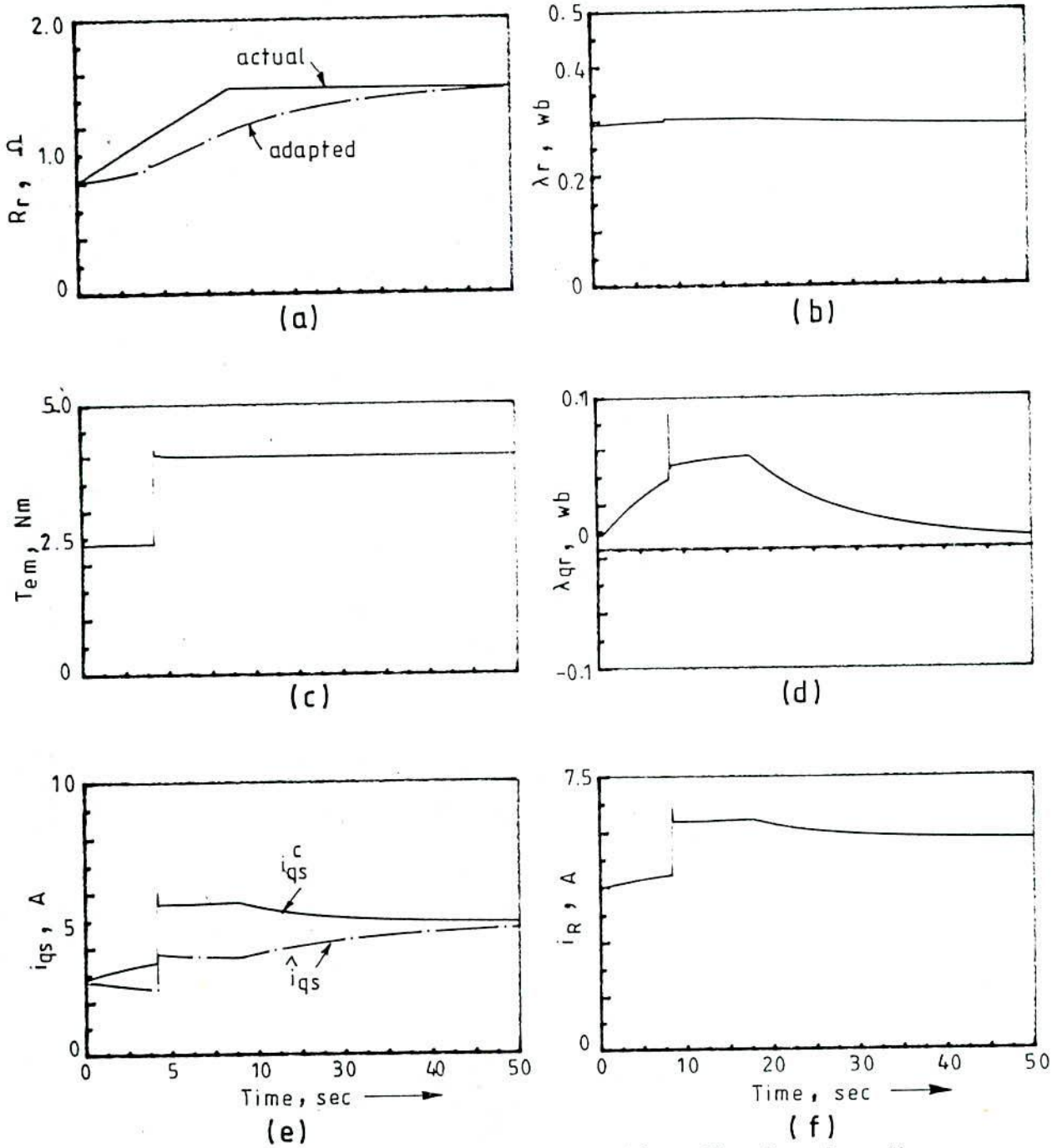

Fig. 4.15 Simulation results for machine-II showing the responses and adapted rotor resistance in the q-axis stator current based adaptation scheme for sudden step increase in torque [2.35 Nm to 4.0 Nm] during the linear charge in R_r

However, the reliability of a parameter compensating scheme depends on the extent of the use of motor parameters in the scheme itself. An influencing parameter affecting the adaptive schemes, proposed in the above sections, is the stator resistance which is dependent on temperature. As a result the estimated torque from the dc link power measurement will suffer from accuracy if the stator resistance change is not duly accounted for in the adaptive algorithms. This estimated torque has been used in the analytic calculation of rotor resistance (eqn. 4.3) and in the quadrature-axis current model (eqn. 4.27) of the MRAC technique. This short coming can be offset to significant extent if the stator resistance is assumed to change at the same rate as that of the rotor. In the MRAC scheme with inverter input voltage model (eqn. 4.17) the effect of the variation of stator resistance drop due to temperature can be ignored for higher speeds. But at low speeds, accuracy of the voltage model will depend upon the stator resistance drop owing to the reduced value of speed emf. This invariably calls for a correction to stator resistance drop. Here also, under the conditions of equal change rates of stator and rotor resistances [124] compensating action will be significantly improved.

CHAPTER V

CONTROLLER SELECTION AND ROBUST STABILITY

5.1 INTRODUCTION

The vector controlled induction motor system described in Fig.2.7 consists of two PI controllers which should be properly designed for stable operation of the drive system. Normally, a rotor flux model-based vector controlled system is more robust than other flux models [18, 21]. A CSI-IM system suffers from stability problems in the open loop [75] and at low loads [10]. In the case of feedforward slip frequency control strategy any deviation of motor parameters in the controllers from their actual values in the machine causes loss of orientation. To counteract such parameter deviation effects, adaptive controllers are used to restore the decoupling state, and this in turn results in the change of the transfer function of the system. In such eventuality, selection of controller constants will be such that it will fulfill the demand for fast response and at the same time must ensure good margins for stability limit so that perturbations arising out of the change in parameters, uncertainty in modelling, torque disturbance, measurement noise, etc., do not destabilise the system. Operation with a sufficient stability margin is desirable in selecting controller constants.

Robustness consists in delineating the parameter space into finite regions about the nominal model for which the stability of the system

is preserved. There are two types of disturbances which create stability problems in a system, and the robustness of the system is expressed in terms of stability margins against such disturbances. The stability margins are (i) the structured stability margin for parametric perturbations, and (ii) the unstructured stability margin in respect of unmodelled dynamics or external noises.

A number of methods exist in the literature to determine the stability and robustness of control systems. From the classical point of view, the important ones are the Routh Hurwitz criterion, the Nyquist plot, the Bode plots, etc. Direct application of these methods to determine robustness of control systems with parametric variations is difficult and appears to be almost insurmountable. An epoch making method to check stability of plants with parameters varying within known intervals was first reported in 1978 by V. L. Kharitonov [90]. The H_∞-norm control along with Kharitonov's theorem has aroused considerable interest for studying robustness of control systems under parametric perturbations and unmodelled dynamics. A very limited number of references on the study of robustness of field-oriented induction motor due to parametric perturbations are available. Studies reported on the robust control of field oriented induction motor are mainly based on robust selection of observer poles or constants of adaptive controllers [23, 37]. Y-y. Tzou and H-j Wu have proposed a complementary model reference type controller for stable operation of an ac servo motor. LQG and Kalman Filter- based robust controller design for CSI-fed induction motor is presented in [30]

In this chapter, first, selection of PI controller constants for a suitable norm-bounded stability margin with an appropriate bandwidth is presented, and then study of robustness of the control system is carried out. Since Kharitonov's polynomials produce conservative results for linearly dependent coefficients, study of robustness is carried out by testing the segments resulting out of generalization of Kharitonov's theorem.

5.2 BLOCK DIAGRAM OF CSI-FED INDUCTION MOTOR UNDER FIELD ORIENTATION CONDITION

The voltage equation of a field oriented induction motor, viewed from the rectifier output terminal and expressed in (2.20), with constant rotor flux linkage and no change in torque angle can be written as

$$v_R' = (R_e + L_e p)\, i_R' + \frac{L_m\, g_{qs}\, \lambda_r}{L_r} (\omega_r + \omega_{sl}) \qquad (5.1)$$

The schematic block diagram of the rotor flux orientation control of the CSI-fed induction machine condition extracted from the system in Fig.2.7 is redrawn in Fig.5.1 which includes the block diagram representation of the induction motor under field orientation condition based on eqns. 5.1, 2.37 and 2.43. Physically, the factors g_{qs}^* and g_{qs} determine respectively the commanded value and the actual value of torque producing component of normalized current (I_R') from the current source inverter. In the steady state conditions, g_{qs}^* is equal to g_{qs}. The signal flow graph of the system in Fig.5.1 is shown in Fig.5.2.

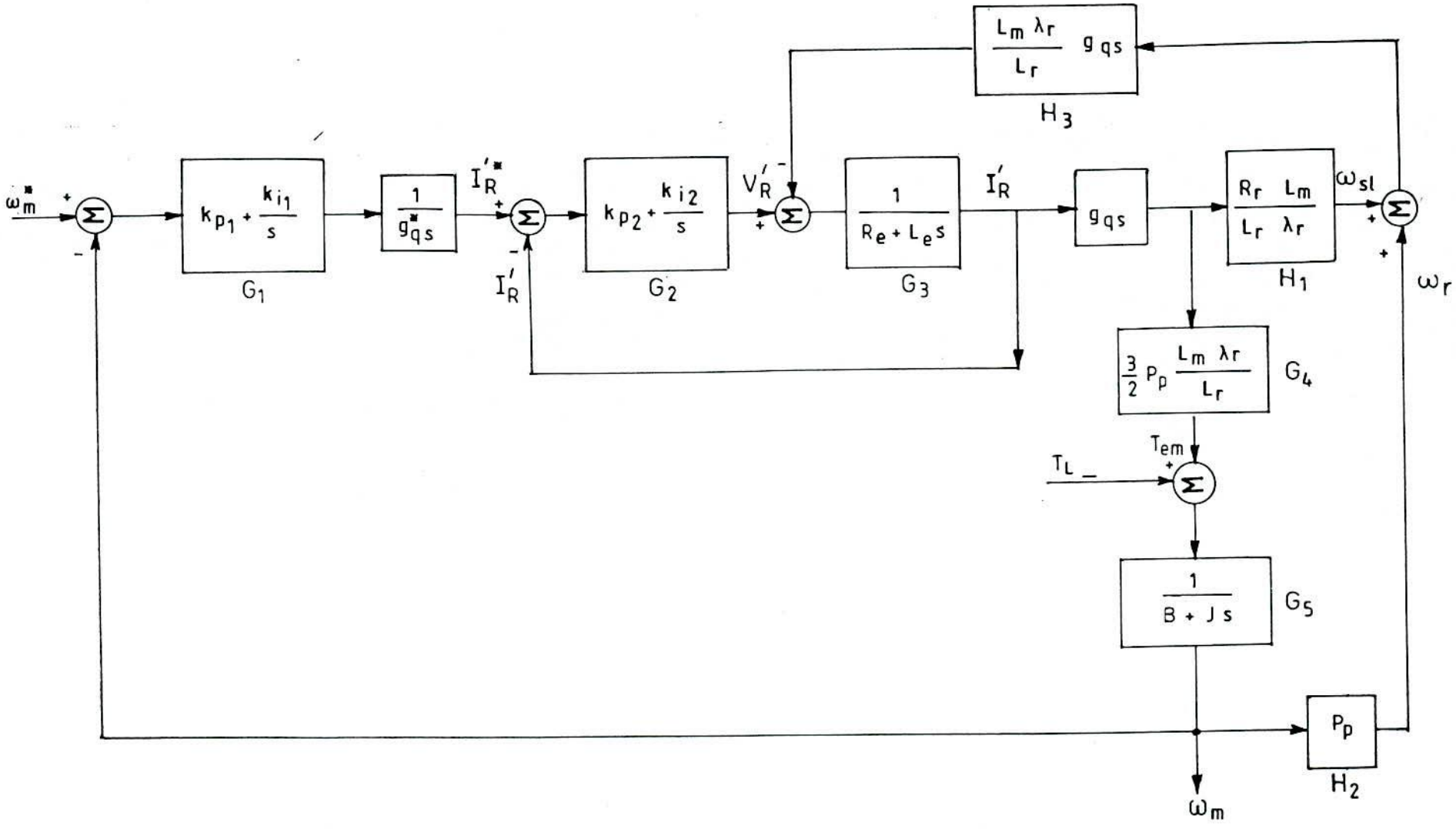

Fig. 5.1 Simplified block diagram for field orientation control and induction motor

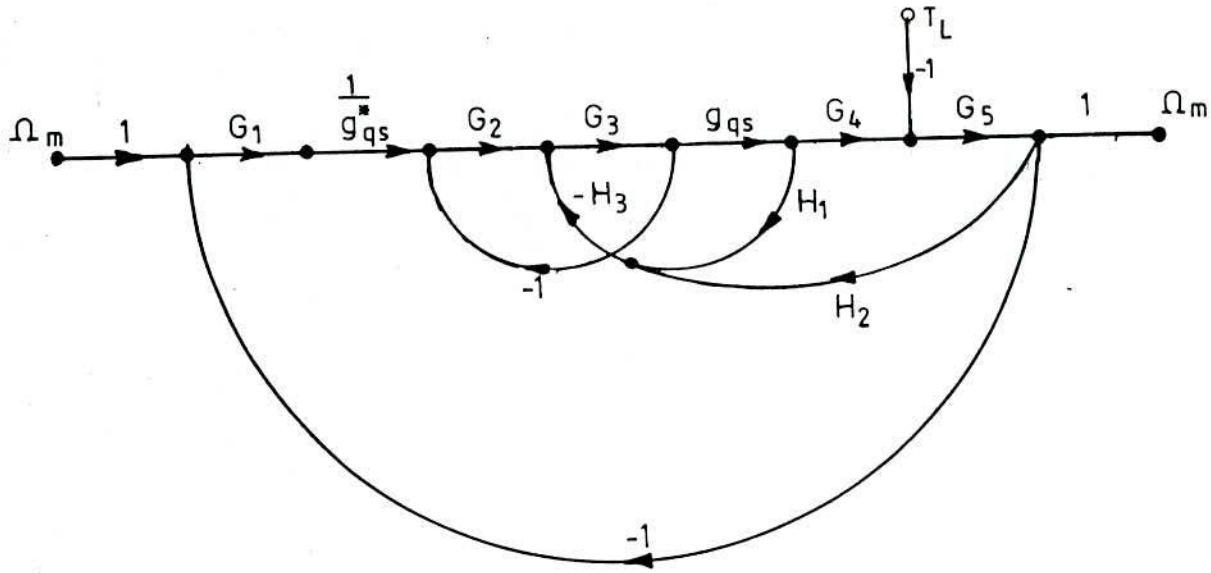

Fig. 5.2 Signal flow graph of the vector controlled CSI-IM Drive system

Using Mason's gain formula [119] the following transfer functions are deduced. These transfer functions are used to select the PI controller constants and study the stability of the system.

$$G_I(s) = \frac{i'_R(s)}{i'^*_R(s)} = \frac{J\,k_{p2}\,s^2 + (B\,k_{p2} + J\,k_{i2})s + B\,k_{i2}}{J\,L\,s^3 + (B\,L + J\,C_4)\,s^2 + (B\,C_4 + J\,k_{i2} + C_2)s + B\,k_{i2}} \qquad \text{---------- (5.2)}$$

$$G_\omega(s) = \frac{\Omega_m(s)}{\Omega^*_m(s)} = \frac{C_3\left\{ k_{p1}\,k_{p2}\,s^2 + (k_{p1}\,k_{i2} + k_{p2}\,k_{i1})\,s + k_{i2}\,k_{i1} \right\}}{\delta(s)} \qquad \text{---------- (5.3)}$$

$$G_T(s) = \frac{\Omega_m(s)}{T_L(s)} = \frac{-s\,\{ L\,s^2 + C_4\,s + k_{i2} \}}{\delta(s)} \qquad (5.4)$$

where,

$$\delta(s) = J\,L\,s^4 + \{B\,L + J\,C_4\}\,s^3 + \{B\,C_4 + J\,k_{i2} + C_2 + C_3\,k_{p1}k_{p2}\}s^2 + \{B\,k_{i2} + C_3(\,k_{p1}k_{i2} + k_{p2}k_{i1})\}\,s + C_3k_{i1}k_{i2}$$

---------- (5.5)

$$\left.\begin{aligned} C_1 &= \left(\frac{L_m\,g_{qs}}{L_r}\right)^2 R_r \qquad C_2 = \frac{3}{2}\left(\frac{P_p\,L_m\,g_{qs}\,\lambda_r}{L_r}\right)^2 \\ C_3 &= \frac{3}{2}\,P_p\,\frac{L_m}{L_r}\,\lambda_r\,\frac{g_{qs}}{g_{qs}^*} \qquad C_4 = R + k_{p2} + C_1 \end{aligned}\right\} - \qquad (5.6)$$

5.3 SELECTION OF ROBUST PI CONTROLLER CONSTANTS

In selecting the controller gains emphasis is placed on the reduction of H_∞ -norm of the transfer function. The roots of the characterstic polynomial are prescribed to be as deep in the left half plane as practicable and satisfying simultaneously a prescribed bandwidth specification. To accommodate the effects of parametric perturbations and unmodelled dynamics, higher order filters based on H_∞-norm optimal controller design are required for a suitable stability margin. However, for ease of implementation, H_∞- norm based PI-controllers are selected on trial-and-error basis to satisfy the above mentioned criteria as far as possible. The basic ideas of H_∞-norm are included briefly in the following subsection.

5.3.1 The H_∞ -norm and sensitivity

The H_∞-norm of a transfer function $F(j\omega)$ is the maximum value of its modulus expressed [122] as

$$\| F \|_\infty = \sup \{ \, | F(j\omega) | : \omega \in R \, \} \qquad (5.7)$$

The mathematical definition in (5.7) implies that the H_∞ -norm ($\|F\|_\infty$) may be expressed as the distance of the farthest point on the Nyquist plot from the origin. A suitable margin that qualitatively indicates the internal stability of the system against unknown perturbations may be assigned to a control system in terms of H_∞ -norm by properly selecting the controller constants. For the study of robustness against perturbations like unmodelled dynamics, parametric deviations, etc., an important relation between the complementary sensitivity function and stability of the system due to model uncertainty is presented in [95]. The stability criterion is defined as

$$\sup_{\omega} \left| T_o(j\omega)\, B_M(\omega) \right| < 1 \qquad (5.8)$$

where, $T_o(s)$ $\{s \equiv j\omega\}$ is the complementary sensitivity function with nominal parameters and $B_M(\omega)$ is the magnitude bound on the uncertainty $\Delta G_M(j\omega)$ at frequency ω. By definition, from Fig. 5.3

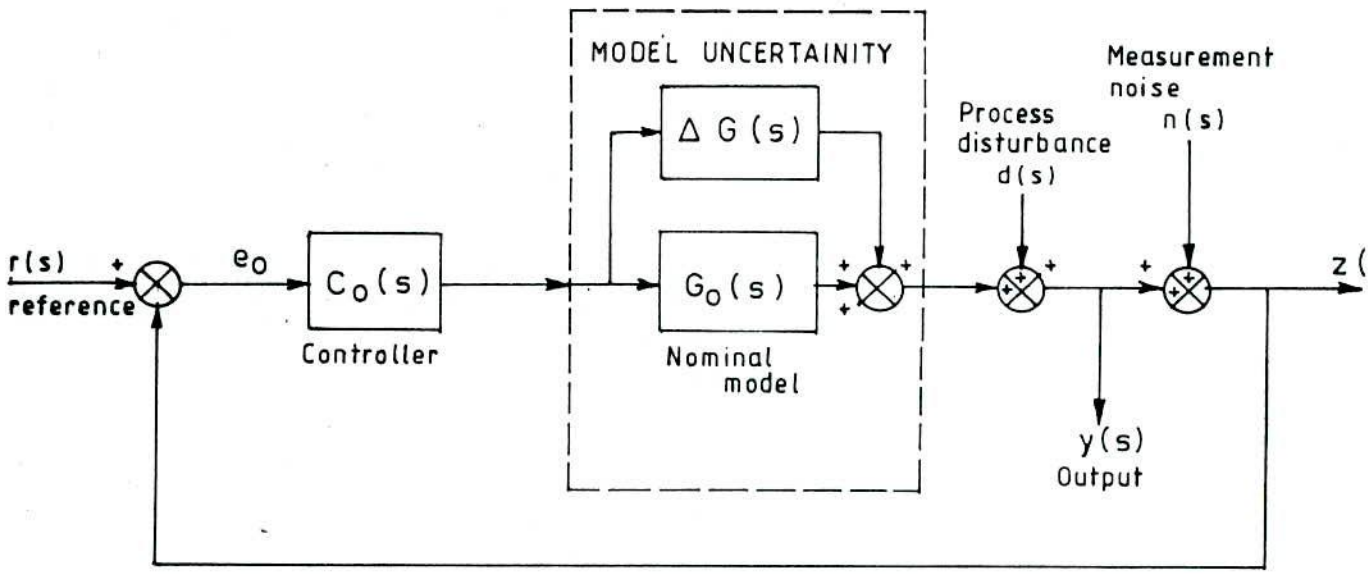

Fig. 5.3 A physical control system configuration representing model uncertainty and noises.

$$T_o(s) = \frac{G_o(s)\ C_o(s)}{1 + G_o(s)\ C_o(s)} \qquad (5.9)$$

5.3.2 Selection of PI controller constants

The second PI controller denoted by the transfer function $G_2(s)$ in the block diagram of Fig. 5.1 converts the current error signal to rectifier voltage V_R' while the transfer function $G_I(s)$, incorporating the first PI controller transforms the speed error signal into the current command $I_R'^*$. The controllers in the current and speed loops are designed with the objective to attain fast and non-oscillatory dynamic response as well as to maintain the robustness of the system. To say explicitly, the constants in each controller are determined in such a way that the poles associated with the respective transfer function lies inside the negative half plane and that the H_∞-norm is as small as practicable. Secondly, in nested loop approach, the loop bandwidth increase inwardly. In practice, the bandwidth of the current loop is made much greater than that of the speed loop [108].

The transfer function $G_I(s)$ of (5.2) with nominal set of parameters and quantities becomes

$$G_I(s) = \frac{8.7997\ k_{p2}s^2 + (0.4824\ k_{p2} + 8.7997\ k_{i2})\ s + 0.4824\ k_{i2}}{\delta_I(s)} \qquad (5.10)$$

where,

$$\delta_I(s) = s^3 + \{29.647 + 8.7997 k_{p2}\}\ s^2 + \{220.387 + 0.4824\ k_{p2} + 8.7997\ k_{i2}\}\ s + 0.4824\ k_{i2}$$

The selection of suitable values for gain constants was carried out for different combinations of k_{p2} and k_{i2} after having got their initial guesses following the ideas in [108]. and using the CC program (Ver. 3).

Finally, the following sets were arrived at for the current controller :

$$k_{p2} = 30 \quad \text{and} \quad k_{i2} = 10$$

for which H_∞-norm is 0.899 and roots of $\delta_I(s)$ are - 0.01515, -1.000 and -292.53.

Using the above mentioned controller constants the speed loop transfer function in (5.3) becomes

$$G_\omega(s) = \frac{251.64 \{ 30\, k_{p1}\, s^2 + (10\, k_{p1} + 30\, k_{i1})\, s + 10\, k_{i1}}{\delta_\omega(s)}$$

where - - - (5.11)

$$\delta_\omega(s) = s^4 + 293.635\, s^3 + \{ 322.86 + 7549.2\, k_{p1} \}\, s^2 + \{ 4.824 + 2516.4\, k_{p1} + 7549.3\, k_{i1} \}\, s + 2516.4\, k_{i1}$$

Adopting the same procedure as in the case of current control loop, the PI controller constants for the speed loop become

$$k_{p1} = 2.0 \quad \text{and} \quad k_{i1} = 0.5$$

for which H_∞ - norm is 1.0035 and the roots of $\delta_\omega(s)$ are -0.26566, -0.31052 and -225.33. The bandwidths for the speed and current loops are 62.0 rad/sec. and 230.0 rad/sec. respectively. The unit step response for the closed loop system using CC program is shown in Fig.5.4.

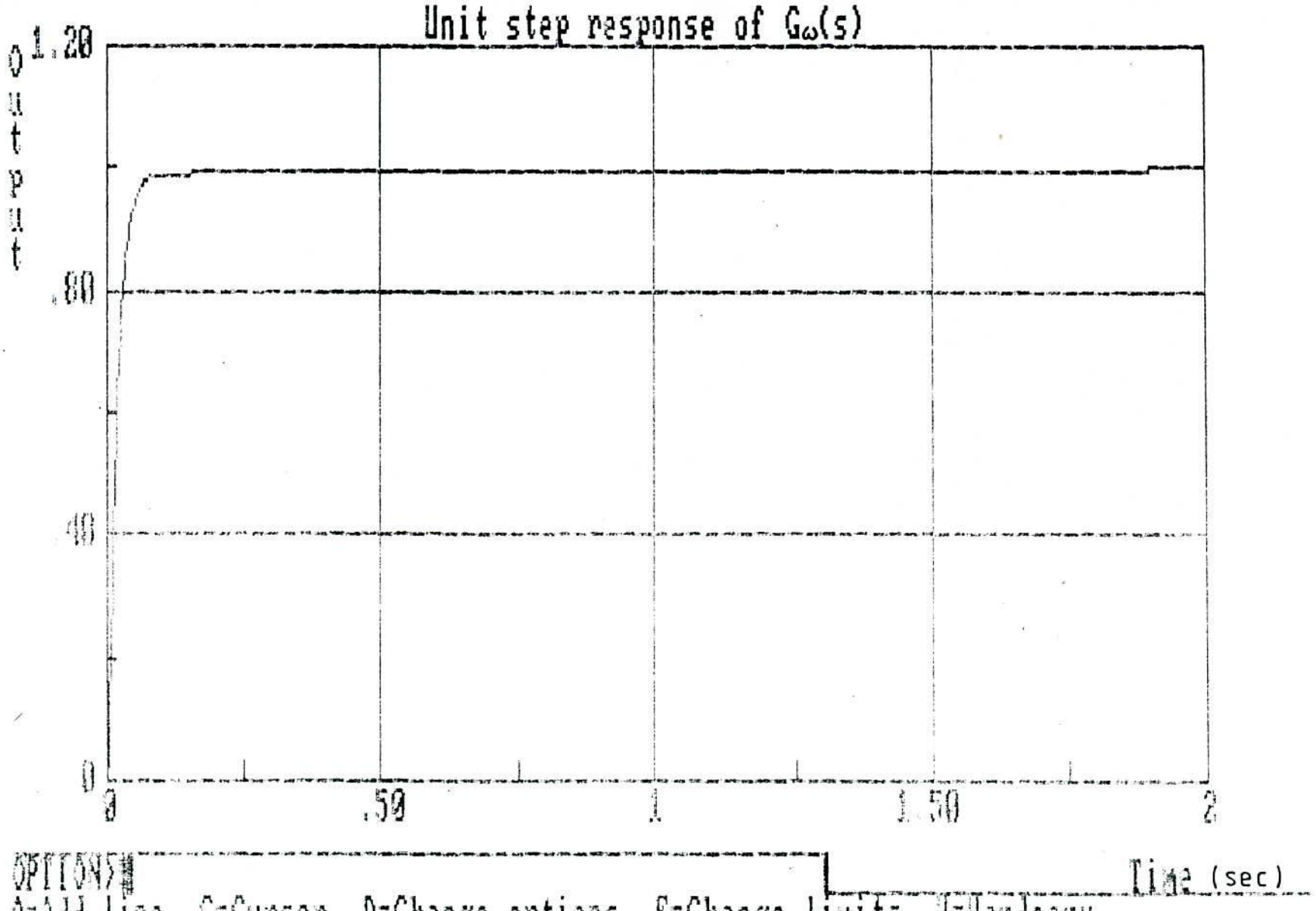
Unit step response of Gω(s)
output
1.20
.80
.40
0
0
.50
1
1.50
2
Time (sec)
OPTION>
A=Add line, C=Cursor, D=Change options, E=Change limits, H=Hardcopy
L=Label, M=50% more time, P=Plot again, Q=Quit, T=Thick lines, Z=Center

FIG. 5.4

5.4 STABILITY PROBLEM AND ROBUSTNESS STUDY

In a physical system both the parametric perturbations and unmodelled dynamics are assumed to take place simultaneously, and normally in H_∞-norm based robustness study, the unstructured stability margin is found out by applying reasonable level of structured perturbations to the system and then the maximum norm-bounded unstructured stability margin is computed. A procedure of determining unstructured stability margins after introducing the parametric perturbations is presented in [97].

5.4.1 Considerations of parametric perturbations

The performance of a vector controlled induction motor is characterized by the transfer functions shown in eqns.5.2-5.4. The coefficients in the polynomials are subject to changes due to deviations in the parameters and/or the operating point and errors in the instrumentation. The parameters of an induction motor which are normally subject to changes with operating conditions are discussed below:

(a) Rotor resistance (R_r) : The rotor resistance is a function of rotor temperature and in an extreme condition the value may increase by 50% from its nominal value [46] which we consider as the maximum for our study here. On the lower side a reduction of the value by 20% from the nominal value is considered to take into account the fall in ambient temperature and measurement error.

(b) Stator resistance (R_s). Like the rotor resistance, the variation of stator resistance is considered over the ranges from 80% to 150% of its nominal value.

(c) Mutual inductance (L_m) : The mutual inductance changes due to nonlinearity in the magnetic circuit. In this study, magnetic saturation effect and operation in the linear region are considered by attributing a range of variation to both L_m and L_r. 20% changes of L_m in both the directions from the nominal value is considered to be sufficient to take into account of the decrease in the mutual inductance due to magnetic saturation and operation of the induction motor in the linear region. L_s and L_r are computed by adding leakage inductances to L_m.

Apart from the induction motor parameters, the following operating point dependent quantities are also considered which are responsible for deviations of dynamic conditions and stability and are considered as generating structured perturbations to the system.

(a) Rotor flux linkage (λ_r). Field orientation control may require adjustment of the rotor flux linkage of the induction motor. Variations may also be caused by extraneous factors. A ± 20% variation of λ_r from the set value of the flux is considered.

(b) Torque producing factor (g_{qs}). The factor g_{qs} is expressed by (2.6). This factor is mainly dependent on disturbance torque T_L. A constant torque of about 4 Nm due to bearing friction is considered and a maximum disturbance torque 20 Nm is considered to act on the motor. This is considered by selecting an interval 0.2-0.8 for g_{qs}.

(c) Mismatch factor (g_{qs}/g^*_{qs}). This ratio has a value of unity under idealized conditions. The deviation of mismatch of this ratio from unity is due to difference in reference and actual values of

torque producing component of current subjected to speed or torque disturbances for the closed loop control. This ratio is considered to vary over the range of 0.2 to 0.8.

5.4.2 Stability and the Box Theorem

Kharitonov's theorem [90] provides an easy method to study the robustness of interval plants with independent variations of the coefficients but offers conservative results when applied to study a real system in which the coefficients of the characteristic polynomial are dependent. In this case, generalization of the theorem is required by considering the variation of the coefficients within a prescribed box and stability study is conducted for a prescribed number of line segments. The theorem named as 'Box Theorem' [94] suggests that if a system (plant and controller) is stable then the characteristic polynomial of the system should remain stable within the prescribed parametric perturbations if the segments defined by the expression

$$(1 - \lambda)\, E_{v\phi}(s)_{max} + \lambda\, E_{v\phi}(s)_{min} + (1- \mu)\, E_{o\phi}(s)_{max} + \mu\, E_{o\phi}(s)_{min} \tag{5.12}$$

are stable for all possible λ and μ in the interval

$$\lambda \in [0,\ 1] \quad \text{and} \quad \mu \in [0,\ 1]$$

where, $E_{v\phi}(s)$ and $E_{o\phi}(s)$ are odd and even parts of the characteristic polynomial.

5.4.3 Test for robustness of the proposed control scheme

The control scheme is tested for robustness using Kharitonov's segments [94] with the parametric variations indicated in Sec 5.4.1,

and the unstructured stability margin is evaluated. For the test of robustness only the transfer function $G_\omega(s)$ is considered here. The coefficients of the numerator and denominator polynomials are found to vary within the following intervals:

$d_0 \in (5.1077, 31.746)$, $d_1 \in (35.804, 222.27)$,

$d_2 \in (62.476, 386.34)$, $d_3 \in (2.9372, 3.225)$,

$d_4 \in (0.010341, 0.01038)$, $n_0 \in (5.1077, 31.746)$,

$n_1 \in (35.754, 222.22)$, $n_2 \in (61.292, 380.95)$

The minimum and maximum values of the odd and even functions of the characteristic polynomial are

$$E_{v\phi}(s)_{min} = 5.108 + 386.34s^2 + 0.01034s^4$$

$$E_{v\phi}(s)_{max} = 31.746 + 62.476s^2 + 0.01038s^4$$

$$E_{o\phi}(s)_{min} = 35.864s + 3.2245s^3$$

$$E_{o\phi}(s)_{max} = 222.27s + 2.9372s^3$$

Applying the criterion in (5.12) gives

$$(0.01034 + 0.00004\lambda)s^4 + (3.2245 - 0.2868\mu)s^3 + (386.34 - 323.844\lambda)s^2 + (35.864 + 186.406\mu)s + (5.108 + 26.638\lambda) \quad \text{- - - - -} \quad (5.13)$$

By Routh's criterion, the polynomial (5.13) for both λ and μ varying in the interval [0,1] is found to be stable. The numerator of $G_\omega(s)$ can also be written in the fashion as (5.13) containing two more parameters, say, δ and κ. The parameters λ, μ, δ and κ are so selected that the H_∞-norm of the closed-loop transfer function assumes maximum

value which is found to be 10.088402 (at ω = 0.103673). The unstructured norm-bounded stability margin for the worst case is, therefore, equal to 0.099124.

5.5 SIMULATION RESULTS AND OBSERVATIONS

The validity of the robustness study using Kharitonov's segments is justified by simulating the induction motor model in (2.44) with the controller structure in Fig.2.7. Results for a typical simulation study for simultaneous changes in motor parameters and set flux with torque disturbances is shown in Fig.5.5. In this case, R_r and R_s were increased by 50% from their nominal values and rotor flux was increased by 10% from its set value at a certain instant of steady state operation. Saturation was incorporated in the machine model. At the same instant of introducing the above mentioned changes a torque disturbance (step increase from 5Nm to 10 Nm) was applied. For such simultaneous changes with the uncompensated and dc link voltage based parameter adaptive system, stability of the control system is distinctly observed. It may also be noted that for the non-adaptive system the response is poor than the parameter adaptive system.

The stability margin predicted by the H_∞ - based control theory is found to be small. But the worst situation has been considered for this study and this is unlikely to be met with in practice.

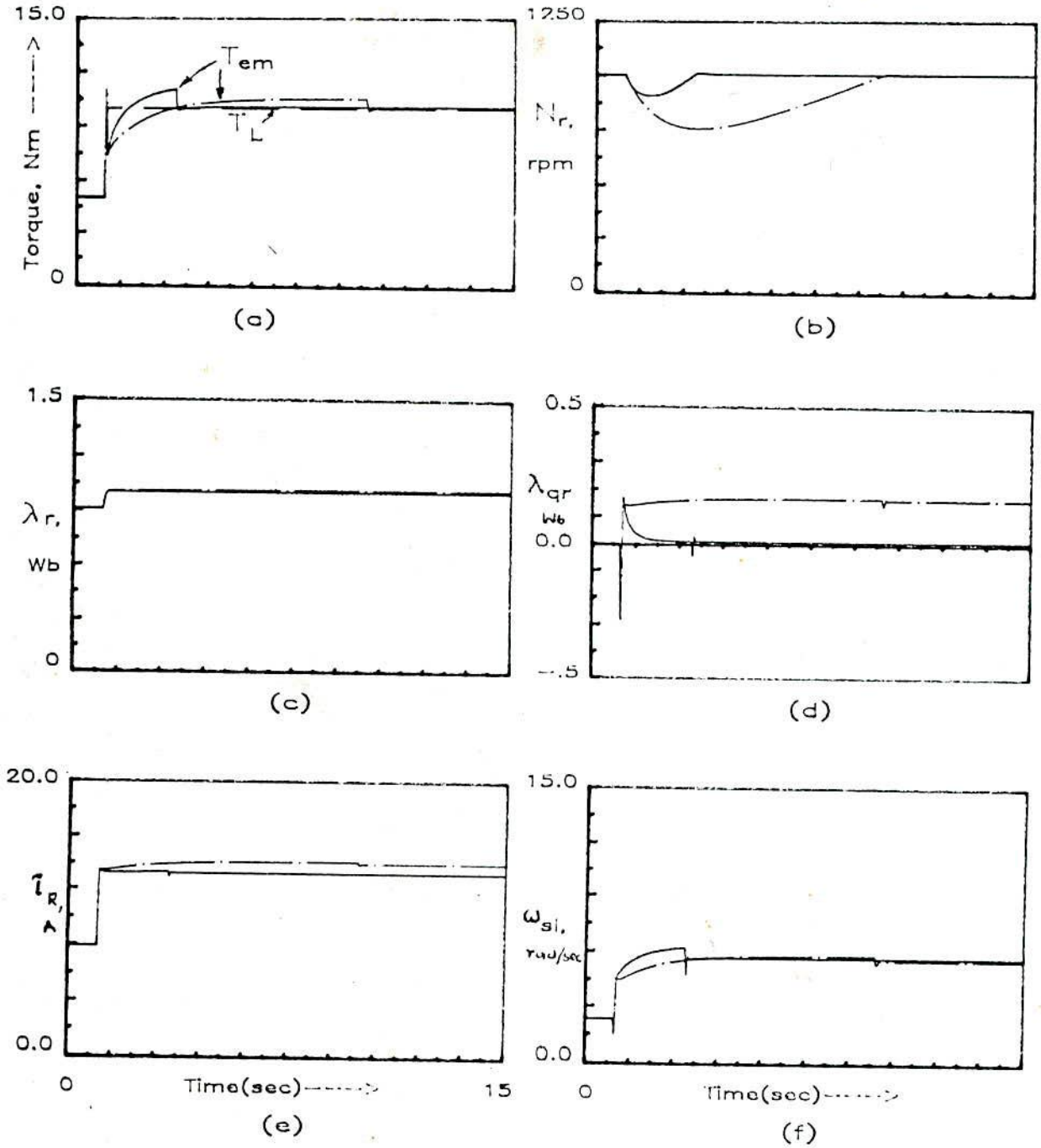

Fig.5.5 Simulation traces for simultaneous changes of R_s & R_r (each increased by 50%), rotor flux increased by 10%, and step change in load torque (5 Nm to 10 Nm)

——— with compensation, —·—·—without compensation

CHAPTER VI

HARDWARE AND SOFTWARE IMPLEMENTATION OF THE VECTOR CONTROLLED CSI-IM DRIVE SYSTEM

6.1 INTRODUCTION

The effectiveness of implementation of an indirect field oriented induction motor drive system depends on the accuracy with which the quantities such as voltage, current and speed are measured and processed to generate desired signals and estimate parameters for detuning correction. Sampling time is another important factor in digital processing. It is desirable that the sampling interval is as small as possible to ensure stable and effective performance of the system. Compensation due to parameter deviation in the drive system is also necessary to avoid degradation of performance. The following aspects are to be kept in mind in the overall implementation of the system.

1) Floating point computations are preferred to minimize discretization error.

2) Use of minimum hardware components and framing the software in modular form with utmost flexibility suitable for multi-microcomputer-based system.

3) A good man-machine interaction providing scope for checking the parameter estimation results and commanding the compensation schemes to work in the right direction.

4) To keep the sampling time at its minimum possible value.

In this chapter, starting from the generalized functional diagram, hardware and software implementation of each control aspect are discussed. For a better appraisal of the proposed vector control structure and compensation schemes, tests were conducted on two laboratory type induction motors (squirrel cage and slip-ring type) whose nominal parameters are listed in Tables A.1 and A.2 under Appendix I. Circuit topology and software were the same for both the motors excepting the speed sensing arrangements.

A general layout of the drive system and its hardware and software details are presented in the subsequent sections without going into the details of the principle of operation of the power conditioners and the characteristics of the devices and components. Extensive tests were carried out and certain test results are furnished in support of the operating principle and associated algorithms of the proposed control system.

6.2 THE DRIVE SYSTEM

6.2.1. Functional diagram

The proposed control methodology in Fig.2.7 with compensation schemes (Chapter IV) for parameter deviation basically comprises of a number of functional blocks. From the implementation point of view their interactions can be described through the generalized functional block diagram in Fig.6.1. This diagram, in fact outlines the mutual action between (i) software and control block on one side and (ii) transducers, power circuits, and other necessities, such as, storage,

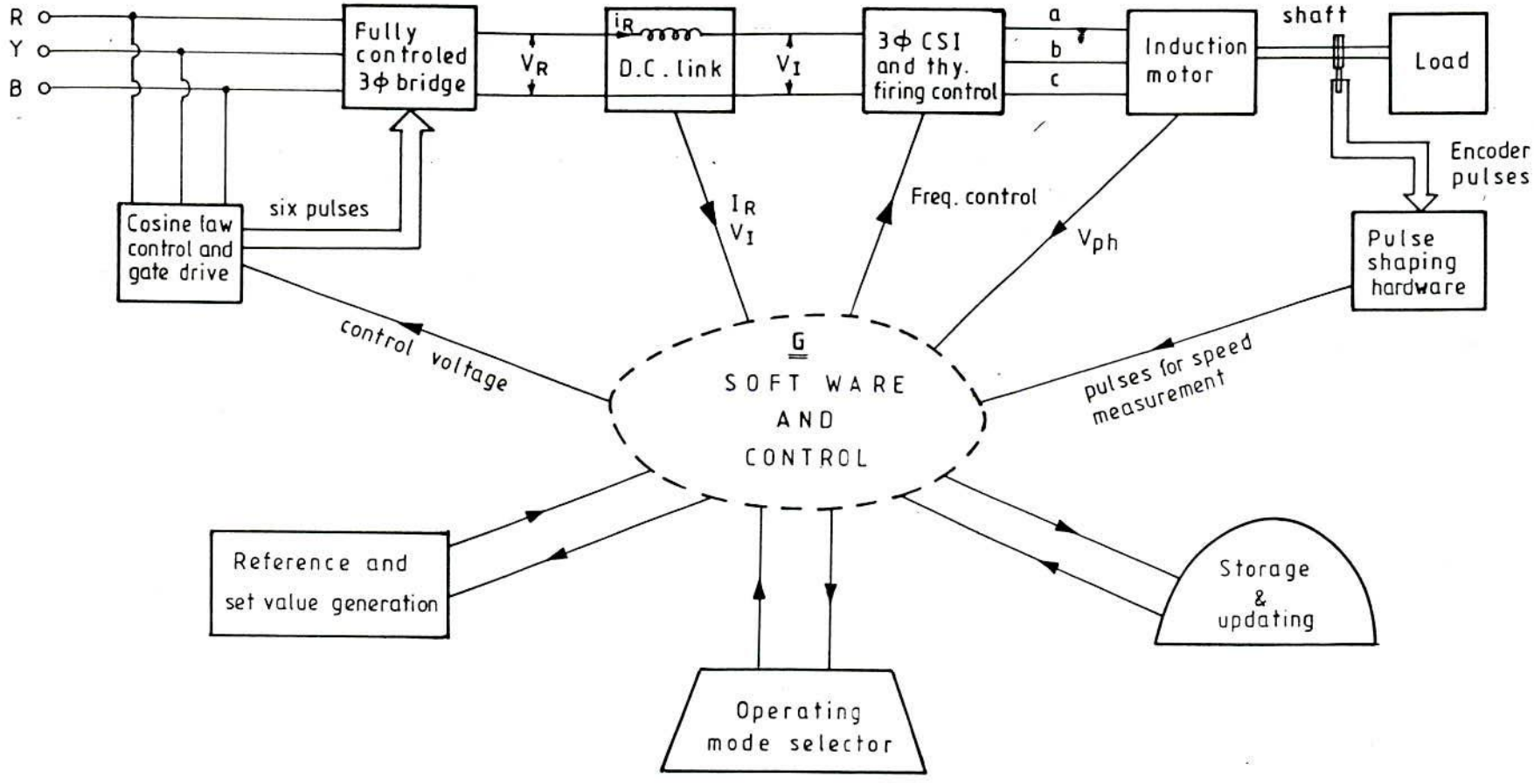

Fig.6.1 Generalised functional block diagram.

mode selector etc, on the other side. A general description of the drive system hardware and software is presented in the following sections.

6.2.2 Software description

The overall software and control algorithms are shown under one block in Fig. 6.1. The overall software is divided into a number of tasks and each task is subdivided and processed by some modules. An elaborate pictorial representation of software blocks used for the control strategy is shown in Fig 6.2 indicating the direction of interactions (analog and digital). The major tasks assigned to the 'software and control' functional block are:

(i) Generation of control voltage (PI-based) for the cosine law controller to adjust the dc link current through the three phase converter.

(ii) Processing the output signal from the optical encoder to obtain the instantaneous speed.

(iii) Computation of slip speed and $d\theta/dt$, and control of frequency for the inverter.

(iv) Parameter identification and execution of the algorithm for the selected compensation scheme.

Operating mode selector enables one to choose particular control strategy for the drive as well as to give commands for recording desired data to study system behavior. For such utilities modular programming approach has been used.

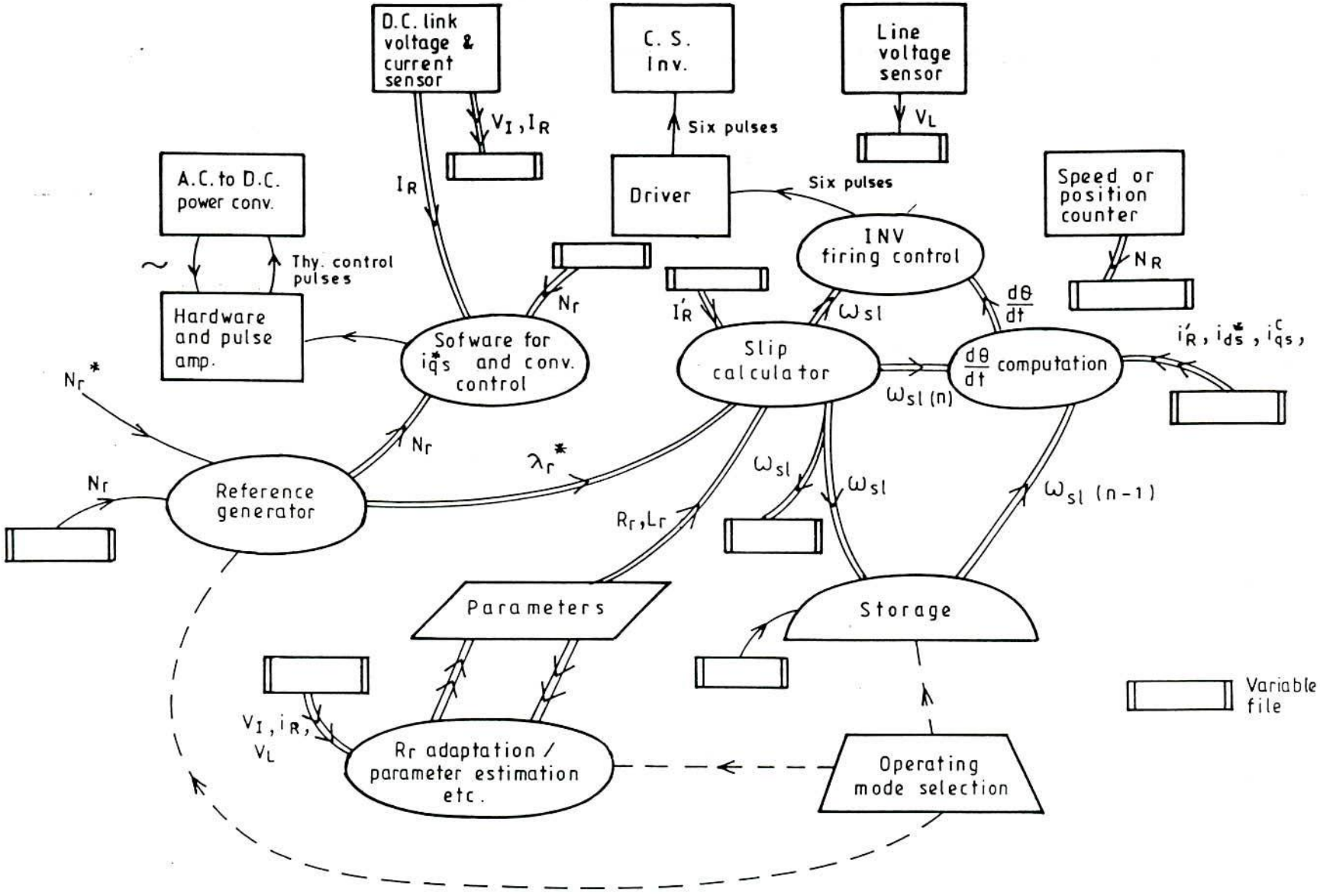

Fig. 6.2 Block diagram of application software.

6.2.3 Hardware description

Functional block diagrams of Fig. 6.1 and the overall system configuration in Fig.6.2 require the following basic systems.

(a) Microcomputers with peripherals for external communication and data acquisition.

(b) PC/AT with instrumentation modules.

(c) Pulse generating and processing circuits for speed measurement.

(d) Three phase fully controlled bridge converter with gate triggering circuit.

(e) Three phase current source inverter with triggering circuit.

(f) Transducers for sensing voltage and currents of the power circuit.

Figure 6.3 shows the hardware configuration of the drive system. Two microcomputers, each with i-8086 CPU and i-8087 math co-processor, are used for non adaptive operation of the drive system (implementation of the control system strategy in Fig.2.7) and generating the gate signals for the inverter and the input voltage for the cosine wave gating circuit of the converter. When adaptive control is required, parameter estimation/correction is carried out by PC/AT with the help of its data acquisition modules and the results are sent to the microcomputer used for slip computation. The following section outlines in brief, the key features of the digital processors. Photograph 1 and 2 show the experimental set up.

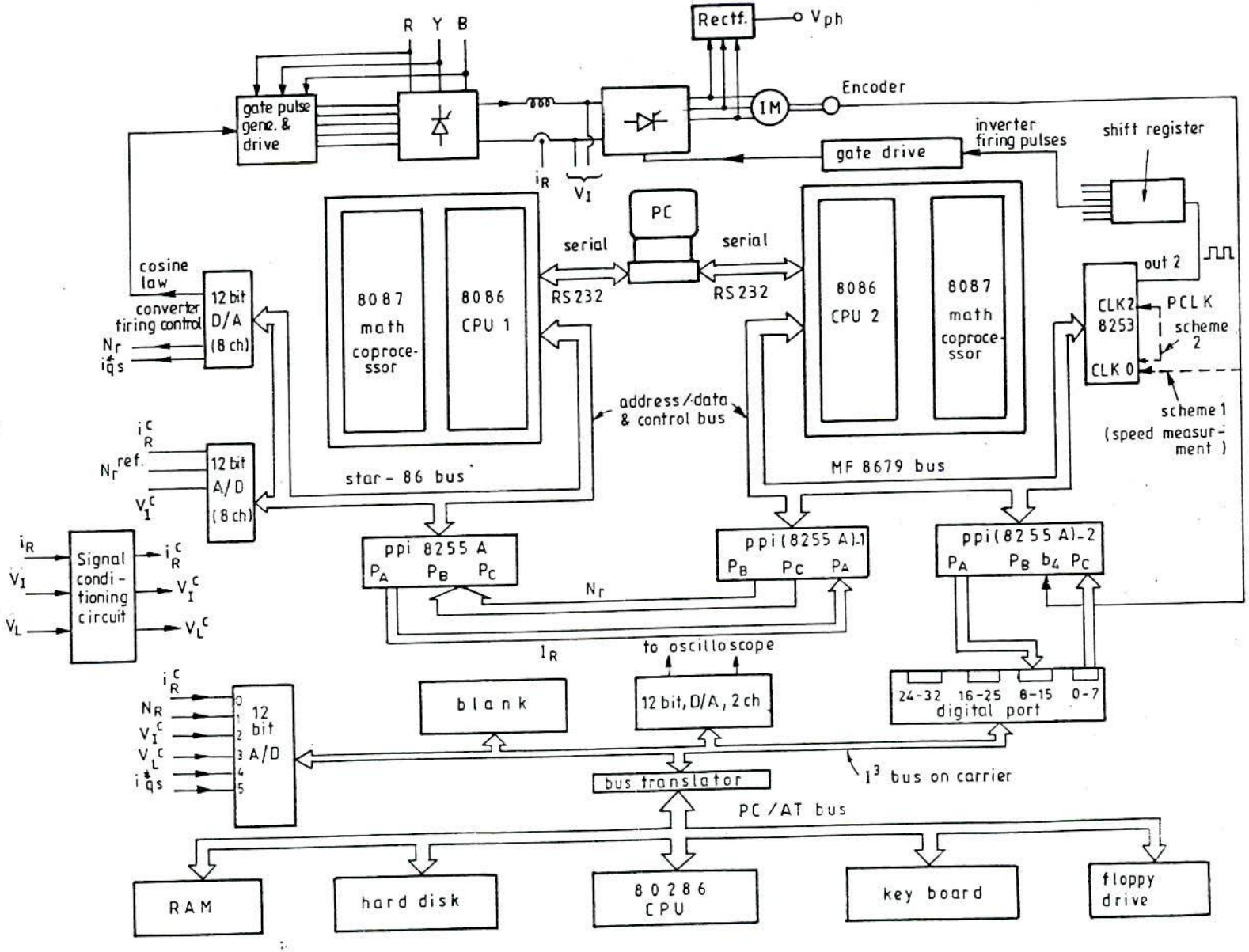

Fig.6.3 Hardware schematic.

Photograph 1 : Experimental set up

Photograph 2 : Induction motors with loads

6.3 DESCRIPTION OF COMPUTING AND DATA ACQUISITION SYSTEMS

Two microcomputers, namely, Microfriend MF8679 and the Microfriend Star-86 were used for implementing the non-adaptive system. During simulation study sampling period of the order of 2.5m sec was found to be adequate for desirable operation of the system. The above microcomputers were capable of meeting the requirement. PC/AT with Burr Brown's instrumentation module PCI20000 was used when parameter estimation adaptation and storage of variables were required. The systems are described in brief in the following sub-sections.

6.3.1 Microfriend MF-8679 microcomputer

The dual board microcomputer Microfriend MF-8679 (8086/8087) is supplied by Dynalog Micro-systems, Bombay, India, with the following interfaced ICs.

* A daughter board with IC 8279, key board, EPROM programmer with ZIF socket, 8X7 LED display and two 8255-A for interfacing the following peripheral devices.

* Two 8255-A on the mother board.

* Two counters of 8253, namely C # 0 and C # 2.

* One USART 8251 with accessories for serial communication through RS232.

* Two 2764 EPROMs loaded with monitor programs.

* 16 k-byte static RAM for temporary storage of data.

Certain Important Features of MF8679 are:

* The microcomputer provides easy expansion of RAM and ROM memories via blank sockets.

* It provides easy communication with external world through serial and parallel ports.

* 86-pin multi-bus connection facility for expansion of interfacing

* The clock frequency is 4.77MHz and pclk(peripheral clock) frequency is 2.38636MHz.

Computing and controlling tasks carried out by MF8679:

* Detection of instantaneous speed of the motor.

* Computation of ω_{sl} and $d\theta/dt$.

* Control of frequency for the CS-Inverter.

* Receipt of adjusted value of R_r in the case of adaptive control from the PC/AT through a digital port.

6.3.2 Microfriend Star-86 microcomputer

The single-board 'Microfriend Star 86' microcomputer from Dynalog micro-systems, Bombay (India), comprises of the following processors, ICs and interfaced devices

* Central processing unit, i-8086.

* Math-Co-Processor, i-8087.

* Two 8255A one for users' purpose and another for keyboard interfacing.

* One counter of 8254 is available for user application.

* One 8150 UART for Serial Communications through RS232.

* Two 2764 EPROMS with monitor programs

* Two static RAMS each of 8 kbytes with battery backup.

The important features and peripherals interfaced with the Star-86 microcomputer are :

a) IBM expansion slots for interfacing ADC (PCL 207) and DAC (PCL 204) modules or other modules, if necessary.

b) The ADC module (PCL 207) uses AD 574AJ as the A/D converter chip. Multiplexing is used to have 8 input channels. PCL 207 also contains single channel 12 bit DAC (AD754 AKN) on board with 30 μsec settling time. The ADC is used in trigger mode for start of conversion.

c) Like PCL 207, the 8- channel 12 bit DAC module PCL 204 (AD 7521 based) can be easily interfaced with star 86 through the IBM expansion slots.

d) The Star 86 provides RAM expansion sockets to have a very large space for data storage with RAM type selectivity through jumpers.

The Star-86 is called for to execute the following operations.

* Taking in i_R, v_I and reference speed through ADC with 11 bit resolution (bipolar operation) and motor speed through digital port

* Computation of i_{qs}^{*} and $i_R^{'*}$.

* Generation of control voltage for the cosine law firing of the converter.

6.3.3 PC/AT with data acquisition

The PC/AT for data acquisition and tuning for the proposed indirect field oriented control system is from Samsung Semiconductor and Telecommunications Co. Ltd. (Republic of Korea) and uses intel

80286 as CPU operating at 10 MHz. Burr-Browns PCI 20000 system for data acquisition can easily be installed as plug-in boards in the expansion slots. The use of PC/AT with the PCI system provides the facility of writing programs in high level language and a large storage space for results. Another important advantage is the provision of better on-line interaction between the users and the control system through keyboard and video display.

The data acquisition and interfacing devices used by PCI 20000 system are all modular type and can be tailored effectively by choosing the modules according to requirement. The PC/AT has three expansion slots and two of them can be used by PCI system. Communication between the modules and the PC/AT takes place through carrier boards. Each carrier board can extend connection up to three modules and provides a 32-bit digital communication link. The carriers are connected as memory mapped i/o devices and each occupies 1k byte of memory space and each module can occupy 256 bytes of memory locations. The absolute address of the register of any module is set through a number of switch groups and is expressed as:

Absolute address of register = Carrier base address + module block address + local register offset.

For data acquisition and communication with external world through the modules, absolute address of its register is required if programming is done in assembly language but in high level language an "initialization software package" takes care of it and also configures each module or each digital bit according to the information supplied

by the user through the "header software" utilities. Only segment address of the carrier, module type and channel number are required for initializing configuration. The structure of a PCI bus system called the I^3 (Intelligent Instrumentation Interface) bus is shown in Fig.6.4.

In the proposed control scheme PCI 20041C-2A, the high performance carrier with high speed data transfer capability was used along with the modules listed below :

Module name	Module Characteristics
(a) PCI 20002M-1	A/D: 16 single ended or 8 differential input 12 bit resolution, 25μsec conversion time 4% linearity error.
(b) PCI 20003M-4	D/A: 2 output channels (voltage or current) 12 bit resolution, settling time 30μsec.
(c) 4-byte digital i/o:	Each bit/byte can be individually programmed as input or output through bidirectional buffers.

6.4 SPEED MEASUREMENT

Accurate measurement of speed over a wide range is a basic need for desirable operation of speed controlled systems. Specially, the efficacy of high performance drive systems, such as field orientation control, depends on the accuracy of the measured speed. Ordinary tachogenerators fail to meet this requirement [5].

A number of methods have been developed to measure the average

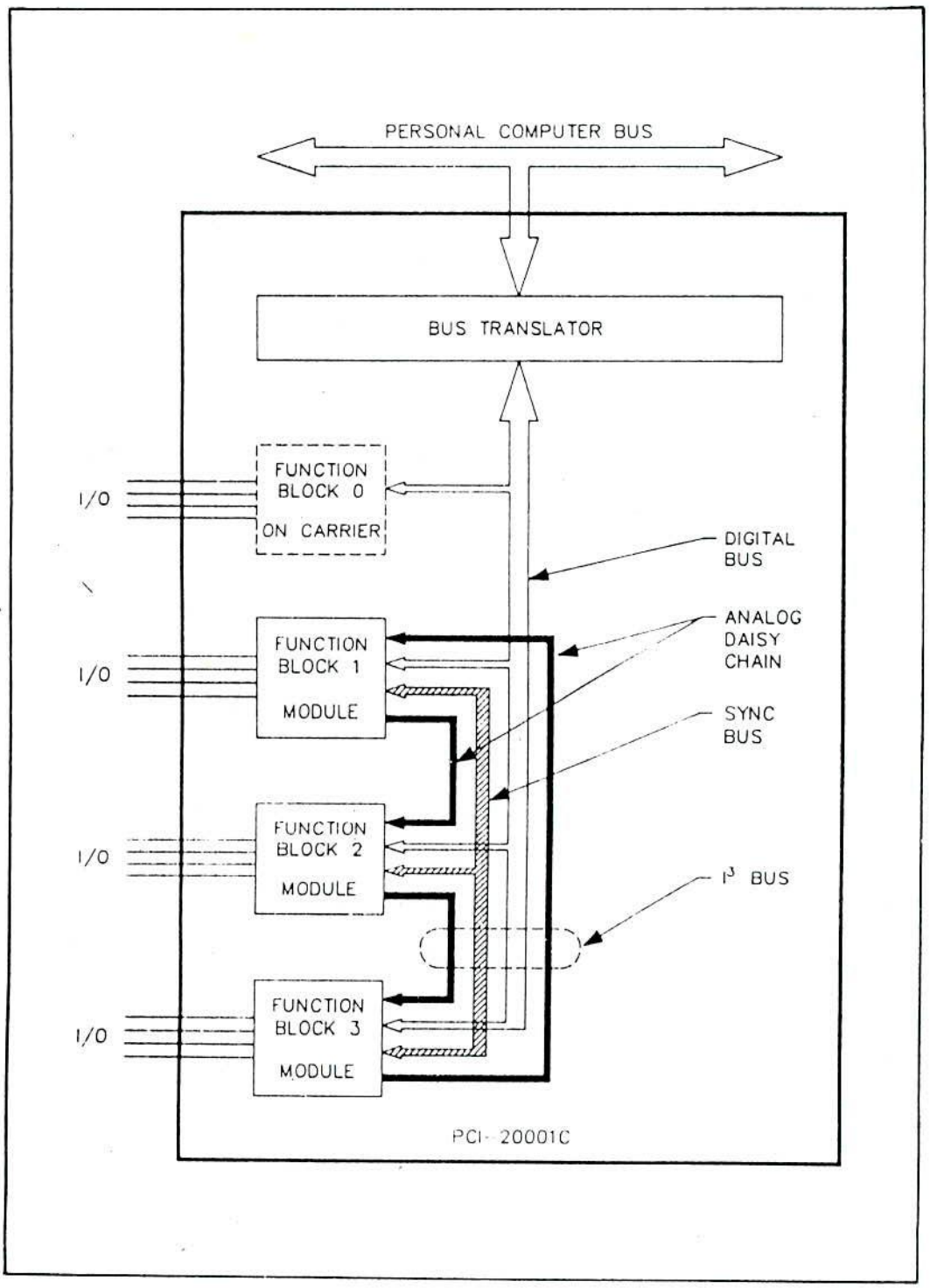

Fig. 6.4 PCI-20000 I^3 bus structure.

speed over an interval using optical encoder and microcomputer combination. These are termed (i) m-method, (ii) T-method and (iii) m/T-method, where m is the number of encoder pulses over the detection period T. Relative merits and demerits of these methods have been discussed in [99]. The m/T-method shows better performance in respect of accuracy over the range of measurement excepting in the low speed region. To improve the accuracy throughout the range of measurement an adaptive optimization technique is suggested in [100] which automatically adjusts the sampling time according to the width of the encoder pulse. The technique computes average speed of the drive over an interval which causes phase and gain errors with respect to actual speed at a particular instant for variable speed drive systems. If such average speed is used to generate control signal for highly dynamic or vibratory drive systems with large detection intervals degradation in performance and instability may result [101]

Considering the above problems, two methodologies are presented to obtain instantaneous speed of the induction motor for the proposed speed control system.

6.4.1 Scheme 1: Instantaneous Speed Detection by m/T Optimization.

6.4.1.1 Principle of operation

In the case of varying speed the smaller the value of T, the closer will be the average speed to the instantaneous speed. For estimation of instantaneous speed the m/T method is used with maximum detection time T (or m) optimized according to speed and the time available for the microprocessor between the firing instants of two

consecutive inverter thyristors. In each step of measurement, time elapsed for a particular number of encoder pulses is detected through a programmable counter interfaced on board. Let there be m number of encoder pulses for which n number of counter clock pulses of frequency f_c are counted, then the detection period

$$T = \frac{n}{f_c} \tag{6.1}$$

If M pulses are generated by the optical encoder-pulse generator per rotation of the motor shaft, the average speed in rpm

$$N_r = \frac{60}{M} \frac{m}{T}, \tag{6.2}$$

i.e.,

$$N_r = \frac{60\ f_c\ m}{n\ M} \tag{6.3}$$

Since M and f_c are fixed the frequency of encoder pulse, or the width of encoder pulse, at any instant depends on actual speed of the motor. From (6.3) resolution [99] can be expressed as

$$Q_n = \frac{60\ f_c\ m}{M} \frac{1}{n\ (n-1)} \tag{6.4}$$

Since n is proportional to detection interval it reduces if m is kept constant. Therefore, resolution becomes poor at higher speeds.

6.4.1.2 Optimization procedure

In the proposed control system the speed measurement by microprocessor is a part in the process control. So the speed detection time is constrained by the availability of time between two consecutive

firing instants of inverter thyristors. In the present case microcomputer MF 8679 is used to measure speed and compute slip, and also to control the firing of the inverter thyristors. Firing intervals of inverter thyristors is inversely proportional to the frequency of the stator current of which motor speed is the dominant part. At low speeds, firing interval as well as detection period is large. But bit size puts a constraint and also averaging over a long interval causes considerable deviation of the detected speed much from the instantaneous value. So at low speeds m should be kept low. At medium speeds (1000rpm) m attains its maximum value (6 here) and again decreases with speed. The speed ranges with optimum values of m are stored in the computer memory. Optimized values of m for different speed ranges are selected through logical statements and the updated value of m corresponds to the previous measured speed.

6.4.1.3 Hardware description

The proposed speed measurement system works by sensing pulses produced by rotation of an optical encoder. The pulses are sensed and counted through ppi-8255A interfaced on board by testing the falling edge of encoder pulse. The hardware configuration of the system is shown in Fig.6.5. The pulse generator circuit comprises of an aluminium disc having single row of 128 holes and uses infra-red LEDs as optical devices for both emitting and receiving. The output of the receiver LED is applied to a 555 timer (pins 2 and 6) used as level comparator to generate a square wave. The resistor R_k is adjusted for appropriate swing of the input voltage (less than $\frac{1}{3} V_{cc}$ to greater than $\frac{2}{3} V_{cc}$) to the level comparator.

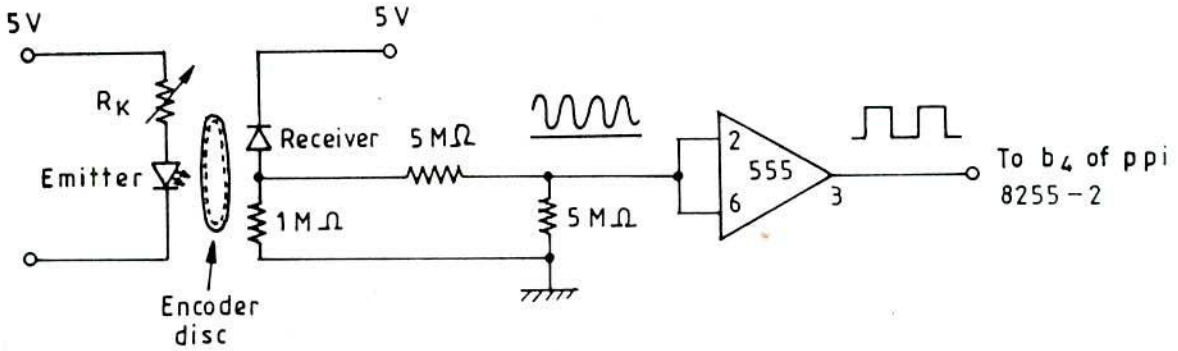

Fig. 6.5 Pulse generation circuit for optical encoder - scheme 1.

6.4.1.4 Software description

The computation of speed is done by detecting n for a previously selected number of encoder pulses. The number of counter clock pulses (f_c=2.38636 MHz) is counted by the programming counter 0 of 8253 in mode 0. Computation of speed is carried out by math-co-processor 8087 in real format. Data transfer, logical statements etc, are done by the CPU 8086. The computational execution sequence for the proposed speed measurement technique is explained through the flow diagram in Fig.6.6. It may be noted here that the initialization shown in the flow diagram is actually accommodated in the main program (vide section 6.7).

6.4.1.5 Experimental verification

The proposed scheme of measurement was tested for determining its accuracy at different speeds of a separately excited dc motor and the measured speed was compared with that indicated by a calibrated tachometer. A good agreement between the two sets of measurements in the range of operation was noted. To study the closeness of the measured speed with the instantaneous values for fast changes, the

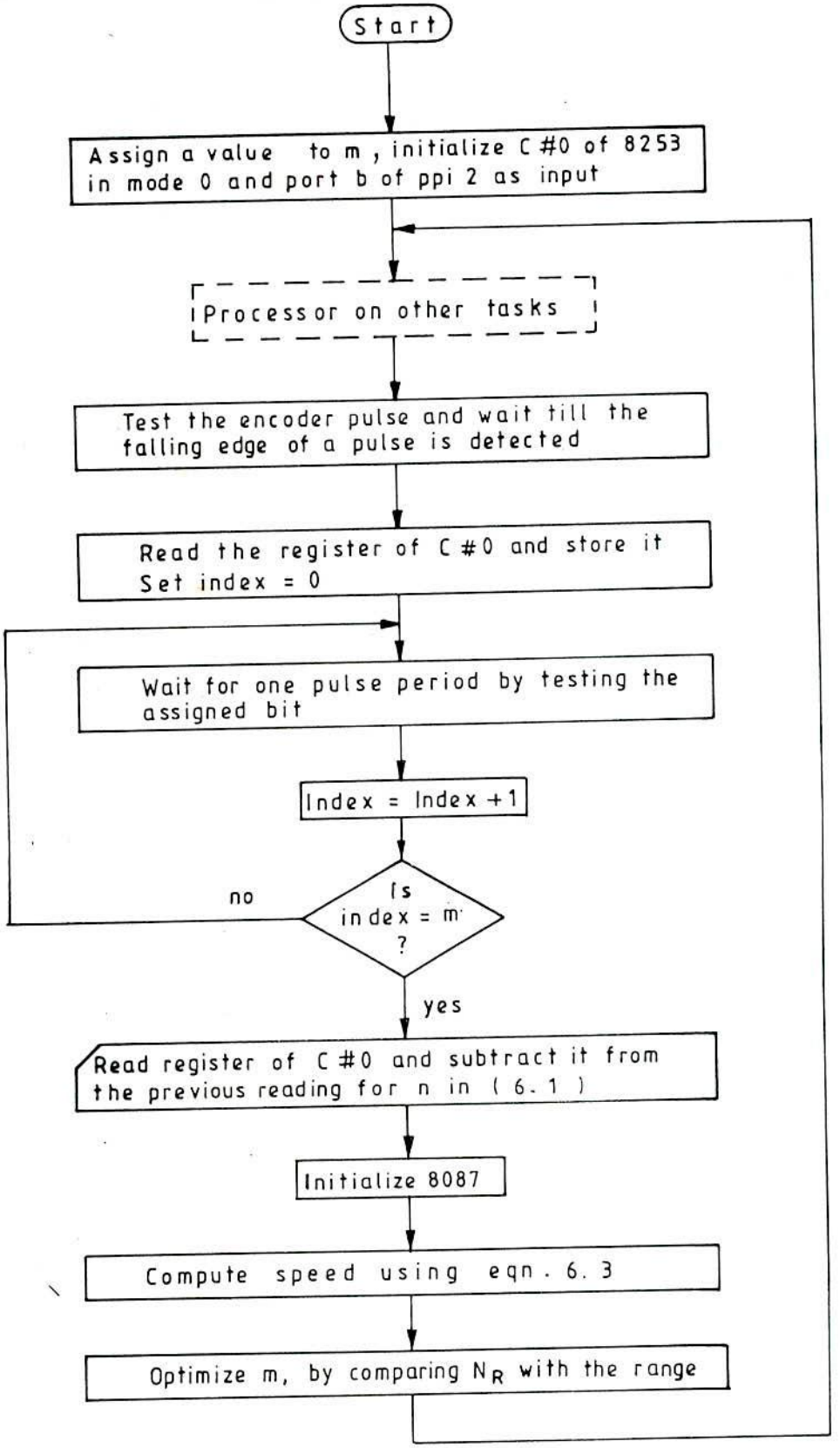

Fig. 6.6 Computation sequence for speed measurement - Scheme-1.

scheme was applied to measure the speed rise of a dc motor starting from standstill. The plots in Fig. 6.7 (a) compare the measured values with those indicated by a tachogenerator coupled with the machine set. The portion of the plots during the acceleration period are presented in Fig. 6.7 (b) on expanded time scale.

6.4.2 Scheme 2 - instantaneous speed estimation from average speed.

This scheme proposes some modifications over the m/T method [99] for estimation of the instantaneous speed from the average speed. The modifications imparted are:

i) Adjustment of detection time according to speed of the induction motor.

ii) Computation of detection time for integral number of encoder pulses.

After determining the average speed of the drive, the speed at the end of the detection interval is estimated considering linear variation of speed over two consecutive detection intervals.

6.4.2.1 Principle of computing average speed.

The computation of average speed is based on obtaining the detection interval accurately by correcting the preset interval for an integral number of encoder pulses. If the number of encoder pulses counted is m, for the detection interval T second, the average speed in rpm is given by

$$N_r = \frac{60\ m}{T\ M} \qquad (6.5)$$

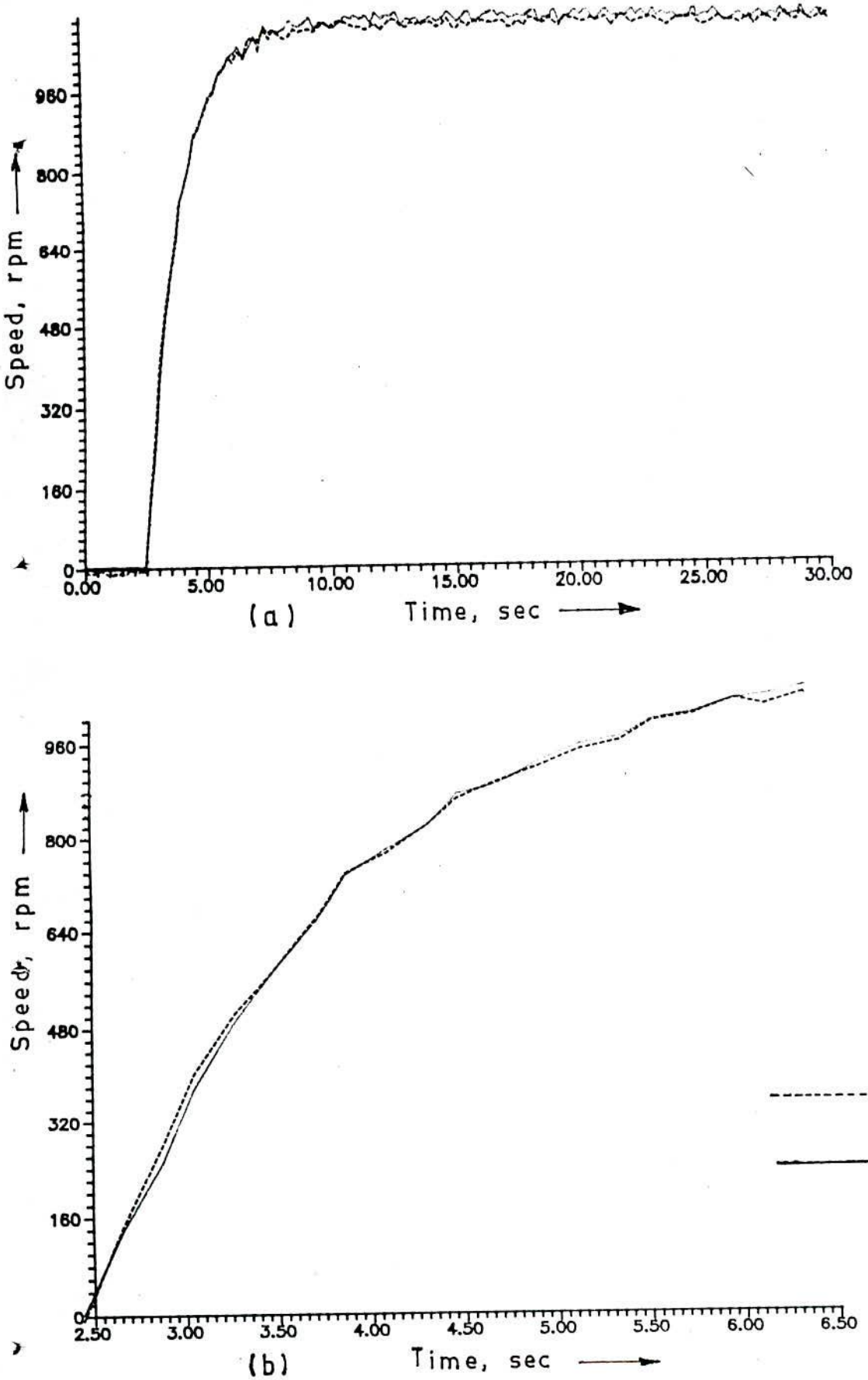

Fig. 6.7 Detection of instantaneous speed by the proposed scheme and comparison with the tachogenerator output
(a) Up to steady state speed (b) expanded plot of the accelerating period

A preset detection period T_p is made equal to the sum of a suitable number of firing intervals of the inverter thyristors. If f_c is the frequency of the counter clock (used for inverter firing control), the preset detection time T_p spanning k number of inverter thyristor gating intervals between the consecutive instants of speed detection is

$$T_p = \sum_{i=1}^{K} \Delta T_i = \frac{1}{f_c} \sum_{i=1}^{K} n_i \qquad (6.6)$$

where n_i is the number of counts corresponding to ΔT_i, the firing interval between two consecutive thyristors.

The difference between T_p and T is evident from Fig.6.8(a). The correction time ΔT_p should be added to T_p for accurate determination of T. This is implemented by testing the rising edge of the encoder pulse through digital port prior to detect the number of encoder pulses.

So, that

$$T = T_p + \Delta T_p \qquad (6.7)$$

The average speed N_r in (6.5) can be written as

$$N_r = \frac{60\ m\ f_c}{n\ M} \qquad (6.8)$$

where n is the total number of counter clock pulses over the period T.

6.4.2.2 Accuracy and range of measurement.

The resolution Q_n expressed in (6.4) indicates that the scheme is capable to compute detection time with a very small resolution. As the peripheral clock frequency is very high (2.38636MHz for the present

study), n is a large number and n^2 becomes very large if the detection time is of the order of some tens of milliseconds. The resolution is also controllable by adjusting the value of k. The error in the detection process depends on the missing of optical encoder pulses. The hardware is designed to generate the exact number of pulses, however, if one pulse is assumed to be missing, then percentage error in detected speed is expressed as:

$$e_p = \frac{1}{m} \cdot 100 \qquad (6.9)$$

Equation 6.9 indicates that the detection time should be increased to have a count of more number of encoder pulses to reduce the error. However, increased detection time is not allowable for a highly dynamic speed control system. For the present drive system, detection time is adjusted with speed of the motor and m varies within a narrow band (due to variation of slip speed) which is selected by choosing k. For a specific case, with k = 6, ω_{sl} = 0, and the optical encoder generating 360 pulses per revolution of the motor, Table 6.1 indicates the accuracy, resolution and other variables of interest.

Table 6.1

Speed N, rpm	T sec	m	e_p in %	n	Q_n	Qn/N
300	0.1	180	0.55	2.38636E+5	1.26E-4	4.19E-7
600	0.05	180	0.55	1.19318E+5	5.03E-4	8.38E-7
1200	0.025	180	0.55	5.96590E+4	0.020	1.67E-5
3000	0.01	180	0.55	2.38636E+4	0.126	4.20E-5

Since the detection interval is determined by inverter firing frequency

and in the preparation of Table 6.1, slip speed is assumed zero. It is seen that the number of encoder pulses and accuracy remain the same for all the speeds under study. Q_n is showing a tendency to increase with increase in speed. However, Q_n/N is a very small quantity and does not increase too much. The maximum detection time possible with 16-bit down counting is 0.165 sec (for k = 6) and the minimum speed to be measured is approximately 10 rpm.

6.4.2.3 Instantaneous speed estimation

It has been discussed in the previous sub-section that the sampling time is a vital factor for accurate detection of average speed. The indirectly field oriented controlled induction motor drive system requires instantaneous speed for effective operation. The difference between the average speed and instantaneous speed is illustrated in Fig.6.8(b), in which n_i stands for speed at $t=t_i$, and N_i average speed over the interval $T_i = (t_i - t_{i-1})$. In this subsection an approach is presented to estimate the instantaneous speed of the induction motor from average speed values.

Estimation of instantaneous speed from moving average speeds for an equi-sampling interval scheme has been developed and used by Saito et. al [101]. For the present case, estimation of speed is carried out by considering a linear variation of speed over two consecutive unequal intervals. Let this linear speed variation be represented by

$$n(t) = a\ t + b \qquad (6.10)$$

To estimate the speed $\hat{n}_i$ at any instant, it is necessary to find out the constants a and b from the moving average speeds. If the origin is

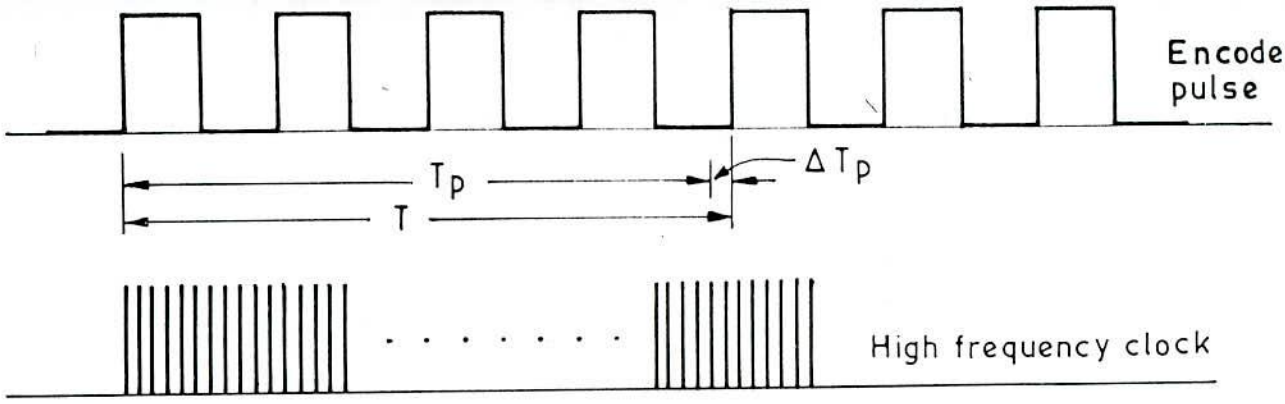

Fig.6.8(a) Adjustment of preset detection time for integral number of encoder pulses.

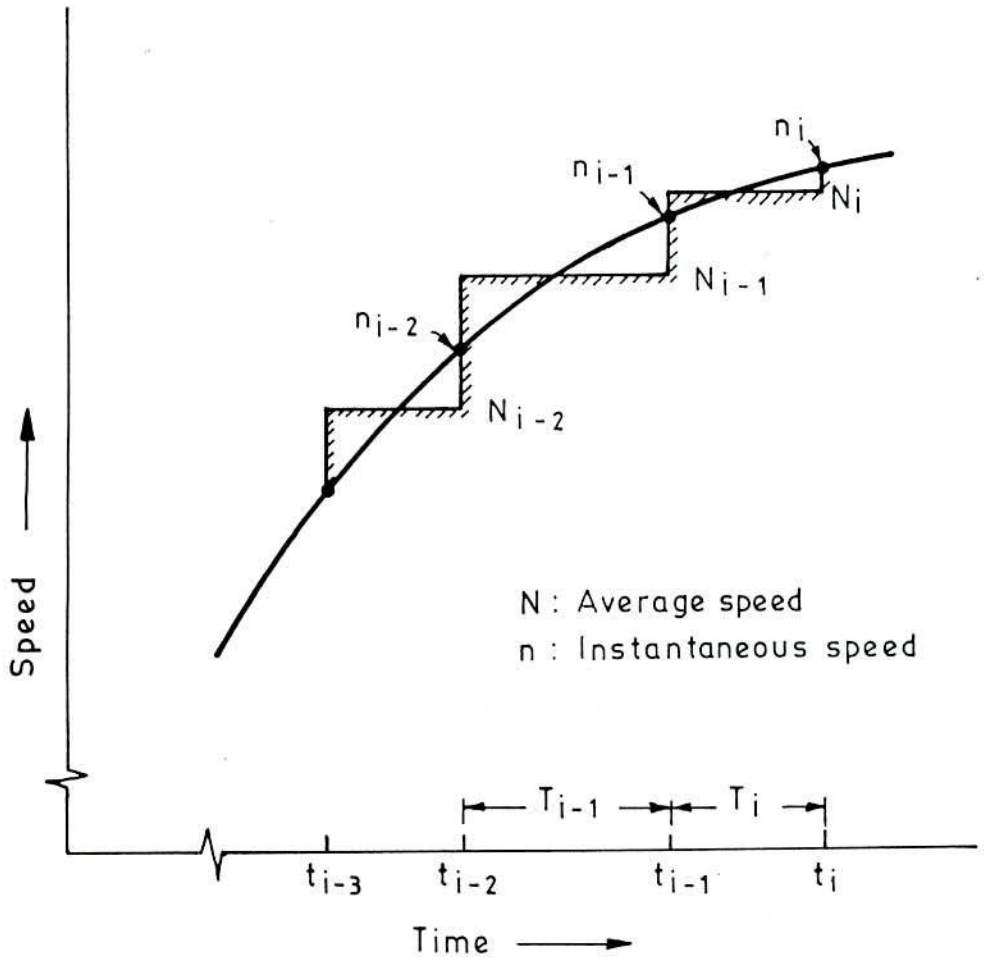

Fig.6.8(b) An arbitrary speed profile showing average and instantaneous speeds.

shifted at $t = t_{i-1}$ (Fig. 6.8(b)) the average speeds for the intervals T_i and T_{i-1} are given by

$$N_i = \frac{1}{T_i} \int_0^{T_i} (a\ t + b)\ dt = \frac{1}{2}\ a\ T_i + b \qquad (6.11)$$

$$N_{i-1} = \frac{1}{T_{i-1}} \int_{-T_{i-1}}^{0} (a\ t + b)\ dt = -\frac{1}{2}\ a\ T_{i-1} + b \qquad (6.12)$$

Determining the coefficients a and b from (6.11) and (6.12) the estimated instantaneous speed at the t_i-th instant is written as

$$\hat{n}_i = a\ T_i + b = N_i + (N_i - N_{i-1}) * \frac{T_i}{T_i + T_{i-1}} \qquad (6.13)$$

6.4.2.4 Hardware description

The accuracy of detected speed depends on the number of encoder pulses generated per revolution. To have large number of pulses, the encoder disc is provided with 360 equi-spaced holes arranged circumferentially in four rows as shown in Fig.6.9(a). The encoder is equipped with infrared LEDs for both emitting and detecting purposes. The circuit arrangement for pulse generation and subsequent shaping is shown in Fig.6.9(b). The output of the LED detector is applied to pins 2 and 6 of 555-timer that compares the levels (1/3 V_{cc} and 2/3 V_{cc}) and generates rectangular waves. After reducing their widths the four signals are ORed and then passed through a monostable to have well conditioned pulse trains. The encoder pulses are finally applied to the clock # 0 of programmable interval timer 8253.

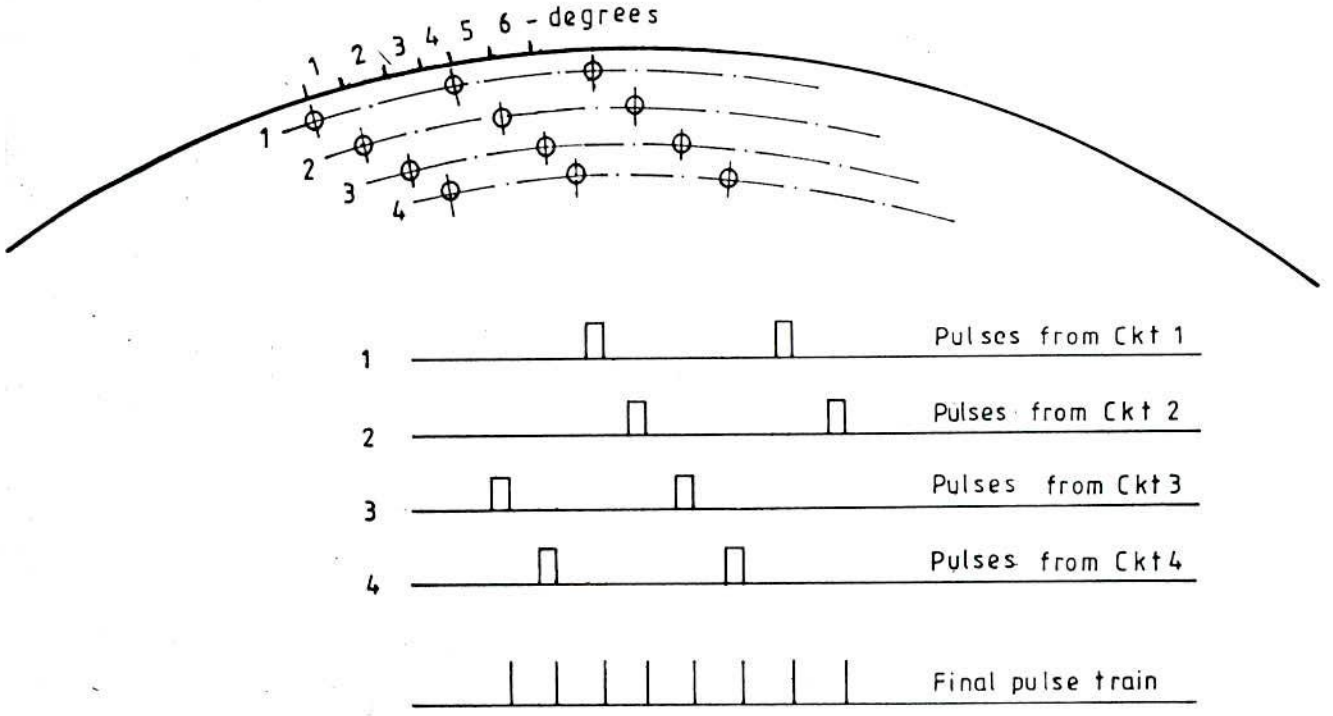

Fig. 6.9(a) Optical encoder and pulses.

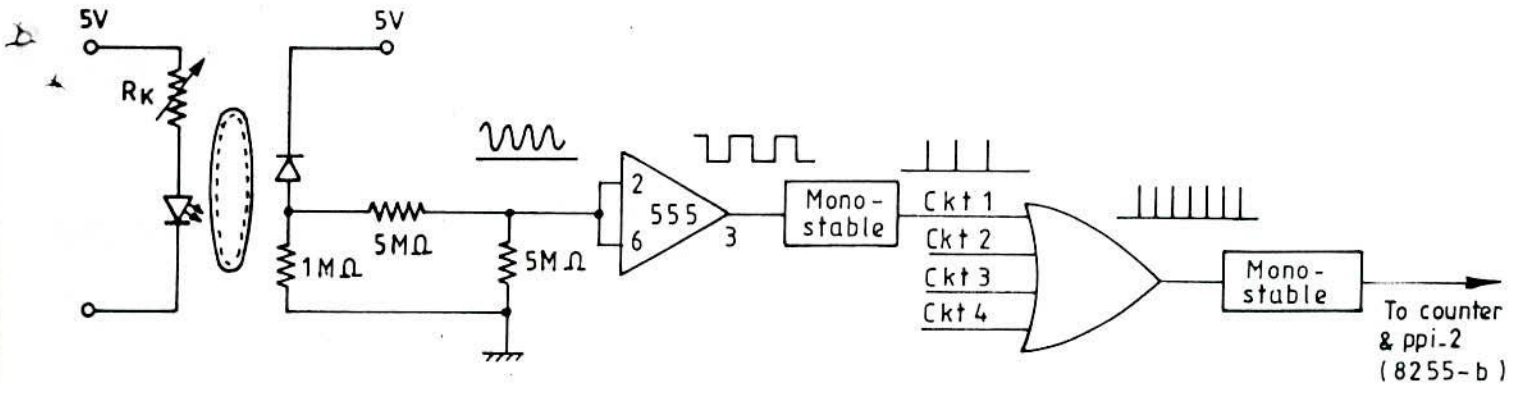

Fig. 6.9(b) Pulse generation circuit for 4-channel encoder disc - scheme 2.

6.4.2.5 Software Description

The counters 0 and 2 of the on board programmable interval timer 8253 are operated in mode 3 for counting encoder pulses and for incorporating delay between the firing instants of two consecutive thyristors. Counter 0 is clocked by the encoder pulse while counter 2 is clocked by pclk of 2.38636MHz. Since in mode 3 the counter register decreases by 2 for each clock pulse, the average speed in (6,8) for 360 pulses per rotation of the encoder disc is modified as

$$N_r = \frac{60\ m/2\ f_c}{360\ n/2} = \frac{m\ f_c}{6\ n} = \frac{m}{6}\ \frac{1}{T} \qquad (6.14)$$

The correction time ΔT_p is obtained from the difference of the counts (Present Value - Previous Value) by which the microprocessor waits in a loop and then converts it to time as :

$$\Delta T_p = (Count_i - Count_{i-1})\ \frac{\text{no. of clock pulses in the loop}}{\mu p.\ \text{clock frequency}} \qquad .....(6.15)$$

The initialization for this case is done in the main program in Sec. 6.7 though presented in the flow-chart diagram of Fig. 6.10 for convenience.

Flow diagram in Fig. 6.10 presents the sequence of computation for the proposed speed measurement scheme. Counter 2 is loaded at each instant of inverter thyristor firing and the counter loading is used to compute the incremental time for each step. All the computations are done in floating point by the math-co-processor i-8087. The correction time is sensed by testing the encoder pulse through a ppi 8255 port.

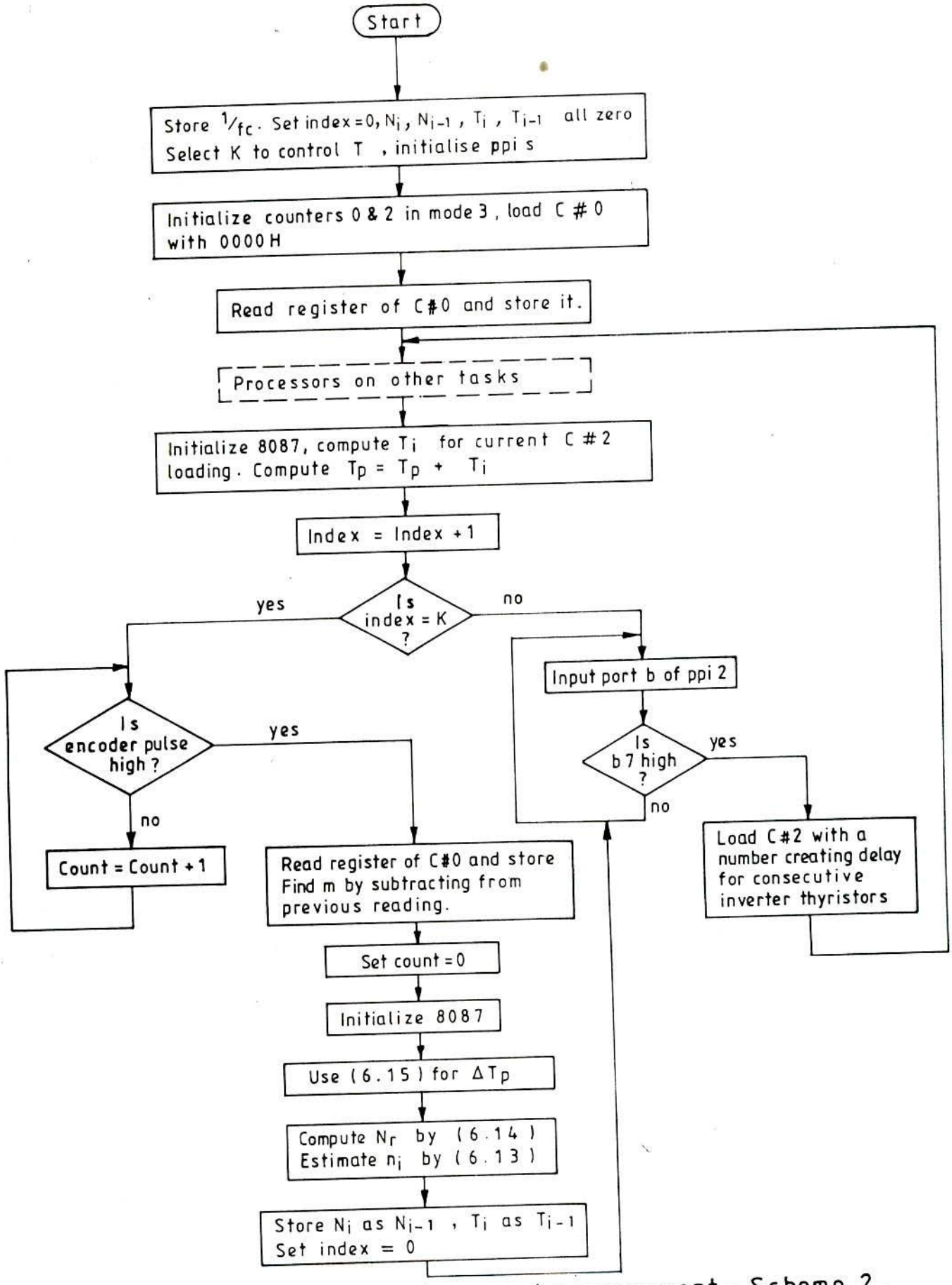

Fig.6.10 Computational sequence for speed measurement - Scheme 2.

6.4.2.6 Experimental verification of the scheme

The proposed scheme was first tested for accuracy under steady state operating condition for different values of speed ranging from 300 rpm to 1500 rpm. A close agreement with the readings of a calibrated tachometer was observed. To confirm the usefulness of the method to measure the instantaneous speed the speed rise of a dc motor given by the proposed method is shown in Fig.6.11. The difference between the detected average and estimated instantaneous values is evident from Fig.6.11(b).

6.5 ISOLATION AND SIGNAL CONDITIONING CIRCUITS

In a controlled drive system certain variables from the power circuit need to be transduced to decide on the controlling variables. Owing to non-availability of common signal ground and difference in voltage levels, the signals are processed through isolating devices with linear reproduction characteristics. The transduced signals are duly conditioned for compatibility with controllers, data acquisition systems, etc. and also of proper level for good resolution.

Hardware schematic of the drive system in Fig.6.3 requires sensing of the followings besides the speed.

1) The level of dc link current,

2) the level of inverter side link voltage and

3) the rms value of the machine phase voltage (fundamental component).

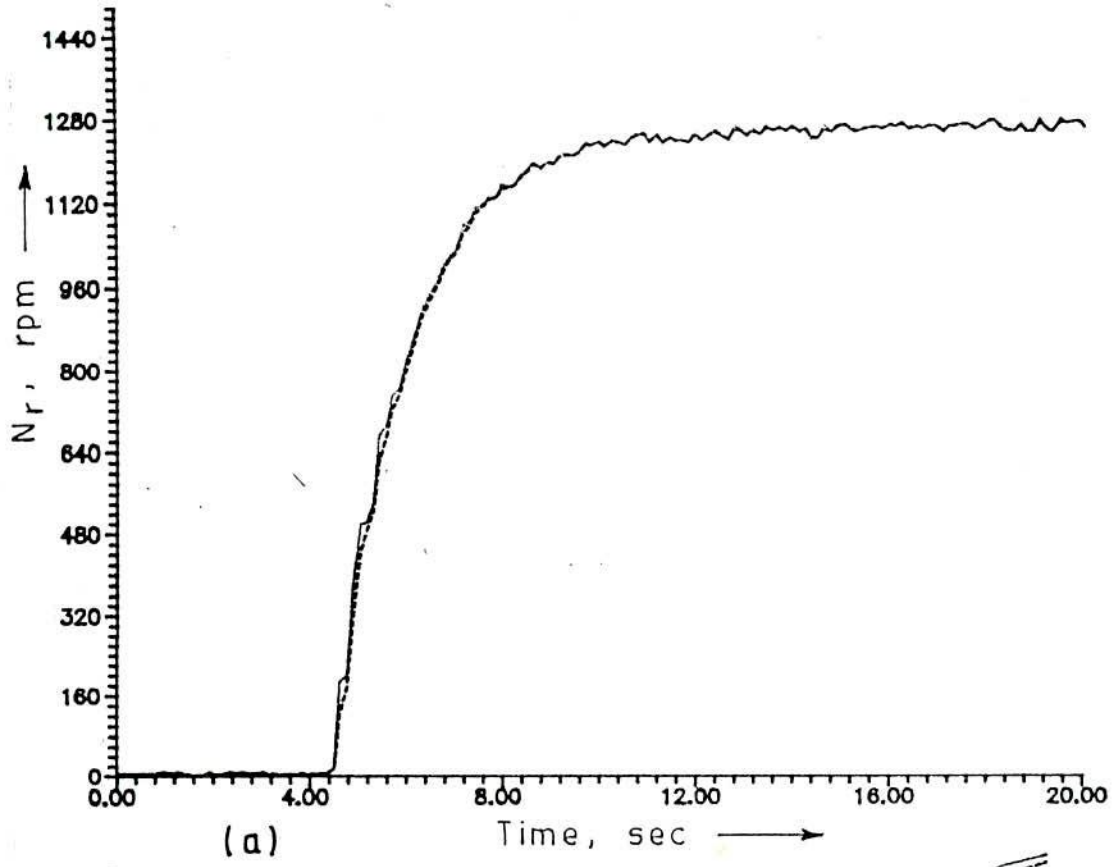

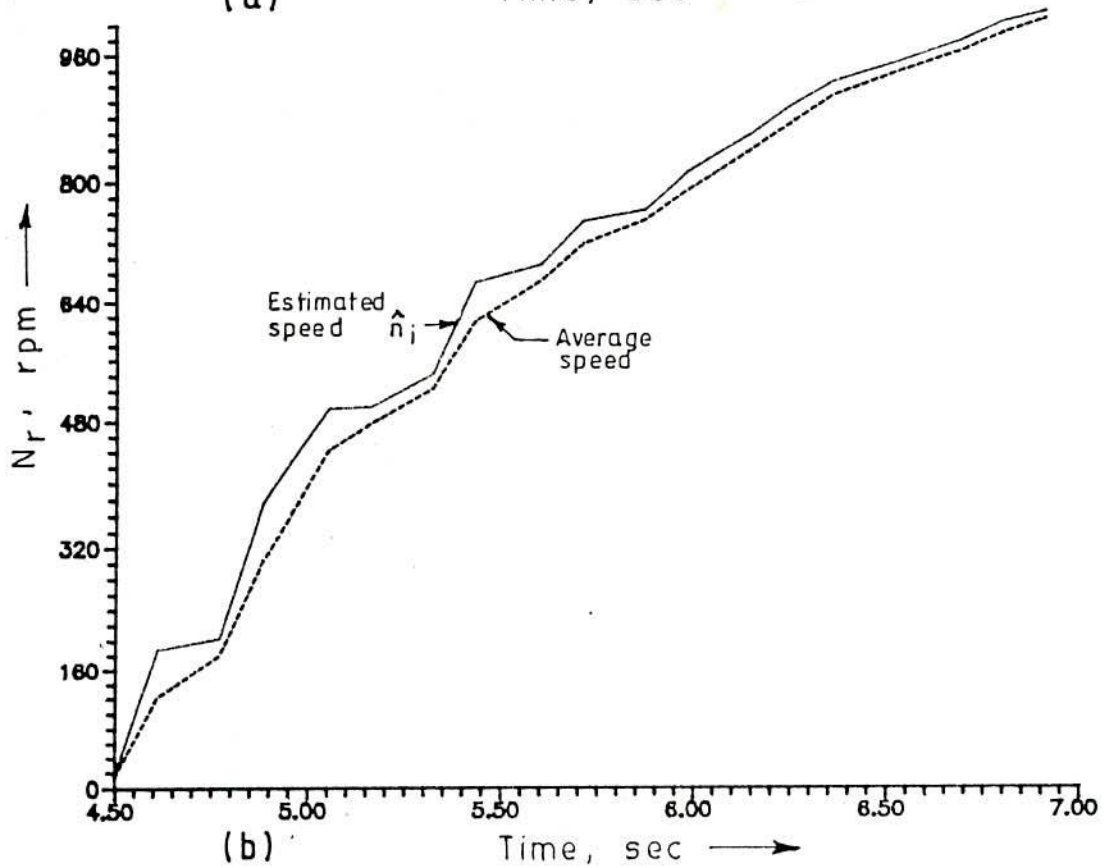

Fig. 6.11 Detected average and estimated instantaneous speed of start up condition of a d. c. motor (a) speed detection curve upto steady state (b) expanded

Corresponding to maximum variation of these signals, the maximum excursion of the output from signal conditioning circuit should equal to or lie within ±5V. The following sub-sections present in brief, the signal sensing and conditioning circuits.

6.5.1 DC link current sensing

Fig.6.12(a) presents the circuit to obtain a signal proportional to dc link current over the wide working current range. The voltage output from the CTs and the rectifier combination on the input side of the converter is filtered to eliminate the high frequency components. The cut-off frequency of the low pass filter (LPF) is chosen 10 Hz. Considering the setting of the ADC module PCL 207 and the size of the drive system, the output of the LPF was adjusted to 5 volts for 15A.

6.5.2 DC Link voltage sensing circuit

Sensing circuit for the dc link voltage consists of a differential amplifier with high input impedances and a low pass filter (LPF) as shown in Fig.6.12(b). The resistors for the differential amplifier(μA 741 based) are selected for balanced operation, so that the output of the differential amplifier V_{od} is defined by the gain expressed as

$$A_d = \frac{V_{od}}{V_I} = \frac{R_3}{R_1} = \frac{R_4}{R_2} \qquad (6.16)$$

The second order LPF with 10 Hz cut off, follows the design of the Butterworth filter.

6.5.3 Line voltage sensing circuit

The measuring circuit for obtaining the rms value of the

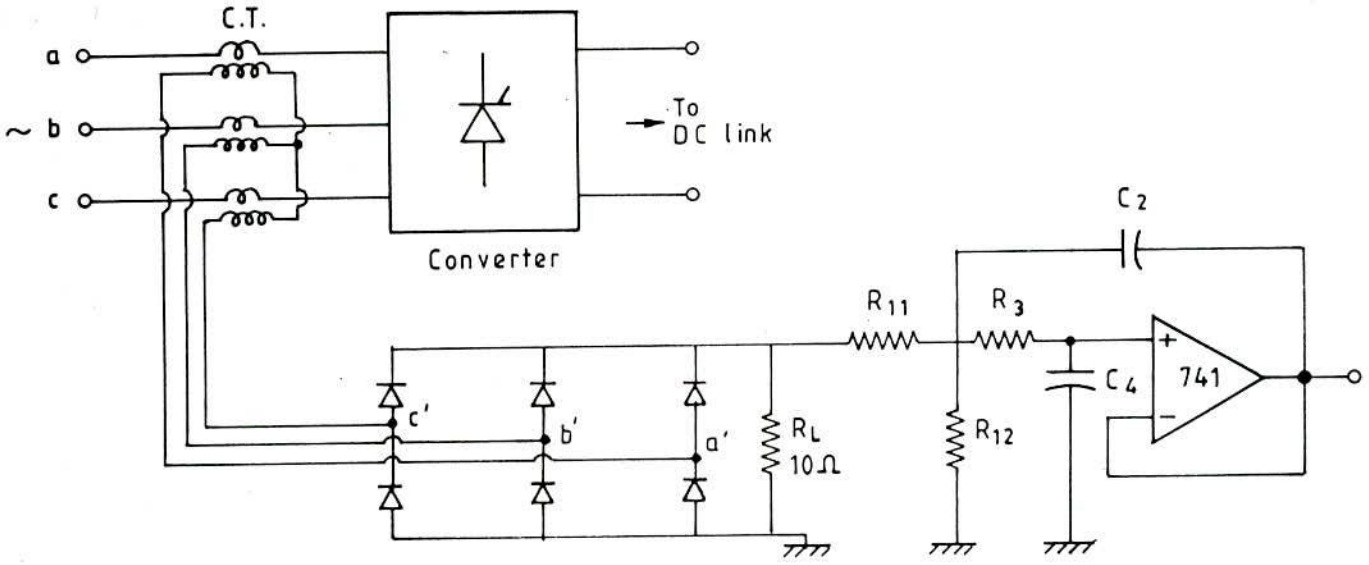

$R_{11} = R_{12} = 660\ K\Omega$, $R_3 = 1.1115 \times 10^7\ \Omega$

$C_2 = 0.069\ \mu F$, $C_4 = 0.001\ \mu F$

Fig.6.12(a) Signal conditioning circuit for DC link current sensing.

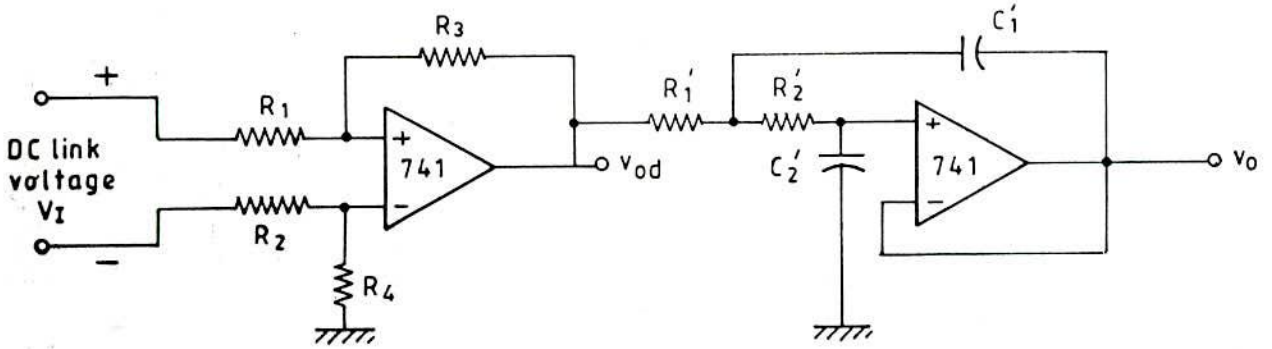

Differential amplifier

$R_1 = R_2 = 9.4\ M\Omega$

$R_3 = R_4 = 192\ K\Omega$

Low power filter

$R_1' = 480\ K\Omega$ $R_2' = 480\ K\Omega$

$C_1' = 0.047\ \mu F$ $C_2' = 0.0235\ \mu F$

Fig.6.12(b) Signal conditioning circuit for D.C. link voltage sensing.

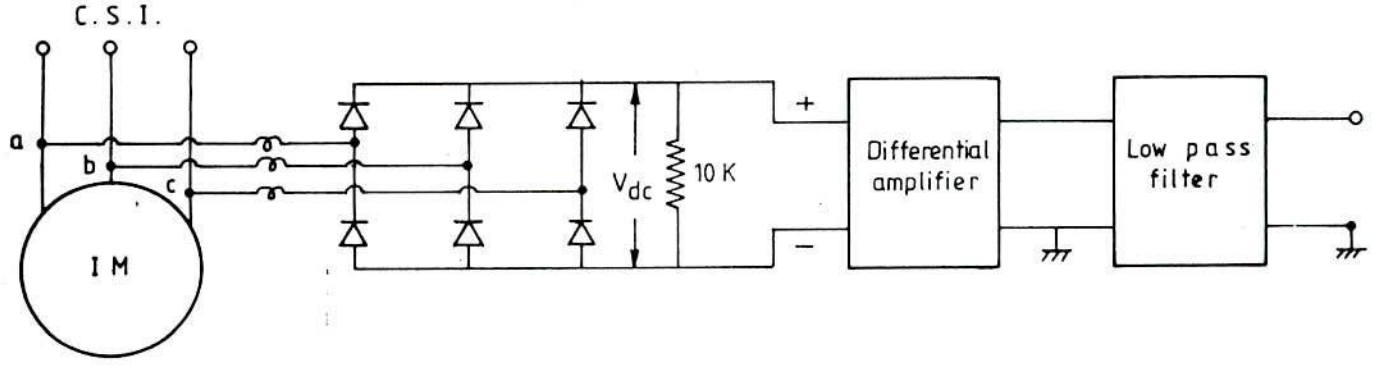

Fig.6.12(c) Signal conditioning circuit for sensing line voltage.

fundamental component of the machine terminal voltage is shown in Fig.6.12(c). The rms line voltage (fundamental component) is related to rectifier output voltage by

$$V_{L-L} = \frac{V_{dc}}{1.35} \qquad (6.17)$$

Differential amplifier and LPF represented by the blocks in the figure follow the same circuit configuration and design as in Fig.6.12(b). Small inductor between the rectifier and machine terminals are to reduce the effect of spikes.

6.6 CONVERTER FIRING CONTROL

Fully controlled thyristorized bridge converter is utilized for controlling the dc link current. For linear relationship between the control signal and the converter output voltage, cosine law firing scheme is used [28]. Fig.6.13 presents the gate triggering circuit for thyristor 1 (Th_1). The gate triggering circuit configurations for other thyristors are similar. The flow chart for the converter control software is shown in Fig.6.14. Computations are done on NDP 8087 in real format for a selected value of magnetizing component of stator current i^*_{ds}. Speed errors $e_\omega(n)$ and $e_\omega(n-1)$ (Ref.Fig.2.7) are used to compute the command value of i^*_{qs}, the torque component of stator current, and current errors $e_i(n)$ and $e_i(n-1)$ to compute control voltage C_V for converter firing. The variable i^*_{qs} is not allowed to go beyond a preset (maximum) value depending on drive rating. Similarly, the signal C_V is limited to the value less than the maximum value of the cosine wave.

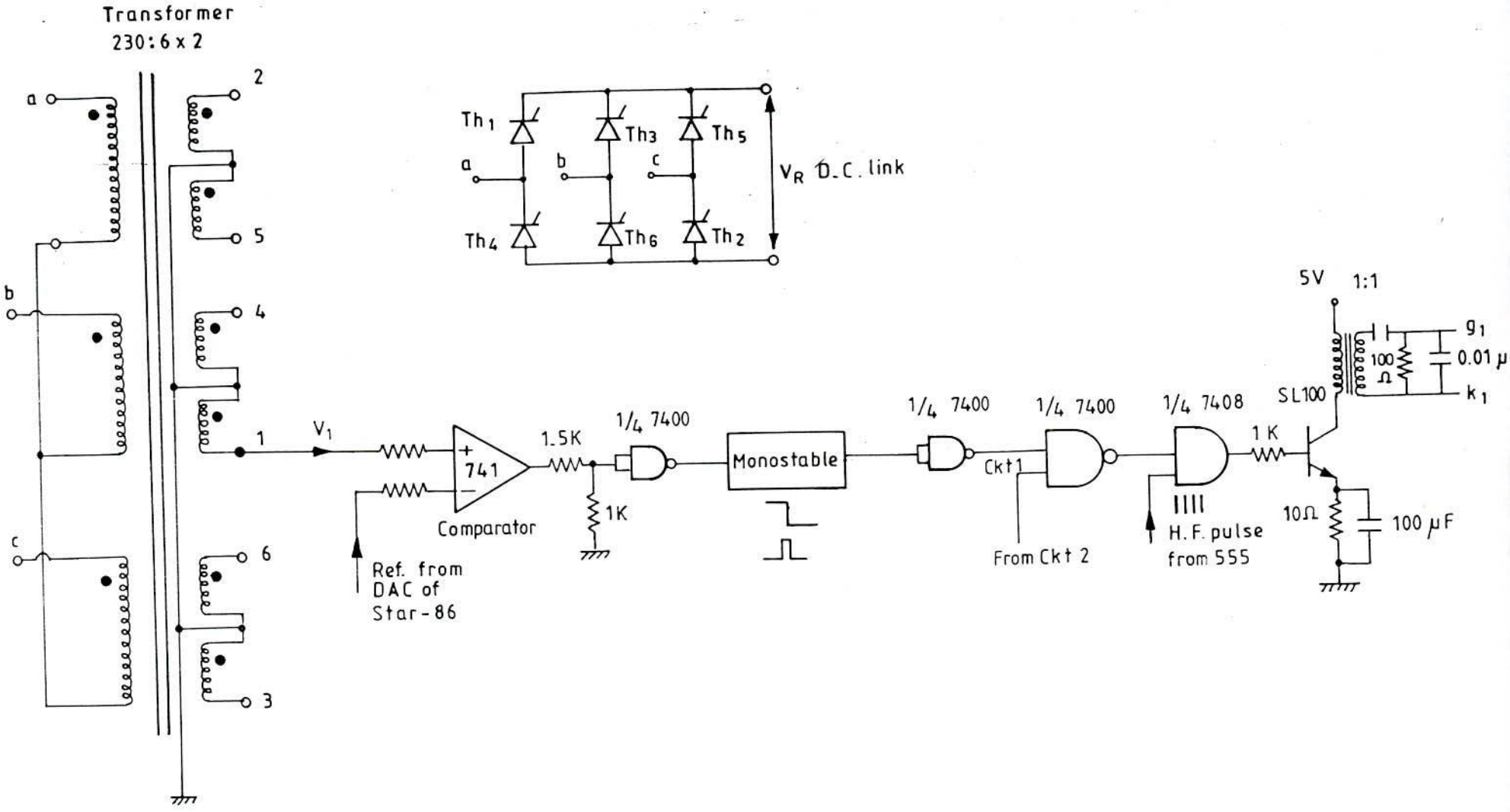

Fig. 6.13 Cosine law firing control and converter thyristor gate pulse generating circuit .

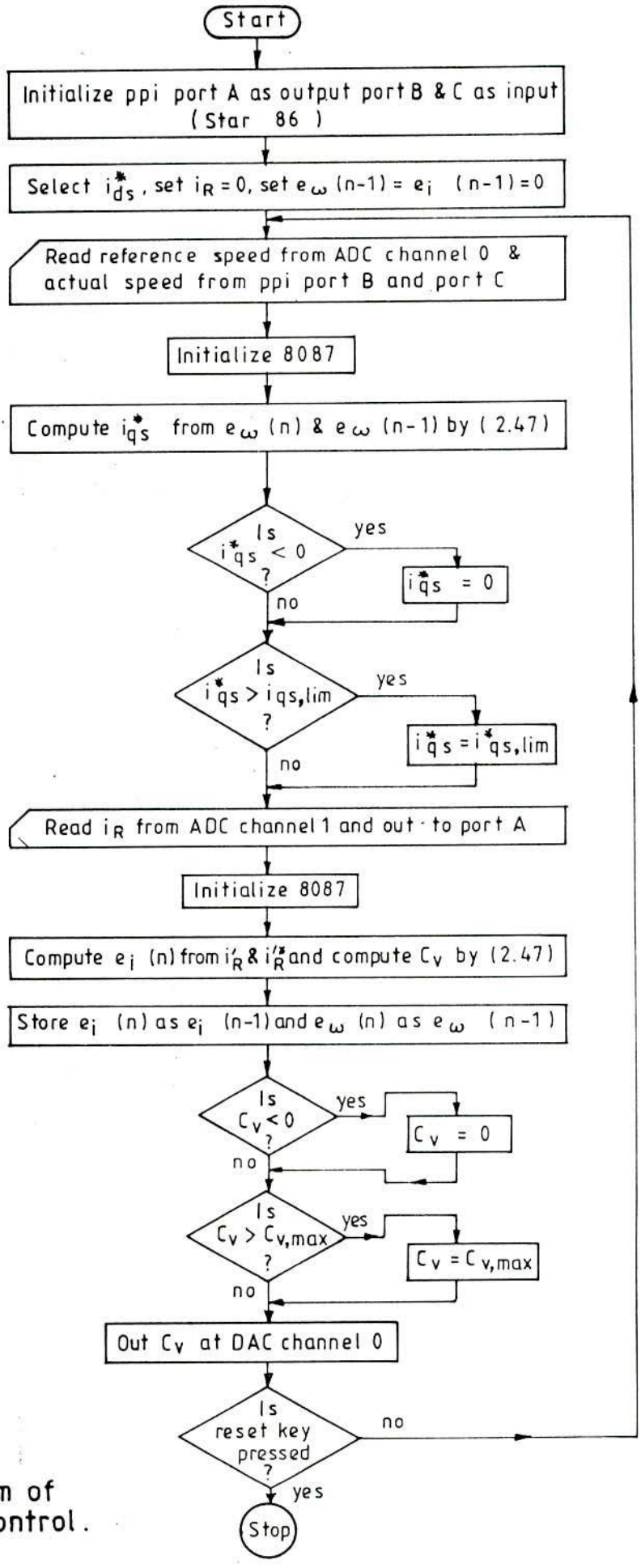

Fig. 6.14
Flow diagram of converter control.

6.7 CURRENT SOURCE INVERTER (CSI) FIRING CONTROL

The six thyristors of the CSI shown in Fig.6.15(a) are triggered in the sequence of Th_1, Th_2 ..., Th_5, Th_6, Th_1,... . Gate triggering interval for two consecutive thyristors is computed and firing instants are controlled by microcomputer MF 8679, as shown in Fig.6.3 with the help of counter 2 of programmable interval timer 8253 (initialized in mode 3). The firing control logic generated by the output of C#2 of 8253 along with the gating pattern of the inverter thyristors is shown in Fig.6.15(b). Pulse generation in sequence is done by shift register. The shift register controls six bit binary pattern according to the input signal pulses and at the falling edge of the signal out of timer, the pattern is changed as shown in Fig.6.15(c). Circuit for triggering pulse generation is shown in Fig.6.15(d). In the experimental set up, task required of the shift register was accomplished through μp 8085 cpu in conjunction with PPi-8255.

It is indicated above that appropriate loading of a counter (C#2) of 8253 initialized in mode 3, controls the firing instants of the inverter thyristors, this is achieved through the microcomputer MF 8679 with the following modules (Fig.6.16).

1) Modulo_slip : for computation of ω_{sl}
2) Modulo_ $\frac{d\theta}{dt}$: for computation of $\frac{d\theta}{dt}$
3) Modulo_ speed : for computation of instantaneous speed.
4) Modulo_invf. : for computing delay in terms of binary number in inverter firing.

Two speed detecting schemes have been discussed in section 6.4

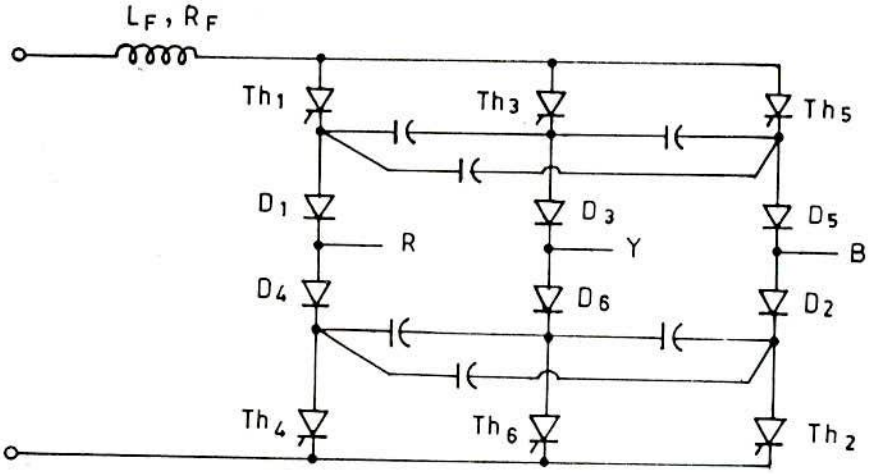

(a)

b_0 - Th_1	1	0	0	0	0	1	1	0	0	0
b_1 - Th_2	1	1	0	0	0	0	1	1	0	0
b_2 - Th_3	0	1	1	0	0	0	0	1	1	0
b_3 - Th_4	0	0	1	1	0	0	0	0	1	1
b_4 - Th_5	0	0	0	1	1	0	0	0	0	1
b_5 - Th_6	0	0	0	0	1	1	0	0	0	0

(b)

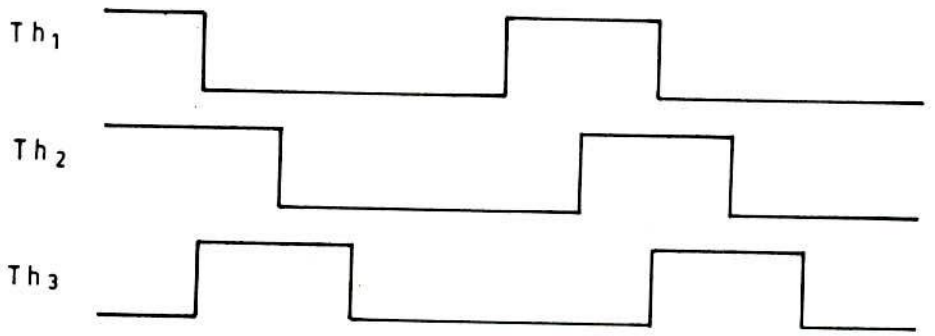

(c)

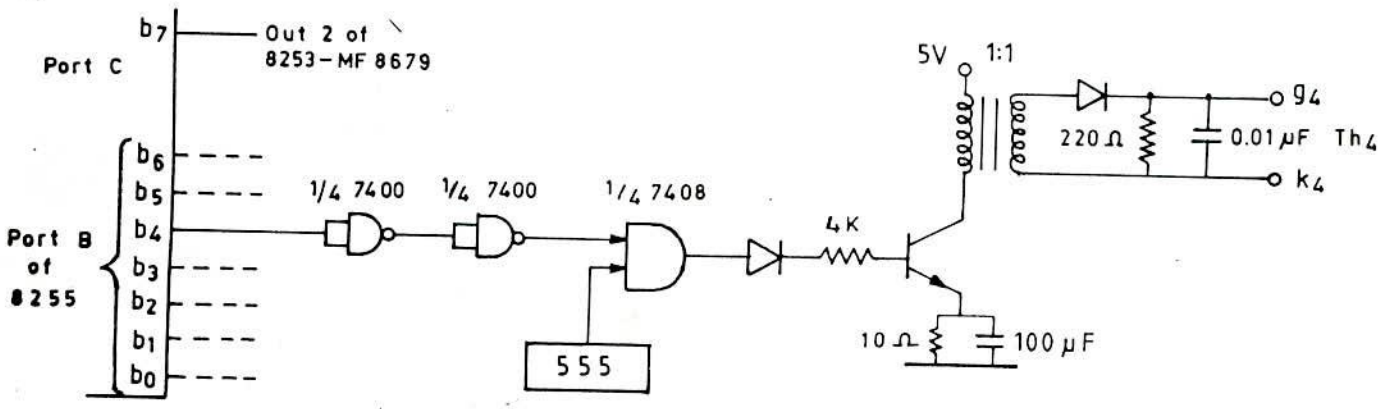

(d)

Fig. 6.15 (a) Inverter power circuit, (b) Binary gating pattern, (c) gating sequence, (d) trigger pulse

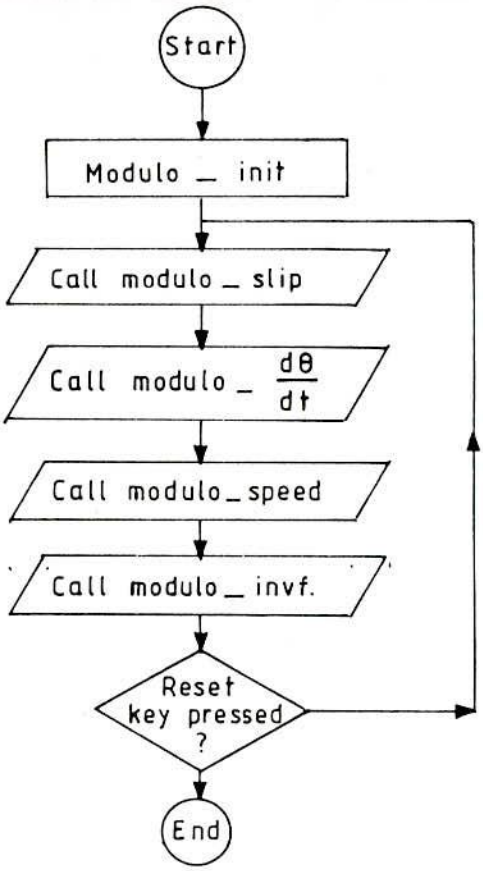

Fig.6.16(a) Flow chart for the main program for inverter firing

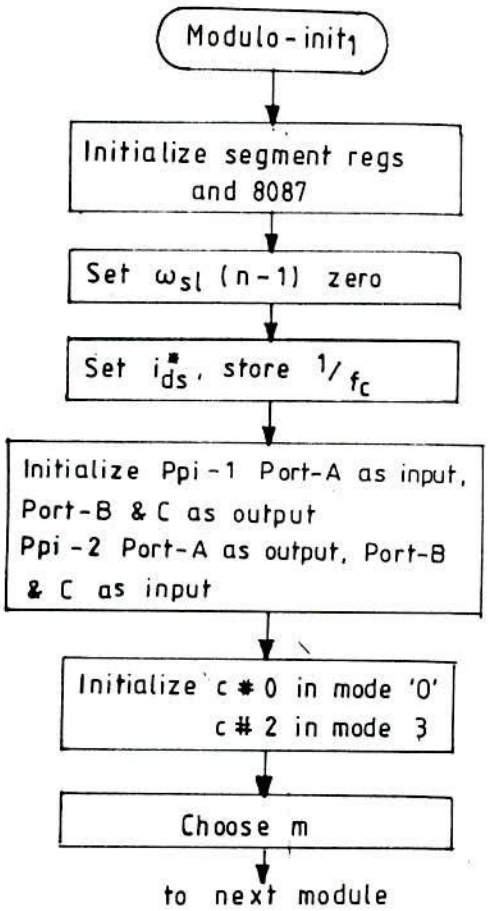

Fig. 6.16(b) Initialize for speed measurement scheme-1

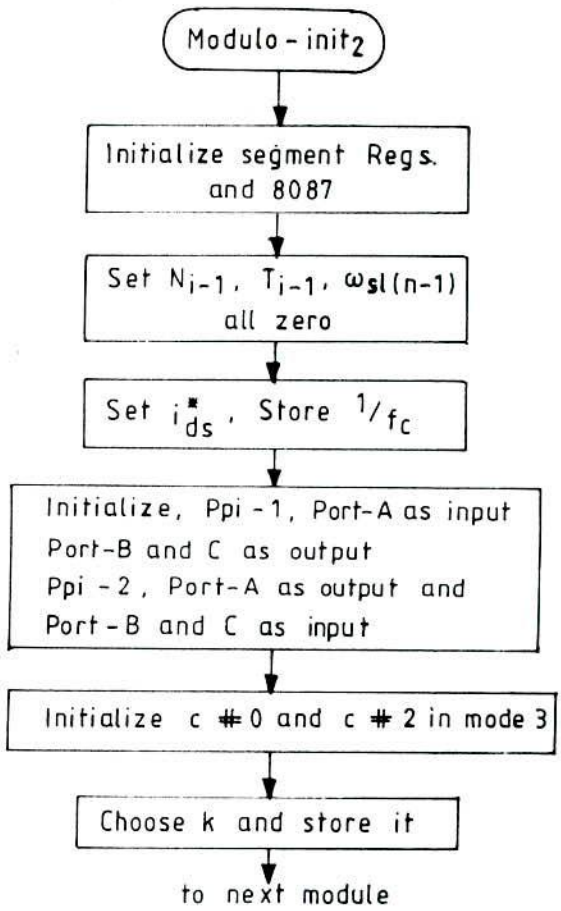

Fig. 6.16(c) Initialize for speed measurei scheme-2

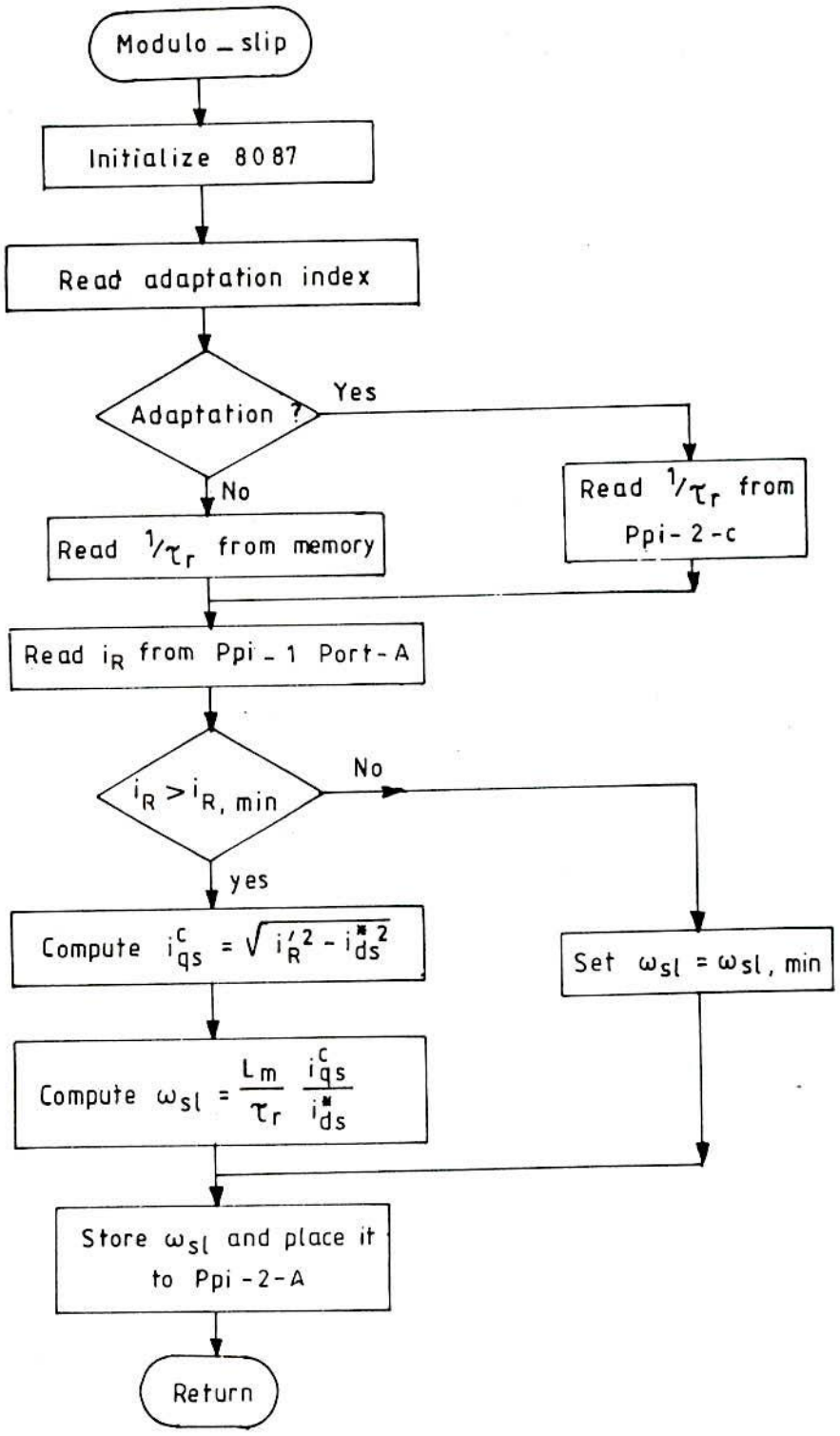

Fig. 6.16(d) Module for computation of slip speed

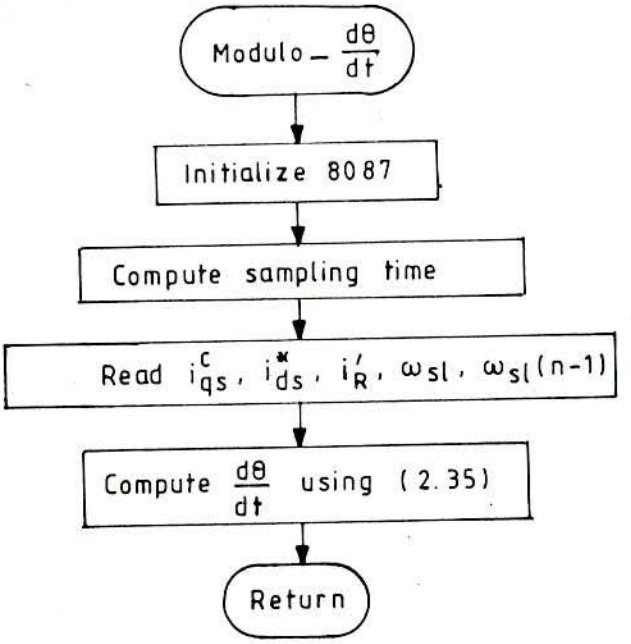

Fig. 6.16 (e) Module for computation of $\frac{d\theta}{dt}$

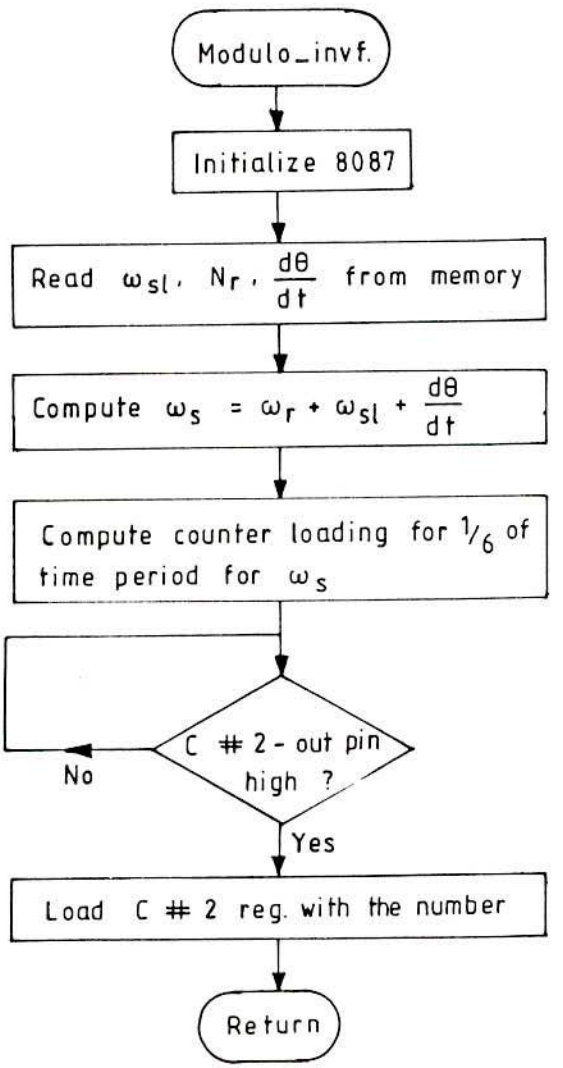

Fig. 6.16 (f) Module for inverter firing delay implementation

which requires initialization routines differing slightly for the two drive systems and a minor modification in the main program of flow chart 6.16(a), where the speed calculating routine is called after a definite number of intervals (k = 6 here). The initialization modules are represented in Figs.6.16(b) and 6.16(c). The computation of ω_{sl} follows the sequence (Fig.6.16(d)), which requires alteration for adaptive and non-adaptive implementation of the scheme. A preset index determines through a logical statement, the selection of adaptive or non-adaptive control algorithm. To guard against the situation (e.g. during starting period or transient state) of i_R' becoming less than i_{ds}^* a minimum value of slip is preserved in the feed forward path as a measure to avoid saturation.

The computational sequence for $d\theta/dt$ shown in Fig.6.16(e) is based on eqn. 2.35 under chapter II. Limitations on both the sides for the variable is provided in the software (not shown in the flow-diagram) to guard against highly changing conditions. The module invf in Fig.6.16(f) computes the inverter firing frequency. The computed value of inverter frequency is converted into an appropriate binary number (corresponding to 1/6th of the time period) for loading into the register of counter 2. The counter register is released with the new delay every time at high level of signal from the pin out 2 of 8253.

6.8 DATA ACQUISITION, PARAMETER ESTIMATION AND TUNING

It has been mentioned in Sec.6.3.3 that PC/AT with Burr Brown's PCI 20000 system is used for data acquisition and subsequent processing. All the channels of A/D module are configured for unipolar

operation for which the absolute resolution of a detected variable x is expressed as:

$$\frac{Q_x}{x} = \frac{1}{2^{12}} = \frac{1}{4096} \qquad (6.18)$$

Exact value of ω_{sl} at any instant is obtained directly through digital port (b_0-b_7) of the microcomputer MF8679 and all other variables are acquired in the PC/AT through A/D converters.

The software implementation of the proposed parameter compensation techniques is written in Turbo Pascal. The complete software consists of a number of modules which can easily be selected for any one of the following operational modes.

For observation of steady state and transient performances:

Mode 1 : Data acquisition and storage.

Data acquisition and tuning based on:

Mode 2 : Estimation of R_r using air-gap power.

Mode 3 : Adaptation of R_r using dc link voltage.

Mode 4 : Adaptation of R_r using torque component of stator current.

The programs under the modes 2, 3, and 4 are based on the methodologies detailed under sections 4.2, 4.3.1 and 4.3.2 of ChapterIV respectively. In mode 2, average value of rotor resistance from a set of consecutive estimated values is applied to the slip calculator. This is to reduce the effects of external noise and measurement error.

6.9 CONTROL SCHEME IMPLEMENTATION AND TEST RESULTS

In order to study the viability of the control schemes formulated

in the previous chapters, the microprocessor-based controllers implementing the indirect field orientation algorithms were applied to two laboratory type induction motors. They were 3.75 kw squirrel cage (machine I) and 0.75 kw slip ring (machine II) induction motors whose nominal parameters are furnished in Appendix I. The load to the induction motors was chosen to be separately excited dc generator supplying an adjustable resistive load. An X-Y plotter was interfaced with the PC/AT for obtaining various plots. The closed loop dynamic responses of the drive systems were studied under the following conditions.

a. Starting of the system from stand still condition.

b. Step change in speed at constant torque

c. Step change in torque at constant speed.

In all these studies i_{ds}^{*} for the 3.75 kw machine (squirrel cage) was set at 5.85A, while for the 0.75 kw machine (SR) was set at 3.85A.

Besides the above, experiments were also conducted to verify the feasibility of the rotor resistance estimation/adaptation schemes and study certain steady state performances. The following sections present some of the experimental observations.

6.9.1 Start up from rest

The induction motors were started with load through the software control of the drive system. Prior to start, rated ac voltage was applied to the converter and the field current of the coupled dc generator was set at a particular value while the armature was

connected to a specific resistive load. Such a loading condition made the load torque on the induction motor assume closely the following form [102] (neglecting the effect of dc machine armature inductance)

$$T_L = K_L N + T_f \qquad (6.19)$$

where

K_L : a constant defined by the emf constant of the generator at the specific field excitation and armature and load resistances

N : speed in rpm.

T_f : frictional torque

Computer plots in Figs. 6.17 and 6.18, through data acquisition show the speed and two current values as a function of time for motor-I and II respectively when they were accelerated from rest to set speeds (step response for set speed from rest) with torque load given by (6.19). Set speeds for machines I and II were 825 and 975 rpm respectively. During the start up process parameter adaptive algorithms were kept inoperative (run being of short duration) for both the machines. Speed profiles in Figs.6.17(a) and 6.18(a) reveal quite fast response of the machines to reach their set speeds. Current overshoot, particularly, in respect of torque producing component, occurs when the load torque is found to be well below the rated torque output. This is evidenced in Fig.6.17(c) but not in Fig.6.18(c).

Figs in PL-1 and PL-2 present the oscillographic records of the plots given in Figs.6.17(a&c) and 6.18(a&c) respectively. Oscillographic record in Fig. PL-3 shows the speed and dc link current for the machine 2 corresponding to plots in Fig.6.18(a&b). For the same

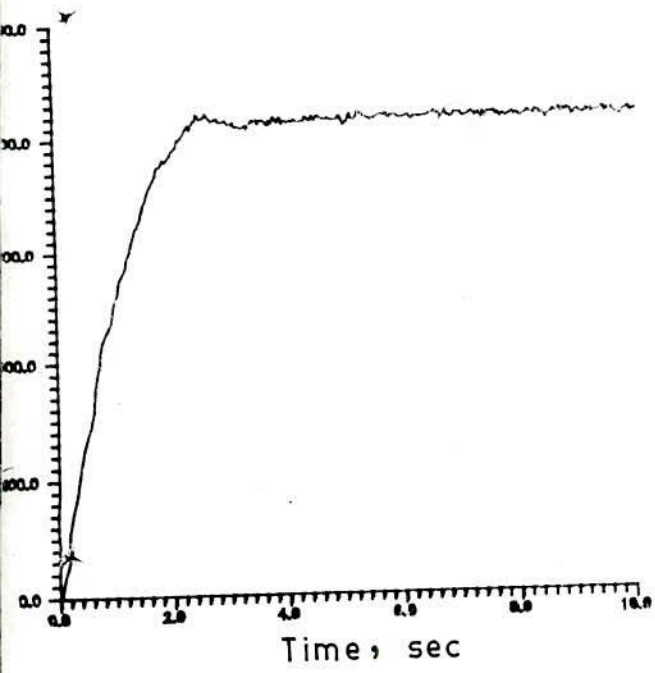

(a)

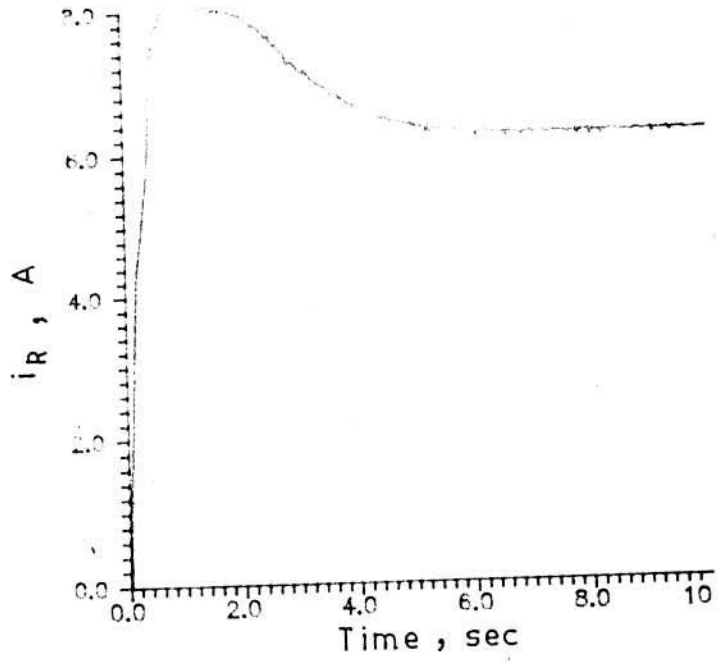

(b)

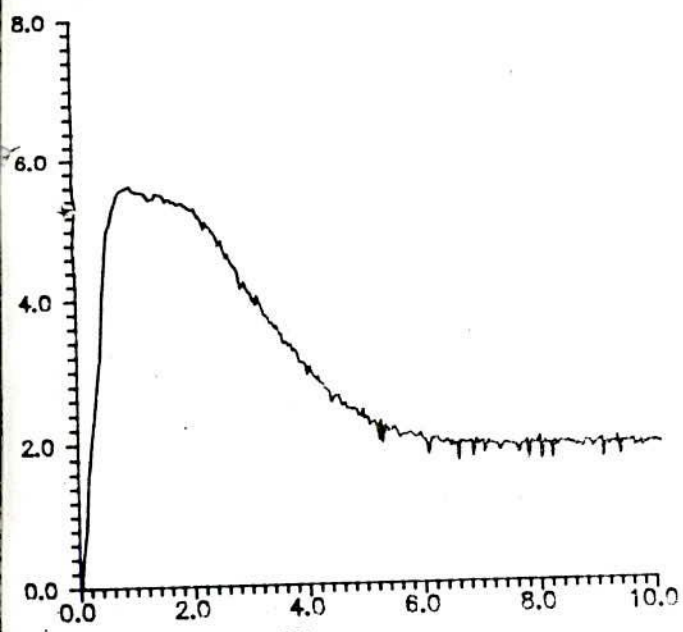

(c)

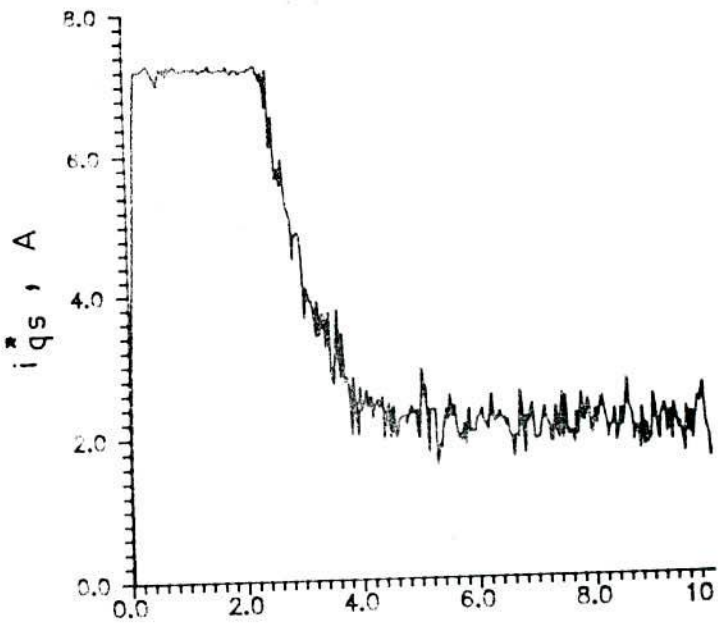

(d)

g. 6.17 Test results : start-up response for 825 rpm of the drive system in Fig. 2.7 with machine-I (a) speed, (b) i_R, (c) i^c_{qs} and (d) i^*_{qs}. (Torque load : $T_L = 2.5 + 0.025\ \omega_m$ Nm)

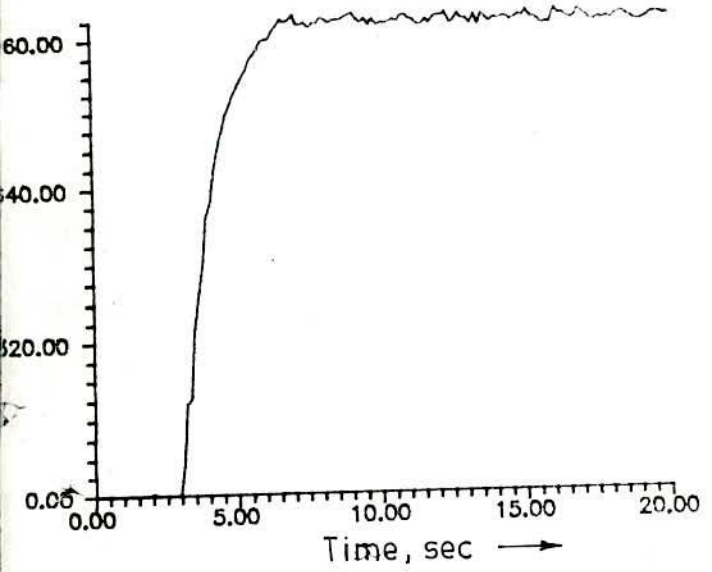

(a)

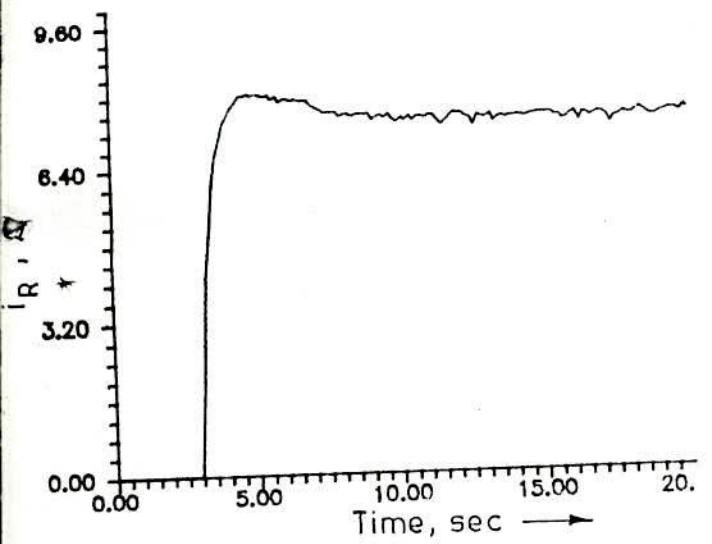

(b)

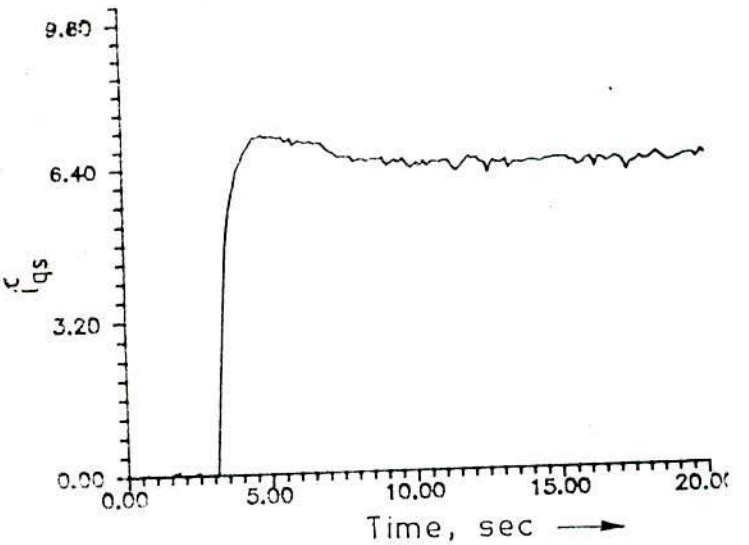

(c)

Fig. 6.18 Test results : Start up response of the drive system from machine II (WR type), (a) speed (b) d.c. link current (c) i^c_{qs}, with torque load $T_L = 0.4 + 0.05\ \omega_m$ Nm ; set speed = 975 rpm; set flux = 0.298 wb

Fig. PL-1 : Oscillographic record for starting condition of machine I

Fig. PL-2 : Oscillographic record for starting condition of machine II

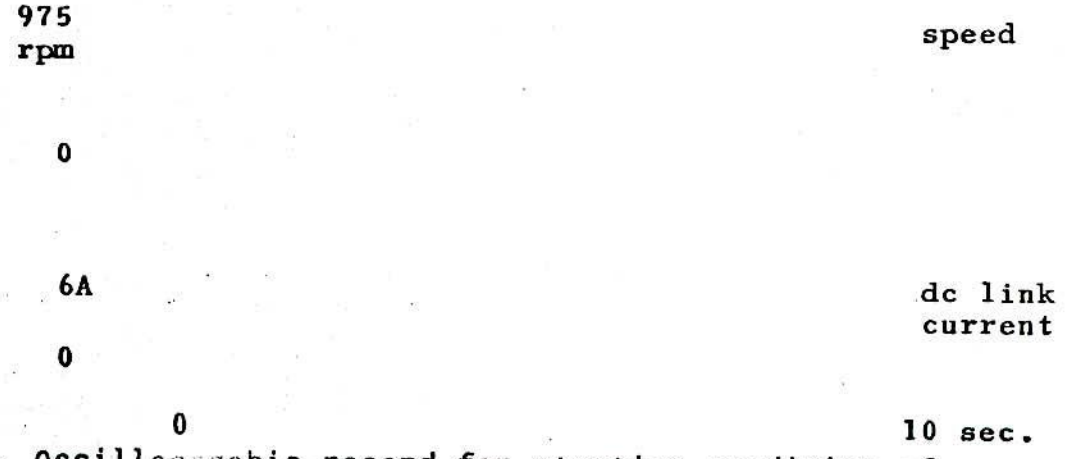

Fig. PL-3 : Oscillographic record for starting condition of machine III

starting conditions, digital simulation results for machines I and II are shown in Figs.6.19 and 6.20 respectively.

Though not an exact agreement, an overall correspondence between the recorded test results in Figs.6.17 and 6.18 with the corresponding simulation studies in Figs.6.19 and 6.20 (a,d,f) respectively indirectly indicate the working of the implemented drive system in the field-oriented condition. The discrepancies can be attributed to assumed load characteristics given by (6.19), measurement noise, neglecting harmonics and assumptions in the saturation model.

6.9.2 Step change in speeds

The observed dynamic response of the drive system with machine I to step change in reference speed from 400 to 800 rpm is shown in Fig.6.21. Almost identical profiles of the developed torque and the quadrature axis stator current indicate the presence of constant flux level and field orientation. The ratio of their values (average) is found to be close to 2.0 over the entire transient period as well as during steady state operation before and after the speed setting. Fig.6.22 presents the simulated responses of the system for the same change in set speed.

6.9.3 Step change in torque

With speed set at 525 rpm and initial torque load at 4.5 Nm the machine I was given a step change in torque (3.5 N.m) making the total (torque load of 8.0 N.M. Fig.6.23 shows the recorded response of torque, torque component of state current (i_{qs}^{c}) and speed. For the same

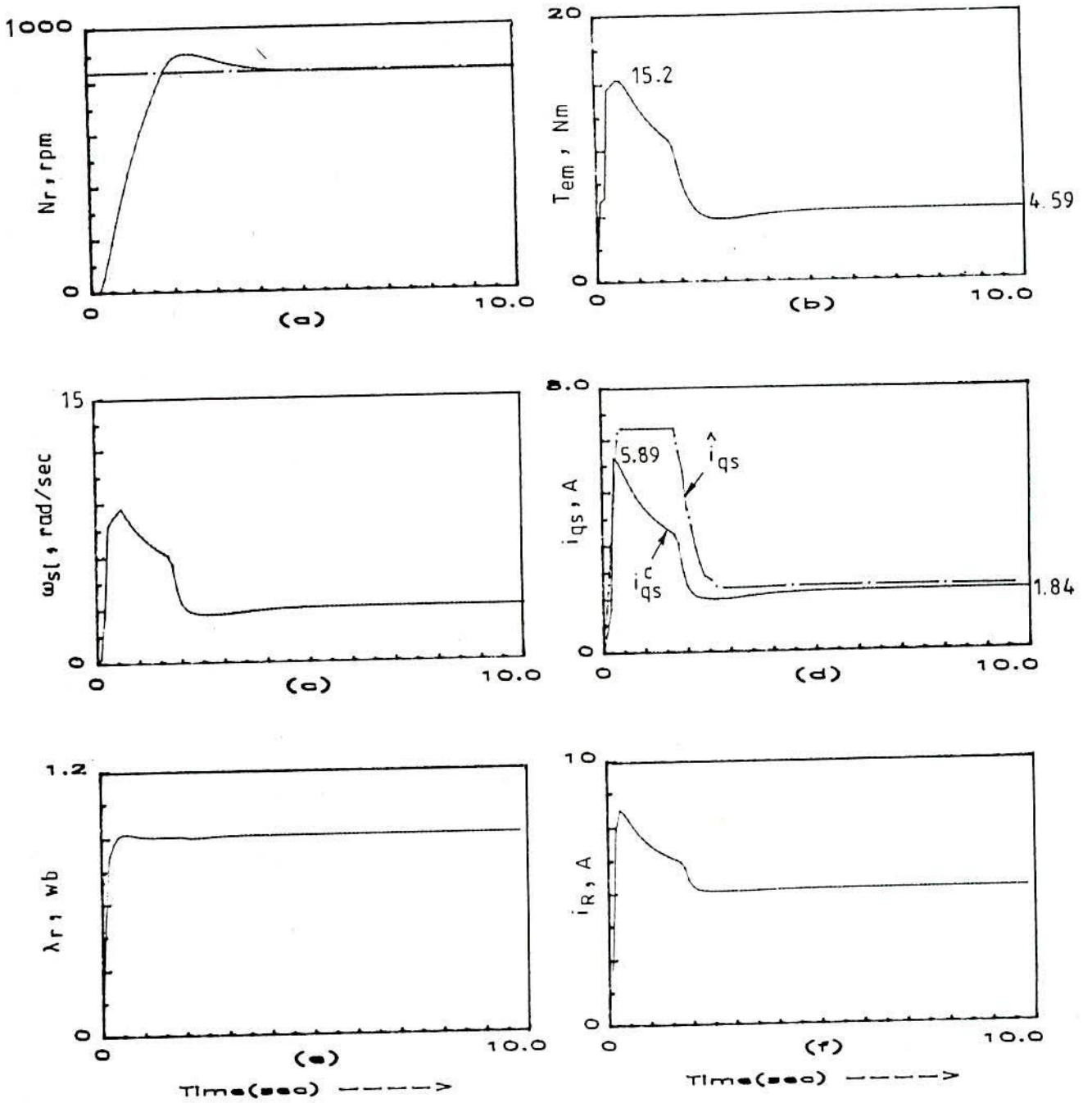

Fig. 6.19 Simulation result : Start up response for the drive system in Fig. 2.7 with machine-I (cf. Fig. 6.17), set speed 825 rpm, set flux = 0.92 wb-turn $T_L = 2.5 + 0.025\ \omega m$ Nm

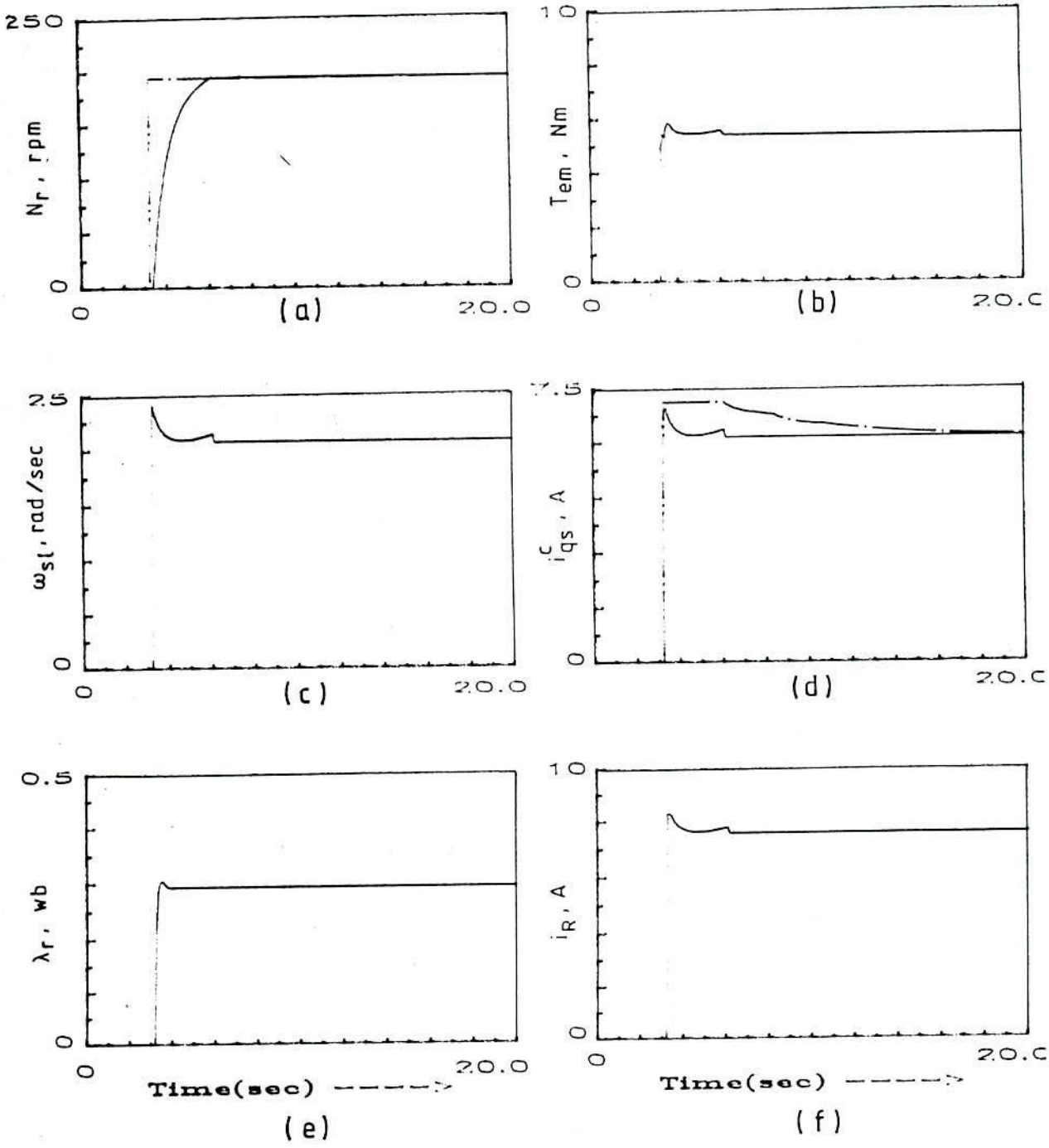

Fig. 6.20 Simulation results : start up response for machine II
$T_L = 0.4 + 0.05\ w_m$ Nm ; set speed = 975 rpm ;
set flux (λ_r) = 0.295 wb

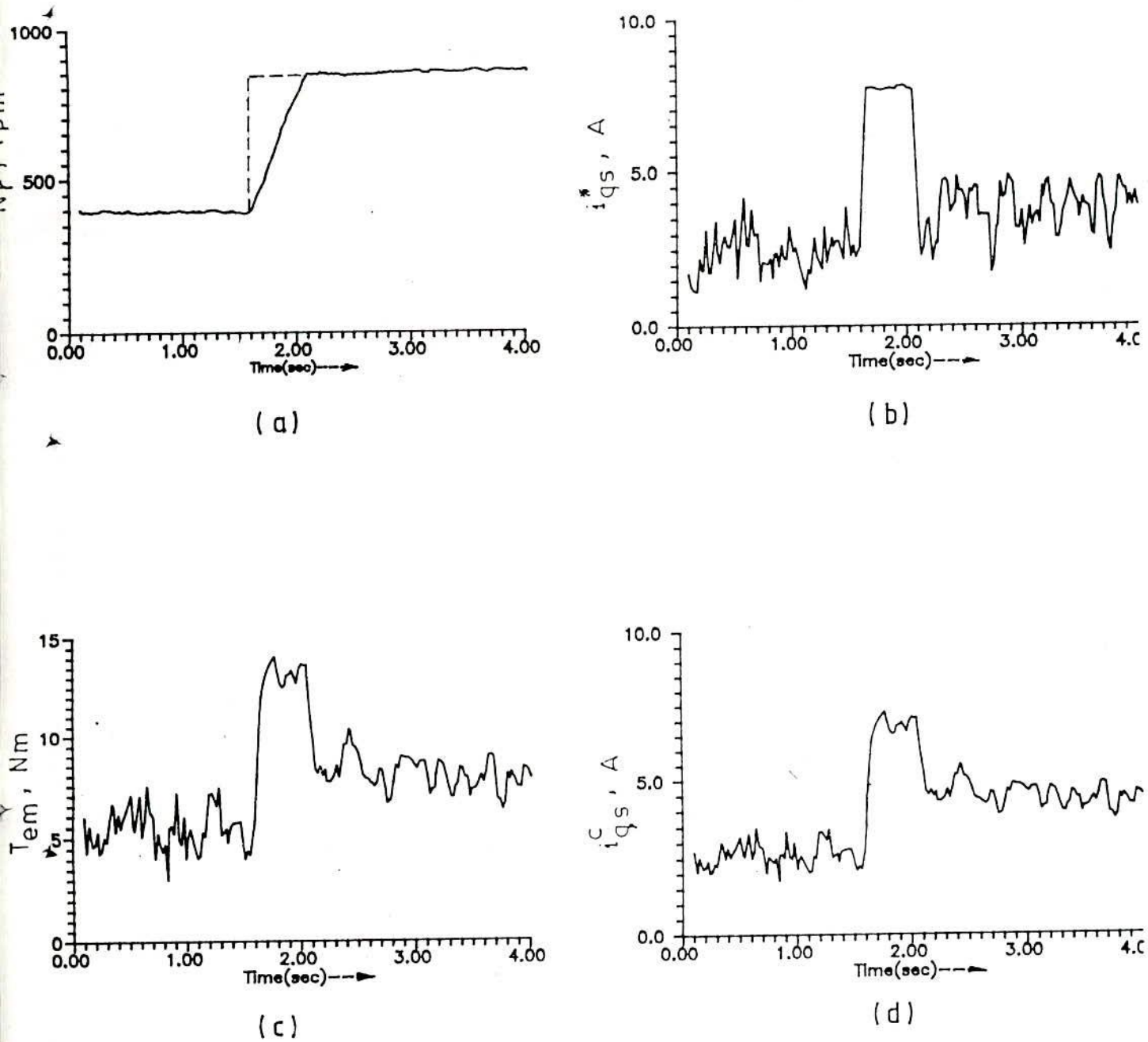

Fig. 6.21 Experimental results : Response to step change in set speed (400 to 750 rpm) for machine I with load torque proportional to speed (eqn. 6.20) ; set flux = 0.95 wb

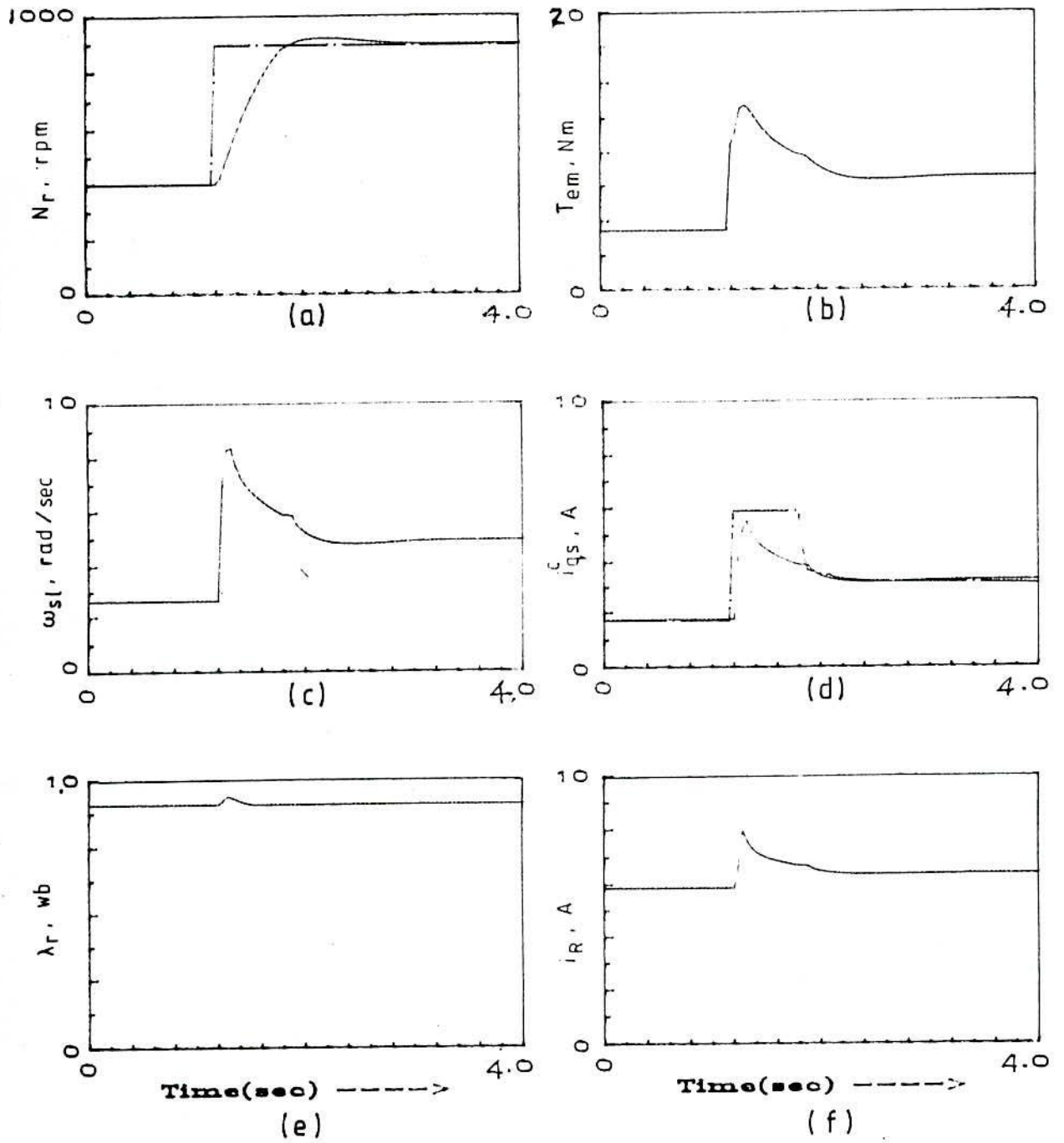

Fig. 6.22 Simulation results for step change in set speed as in fig. 4.21 for machine I with load torque proportional to speed (eqn. 6.20)

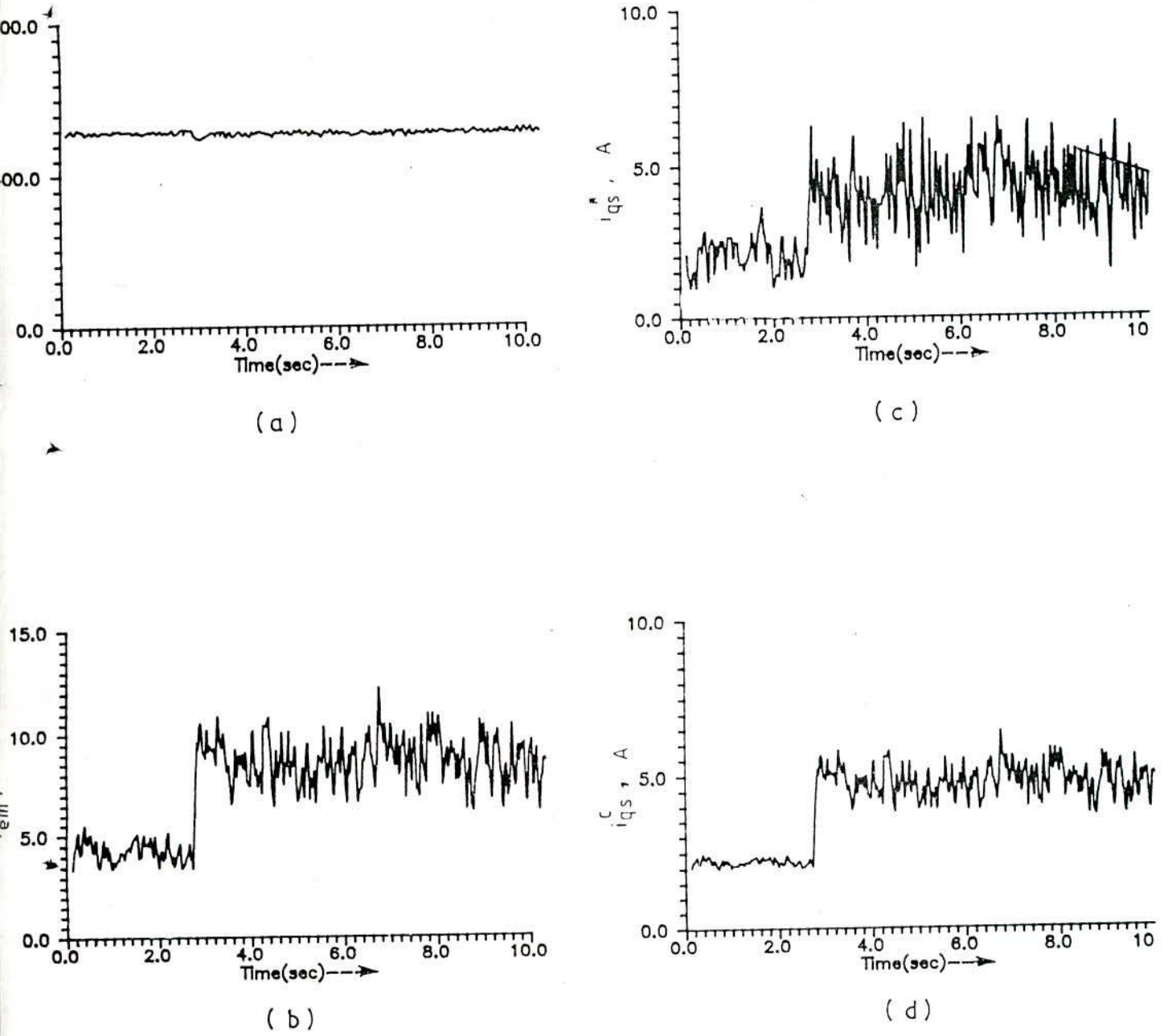

Fig. 6.23 Test results : Response to step change in torque (4.5 to 8.5 Nm) at set speed 525 rpm for the drive system in Fig. 2.7 with machine-I (a) Speed , (b) developed torque, (c) torque component of stator current reference , i^*_{qs} (d) torque component of stator current in slip calculator, i^c_{qs}

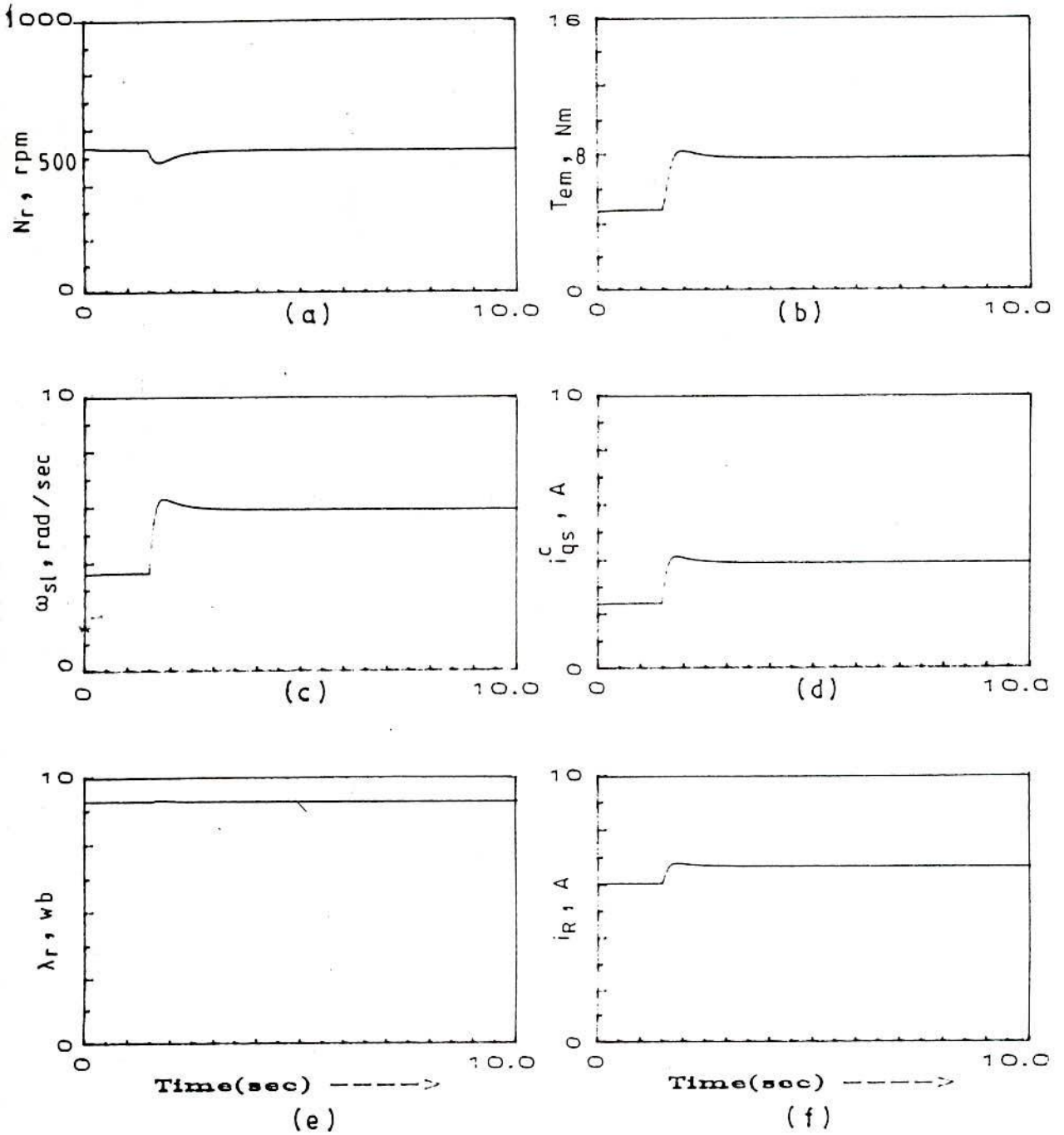

Fig. 6.24 Simulation results : Response to step change in torque (4.5 to 8.5 Nm) at set speed 525 rpm for the drive system in Fig. 2.7 with machine-I (cf. Fig. 6.23)

Fig. PL.4 : Oscillographic record for step change in torque for machine I

step change in torque the simulated responses are given in Fig.6.24. It may be noted that the correlation of i_{qs}^{c} and T_{em} of the simulation with those of recorded responses, though not exact, is reasonable. Fig. PL-4 shows the oscillographic record of speed and dc link current. Good agreement with the simulated response can be noted.

6.9.4 Rotor resistance estimation by air-gap power

In order to establish the validity of approach for rotor resistance estimation from air gap power measurement (see chapter IV) and the criteria for selecting the appropriate value of resistance, (one of the two solutions) test was conducted on machine-II with external adjustable resistor in the rotor circuit. The system was operated without correcting the gain of the slip calculator incorporating the estimated rotor resistance and the external resistance was changed in steps over a period of 20 minutes. Fig.6.25(b) shows the plot of total rotor circuit resistance, referred to stator, with respect to time. The plot-1 in Fig.6.25(a) gives the estimated rotor circuit resistance R_{r1}, while the plot-2 gives the other solution R_{r2} which is non-acceptable. The decision is indicated by the plots in Fig. 6.25 (c) where it is noted that the calculated motor terminal phase voltage V_{ph} corresponding to R_{r1}, runs quite close to the measured terminal voltage ($V_{ph,actual}$) while V_{ph}, corresponding to R_{r2}, differs significantly. The traces in Fig.6.25(e) shows the variation of estimated rotor resistance with respect to total rotor circuit resistance. The deviations from the desired values at higher values of external resistance corresponds to those observed in the case

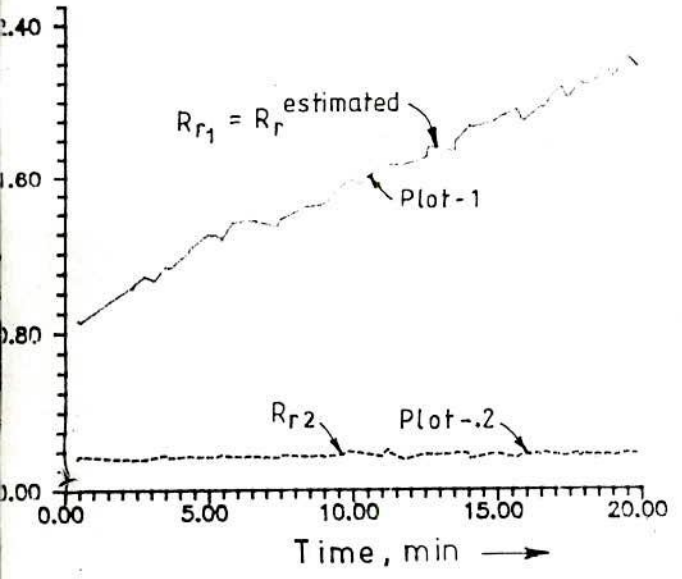

(a)

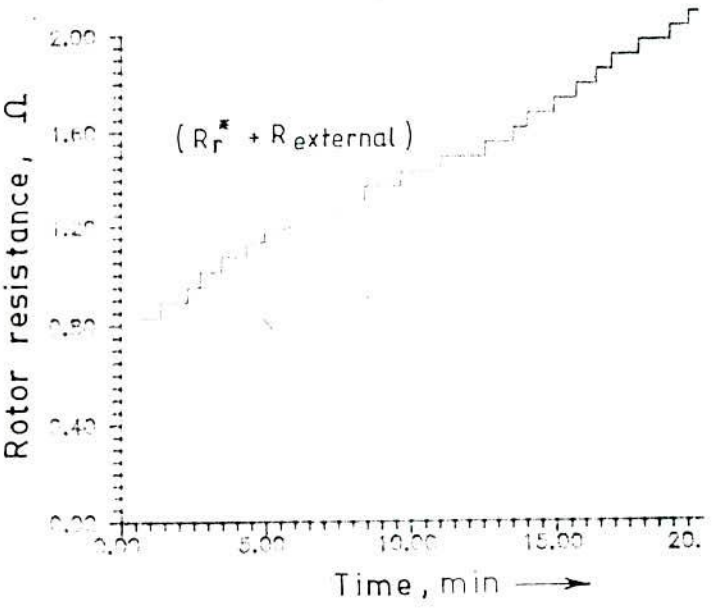

(b)

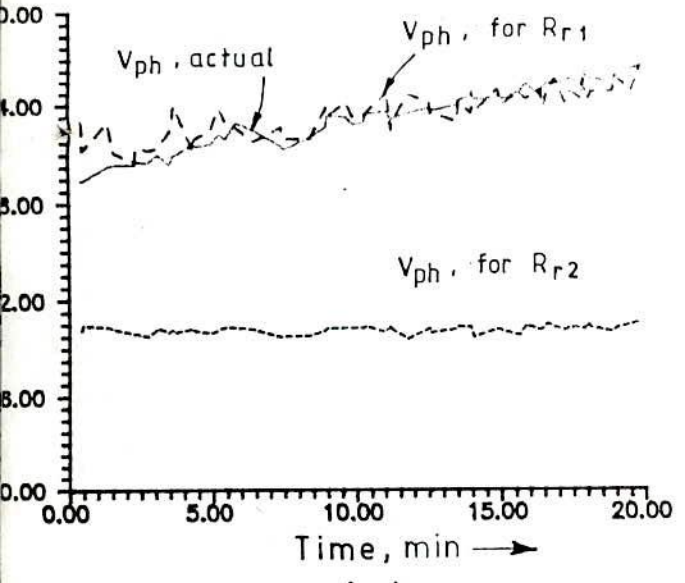

(c)

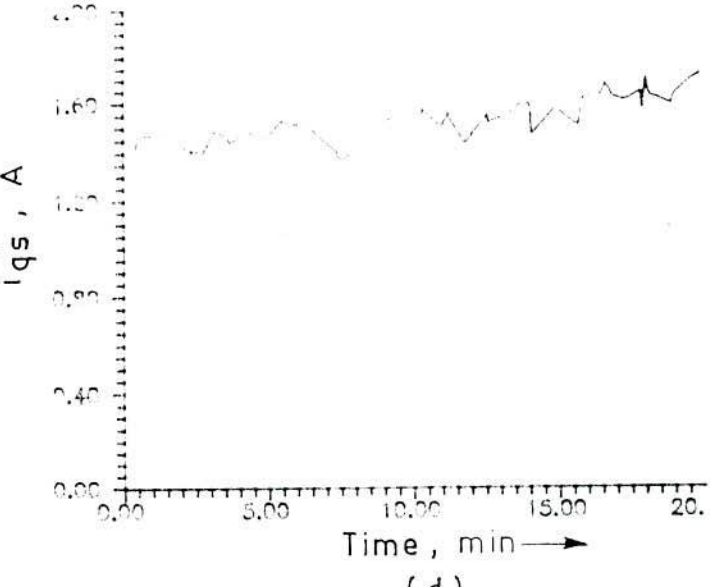

(d)

6.25 Experimental results : R_r estimation for machine-II from air gap power with stepwise change in resistance in rotor circuit of machine-II (a) estimated resistance; (b) actual resistance (total); (c) machine phase voltage (fundamental component); (d) torque component of stator current

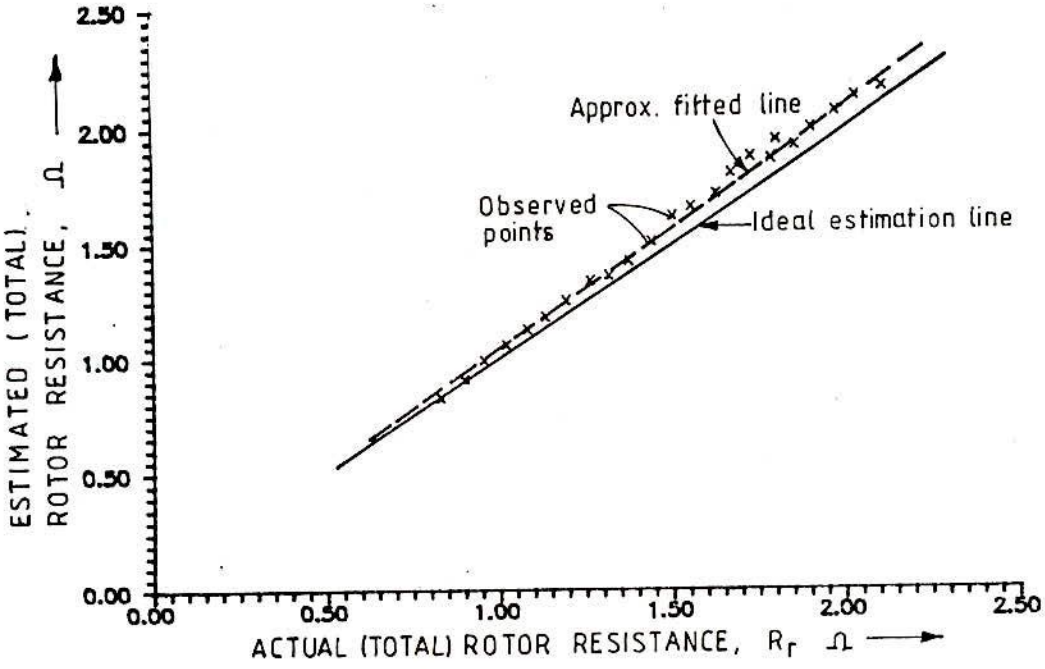

Fig. 6.25 (e) R_r estimation characteristic

of Fig.4.1 due to the causes mentioned thereof. This discrepancy can also be attributed to the possible measurement error, noise in the data acquisition system and the assumptions involved in the estimation of inverter and stator losses. Plots in Fig.6.26 pertains to machine I(SC). The machine was run at varying speed. Results in 6.26(a) gives the accepted (out of the two solutions) estimated rotor resistance as indicated by the proximity of the estimated terminal voltage (v_{s2}) with measured terminal voltage, $V_{s,actual}$ (Fig. 6.26(c)). The variation of speed (Fig.6.26(b)) does not seem to affect the rotor resistance estimation.

6.9.5 Air gap power- based R_r estimation and compensation

Fig.6.27 shows the results of the application of detuning correction scheme, based on air gap power method to machine II. In Fig.6.27(a) is shown the manner in which the external resistance in the rotor circuit was changed in an arbitrary manner. The continuous line in Fig.6.27(b) shows the total estimated resistance (external plus rotor itself) estimated rotor resistance as a function of time. The parameter correction in the slip calculator was not made in a continuous process; rather estimated rotor resistance along with the inductance was incorporated in the slip calculator in a step wise manner (dashed line in Fig.6.27b). Fig.6.27(c) shows how λ_{qr} took near zero values when correction was effected. The scheme as a whole presents detuning correction for steady state operation. Simulation results for such types of rotor resistance variation (not exact) and accompanying correction, are shown in Fig.4.6.

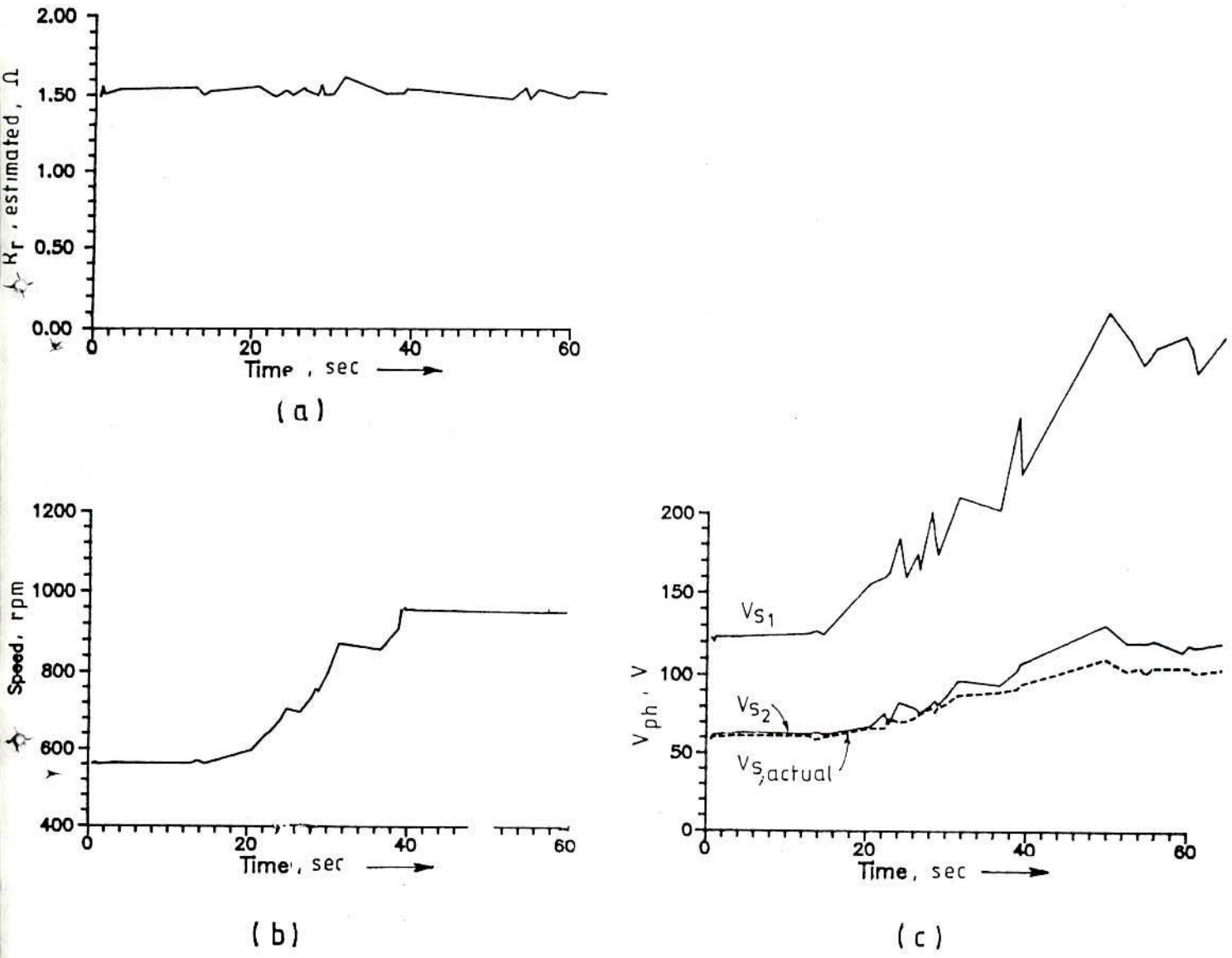

Fig. 6.26 Experimental results : air gap power based rotor resistance estimation for machine I at different speeds

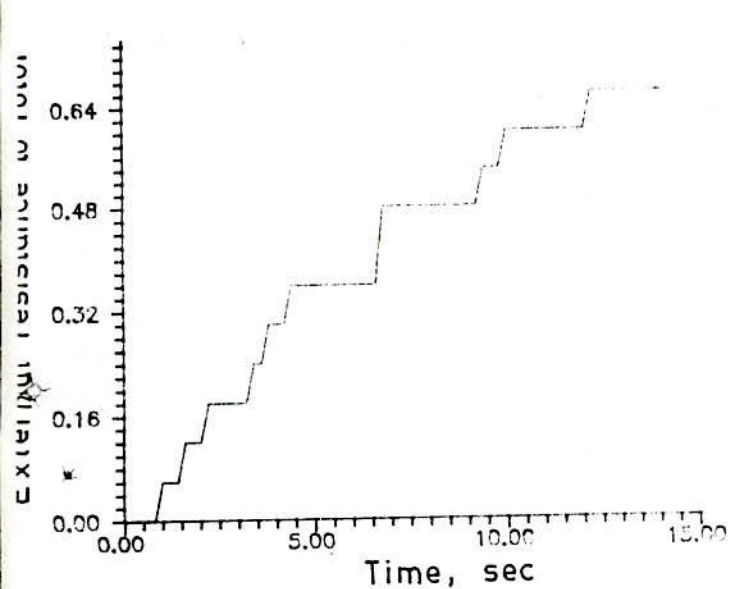

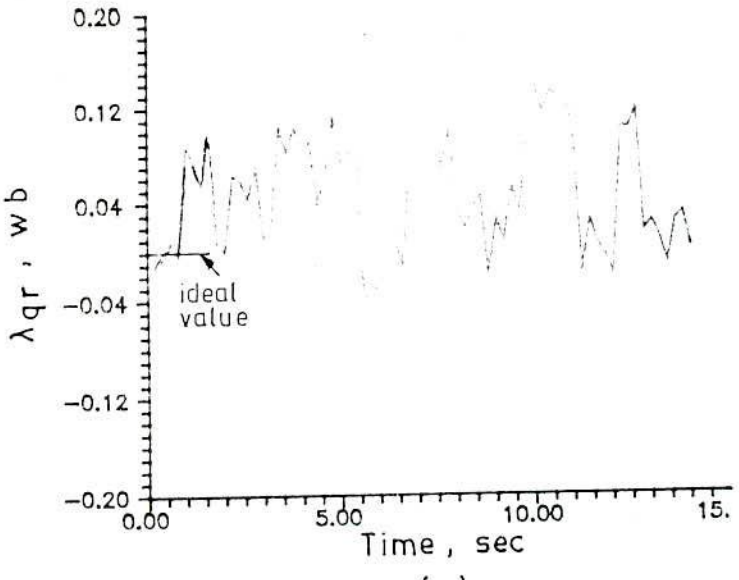

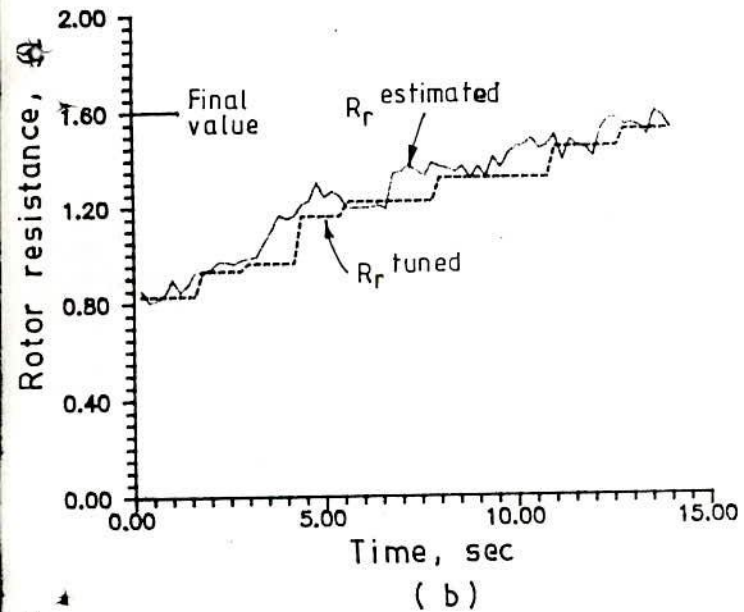

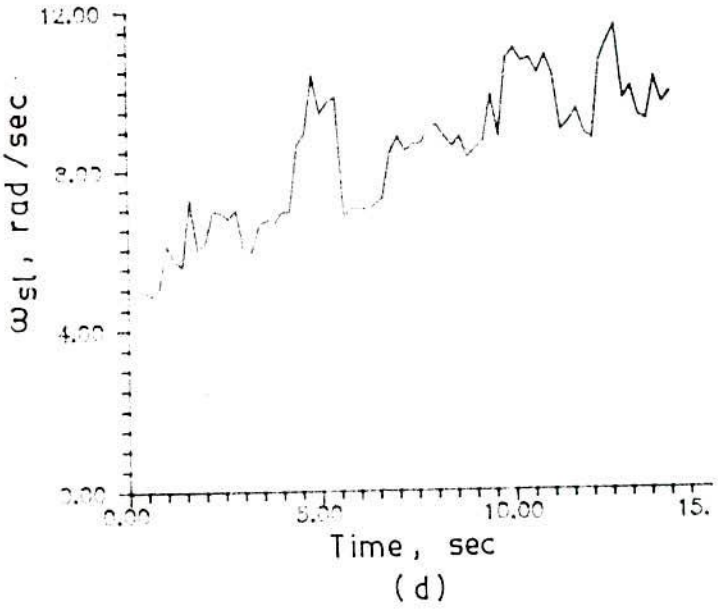

Fig. 6.27 Experimental result : Tuning by incorporating estimated rotor resistance from air gap power in the slip calculator of the drive system in Fig. 2.7 at constant set speed

6.9.6 DC link voltage-based R_r adaptation scheme

Results of parameter adaptation in the slip calculator, based on the comparison of actual dc input voltage to the inverter and its model reference (4.15) are shown in Figs.6.28 and 6.29 for squirrel cage (machine I) and slip ring (Machine II) machines respectively. In the case of machine I, initially, a value of rotor resistance less than its normal value was used in the slip calculator to introduce detuning. Fig.6.28(b) shows how the resistance in the slip calculator improves its value after the adaptation process was set in. When the two voltage V_I^{ref} and V_I^{actual} became practically equal, adaptation process ceased and R_r in the slip calculator attained the value of 1.57Ω, which is little higher than its nominal value. This was expected, as the test run was for a short duration. It is noted from Fig. 6.28(c) that magnetizing current decreases and approaches to set value i_{ds}^* as the decoupled condition is restored.

In the slip ring induction motor rotor resistance was changed in two steps at instants t_o and t_1 and adaptive scheme was made inoperative over the period (t_2-t_1) and restored at the instant t_2. Plots in Fig.6.29(a) and (b) show how the rotor resistance in the controller (slip calculator) gets adjusted as V_I^{ref} and V_I^{actual} become closer. Fig.6.28(c) indicates how the quadrature axis component of rotor flux, arising out of detuning condition, decreases to very low value indicating the correct adaptation for rotor resistance in the slip calculator.

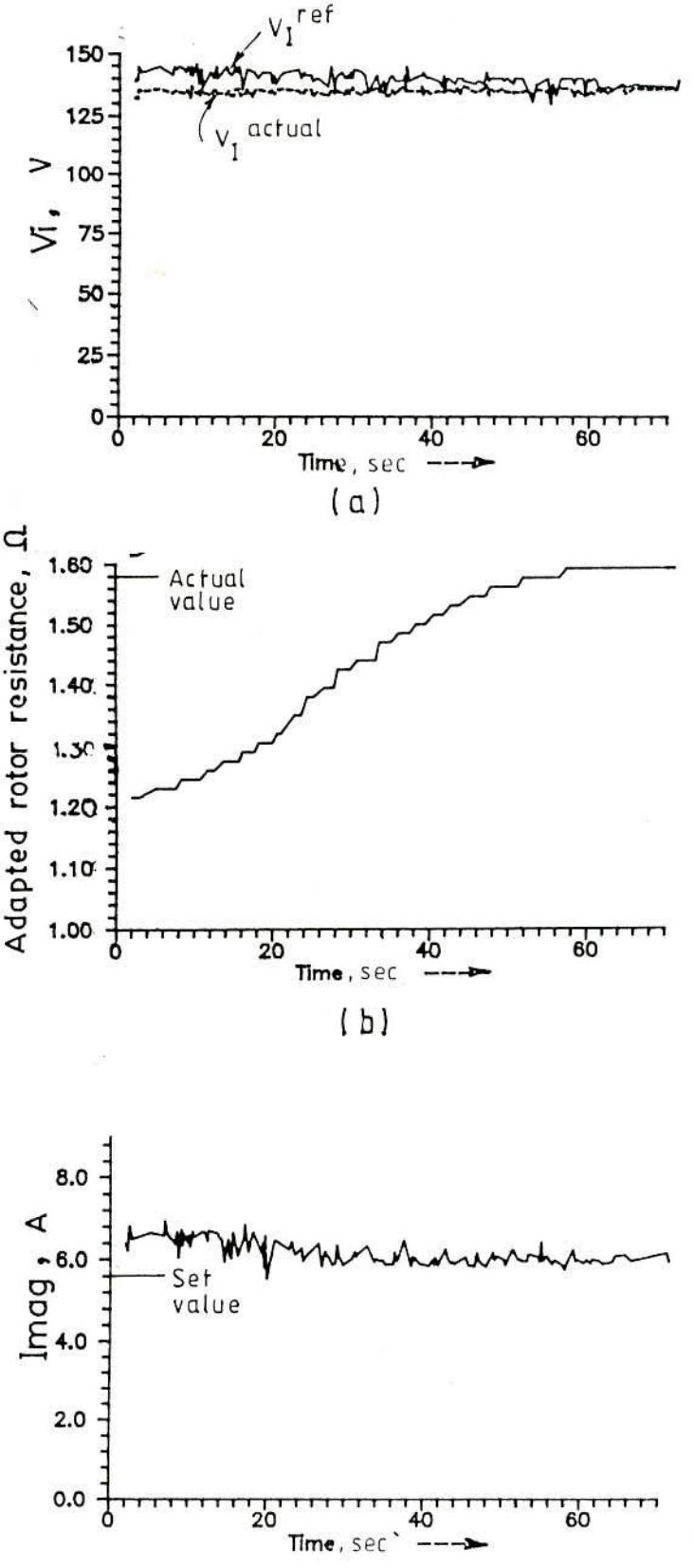

Fig.6.28 Experimental result : Adaptation of rotor resistance by dc link voltage based MRAC scheme for the system in Fig. 2.7 with machine - I

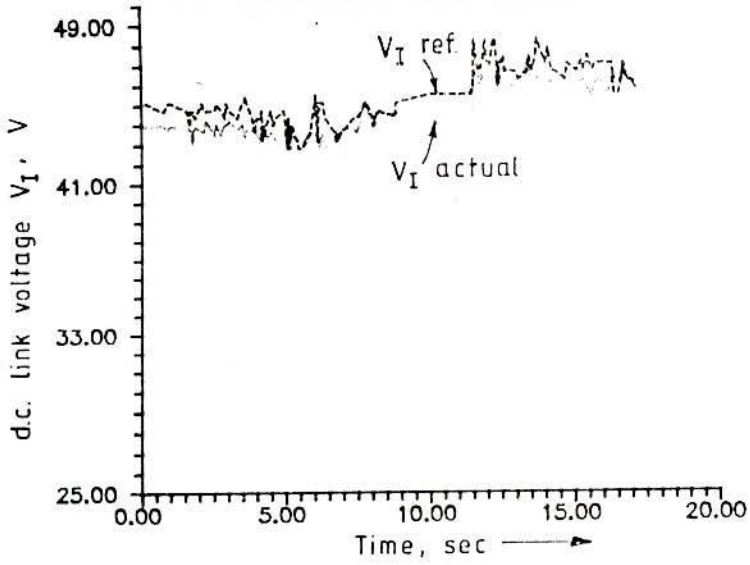

(a)

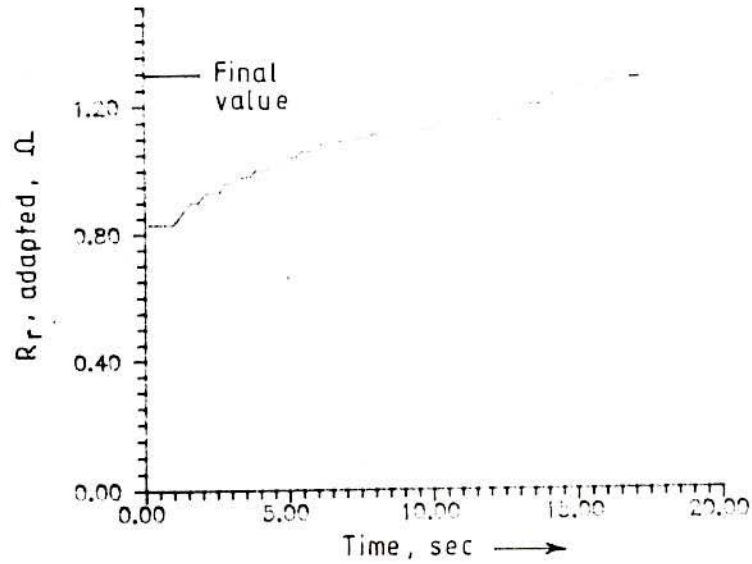

(b)

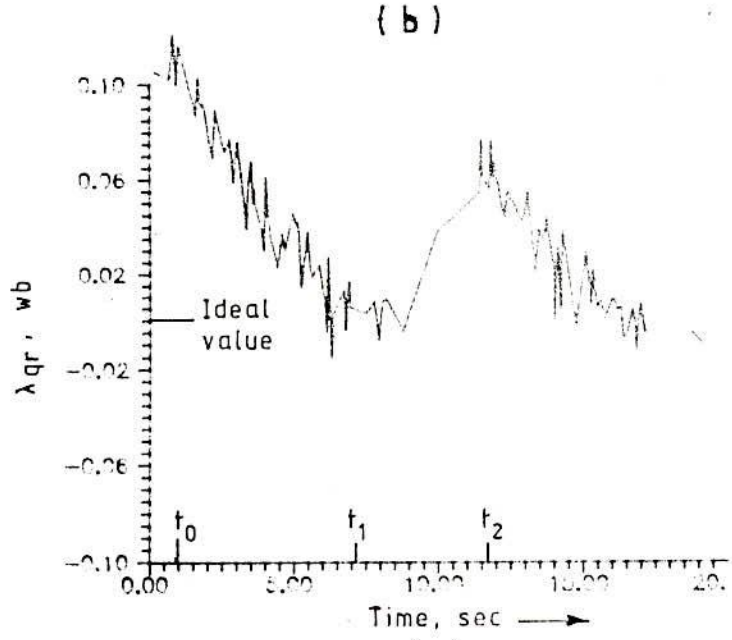

(c)

Fig.6.29 Experimental results: adaptation by dc link voltage based model reference adaptive control for two-step increase in rotor resistance in machine II

6.9.7 Torque component of stator current-based R_r adaptation scheme

The ability of the adaptation scheme based on the torque component of stator current is shown by two sets of results in Fig.6.30 and 6.31. The difference ($i_{qs}^{c} - \hat{i}_{qs}$) was used for generating the correction terms for the rotor resistance in the slip calculator. Fig.6.30 pertains to machine I. After having made deliberately the rotor resistance in the slip calculator more than its nominal value, the correction process was set on. Fig.6.30(b) shows how the adapted resistance in the slip calculator gradually decreased and came to actual value when when $\hat{i}_{qs}$ and i_{qs}^{c} agreed. As expected, magnetizing current gradually increased and approached to i_{ds}^{*}.

In the case of slip ring machine (machine II) an external resistance of approximately 0.42 ohm was inserted making the total rotor resistance to the order of 1.24Ω. Fig.6.31(b) shows a how the resistance in the slip calculator adapted the rotor circuit resistance when $\hat{i}_{qs}$ and i_{qs}^{c} became almost equal. Fig.6.31(c) illustrates the gradual decay of λ_{qr} to zero average value while Fig.6.31(d) shows how magnetizing current approached i_{ds}^{*} as decoupled condition was restored.

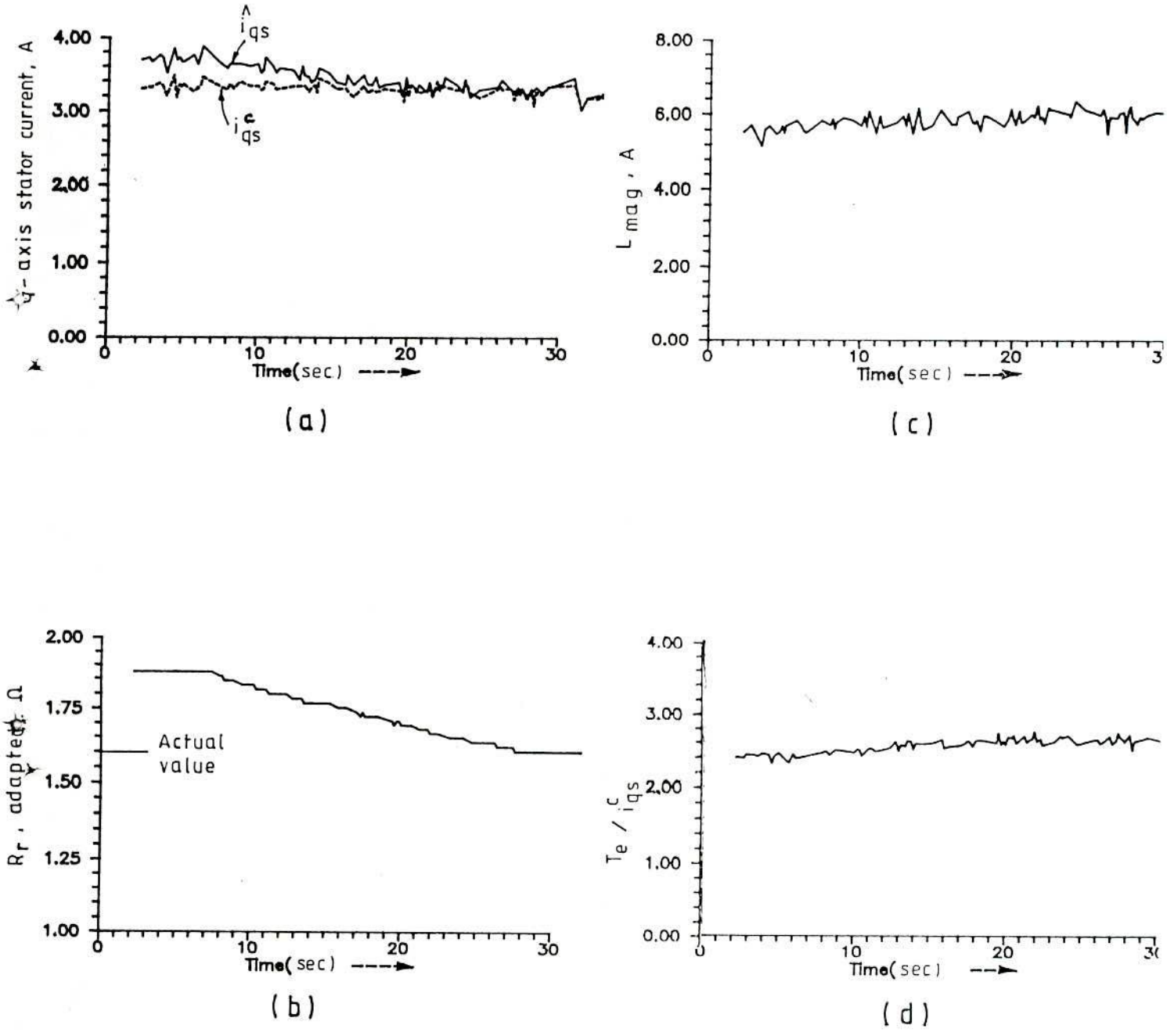

Fig. 6.30 Experimental results: Adaptation of rotor resistance in the controller with initial rotor resistance set at a higher value than the actual resistance. (Torque component of stator current based MRAC scheme for machine I)

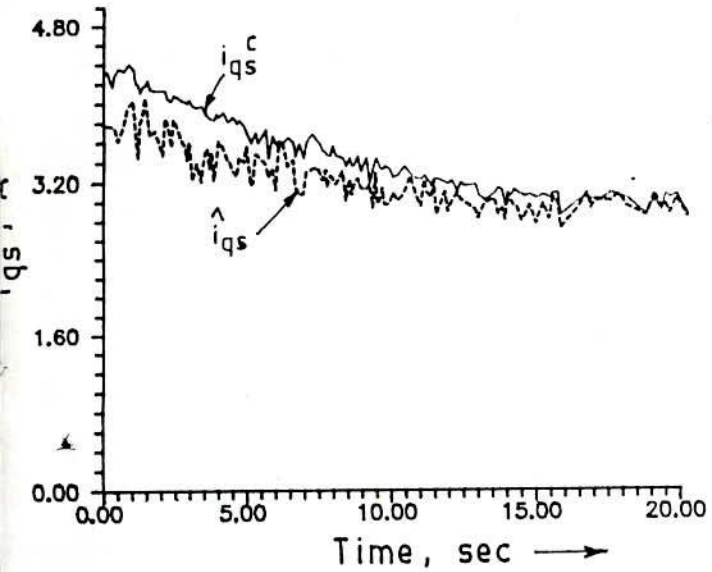

(a)

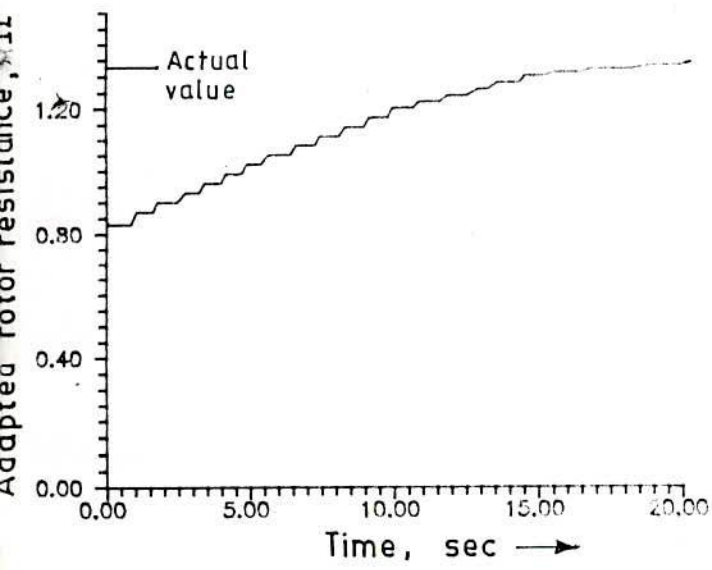

(b)

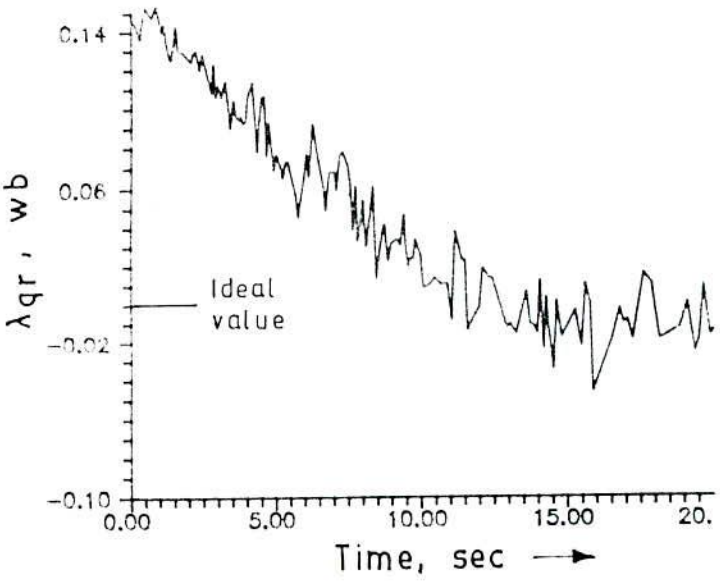

(c)

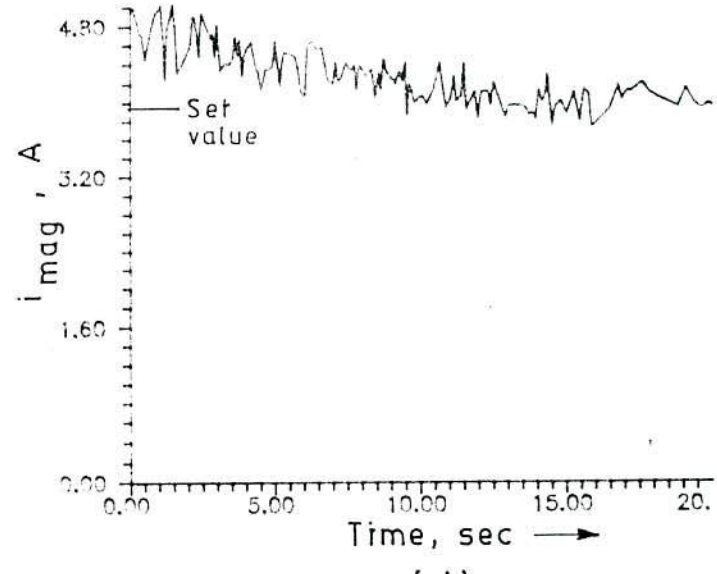

(d)

Fig. 6.31 Tuning by torque component of stator current based MRAC scheme following insertion of external resistance in the rotor circuit of machine-II in the system of Fig. 2.7.

CHAPTER VII

GENERALIZED APPROACHES FOR SIMULATION OF CSI-IM SYSTEM

7.1 INTRODUCTION

Computer simulation of adjustable frequency ac drives is a very valuable tool to study the complex dynamic behaviour of systems and also to investigate the effects of various parameters on the system performances prior to their hardware realization. Based on different assumptions and circuit topologies, studies for analyzing performances of controlled current fed inverter with asynchronous motor have been differently carried out over the past one and half a decade, and this is evident from the extensive literature on the subject [70 - 76, 103, 104]. Various modes of normal operation have been studied by many investigators [70-71]. They have assumed dc link current as constant and quasi-square wave pattern for the currents to the motor. Counter emf and its change and phase shift are not properly considered in most of them. On the other hand, very limited references are available in regard to the study of the transients and fault conditions in controlled current inverter driven induction motor [72-74]. Those are based on various restrictive aspects of the composite rectifier-filter-inverter-motor system. Lipo [72] and McMurray [73] have presented hybrid computer simulation to study both normal and abnormal operations of controlled current ASCI (auto sequentially commutated inverter) on a large scale analog computer having a complete logic component. Both

studies have employed the inverter models in considerable details but have taken a simplified model of the induction motor which is represented as an essentially sinusoidal counter emf in series with an inductance and a relatively small resistance. Work in [73] considers an ideal source of steady current while that in [72] retains dc link filter inductor in the simulation but the input voltage is modelled as an idealized, adjustable amplitude dc voltage in place of a thyristor bridge. Consoli and Abela [74] have presented a general digital simulation model of ASCI-IM system to study normal and abnormal operational modes as well as transient working conditions. However, the method is not amenable to study the behaviour of the system following the short circuit between two machine terminals or the opening of any motor terminal. Secondly, a small inductor in series with each diode has been inserted to monitor the diode currents and also to allow one to write sufficient number of independent equations for defining the system. But this considerably enhances the total running time for computation by introducing small time constants. These inductances have to be kept low to conform to the reality. Both the simulation processes, referred to above, require writing series of algebraic and differential equations by inspection of the equivalent circuit, and their judicious blending, particularly, in the case of digital simulation process, to arrive at a suitable simulation model.

The work presented in this chapter provides simulation methods based on 'Nodal method' [105] and 'Bond graph technique' [78 - 81] to develop computer aided algorithms to facilitate study of ASCI driven

induction motor under both normal and abnormal modes, inclusive of fault conditions of the inverter operation. They are based on more realistic modelling of the CSI-IM system dispensing with many assumptions for simulating the system by the conventional circuit theory.

7.2 NODAL METHOD BASED SIMULATION

Nodal method is a routine procedure that one using it, need not write any governing equations (algebraic, differential or integral) for the equivalent circuit from basic laws and to manipulate them to converge on a simulation model. The labour saving routine methodology of the Nodal method is particularly advantageous for an extended network with asymmetry in it. Our study retains all the structures, viz. bridge rectifier, dc link inductor, inverter bridge and induction motor in their generalized circuit model. The induction motor is represented in three phase (a-b-c) stationary coordinate system in which each rotor phase contains a counter emf expressed as functions of magnetising currents and rotor currents of other phases. Thyristors and diodes of the inverter and converter are modelled as resistors having very low and very high values for the conducting and non conducting states respectively. Fault conditions in the system may upset the symmetry inherent in the system, and "in this case, the analyst must rely upon implicit integration of the system equations using simulation to obtain the desired solution" [72]. In Nodal method, the differential equations are converted to matrix algebraic equations in a generalized format, based on implicit (trapezoidal) integration rule [105], and

symmetry of the equivalent circuit is not an essential criterion. The approach conveniently adjusts itself for simulating the system under normal, abnormal or transient conditions on a digital computer. No restructuring of the equivalent circuit is needed. Simulation results for different operating conditions are presented and conformity with published results, based on another model [74], are noted.

7.2.1 Investigated system and models

Equivalent circuit

The basic schematic of the controlled current inverter feeding an induction motor considered in the simulation study is shown in Fig.7.1. A current source inverter induction motor system can be ensured for stable operation by current magnitude and inverter frequency control [75]. In the present case, operation in the stable region is ensured using the method outlined in [104] by controlling slip speed from speed error signal and also by controlling the current for constant flux operation. For simulation study of such circuit and to investigate various aspects of operation, it is necessary to select appropriate equivalent circuits for the inverter, inclusive of the rectifier in the supply system and the load, such that the entire system can conveniently be fitted into the desired model without sacrificing the reality. The equivalent circuit chosen for the power network is shown in Fig.7.2. In order to formulate the system matrices the semiconductor devices should be appropriately modelled in the equivalent circuit. Based on the suggestions in [105] thyristors and diodes can be replaced by resistances having high values during their off-states and low

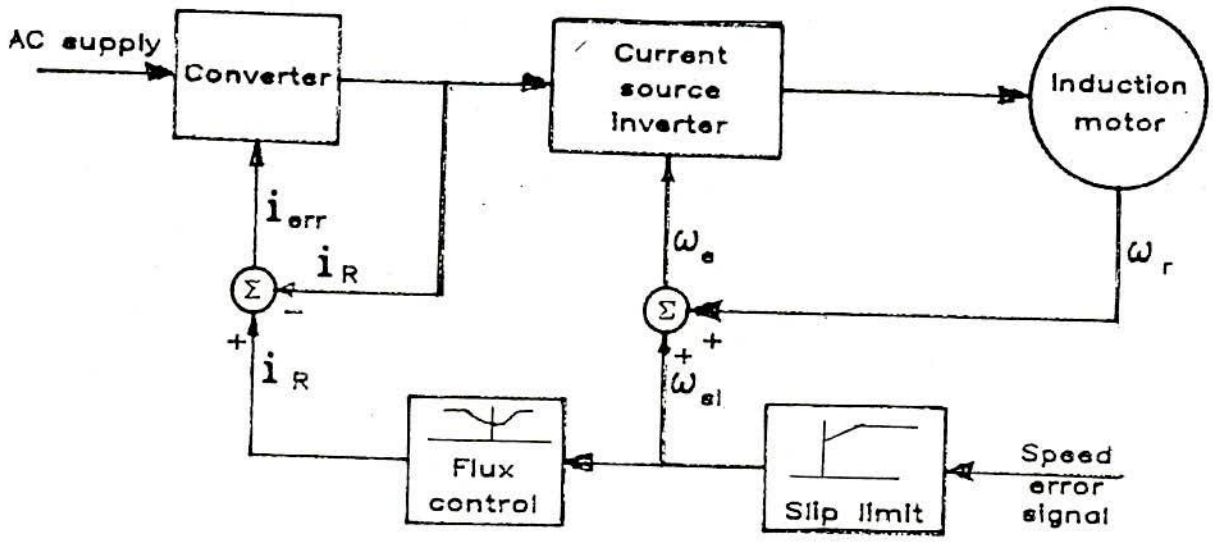

Fig.7.1 Current source inverter–IM drive with slip–frequency control of current reference

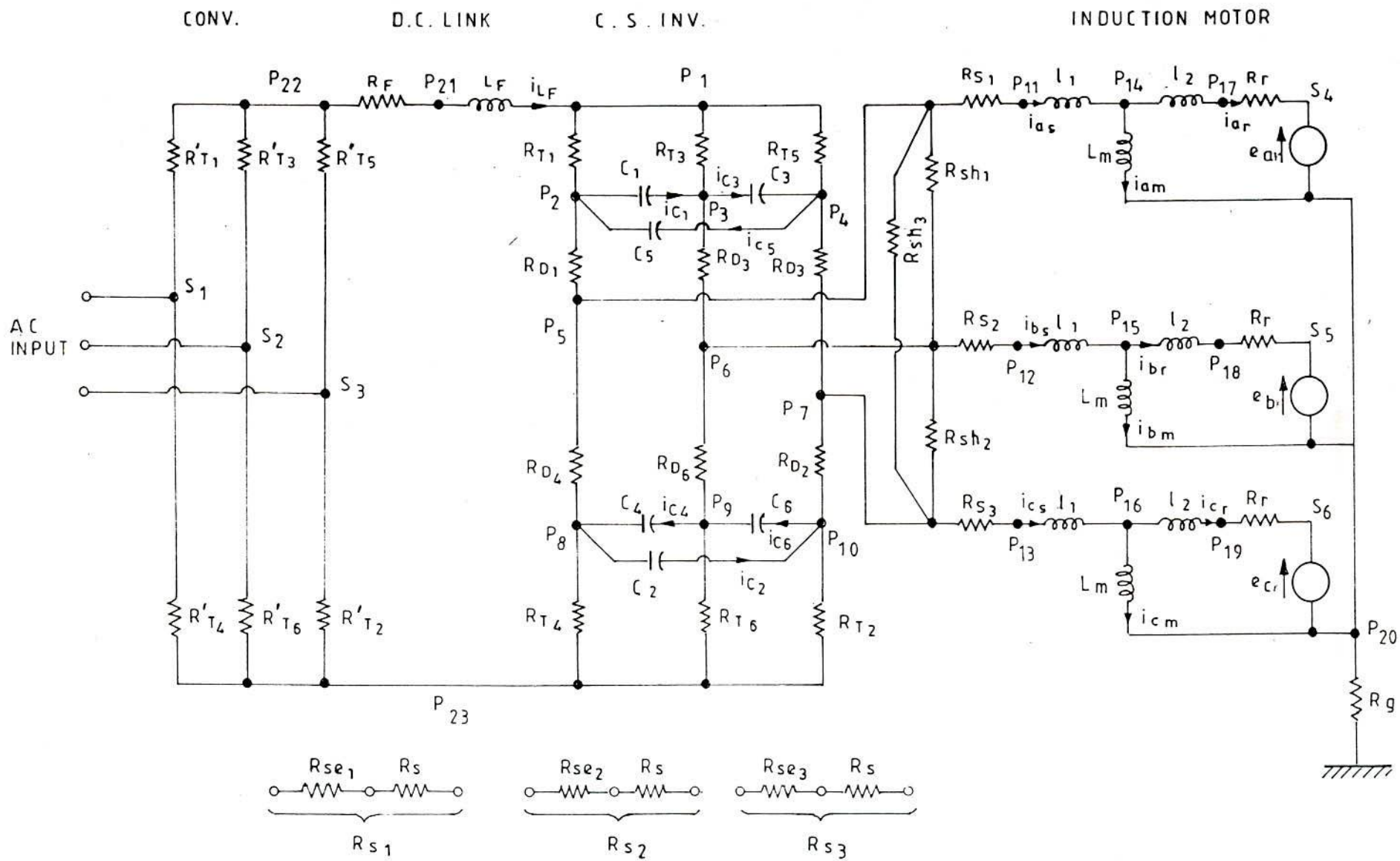

FIG.7.2 EQUIVALENT CIRCUIT OF THE CONVERTER, INVERTER, INDUCTION MOTOR SYSTEM.

values during their on-states. Modulation of the resistances over a wide range, based on their V-I characteristics is not considered in the study. The additional resistors R_{sh}'s and R_{se}'s are incorporated to simulate the short circuit and open circuit of the machine terminals by assigning appropriate values to these added elements. For example, very low value of R_{sh1} would imply a short circuit between the terminals of phases 'a' and 'b' of the motor and a very high value of R_{se1} would mean open circuit of the phase 'a' terminal of the motor. To study normal operation, R_{sh}'s and R_{se}'s are given very high and very low values respectively. In Fig.7.2 R_{s1} is the equivalent of series combination of R_{se1} and R_s. Similar are the cases for R_{se2} and R_{se3}. The induction motor is represented by three identical equivalent circuits each consisting of the stator leakage inductance in series with a parallel circuit that includes magnetising inductance in one branch and rotor leakage impedance in series with a counter emf in the other branch. This counter emf incorporates the coupling effect between the different phases. This aspect is given a little elaboration in the modelling of the induction motor.

A resistance R_g(10kΩ) is added between the star point of the induction motor phases and the ground of the system in order to define the node voltages at S_4, S_5 and S_6.

Induction motor model

It is well known that the transient voltage equations of a symmetrical three phase induction machine in terms of actual phase variables are laboursome to deal with, owing to rotor position

dependence of mutual coupling between the stator and rotor windings. In order to eliminate the rotor position dependent inductance terms d-q transformation is generally applied to the phase variables. If, however, it is desired to retain the actual stator phase variables, maintaining symmetry in the emf equations with position-independent inductance terms, the actual three phase rotor variables must be replaced by an equivalent set of three phase variables on a reference frame stationary relative to the stator. Schematic structure of the CSI-IM system adopted for study is shown in Fig.7.3. Using the concept of power invariance, developed and used extensively by Kron [106] and others [107] for transforming emf equations from one reference frame to other, the emf equation for the three phase machine in Fig.7.3 in a

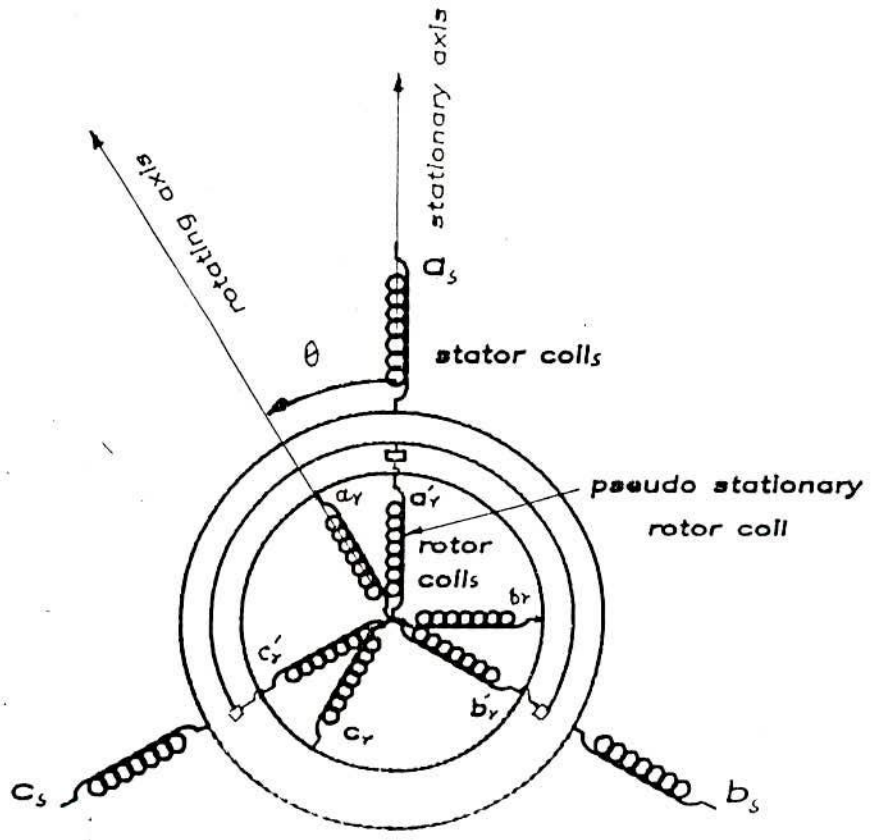

Fig.7.3 Rotating and stationary axes of IM

frame(a-b-c) stationary relative to the stator can be written as:

$$[v] = [R][i] + [L]p[i] + [G]\dot{\theta}[i] \qquad (7.1)$$

where,

$$[v] = [v_{an}\ v_{bn}\ v_{cn}\ \ 0\ \ 0\ \ 0\ ]^t = [v_s\ v_r]^t$$

$$[i] = [i_{as}\ i_{bs}\ i_{cs}\ i_{ar}\ i_{br}\ i_{cr}]^t = [i_s\ i_r]^t$$

The parameter matrices [R], [L] and [G] are given in eqn.A.16 in Appendix III. For star connected stator and rotor windings with no neutral connections, the following voltage equations for the 'a' phase of stator and the equivalent rotor windings can be obtained from eqn.7.1.

$$v_{an} = R_s i_{as} + l_1 p i_{as} + L_m p i_{am} \qquad (7.2)$$

$$0 = R_r i_{ar} + l_2 p i_{ar} - L_m p i_{am} + e_{ar} \qquad (7.3)$$

where,

$$i_{am} = i_{as} - i_{ar}$$

$$l_1 = L_s + \frac{1}{2} M_s - \frac{3}{2} M$$

$$l_2 = L_r + \frac{1}{2} M_r - \frac{3}{2} M$$

$$L_m = \frac{3}{2} M$$

in which, with reference to Fig.7.3,

M_s : mutual inductance between stator phase windings

M_r : mutual inductance between rotor phase windings

M : mutual inductance between stator and rotor phase windings

The counter emf in any phase of rotor arises from the elements in the last term of right hand side of eqn.7.1. Using eqn.A.16 the counter

emf for 'a' phase is expressed as follows:

$$e_{ar} = \frac{1}{\sqrt{3}} [L_m(i_{cm}-i_{bm}) + l_2(i_{br}-i_{cr})]\omega_r \qquad (7.4)$$

where,

$$i_{bm} = i_{bs} - i_{br}$$

$$i_{cm} = i_{cs} - i_{cr}$$

i_{am}, i_{bm}, i_{cm} can be identified as the magnetising currents for the phases 'a', 'b' and 'c' respectively.

Equations similar to eqns.7.2 and 7.3 also exist for the phases 'b', and 'c', and these suggest that each phase of the induction motor can be represented by the equivalent circuit shown in Fig.7.2.

The mechanical power developed by the induction motor is given by

$$P_{mech} = e_{ar}\, i_{ar} + e_{br}\, i_{br} + e_{cr}\, i_{cr} \qquad (7.5)$$

and torque balance equation is

$$T_{em} = (P_{mech}/\omega_r).P_p = J \frac{d\omega_m}{dt} + B\, \omega_m + T_L \qquad (7.6)$$

Controller

Closed loop control for the inverter frequency and the dc input current are provided in the system as shown in Fig.7.1. Slip speed is calculated from the speed error data and the inverter firing frequency is obtained by adding ω_{sl} to ω_r, the actual speed of the motor in electrical radian.

The reference dc link current is adjusted to have constant flux operation according to the desired characteristic [11]. The error in dc link current signal is then fed to a PI controller to generate

reference voltage for cosine-law firing scheme as:

$$(I_R^* - I_R)(K_p + K_I/s) = V_R \qquad (7.7)$$

7.2.2 Nodal method

The circuit model in Fig.7.2 is a complex combination of several series and parallel elements. Nodal method can conveniently be employed to deal with such circuit configurations algebraically by converting the differential equations into algebraic equations through simple integration technique, viz., the trapezoidal rule [105]. The essence of the method is to obtain first, node potentials at any instant $t_n = t_{n-1} + \delta t$, and then to calculate currents in various branches from the knowledge of the node potentials at the beginning and at the end of the time increment δt. In the case of energy storing elements, the values of currents and voltages at the beginning of the time step are also required. The node voltage and current matrix relations of any network for the time increment δt can be expressed [105] as

$$\begin{bmatrix} (i_s)_n \\ 0 \end{bmatrix} = \begin{bmatrix} (i_s)_{n-1} \\ (i_p)_{n-1} \end{bmatrix} + \begin{bmatrix} A_{ss} & A_{sp} \\ A_{ps} & A_{pp} \end{bmatrix} \begin{bmatrix} (v_s)_n \\ (v_p)_n \end{bmatrix} + \begin{bmatrix} B_{ss} & B_{sp} \\ B_{ps} & B_{pp} \end{bmatrix} \begin{bmatrix} (v_s)_{n-1} \\ (v_p)_{n-1} \end{bmatrix} \qquad (7.8)$$

where,

$(\mathbf{v_p})$: the node potential vector for the junctions where only passive elements meet.

$(\mathbf{v_s})$: actual and/or pseudo source voltage vector

$(\mathbf{i_s})_n$: source current vector at $t=t_n$.

$(i_s)_{n-1}, (i_p)_{n-1}$: corrector current vectors for the source and passive junctions respectively, the elements of which are particular combinations of current values through storage elements at the beginning of time step δt [105].

The system under study consists of 23 passive nodes to which R-L-C elements are connected and 6 active nodes (S_1 through S_6) to which voltage sources are connected. Of the six active nodes three are connected to pseudo sources (motor counter emfs). The elements of the admittance matrices A and B are formed from the circuit elements and time step, $H(=\delta t)$ in a manner explained in [105]. The matrix A for the circuit in Fig. 7.2 is given in Appendix III. The elements of the B matrix are formed from those in A with resistive terms omitted and capacitive terms negated. Multiplying and adding the matrices in (7.8) and rearranging them, one obtains the current-values for the node voltages at $t=t_n$ as follows:

$$(v_p)_n = -A_{pp}^{-1}[(i_p)_{n-1} + A_{ps}(v_s)_n + B_{ps}(v_s)_{n-1} + B_{pp}(v_p)_{n-1}] \qquad (7.9)$$

Once the updated node voltages become known, currents in all the resistive, inductive and capacitive elements can be determined from equations 7.10 through 7.12 (vide Fig. 7.4)

$$(i_R)_n = \frac{1}{R}(v_1 - v_2)_n \qquad (7.10)$$

$$(i_L)_n = (i_L)_{n-1} + \frac{\delta t}{2L}[(v_2 - v_3)_n + (v_2 - v_3)_{n-1}] \qquad (7.11)$$

$$(i_C)_n = -(i_c)_{n-1} + \frac{2C}{\delta t}[(v_3 - v_4)_n - (v_3 - v_4)_{n-1}] \qquad (7.12)$$

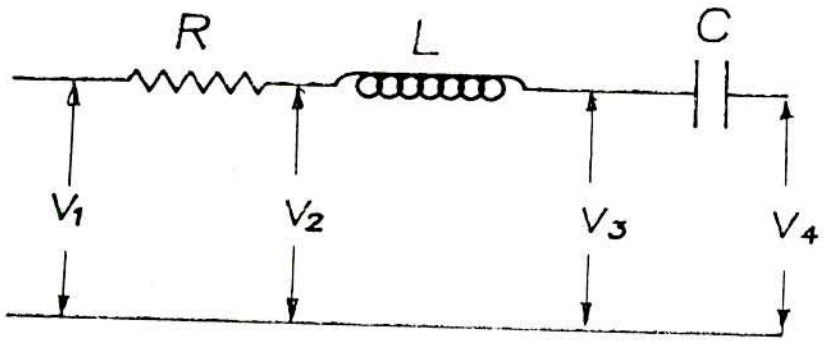

Fig.7.4 R, L and C elements with node voltages

where, indices n and n-1 indicate voltage or current values at the instants t_n and t_{n-1} respectively. Currents flowing through the inductive and capacitive elements are used to frame the corrector current matrix, i.e., $(i_p)_{n-1}$ in eqn.7.8. The components of corrector current matrix $(i_p)_{n-1}$ are shown in Appendix III.

7.2.3 Computational procedure

The flow chart in Fig.7.5 outlines the sequence in which the computations are to be carried out. A few aspects of computational steps that may not be readily evident from Fig.7.5 are given below for clarifications.

(i)Application of eqn.7.9 to the network in Fig.7.2 can not be straight forward because of the existence of pseudo voltage sources in the induction motor model. These voltages are not known *apriori* for the instant $t=t_n$ because they themselves depend on the motor current values at $t=t_n$. Hence an iterative approach is made for every time increment to evaluate $(v_s)_n$. Initially, pseudo voltage source components in $(v_s)_n$ are made equal to those in $(v_s)_{n-1}$, and motor and other current values are computed using eqns.7.10 through 7.12. Then eqn.7.4 and the

drop across R_g are used to update the node potentials at S_4, S_5 and S_6 in $(v_s)_n$. This newly computed $(v_s)_n$ is used in eqn.7.9 again to update it in the same manner until two successive sets of current values agree within the allowed tolerance. Generally, not more than 4 to 5 iterations are required for every time increment in the integration process.

(ii)Motor speed is assumed to remain constant during current calculations over the chosen time-step and is given the change at the end of the time step by eqn.7.6.

(iii)Before the commencement of calculation for the next time-step ON and OFF states of the thyristors in the rectifier are ascertained. If the generated reference voltage through the PI controller equals the cosine law voltage of the next thyristor in the sequence, its representative resistance is made low at the same time making the R_{th} of the outgoing thyristor high.

(iv)Inverter frequency (ω_e) is obtained when a thyristor in the inverter module is triggered ON. Next thyristor in the sequence is turned ON 1/6th period, corresponding to this frequency, later and inverter frequency is adjusted again to determine the triggering instant for the next thyristor.

(v)Simulation of abnormal conditions for the system is carried out as shown in the last part of the flow diagram by assigning suitable ohmic value to the particular resistive element. For example, trigger failure of a thyristor, say, T_{h1} is declared by permanently keeping its representative resistance at a high value throughout the period of computation.

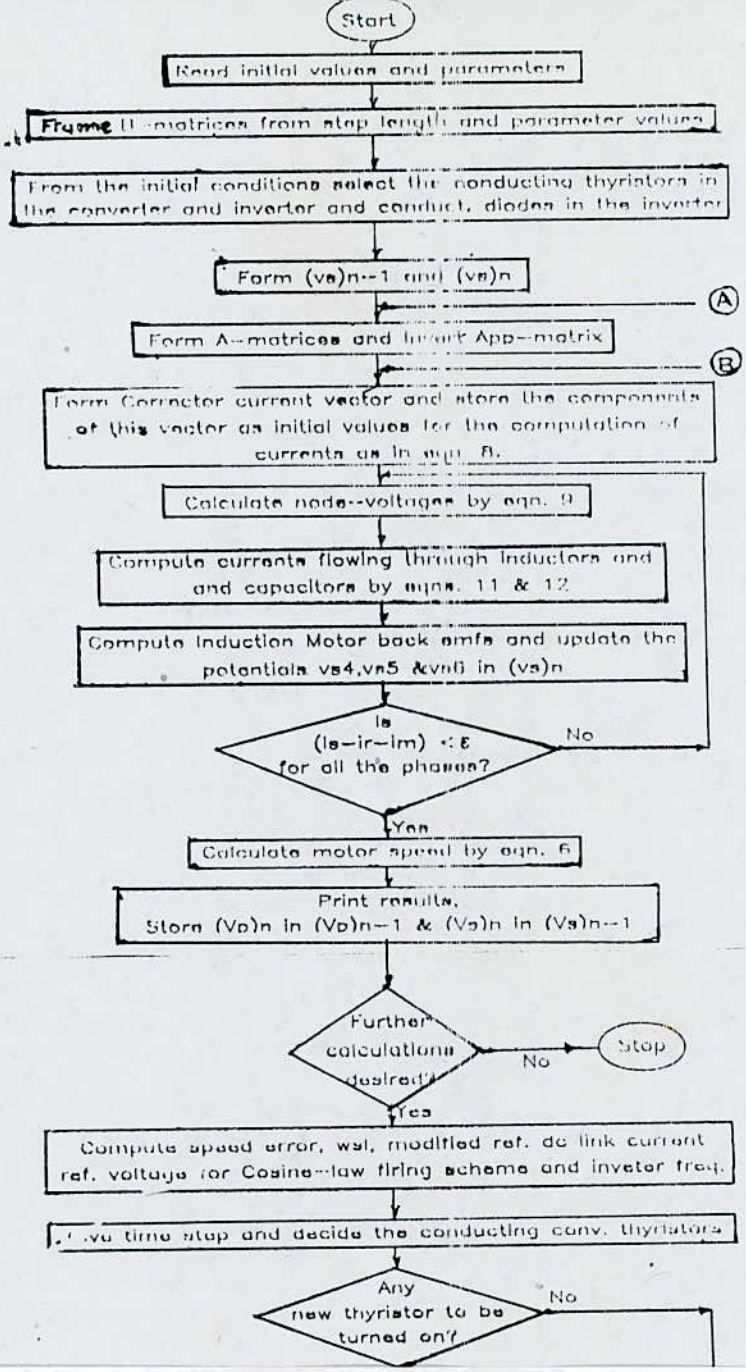
Start
Read initial values and parameters
Frame H-matrices from step length and parameter values
From the initial conditions select the conducting thyristors in the converter and inverter and conduct. diodes in the inverter
Form (vs)n--1 and (vs)n
A
Form A--matrices and Inverse App--matrix
B
Form Corrector current vector and store the components of this vector as initial values for the computation of currents as in eqn. 8.
Calculate node--voltages by eqn. 9
Compute currents flowing through inductors and and capacitors by eqns. 11 & 12
Compute Induction Motor back emfs and update the potentials vs4,vs5 &vs6 in (vs)n
Is (Is-ir-im) < ε for all the phases?
No
Yes
Calculate motor speed by eqn. 6
Print results.
Store (Vp)n in (Vp)n-1 & (Vs)n in (Vs)n--1
Further calculations desired?
No
Stop
Yes
Compute speed error, wsl, modified ref. dc link current ref. voltage for Cosine--law firing scheme and inveter freq.
...vs time step and decide the conducting conv. thyristors
Any new thyristor to be turned on?
No

7.2.4 Simulation results and discussion

Using the method outlined in the above sections, the simulated performances of a CSI-Induction motor drive system for both normal and abnormal conditions are obtained. The parameters of the induction motor I are presented in Appendix I and set conditions used in the simulation study are presented below

Thyristors and diodes:

On-state resistance value	0.05 Ω
Off-state resistance value	10.0 MΩ

Set point:

$(\omega_{sl})_{min}$ = 13.0 rad/sec $\quad\quad$ ω_m^*=150.0rad/sec

$(I_R)_{max}$ = 15.0 Amp

In Fig.7.6 are shown the results of computer runs which demonstrate typical performances under normal condition. For the same starting point and with controlled dc input voltage to the inverter Fig.7.7 shows the simulation results based on the method of Consoli & Abela [74] for the same type of closed loop control. A very close agreement between the traces in Figs.7.6 and 7.7 can be noted, thereby indicating that the nodal method can be relied upon for the digital representation of the system under study. To simulate 1.0 msec of the system the proposed method required 76.0 sec of CPU time on HP1000 with time step of 1.5 μsec while the method in [74] required 160 sec of CPU time with time step of 0.1 μsec. Smaller time step was needed in the later method owing to the essential requirement of small fictitious inductances in the circuit model, resulting in increased computer run

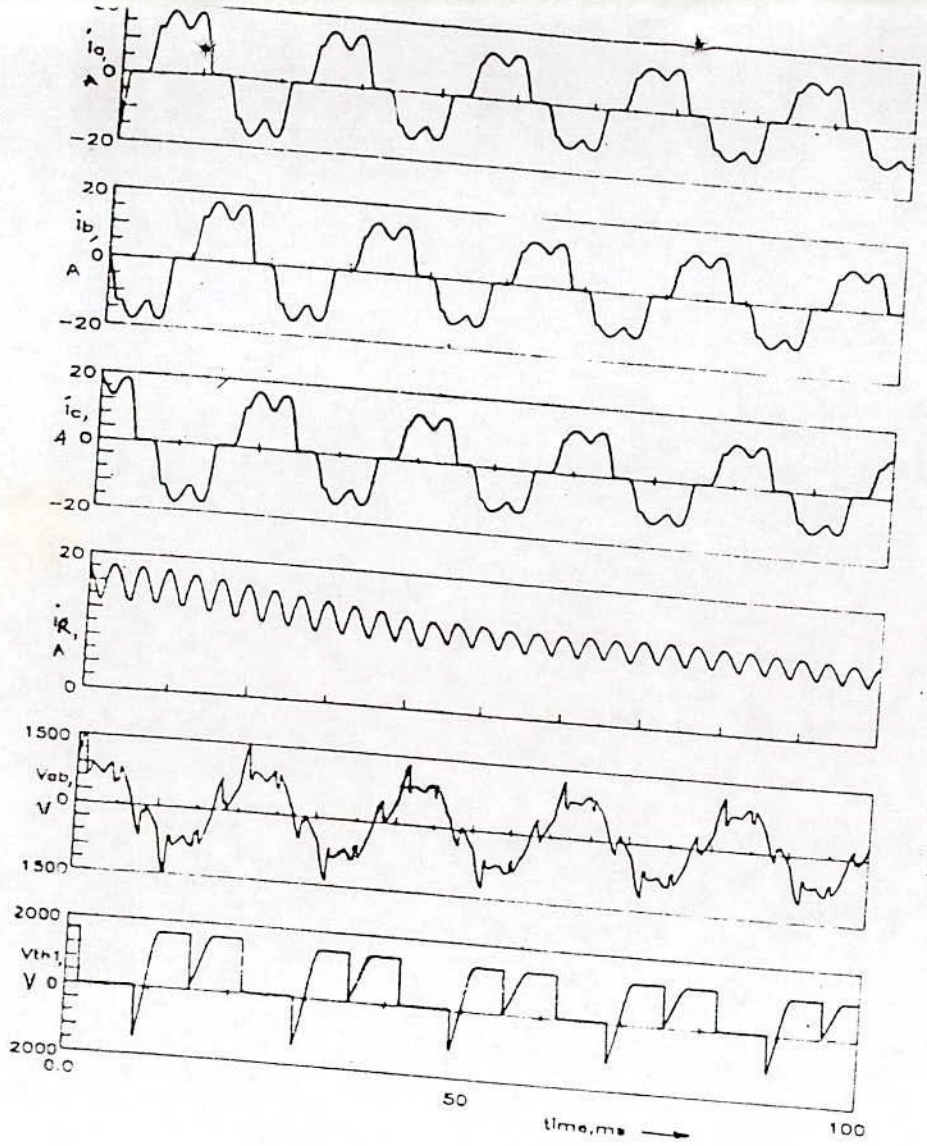

Fig.7.6 Simulation traces for normal operation by nodal method

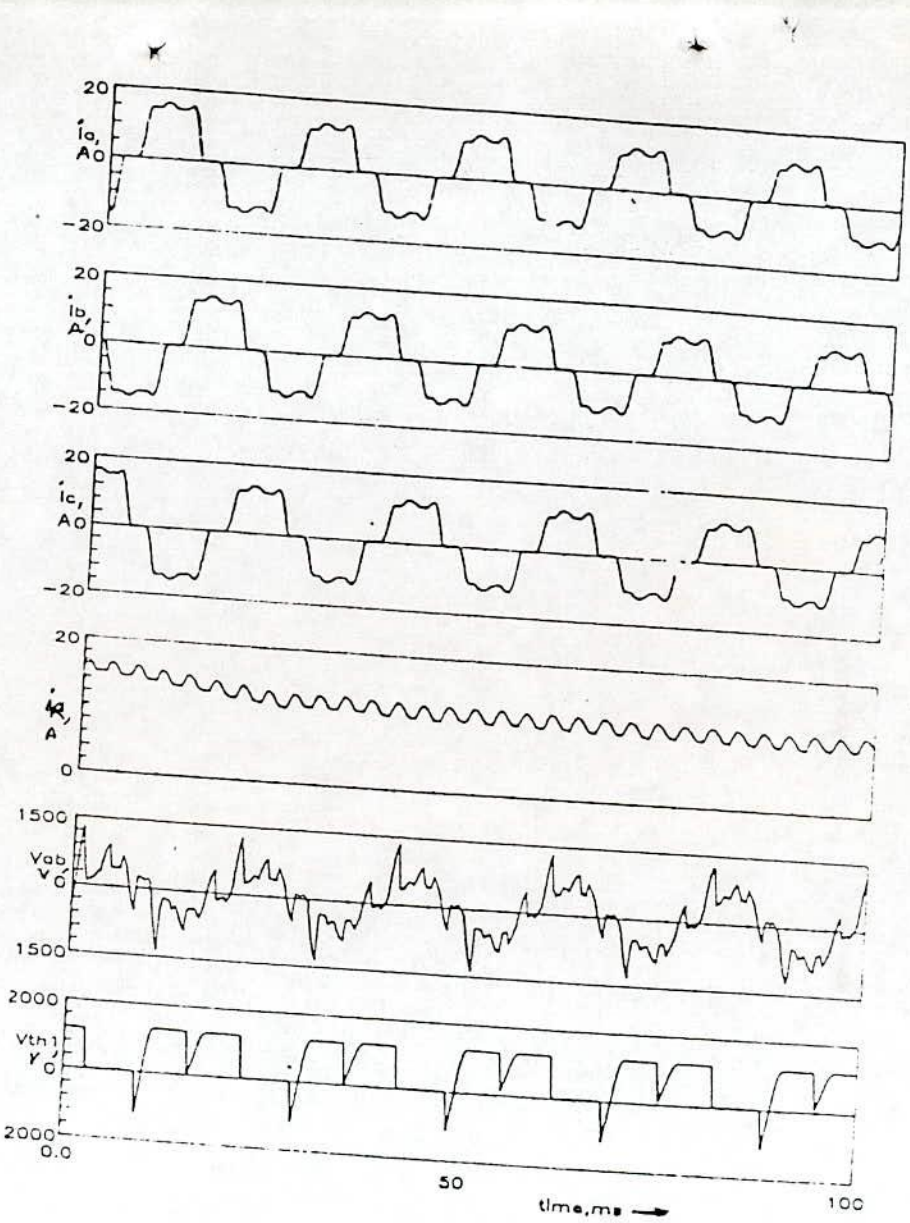

Fig.7.7 Simulation results by the method in Ref.74

time. On the other hand, the proposed method allows larger time step with the consequent reduction in the run time. Reduction in the time step of integration in the proposed method from 1.5μsec to 0.5μsec and variation in the representative on-state and off-state resistances around 0.05 Ω and 10.0 MΩ respectively by 50% did not show any significant variation in the results shown in Fig.7.6.

Specific abnormal situations were introduced in the system for simulation study by imparting and maintaining specific ohmic values to certain resistive elements in the circuit model. This demands no change in the circuit structure, basic equations and computer algorithm. Adjustment of certain parameter need be made only. Simulation following the breakdown of the diode D_1 due to reverse voltage, during ON states of Th_4 and Th_5 are shown in Fig.7.8. In this case, diode resistance is kept low throughout the computing period. This type of failure introduces significant asymmetry in the phase current waveforms but it does not lead to collapse of the inverter and the motor operation. No significant change in the counter emf waveform of the motor is noted, and the dc link current tends towards the set value.

Fig.7.9 presents the results for the failure of thyristor Th_1 to turn ON at the instant when its turning ON is due. This is simulated by keeping always its resistance high. DC components of current are seen to exist in all the phases. This observation is in conformity with the analog simulation results noted in [73]. It is evident from the traces of counter emf and speed in Fig.7.9 that the thyristor failure does not totally upset the working of the motor. It is noted that the diode D_1

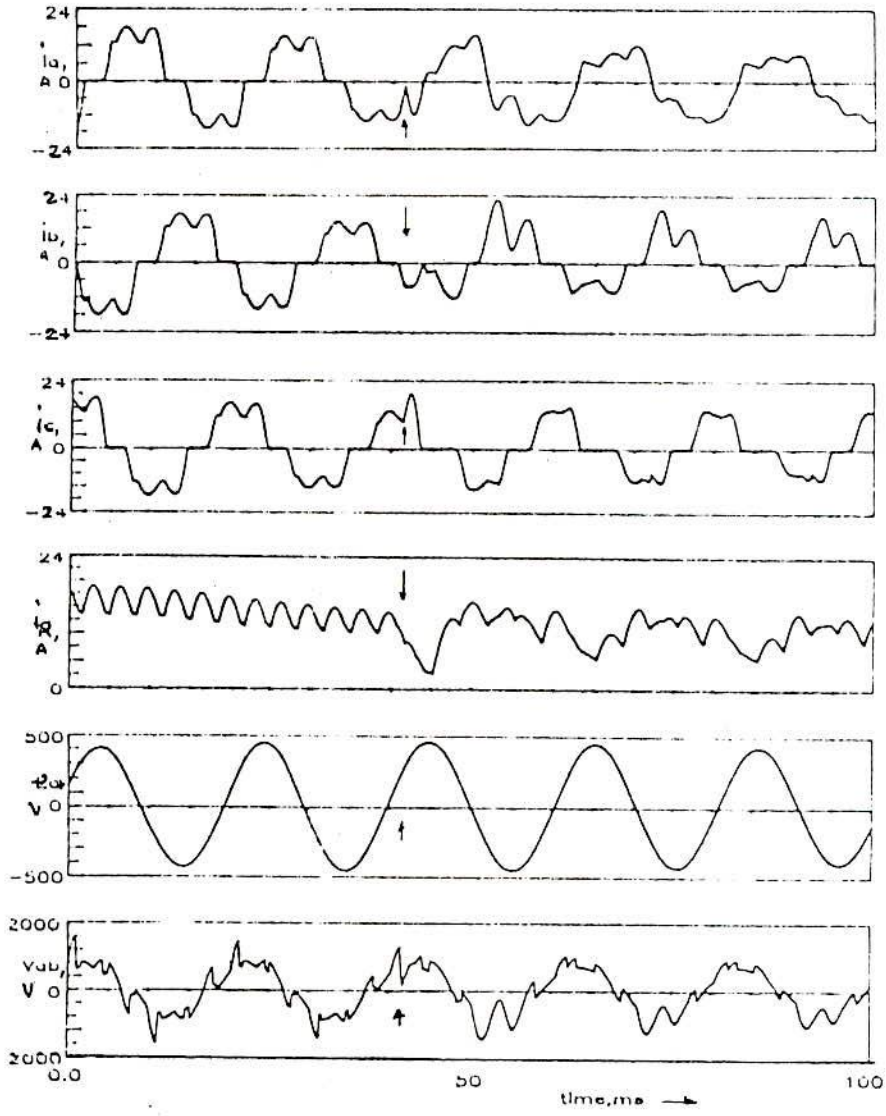

Fig.7.8 *Diode short circuit—failure of D1*

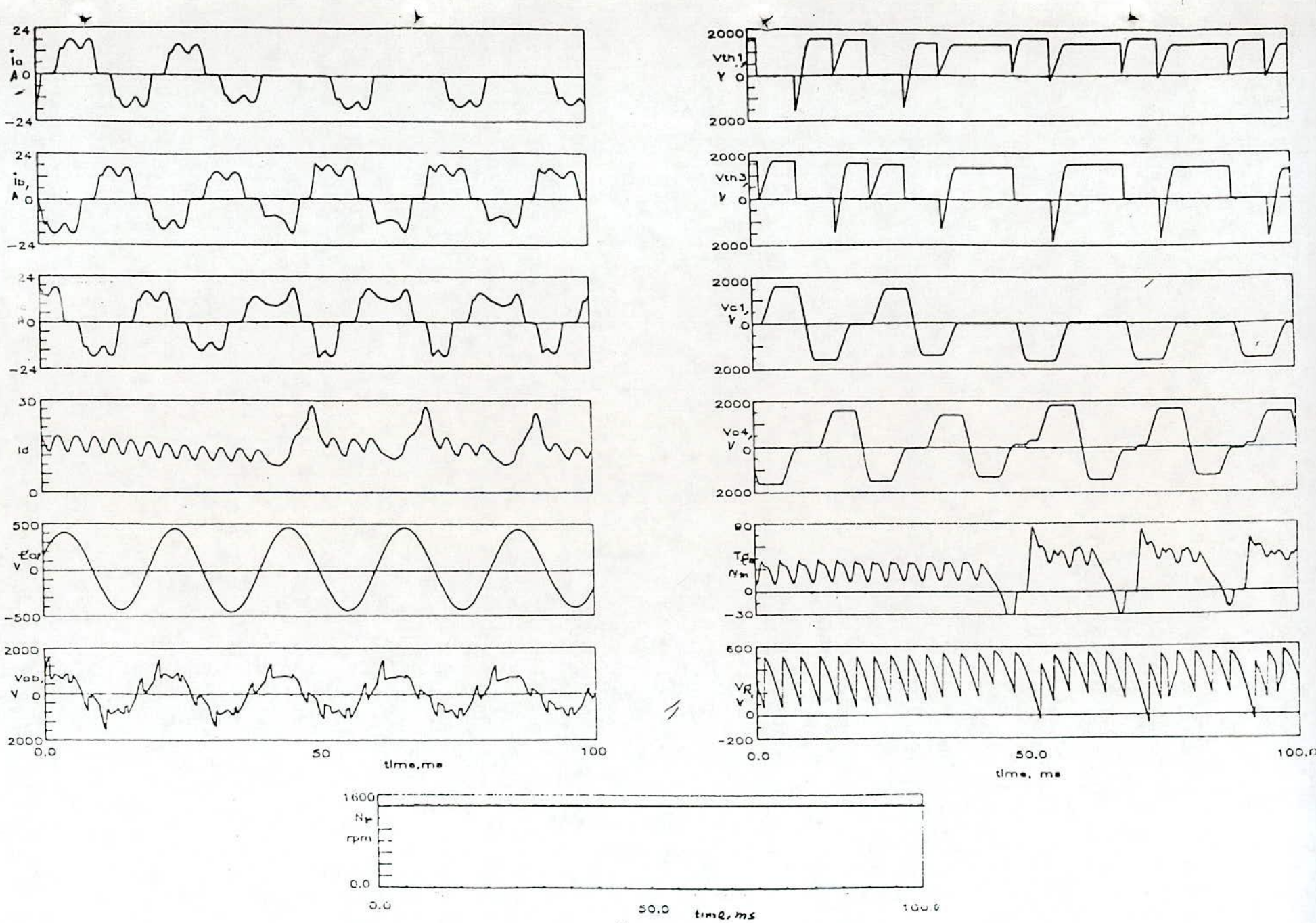

Fig.7.9 *Failure of a thyristor(Th1) to turn ON*

experiences a significant overvoltage while the thyristor Th_1 continues to experience forward voltage equal to the capacitor voltage separated by commutating notches at the intervals of $\frac{2}{3}\pi$ and $\frac{4}{3}\pi$. It is due to the conduction of the tyristors Th_3 and Th_5 respectively, for the above periods. Appearance of peaks in the dc link current is due to simultaneous conduction of thyristors Th_5 and Th_2 for a very brief period during which currents in the stator windings are absent. Development of negative electromagnetic torque can be explained by the fact that temporary reversal of phase sequence takes place during the period when 'c' phase is forcibly made to carry positive current, beyond its normal period, in place of the phase 'a' winding that should have carried the positive current while the 'b'phase still is carrying the negative current.

Results of simulation study for terminal to terminal short circuit are given in Fig.7.10. Short-circuit between the terminals 'a' and 'b' is made when the capacitor voltage across C_4 becomes zero following the turning ON of the thyristor Th_6 (i.e., Th5 and Th_6 in the conducting state). Current waveforms of the short-circuited phases not only differ significantly from that of the current in phase 'c' but also contain dc components that circulate between them. Periodic shoot up in the dc link current is owing to occasional brief short circuits between the thyristor pairs Th_1 and Th_6 or Th_3 and Th_4 via the short circuit link. In fact, severity of the situation and waveform patterns depend on the devices conducting at the instant of short circuit and the capacitor voltage prevailing at that instant. However, the general trend does not

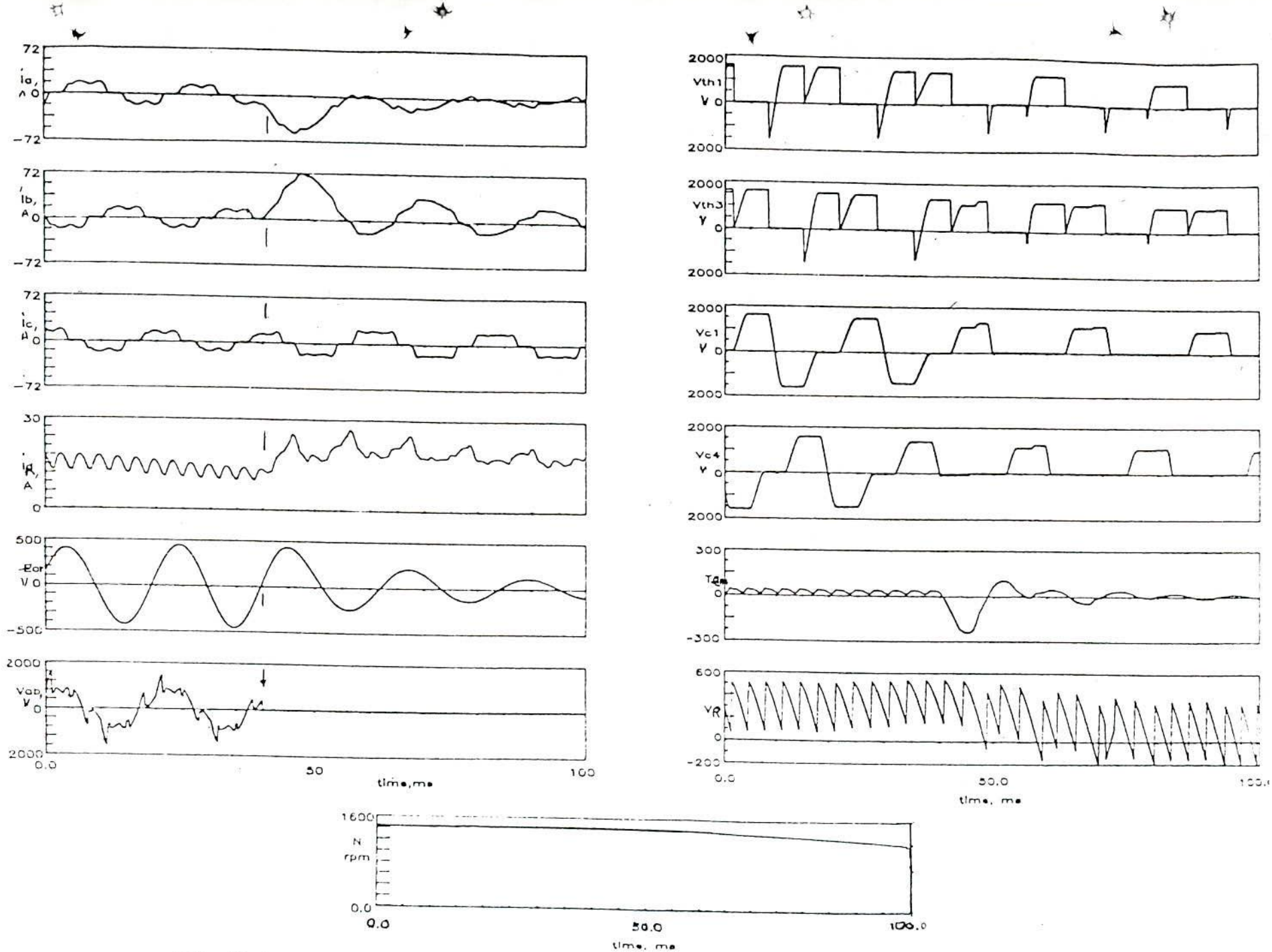

Fig.7.10 *Short circuit of terminals 'a' and 'b'*

differ much from that shown in Fig.7.10. The machine gradually approaches towards the stalling condition.

Open circuit of a motor terminal (phase 'a' in this case) is simulated by making the extra series resistance (R_{se2}) very high. The simulation results are shown in Fig.7.11 which indicate that the failure is of severe type and demands immediate switching off as the voltages across the devices, components and motor terminals and currents as well proceed towards damaging level.

7.2.5 Conclusion

The Nodal method using the trapezoidal integration algorithm is found to be capable to predict the behaviour of a converter controlled auto-sequentially commutated inverter driven induction motor for normal modes as well as for many different modes of failure. All operation of the system can be studied without resorting to different circuit models for different modes of operation as have been the cases with many earlier studies. There is no extra element in the circuit model in Fig.7.2 except the high grounding resistance R_g to define certain node potentials. The model retains the three stator variables explicitly and does resort to any co-ordinate transformation. The computation is faster than that described in [74] owing to the elimination of small fictitious inductances in the circuit model of the proposed method to transduce device currents in the simulation. Another important aspect of the present simulation study is that the counter emf adjusts itself to cope with changing operating condition unlike the constant amplitude or proportional to frequency arrangement as is necessary in hybrid computer simulation [73].

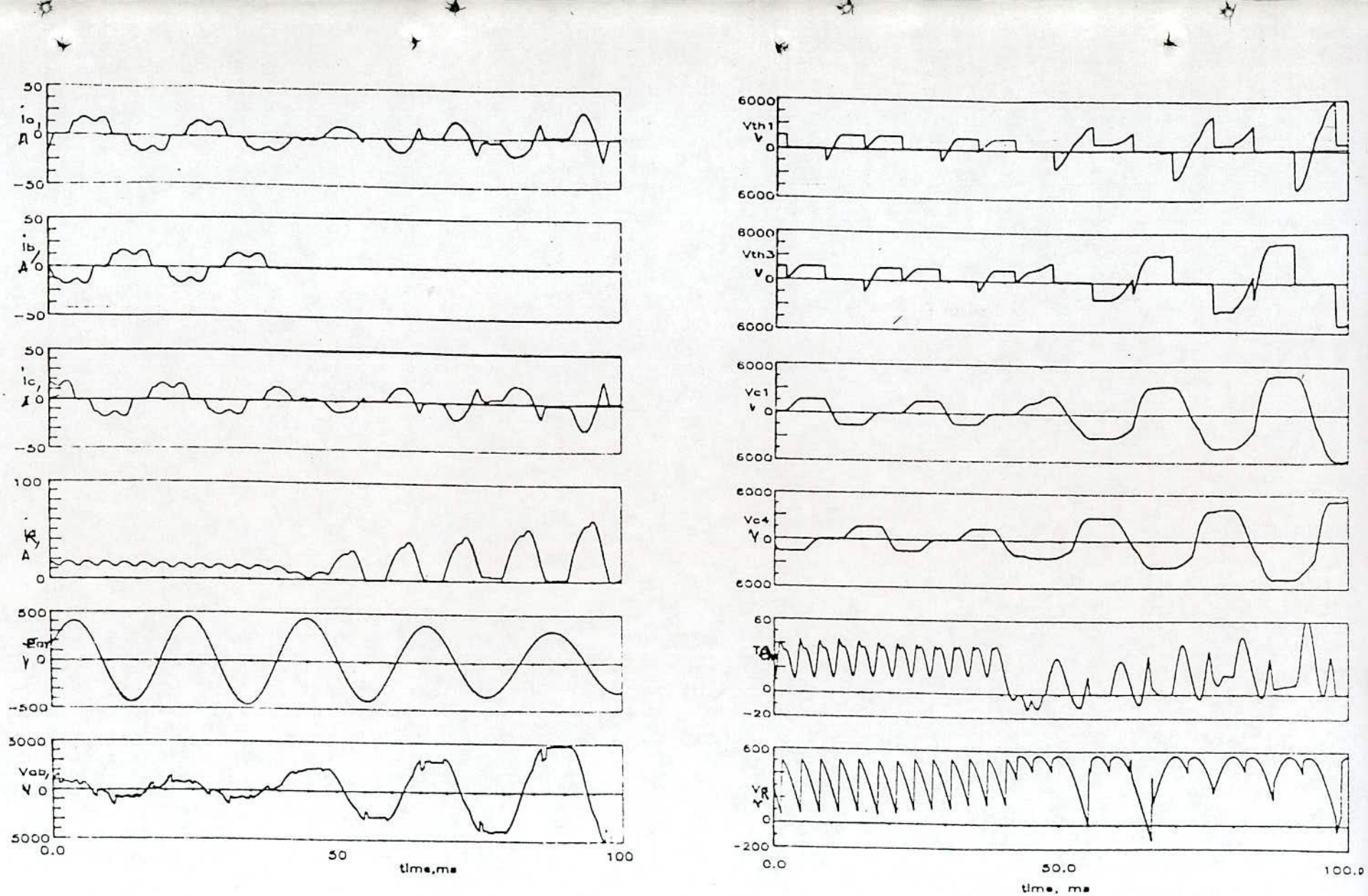

Fig.7.11 *Open circuit of 'b' phase terminal*

7.3 BOND GRAPH METHOD OF SIMULATION

Realistic simulation implies close contact with the actual physical arrangement on one side and a quantitative description in terms of equations on the other side to obtain its dynamic behaviour or steady state characteristics. Bond graph technique is such a link which is based on the flow of power/energy between system elements irrespective of their domains [77, 78]. A CSI-IM drive consists of electrical, electronic, magnetic and mechanical subsystems with non-linearities, and is thus most suited for modelling by bond graph technique. This provides us with a pictorial representation of the entire system by generalized letter symbols and line segments, called bonds. To each bond is associated **effort**(voltage/torque/force) and **flow**(current/rotational speed/velocity) information, the product of which is power. These bonds thus represent transfer of power between system components and junctions. Systematic procedure exists [109] for the generation of state equations from the bond graph and this can readily be acquired through computer software that accepts the structure code, checks the causalities and sets up state equations for another program(a Pascal file in this instance) which yields solution in time domain. The main advantage of the Bond graph approach is its ability for orderly and progressive model development even for situations, which would otherwise demand hard manual labour if approached by conventional procedures, and tedious writing of equations can thus be avoided.

In the matter of systematic method of assembling the differential equations for automatic compilation and simulation one has to use of

combinatorial methods such as graph theories. "In this respect Linear graph theory and Bond graph theory can be placed in parallel since the two methods are simply different pictorial representation of the same combinatorial information", [110]. The motivation for undertaking the simulation study of a specific circuit configuration through bond graph is spelt out in the following paragraph and in the conclusions at the end. In this context, attention of the interested readers is drawn to the papers in [110-113].

Modelling and simulation based on bond graph technique for various mechanical systems are well documented [77, 79, 114]. Contrary to these, very few references are available in Electrical Engineering discipline and these are mostly related to the simulation of networks [77, 115]. For the last 25 years as computer-aided design research organized and "mechanized" the compilation of electric circuit equations for digital simulations, bond graphs have been largely ignored. Application of bond graphs in electromechanical devices is minimal. A step towards modelling of synchronous machines by D. Sahm [80] opened a new dimension in the simulation of dynamics of electrical machines. Sirivadhna et al [81] have discussed the application aspects of bond graph in the field of electrical machines but no simulation results have been provided. To the authors knowledge, no work on simulation using bond graph structure for drives fed through power electronic circuits has so far been reported. The main objective in this section is to present the bond graph modelling technique to simulate an induction motor drive system fed from an adjustable dc voltage source through an Auto-Sequentially commutated Currant source

Inverter. The induction machine is represented by the mutually perpendicular α-β model in a stationary reference frame, and is linked with the three phase current source inverter by a power conserving transformation which is taken as displacement modulated transformer structure in the bond graph model. A specific digital simulation program (**COSMO-CAD**) yields state space representation of the system from the bond graph structure. In this respect no reference to particular circuit configurations, representing various modes, during normal or abnormal operation is required. The acceptability of the simulation technique is shown by comparison of some results with those obtained from an available method of simulation.

7.3.1 The drive system and its equivalent circuit

The basic power circuit taken for study is a CSI-IM drive with independent current and frequency control as shown in Fig.7.12. As the aim is directed to have a realistic modelling for the CSI-IM system, the dc voltage of the rectifier is assumed to have no ripple component and its value is adjusted by closed loop current control with PI controller and the frequency of the inverter is adjusted by the slip speed control strategy. The circuit for the inverter-motor part to be used in the simulation study is shown in Fig.7.13.

Bond graph is explicitly based on the physical structure of the system in which conservation of energy is implied. The CSI-IM system comprises modules of induction motor and its mechanical load, thyristors and diodes, dc link filter, commutating capacitors, dv/dt protecting snubbers, di/dt limiting reactors, observers and

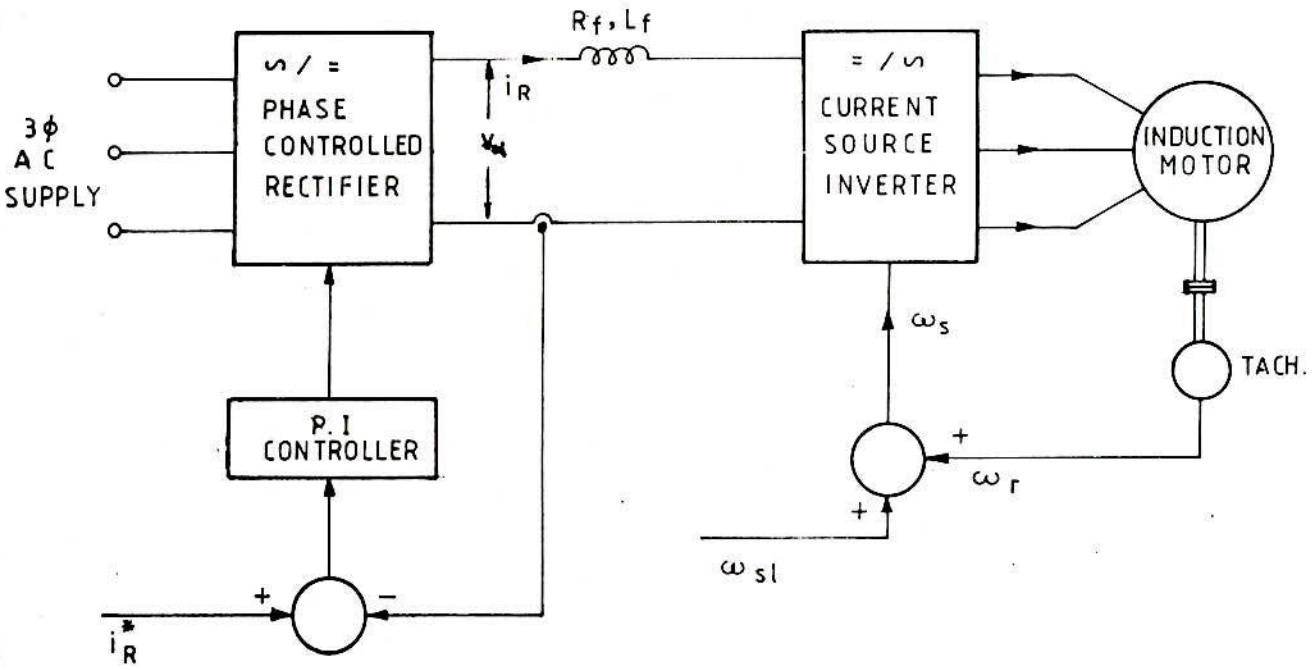

Fig. 7.12 Power circuit arrangement – Independent current and slip-speed control.

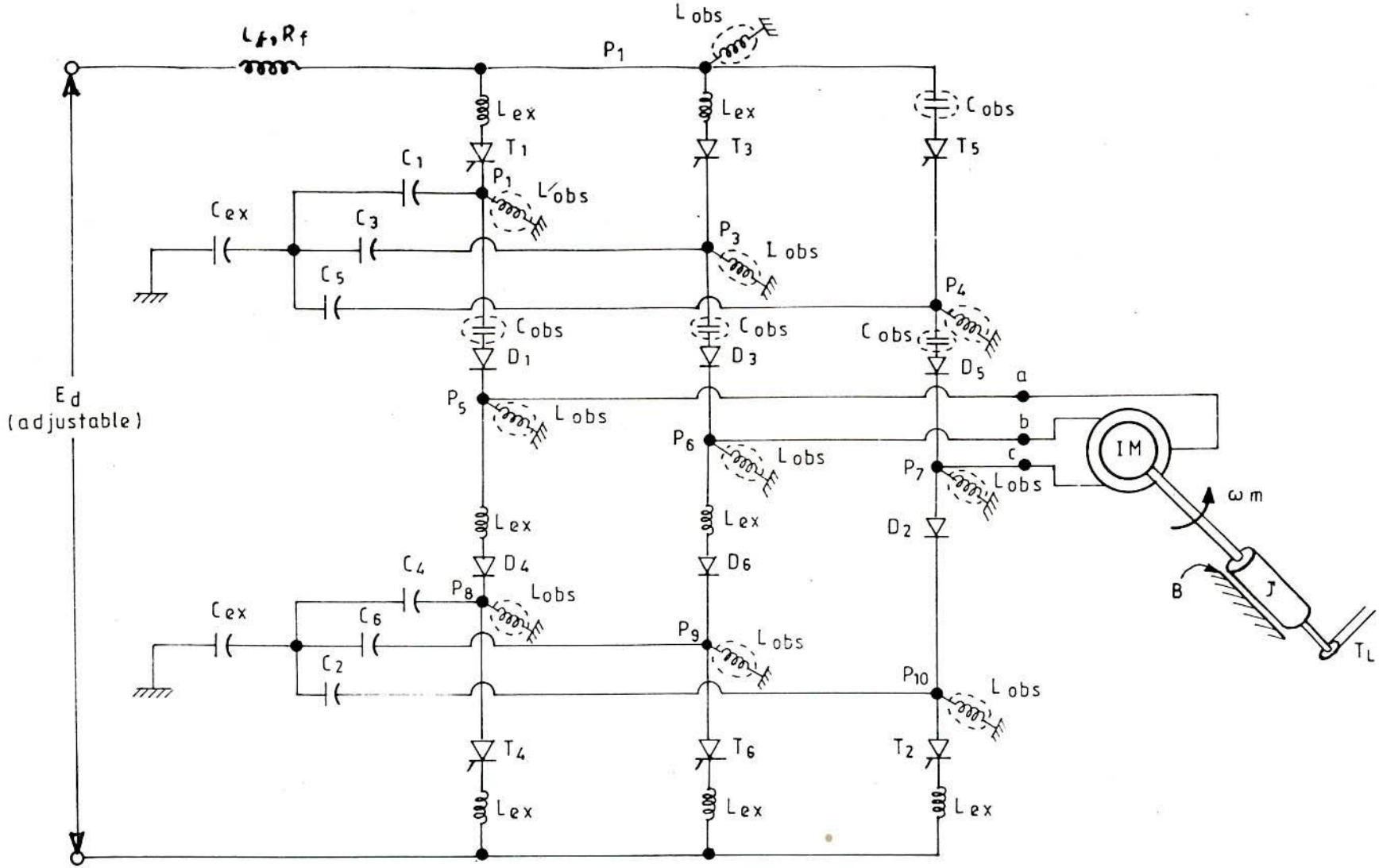

Fig. 7.13 CSI-IM system with extra-energy storing spurious elements and observers.

controllers. Thus the model for the simulation of CSI-IM drive system becomes very large and complex one if all the energy storing and dissipative elements of the system are considered and the solution becomes time consuming. So to obtain a manageable dynamic model describing the drive system, without the loss of reality, certain assumptions need be made. To have fast computer solution certain dissipative and energy storing elements which have very little impact on the performance of the system and which do not interfere significantly in the energy flow pattern in the simulation process, such as core loss of the induction motor, dv/dt snubbers of the semiconductor switches etc., are neglected. In doing so, the problems of causality and algebraic loops are kept in mind , and such elements are not removed those are absolutely necessary to overcome causal conflicts. For these reasons, some di/dt limiting reactors are retained in the circuit. In an actual current controlled inverter each set of three commutating capacitors is usually delta connected and this creates causal loop in bond graph modelling. Hence, they are replaced by a star connected set of capacitors with their common node connected to ground through a capacitor having a very low numerical value. The equivalent circuit in Fig.7.13 further indicates the location of observers to measure voltages and currents at various points. A capacitor observer is to measure the the current while an inductor is to measure the voltage. They are made dummy elements and do not cause any interference in the simulation of the system. This is briefly discussed in Appendix IV. Alternatively, linkages with inductors in series may be used to observe current if such linkages are expressible in terms of the other state variables.

7.3.2 Bond graph representation of the CSI-IM system

Induction Motor

It is well documented in the literature [116] that an induction motor can be adequately modelled using a two axis representation. Under the usual assumptions of sinusoidal distribution of MMFs, ignoring the effect of iron loss and saturation, etc., the dynamic equations which describe a symmetrical induction motor in orthogonal stationary reference frame α-β fixed on the stator may be expressed as:

$$\begin{bmatrix} v_{\alpha s} \\ v_{\beta s} \\ 0 \\ 0 \end{bmatrix} = \begin{bmatrix} R_s+L_s p & 0 & L_m p & 0 \\ 0 & R_s+L_s p & 0 & L_m p \\ L_m p & L_m\omega_r & R_r+L_r p & L_r\omega_r \\ -L_m\omega_r & L_m p & -L_r\omega_r & R_r+L_r p \end{bmatrix} \begin{bmatrix} i_{\alpha s} \\ i_{\beta s} \\ i_{\alpha r} \\ i_{\beta r} \end{bmatrix} \qquad (7.13)$$

The developed electro-magnetic torque for an induction motor of P_P-pole pairs is

$$T_{em} = P_P \left(i_{\alpha r}\left[L_m i_{\beta s} + L_r i_{\beta r} \right] - i_{\beta r}\left[L_m i_{\alpha s} + L_r i_{\beta r} \right] \right) \qquad (7.14)$$

and the motor balance equation is

$$T_{em} = J\frac{d\omega_m}{dt} + B\omega_m + T_L \qquad (7.15)$$

In the above equations

$v_{\alpha s}, v_{\beta s}$ α- and β-axis stator voltages

$i_{\alpha s}, i_{\beta s}$ α- and β-axis stator currents

$i_{\alpha r}, i_{\beta r}$ α- and β-axis rotor currents

Equations 7.13 and 7.14 need be written in proper format with respect to the axis quantities that enables one to draw the bond graph structure of the machine model. They are rewritten as:

$$\begin{bmatrix} v_{\alpha s} \\ 0 \end{bmatrix} = \begin{bmatrix} R_s & 0 \\ 0 & R_r \end{bmatrix} \begin{bmatrix} i_{\alpha s} \\ i_{\alpha r} \end{bmatrix} + \begin{bmatrix} L_s & L_m \\ L_m & L_r \end{bmatrix} p \begin{bmatrix} i_{\alpha s} \\ i_{\alpha r} \end{bmatrix} + \begin{bmatrix} 0 \\ MGY1+MGY2 \end{bmatrix} \omega_r \qquad (7.16)$$

$$\begin{bmatrix} v_{\beta s} \\ 0 \end{bmatrix} = \begin{bmatrix} R_s & 0 \\ 0 & R_r \end{bmatrix} \begin{bmatrix} i_{\beta s} \\ i_{\beta r} \end{bmatrix} + \begin{bmatrix} L_s & L_m \\ L_m & L_r \end{bmatrix} p \begin{bmatrix} i_{\beta s} \\ i_{\beta r} \end{bmatrix} - \begin{bmatrix} 0 \\ MGY3+MGY4 \end{bmatrix} \omega_r \qquad (7.17)$$

$$T_{em} = P_P \{[MGY1+MGY2] i_{\alpha r} - [MGY3+MGY4] i_{\beta r}\} \qquad (7.18)$$

where, modulated gyrators MGYs are:

$MGY1 = L_m i_{\beta s}$

$MGY2 = L_r i_{\beta r}$

$MGY3 = L_m i_{\alpha s}$

$MGY4 = L_r i_{\alpha r}$

A transformer(**TF**) relates **effort**(voltage/force/torque) to effort and **flow**(current/velocity/ rotational speed) to flow. A gyrator(**GY**) expresses the property that a flow at one side exerts an effort on the other side and vice-versa. This is implied in equations 7.16 to 7.18 where modulated gyrators(MGYs) convert flow to effort. They are termed modulated gyrators, because the gyration coupling between the variables concerned depend on external variables. In order that the equivalent machine may represent the real three phase machine in respect of power development at every instant of time its two phase quantities viz., voltage and current, must be related to the corresponding three-phase quantities by the following well known transformation [116] in compliance with the torque expression accepted in equation 7.14.

$$[C] = \begin{bmatrix} \sqrt{\frac{2}{3}} & -\sqrt{\frac{1}{6}} & -\sqrt{\frac{1}{6}} \\ 0 & \sqrt{\frac{1}{2}} & -\sqrt{\frac{1}{2}} \end{bmatrix} \qquad (7.19)$$

In vector matrix notation, α-β and **a-b-c** quantities are related by

$$[F_{\alpha\beta}] = [C][F_{abc}] \qquad (7.20)$$

where **[F]** is either **[v]** or [i] column vector. For representing eqn.7.20 in bond graph structure the elements in (7.19), which are to couple the model two phase machine with the three-phase terminals of the inverter are rewritten as follows in compliance with the terminology in the bond graph literature [77].

$$[C] = \begin{bmatrix} \frac{1}{TF_1} & \frac{1}{TF_2} & \frac{1}{TF_3} \\ 0 & \frac{1}{TF_4} & \frac{1}{TF_5} \end{bmatrix} \qquad (7.21)$$

where **'TF'** stands for modulus of transformer.

Fig.7.14 shows the bond graph structure developed for the equivalent two-phase induction motor on the basis of eqns 7.16 to 7.18 and the transformation matrix in (7.21). The assignment of power flow direction is straightforward, and the graph is made causal, using normal conventions, to determine the number of necessary and sufficient state variables during its run on the computer. Integral causality has been assigned to the generalized inertia elements. Three distinct sections are indicated in Fig.7.14 adjacent to appropriate hardware components, viz. transformation from three-phase to two-phase quantities, electrical part of the model machine, and the mechanical

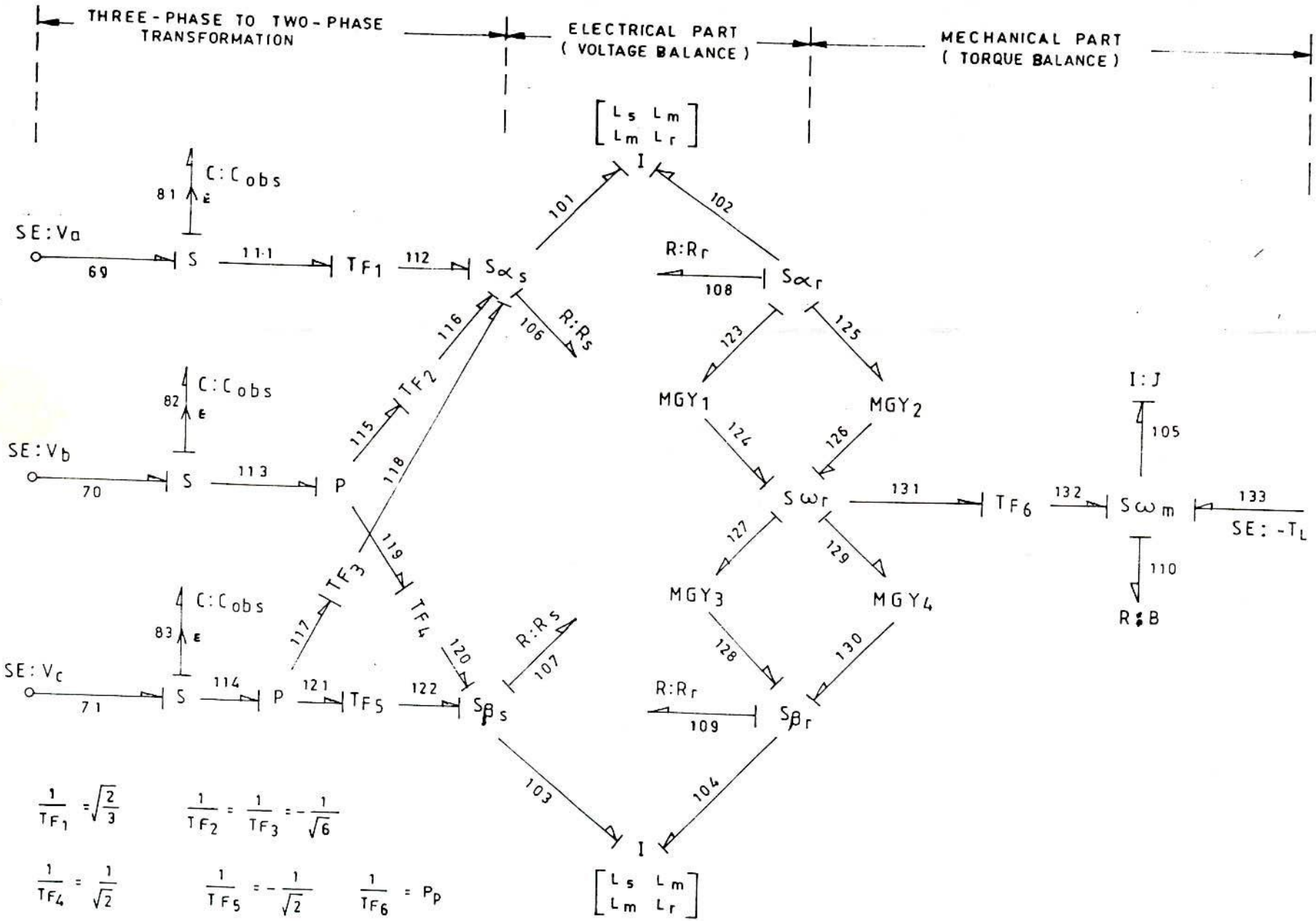

Fig.7.14 Bond graph structure of the Induction Motor and its mechanical load.

part of the drive. Inductance matrices in eqns. 7.16 and 7.17 appear as two-port inductance field (I-field) in the structure of Fig. 7.14. An I-field [77] takes into account of all inductances and is manifested as a single entity. Each two-port I-field is connected with the rest of the system by only two bonds having integral causality as shown.

Thyristor model

Thyristors are modelled as low and high resistors during its **ON** and **OFF** states respectively. The value of the resistor is decided by the triggering sequence chosen for the inverter operation. A thyristor is made **ON** when it is in the forward biased state and goes into **OFF** state when its current falls below the holding current. So observers are required to know the current flowing through and potential across a thyristor. Fig. 7.15 shows the bond graph model of a thyristor equipped

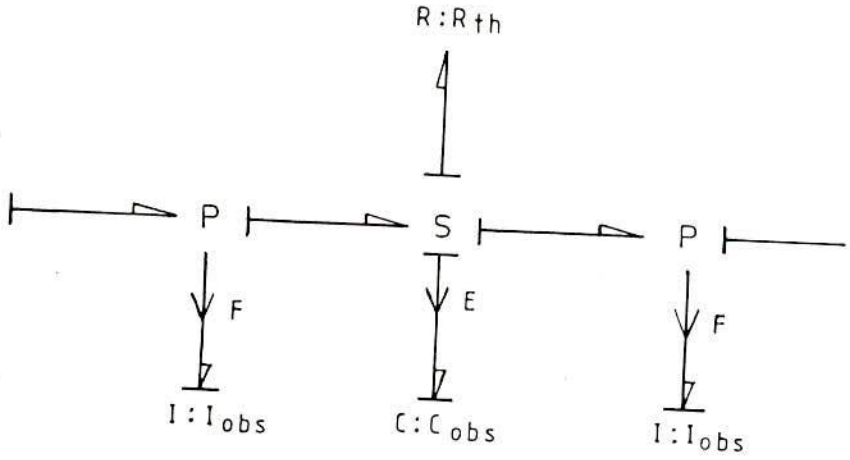

Fig. 7.15 Bond graph model of a thyristor with observers.

with its observers. Bonds connected in the structure for the observers are represented by a full arrow and a symbol indicating type of activation. A capacitor element is used as a current observer and an inductor as a voltage observer.

Diode model

Like thyristors, diodes are also modelled as resistors. But instead of assigning two extreme values(low and high) an approximate **v-i** characteristic is chosen to estimate the diode resistance during its conduction mode. The forward characteristic chosen is of the form

$$v_d = v_{do} + k\, i_d \qquad i_d \geq 0 \tag{7.22}$$

when diode voltage falls below V_{do} or it is in the reverse blocking state, diode resistance is made very large. The representative resistance is kept constant over the time step ΔT_{i-1} and the drop across it at the end of this time step is used to modify the diode resistance for the next time step ΔT_i. This is indicated in Fig.7.16

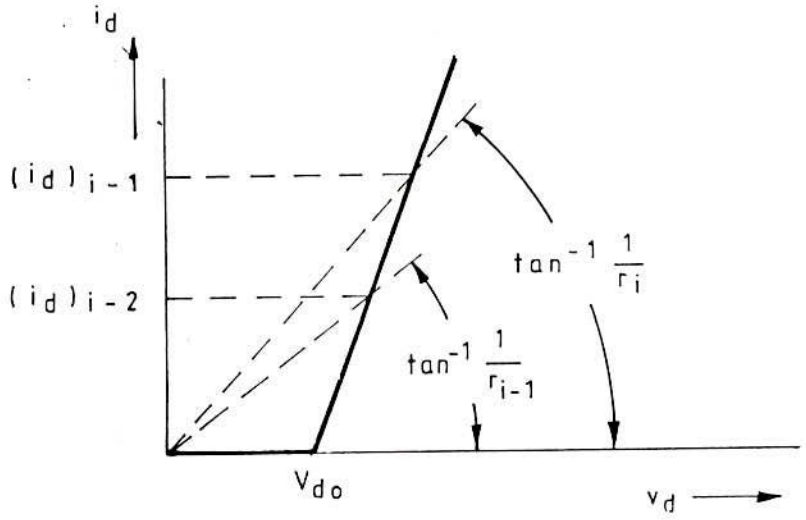

Fig.7.16 Diode characteristic and equivalent resistance.

The reason for adjusting a diode resistor, unlike a thyristor, is that the current through the commutating capacitor gradually decreases to

zero and the charge reversal takes place. Abrupt change in the diode resistance from low to high value, even when the current is small, results in severe abnormality in the numerical computation causing irregular potential pattern and computation becomes slow. To ascertain the effort and flow conditions of a diode, current observer in series with it and potential observer at the ends of the diode are incorporated, and the bond graph of the diode assumes the same structure as that of a thyristor as shown in Fig. 7.15.

Controller

In the scheme shown in Fig. 7.12 the dc voltage of the phase controlled rectifier is adjusted by a proportional integral(PI) controller in the current feedback control loop. If the gate signals for the thyristors are obtained from an inverse-cosine firing-angle control scheme, the output voltage of the rectifier can be expressed as

$$V_R = \left(\frac{1+\tau_1 p}{\tau_2 p}\right)\left(I_R^* - I_R\right) \tag{7.23}$$

where I_R^* is the set value of the dc link current and τ_1 and τ_2 are the controller gain constants. In terms of a new variable Q [75] the rectifier voltage in (7.23) can be expressed as:

$$V_R = Q + \frac{\tau_1}{\tau_2}\left(I_R^* - I_R\right) \tag{7.24}$$

where,

$$\frac{dQ}{dt} = \frac{I_R^* - I_R}{\tau_2} \tag{7.25}$$

Q can be identified to be the output of the integral controller.

As (7.24) and (7.25) are already in the appropriate mathematical form, these need not go into bond graph structure. In the resulting state equations, which will come out from the integrated bond graph structure for the dc link, inverter and motor, V_R will be replaced by (7.24), and (7.25) will add to the set as an additional state equation.

Complete bond graph of the CSI system

Based on the resistance models for thyristors and diodes, discussed in this sub-section, the complete bond graph structure of the CSI network is shown in Fig.7.17. Both current and voltage observers indicated by respective encircled elements in Fig.7.13, have been inserted at appropriate points in Fig.7.17. The output terminals **a, b, c,** in Fig.7.17 serve as inputs to the structure in Fig.7.14 for Induction Motor.

7.3.3 Simulation results

The bond graph processing program **COSMO-CAD** [109] adapted for use on an APOLLO computer was availed of for digital simulation. It has been indicated earlier that the software accepts the structure code, checks the causalities and sets up state-space equations for another program which yields time-domain solution. Runge-Kutta-Fehlberg six order method for integration with variable step length was used to obtain time-domain solution. In order to avoid algebraic loops and derivative causalities, certain spurious/unimportant C and I elements were added/retained in the system in Fig.7.13. This, however, enhances the order of the state vector, and at the sametime, increases the computation time owing to their very low numerical values resulting in

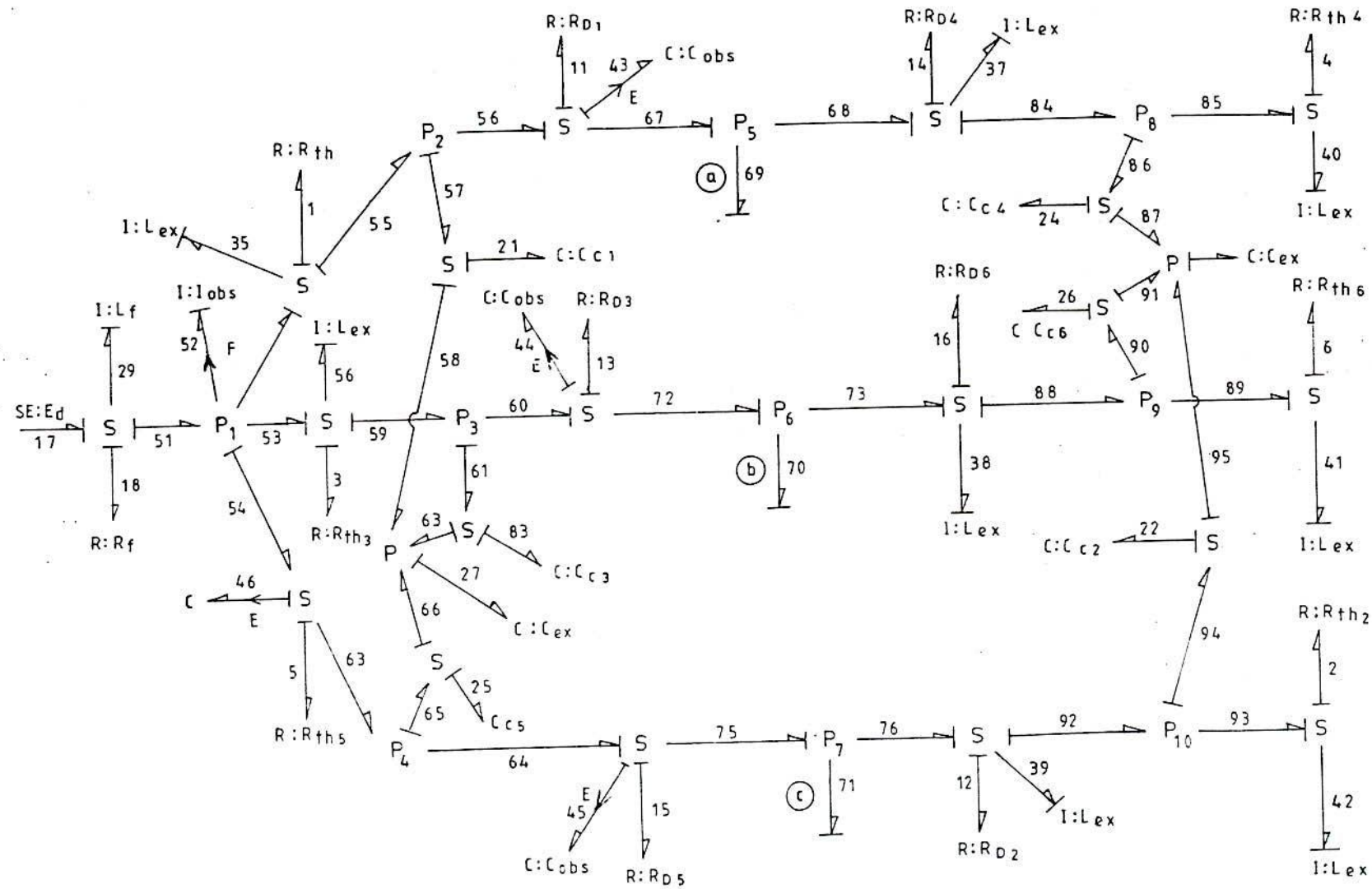

Fig.7.17 Composite bond graph of the CSI system.

small time constants. The values had to be made small to evade their impression on the performance of the system. In order to effect economy in the computation time, these elements were deprived of their power handling capabilities by equating $\frac{d}{dt}(p=Li)$ equal to zero for 'I' elements and $\frac{d}{dt}(q)$ equal to zero for 'C' elements. The algebraic equations obtained in this manner were used to eliminate the state variables associated with these spurious elements from the rest of the equations. Such exercise produces little loss of reality, does not significantly affect the accuracy of the results and at the same time, speeds up computation.

The proposed simulation method was applied to a CSI-Induction Motor drive system represented in Fig.7.12. The parameters of the motor, inverter, dc link etc are given in Appendix-V. For this system, current and slip-speed controllers were set for 70A and 10 rad/sec respectively. Fig.7.18 shows the simulation traces under steady state operation, for motor input currents, dc link current, thyristor(Th1) voltage and the line voltage v_{ab} for a load torque of 50Nm. In order to establish the acceptability of the proposed simulation technique, the same system quantities were computed for the drive system (Fig.7.12) by another digital simulation approach suggested by Consoli and Abela [74]. The results obtained by this approach are shown in Fig.7.19, and these are found to be in good agreement with those in Fig.7.18. Likewise simulation runs for different operating conditions (normal, abnormal and transient) were made and a reasonable correspondence was observed between the results obtained by these two approaches, thereby confirming the acceptability of the bond graph method of modelling and

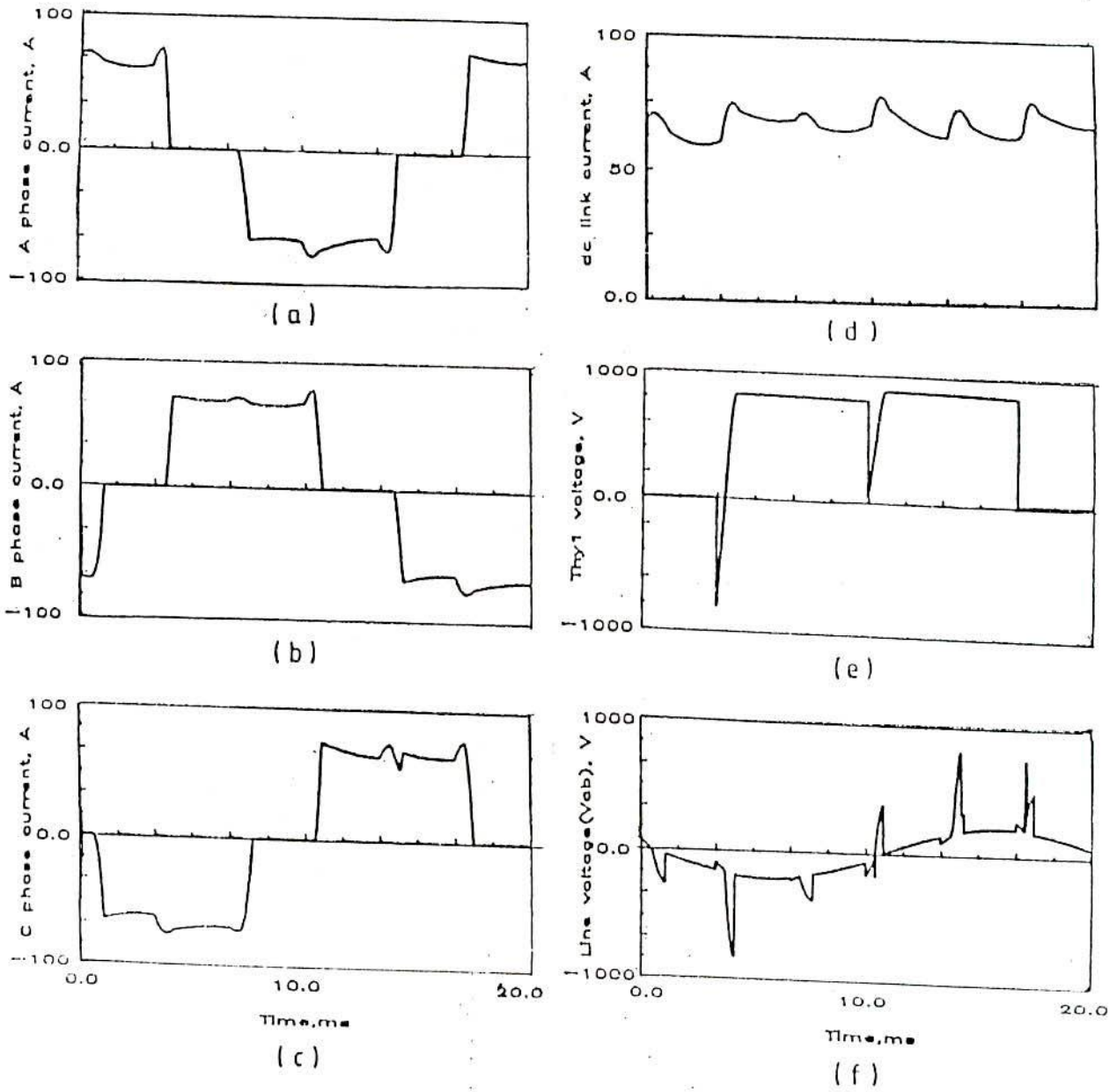

Fig.7.18 Simulation Traces by Bond Graph Method (Normal Operation)

(a) to (c) motor line currents; (d) d.c. link current; (e) T_{h1} voltage; (f) motor terminal voltage, v_{ab} .

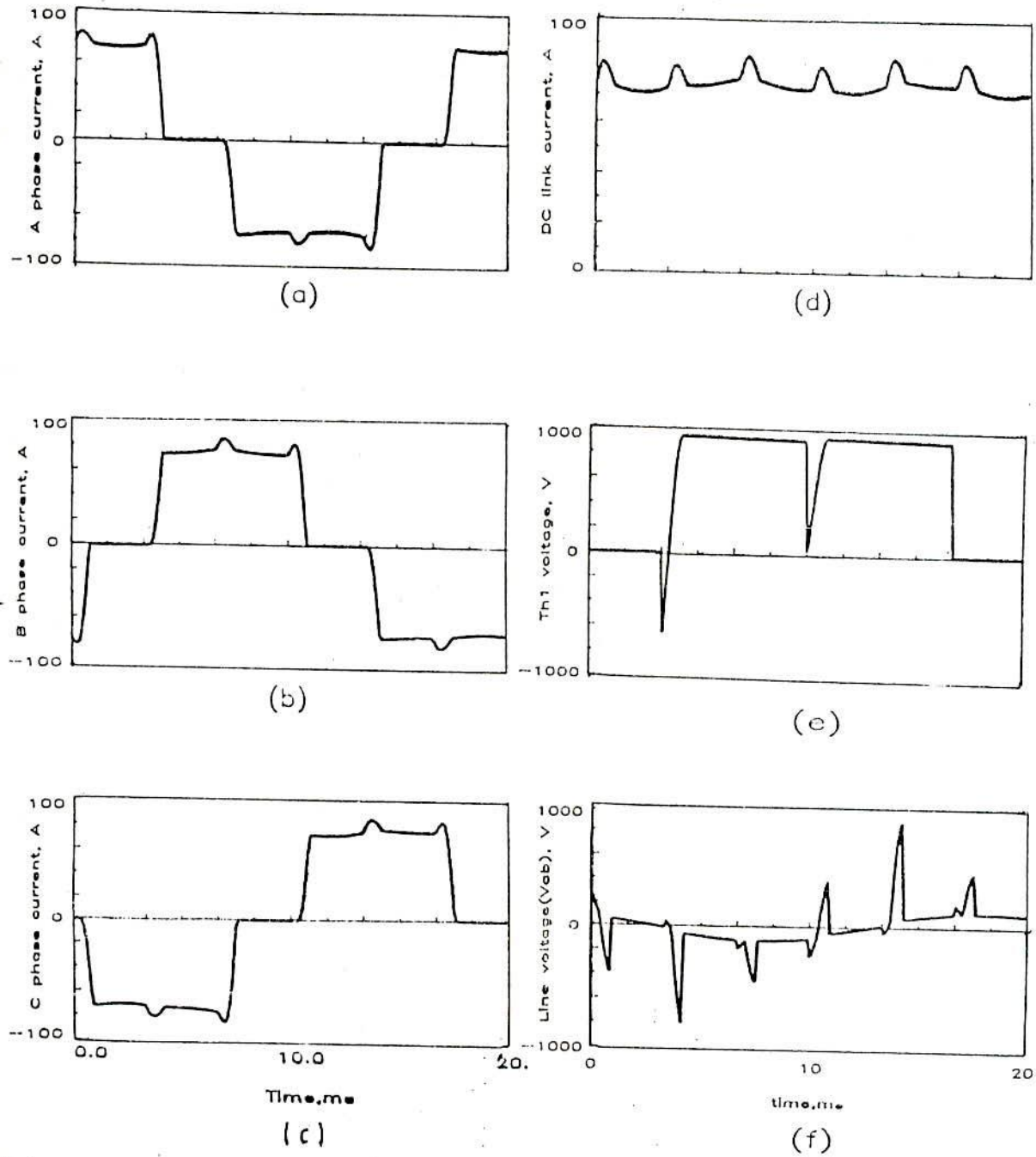

Fig.7.19 Simulation Traces as Suggested in Ref.[74]

(Normal Operation)

(a) to (c) motor line currents; (d) d.c. link current;
(e) T_{h1} voltage; (f) motor terminal voltage, v_{ab} .

simulation of the system under study. Figs.7.20 and 7.21 present the simulation results obtained by the two methods for an abnormal operation which concerns with short circuiting of diode D_1 at the upper limb. A general overall concurrence is noted between two sets of traces. Lack of too close a correlation is attributable to the choice of the values of the current limiting/sensing diode series reactors and artificial resistors(for defining voltages in [74]). The smaller they are made, the closer the results become. To the contrary, the response curves by the proposed method are independent of the additional elements, as these are made dummy by depriving them of their power handling capabilities. Hence larger time step for integration can be used.

7.3.4. Conclusions

The main objective of the work presented was to demonstrate the usefulness of the bond graph technique in simulating the semiconductor driven systems. The technique provides an organised way to develop state equations for a highly dynamic systems, and tedious writing of a number of equations and their arrangement and rearrangement for framing state equations have been avoided. It may be noted that no commonly made assumptions, as indicated in sub-section 7.3.1, were necessary other than those required to economise computer time and comply with bond graph. System can easily be extended without upsetting the original model. For example, a three phase converter with supply side inductances, in place of smooth adjustable dc source can be included, and this will add more state variables but in no way it will affect the

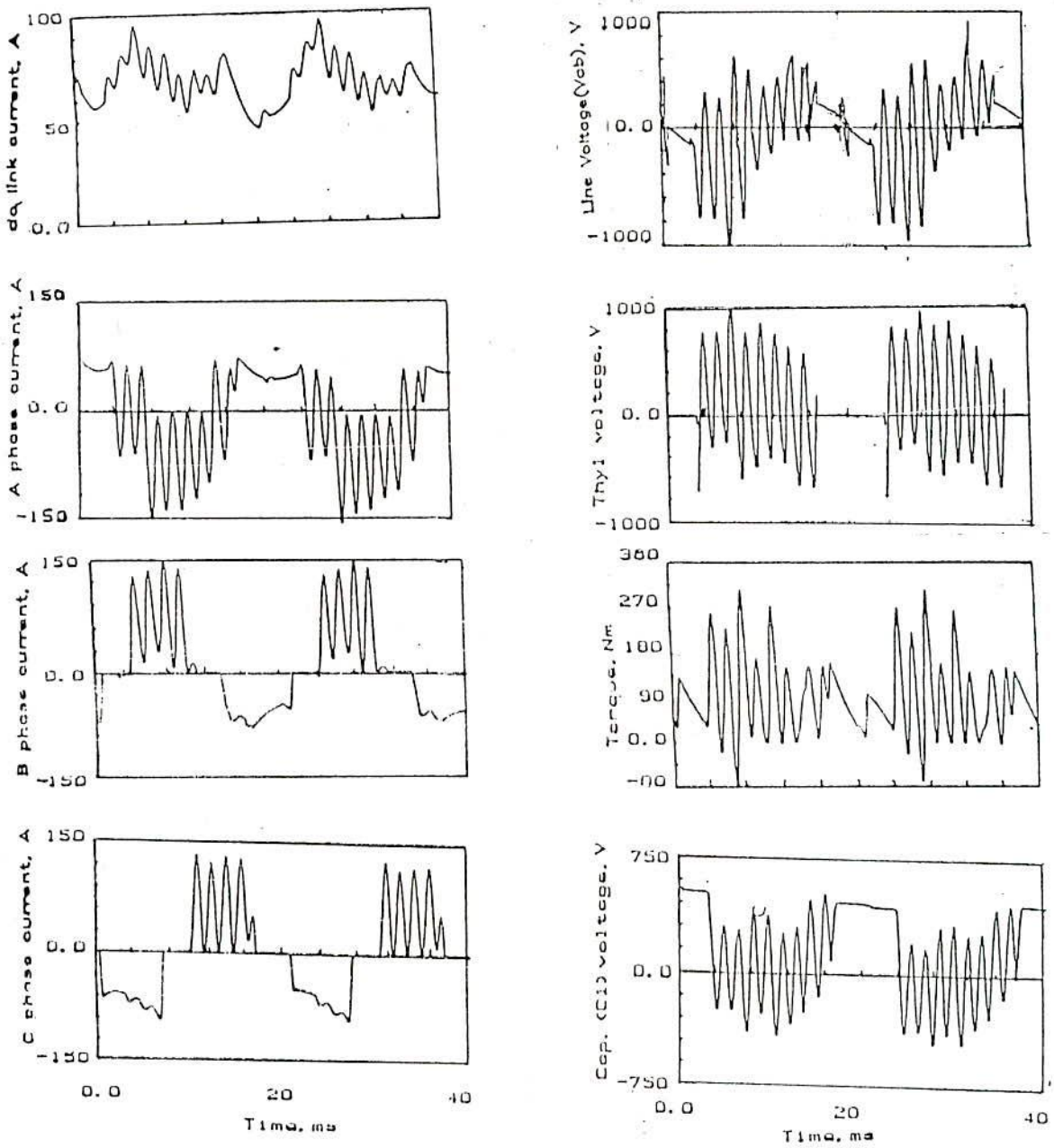

Fig.7.20 Simulation results by Bond Graph method with a diode(D1) shorted.

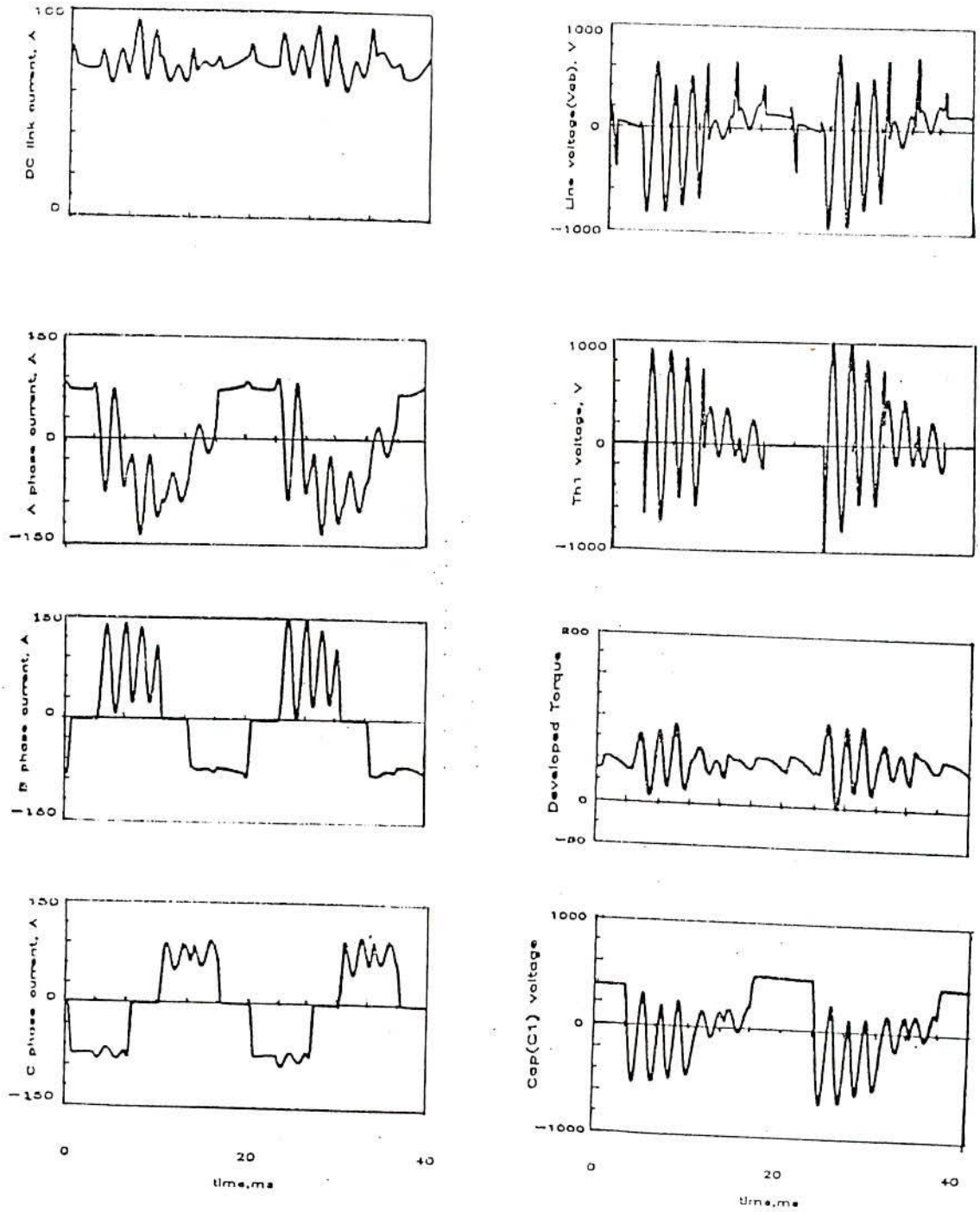

Fig.7.21 Simulation results as suggested in Ref.[74] with a diode(D1) shorted.

modelling of the dc link-inverter-induction motor system. The well structured gramatics of causality in the bond graph theory helps the modeller to have an *apriori* understanding of the completeness of the model. For example, existence of differential causality indicates that under certain dynamic modes, the system may violate the conservation of energy or entropy or at least may lead to the growth or decay of these system measures from sources unaccounted in the model and may lead to erroneous dynamic behavior. The basic completeness in system model is ascertained in bond graph which points towards plausible singularities in the system model, such as, *apriori* indication obtained by a modeller regarding the possibilities of resistive and conductive causalities in the integrated bond graph model. Bond graph models of a physical system are thus easily created keeping in mind the Physics of composite elements and then combining them without going into details of the mathematical aspects in the foreground unlike other graphical methods of system modelling.

CHAPTER VIII

CONCLUSIONS

8.1 GENERAL CONCLUSIONS

The indirect vector control scheme proposed in the dissertation using the rotor model in field co-ordinates for CSI-fed variable speed induction motor drives is quite practical and simple to implement. Algorithms for tuning can easily be realized by micro-computer without much hardware. Implemenation of the schemes, being mainly based on the measurement of dc link voltage and current, avoids mathematical co-ordinate transformations to obtain the ac quantities from the dc quantities and vice-versa.

One of the main features in the proposed control strategies is the absence of flux feedback loop and the direct use of the commanded value of the field current. This is used to compute the torque producing component of the stator current from the actual primary current for obtaining the slip-frequency as there is a time lag between the actual value of the stator current and its commanded value. This makes the actual stator current vector align appropriately with respect to the rotor flux for orientation, and also avoids the transmission of noises and measurement errors of the speed channels into the feedforward slip frequency channel if the controllers can not attenuate them. Once the commanded flux is set up, it is seen from the simulation studies that no significant variation in the flux level appears during the transient

process. This may be attributed to the slow response in rotor flux due to the large time constant of the rotor circuit. The drive system during the test run was operated below the base speed for which the field weakening was not considered.

The effects of the rotor resistance variation under both linear and non-linear magnetic conditions have been extensively investigated. Also the influence of saturation on the machine characteristics under the tuned condition has been studied. It is seen from the analysis and simulation results that at low load torques the linear magnetic model corresponding to the set flux level suffices. As the load torque is increased, the importance of saturation effect can not be ignored. Under non-linear magnetic condition, with flux level at or above the rated condition, peak torque occurs for $i_{qs}/i_{ds} > 1$ unlike in a linear magnetic model, where $i_{qs} = i_{ds}$ is the required criterion for maximum torque production. This is because of the slow increase of the rotor flux with i_{ds} above the nominal value and the best effect is then produced by increasing the percentage of torque component of the stator current. But increase in the proportion of i_{qs} increases the sensitivity to parameter deviation. On the other hand, increase in the saturation level (low i_{qs}/i_{ds}) reduces the sensitivity to detuning conditions. With increased rotor resistance at high load torque predictions of the performances of a slip regulated vector control system will be severely misleading if the saturation effects are ignored.

Three methods for detuning correction have been presented. The

rotor resistance estimation method, based on air gap power, quite reliably estimates the rotor resistance if the saturation level does not show a significant change. In other words, the parameters in the controllers and those of the machine should not differ widely. The scheme need not be used continuously. Since temperature rise is a slow process and if the scheme is invoked at regular intervals from the very beginning of the operation to track the rotor parameters and slip calculator is simultaneously provided with these estimated parameters, field orientation will be fairly maintained. No doubt, the effectiveness of the estimation process is affected during the transient period because the airgap power is derived from the expressions for steady state operation. But the estimation for the rotor resistance is found to show no marked deviation from the actual value as the air gap power gives a fairly good estimate of the generated torque in synchronous watts when the flux level is regulated [89]. The dc link voltage (V_I) based MRAC scheme shows quite fast adaptation capability. The error signal produces a corrective term for the nominal resistance for use in the slip calculator. The reference for V_I (or V_I') should contain this corrected value of R_r but must retain the nominal values of inductances corresponding to the set flux. As the adapted R_r approaches the actual rotor resistance, the actual rotor inductances also tend towards their nominal values. The torque producing stator current (i_{qs}) based scheme also works satisfactorily for adapting the correct rotor resistance but in this case the response is found to be slow and it becomes slower as the load torque in the machine is increased. The i_{qs}-based scheme is able to estimate correct

adaptive resistance for the controllers if the inductances closely correspond to the magnetization characteristics near the operating point. It is seen that the adaptation processes are capable to work under transient conditions.

In selecting the gain of the PI controllers it is observed that if the controller constants are adjusted to have larger bandwidth H_∞-norm of the complementary sensitivity function increases and roots move towards the imaginary axis. Considering this aspect and also to reduce the effect of high frequency dynamics (speed noises, disturbance etc.) a bandwidth of 62.0 rad/sec and 230.0 rad/sec for the speed loop and current loop transfer functions respectively were found to be satisfactory for the implemented scheme. The system with the selected set of PI controller gains were found to be stable in the simulation study and also during experimentation.

The implementation scheme presented in Chapter VI provides an easy on-line interaction with the drive system. Since the programs are written in modular form, they are easy to debug. The implementation scheme could be optimized using one microcomputer with enhanced sampling time and having sufficient peripherals interfaced on board.

Though simulation studies using the generalized approaches, namely, 'Bond Graph' model and 'Nodal' method have been presented for conventional CSI-IM drive schemes with no reference to field orientation, they are, however, indicative of the trends even in the case of field orientation.

8.2 SCOPE FOR FURTHER INVESTIGATION

Workability of the schemes has been tested both by simulation and experimentation using the linear controllers (PI) and conventional current source inverter with quasi-square wave output. Pulse width modulated current source inverters, which provide adequate control of torque and current harmonics, are being increasingly used in industrial production and automation. Using the proposed retuning schemes, experimental evaluation with the PWM-CSI along with simulation study is suggested. Application of H_∞ optimal controllers in lieu of PI controllers may be given a thought.

Stability studies and controller constant determination have been made with current and speed controllers in the system with no reference to the detuning correction controller. Similar investigation is proposed with the parameter adaptive controllers in the system besides the current and speed controllers.

Effect of magnetic non-linearity has been accounted by appropriate adjustment of the magnetizing inductance L_m, and the leakage inductances are taken as constant. This implies that saturation is caused by radial flux, and the circumferentially directed leakage flux has no effect on the state of saturation. It is an incorrect assumption in the sense that the saturation of iron depends on the total flux (i.e., radially directed flux plus the circumferential leakage flux). With constant rotor flux linkage, the stator flux linkage increases with load and additional magnetizing current will be required by the

stator teeth and yoke. This additional current vector will alter the stator current space vector evaluated from linear parameter model for the given rotor flux and torque [89]. An alternative way to study the effect of iron saturation on the field oriented operation is to consider the leakage inductance lumped to the stator side, as a non-linear function of stator current vector and the magnetizing inductance L_m, a function of air gap reluctance, as a constant. This approach is suggested.

Decoupling control at constant rotor flux command has been considered in the dissertation. In certain applications, variable flux reference is deemed a necessity [20, 123]. Efficiency optimization system requires adjustment of the flux level. In view of the limited voltage and current capability of the drive system, selection of the flux level acts upon the output torque capability of the system [20]. These aspects may be studied with due regard to the saturation effect.

Detailed analytical study has been performed for the steady state operation of the proposed scheme and transient and dynamic effects through simulation programs. Analytical studies in respect of parameter sensitivity on the dynamics of speed controlled system along with adaptive controllers are awaited.

As indicated earlier, the 'Bond graph' model and the 'Nodal method' be extended to include all the feedback and feedforward controllers required for field orientation.

APPENDIX-I

TABLES OF MACINES AND POWER CIRCUIT DATA

TABLE A.1 (MACHINE I, SQUIRREL CAGE)

Name plate data: 3-phase, 400/440V, 3.75 kw, 50Hz, 4-pole, Δ-Connected

Coupled dc generator: 240V, 2.0 kw, 10 A

Sl. No	Nominal Parameters (referred to stator)	Values in SI units
1.	Stator resistance, R_s	1.38Ω
2.	Rotor resistance, R_r	1.5087Ω
3.	Mutual inductance, L_m	0.14583H
4.	Stator self inductance, L_s	0.15936H
5.	Rotor self inductance, L_r	0.15936H
6.	Stator leakage inductance, l_1	0.01353H
7.	Rotor leakage inductance, l_2	0.01353H
8.	Moment of inertia, J	0.091kg-m^2
9.	Damping coefficient, B	0.005Nm-sec/rad

Saturation characteristic (i_{mag} - λ_m curve) :

$i_{mag} = a_1\lambda_m + a_5 \lambda_m^5$ where,

$a_1 = 2.35$ and $a_5 = 6.95$ for $\lambda_m \leq 0.57182$

$a_1 = -0.65$ and $a_5 = 12.4$ fpr $\lambda_m > 0.57182$

L_m - i_{mag} curve ($L_m = b_0 + b_1\ i_{mag} + b_2\ i_{mag}^2$):

$b_0 = 0.246$, $b_1 = -.0002$, $b_2 = -0.00269$ for $i_{mag} < 5.8$

$b_0 = 0.316$, $b_1 = -.0360$, $b_2 = -0.00140$ for $5.8 \leq i_{mag} < 7.0$

$b_0 = 0.261$, $b_1 = -.0236$, $b_2 = 0.00075$ for $i_{mag} \geq 7.0$

The PI controller constants are :

$k_{p1} = 2.0$, $k_{i1} = 0.5$, $k_{p2} = 30.0$, $k_{i2} = 10.0$

$k_{p3} = 0.02$, $k_{i3} = 0.01$, $k'_{p3} = 0.5$, $k'_{i3} = 2.0$

TABLE A.2 (MACHINE II, SQUIRREL CAGE)

Name plate data: 3-phase, 220V, 0.75 kw, 50Hz, 4-pole, Y-Connected

Coupled dc generator: 220V, 0.75HP, 4.25A, 1425rpm

Sl. No	Nominal Parameters (referred to stator)	Values in SI units
1.	Stator resistance, R_s	1.798Ω
2.	Rotor resistance, R_r	0.8250Ω
3.	Mutual inductance, L_m	0.07613H
4.	Stator self inductance, L_s	0.08323H
5.	Rotor self inductance, L_r	0.08323H
6.	Stator leakage inductance, l_1	0.00710H
7.	Rotor leakage inductance, l_2	0.00710H
8.	Moment of inertia, J	0.02095kg-m^2
9.	Damping coefficient, B	0.002Nm-sec/rad

Saturation Characteristic (i_{mag} -λ_m curve) :

i_{mag}-λ_m Characteristic ($i_{mag} = a_1\lambda_m + a_5 \lambda_m^5$) $a_1 = 2.35$, $a_5 = 6.95$

L_m-i_{mag} Characteristic ($\lambda_m = b_0 + b_1 i_{mag} + b_2 i_{mag}^2 + b_3 i_{mag}^3$)

$b_0 = 0.1158$, $b_1 = -.00205$, $b_2 = -0.00353$, $b_3 = 0.000353$

The PI controller constants are : $k_{p1} = 0.5$, $k_{i1} = .05$, $k_{p2} = 30.0$

$k_{i2} = 12.0$, $k_{p3} = 0.02$, $k_{i3} = 0.015$, $k'_{p3} = 0.25$, $k'_{i3} = 0.10$

TABLE A.3 DC Link and Power Circuit Data

Resistance of dc link filter, R_f :	0.16Ω
Inductance of dc link filter, L_f :	0.16H
Inverter thyristors :	25A, 1000V each
Converter thyristors :	25A, 600V each
Inverter diodes :	25A, 1000V each

APPENDIX II

THE T-I EQUIVALENT CIRCUTT FOR INDUCTION MOTOR

Machine models in equivalent circuit forms are many times found to be convenient to analyse the behaviour of machines. The T-type circuit model in Fig. A.1 for induction machines is a very familior form. But this form does not readily allow visualizing the operation of rotor flux field oriented cintrol of an induction motor. Appropriate circuit models of a field orientated induction motor can be obtained from the T-form circuit model, and the relations associated with the field orientation can be derived therefrom. But the explanation based on two-axis theory provides a deep insight into working principle of vector controlled systems, and the conceptual clarity is obtained. Therefore, the results obtained from the application of two-axis theory under field orientation scheme when applied to form a corresponding circuit model, will provide a firmer basis for the analysis and understanding of vector control systems. Besides this, as will be seen later, such circuit model will also be of help in devising the compensatory scheme to correct the detuning operation. For any operating condition, there always exists within the machine a specific position of rotor flux vector, which may not be known, but along and perpendicular to which the stator current-vector can be resolved.

From the first row in eqn. (2.1) under steady state condition

$$V_{ds} = R_s I_{ds} - L_s \omega_e I_{qs} - L_m \omega_e I_{qr} \qquad (A.1)$$

Applying the field oriented condition (2.18b) in (A.1) gives

$$V_{ds} = R_s I_{ds} - L_{\sigma s} \omega_e I_{qs} \tag{A.2}$$

where,

$$L_{\sigma s} = L_s - \frac{L_m^2}{L_r} \tag{A.3}$$

$$\text{or} \quad L_{\sigma s} = (L_s - L_m) + \left(L_m - \frac{L_m^2}{L_r} \right)$$

The second row in (2.1) for steady state operation gives

$$V_{qs} = \omega_e L_s I_{ds} + R_s I_{ds} \tag{A.4}$$

Let $\dot{V}_s = V_{qs} - jV_{ds}$ (A.5)

Use of (A.1) and (A.2) in (A.5) gives

$$\dot{V}_s = (R_s + j \omega_e L_{\sigma s}) (I_{qs} - jI_{ds}) + (j \frac{L_m^2}{L_r} \omega_e) (-j I_{ds}) \tag{A.6}$$

Combining (2.23) and (2.24) for steady state operation,

$$\frac{L_m^2}{L_r} I_{ds} = \frac{R_r}{\omega_{sl}} \frac{L_m^2}{L_r^2} I_{qs}$$

$$j\frac{L_m^2}{L_r} (-j I_{ds}) = \left(\frac{L_m^2}{L_r^2} \frac{R_r}{\omega_{sl}} \right) (I_{qs}) \tag{A.7}$$

The following expression for flux linkages are obtained.

Rotor flux linkage : $\dot{\lambda}_r = \frac{L_r}{L_m} \left(-j \frac{L_m^2}{L_r} I_{ds} \right)$ (A.8)

Mutual flux linkage : $\dot{\lambda}_m = (I_{qr} + I_{qs}) L_m + (-j I_{ds}) L_m$

$$= \left(L_m - \frac{L_m^2}{L_r} \right)(I_{qs} - j I_{ds}) + (-j I_{ds}) (\frac{L_m^2}{L_r}) \tag{A.9}$$

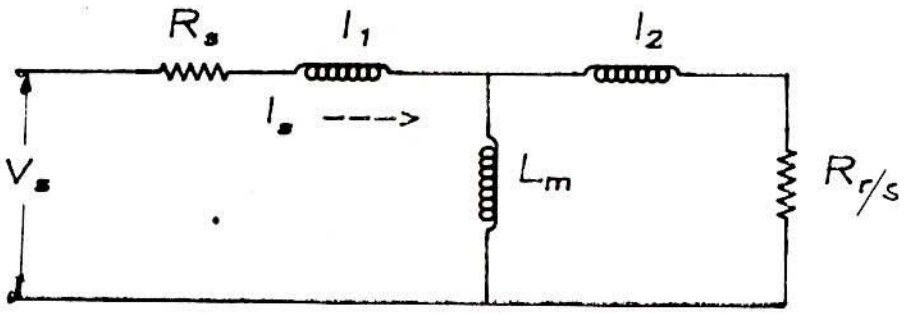

Fig.A.1 T— equivalent circuit of induction motor

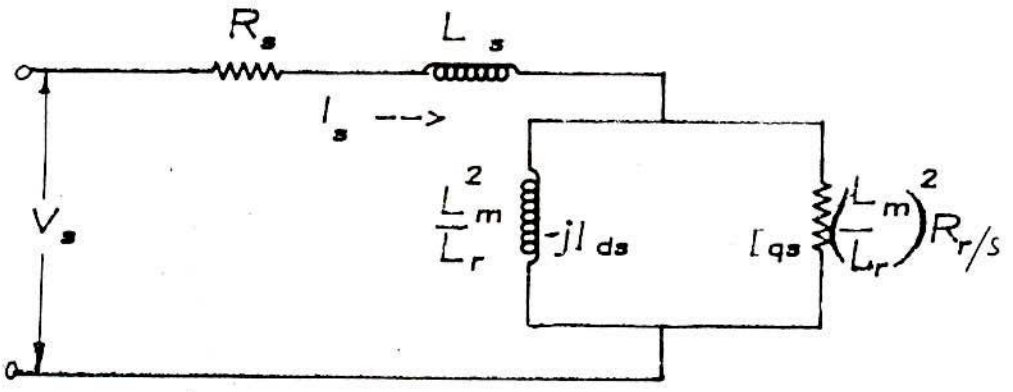

Fig.A.2 T—I equivalent circuit of induction motor

Stator flux linkage :

$$\lambda_s = L_m I_{qr} + L_s I_{qs} - j I_{ds} L_s$$

$$= \left(L_s - \frac{L_m^2}{L_r} \right) (I_{qs} - j I_{ds}) + \frac{L_m^2}{L_r} (-j I_{ds}) \qquad (A.10)$$

Results in (A.6) and (A.7) suggest Fig.A.2 to be the equivalent circuit model for rotor flux oriented induction motor. Various flux linkages, as given by (A.8), (A.9) and (A.10) are indicated in the equivalent circuit.

Per-phase steady state rms voltage

$$V = \frac{1}{\sqrt{2}} \sqrt{V_{ds}^2 + V_{qs}^2} \qquad (A.11)$$

Reactive power under steady state condition

$$Q = 3I_m \left[\frac{(V_{qs} - jV_{ds})}{\sqrt{2}} \frac{(I_{qs} - jI_{ds})^*}{\sqrt{2}} \right]$$

$$= \frac{3}{2} (V_{qs} I_{ds} - V_{ds} I_{qs}) \qquad (A.12)$$

By reference to Fig.A.2 the amplitudes of the two stator current components can be written as

$$I_{ds} = I_s \frac{R_r}{\sqrt{R_r^2 + s^2 \omega_e^2 L_r^2}} \qquad (A.13)$$

$$I_{qs} = I_s \frac{s \omega_e L_r}{\sqrt{R_r^2 + s^2 \omega_e^2 L_r^2}} \qquad (A.14)$$

Using (A.8) and (A.13) in (2.36), the expression for electromagnetic

torque in terms of stator current and rotor parameters becomes

$$T_{em} = \frac{3}{2} P_p I_s^2 \frac{s \omega_e R_r L_m^2}{R_r^2 + s^2 \omega_e^2 L_r^2} \qquad (A.15)$$

which is a familiar expression that can be obtained from conventional T-form equivalent circuit with the peak value of the supply current i.e., I_s.

APPENDIX III

A 3.1 Dynamic equations of induction motor

The voltage equations of a three phase induction motor in a-b-c-phase terms in a stationary reference frame fixed with the stator is written as:

$$\left[\begin{array}{c}[v_s]\\ \hline [v_r]\end{array}\right] = \left[\begin{array}{c|c} R_s[I_3] & 0[I_3] \\ \hline 0[I_3] & R_r[I_3]\end{array}\right]\left[\begin{array}{c}[i_s]\\ \hline [i_r]\end{array}\right] + \left[\begin{array}{c|c} (l_1+L_m)[I_3] & -L_m[I_3] \\ \hline -L_m[I_3] & (l_2+L_m)[I_3]\end{array}\right] p \left[\begin{array}{c}[i_s]\\ \hline [i_r]\end{array}\right]$$

$$+ \frac{\dot{\theta}}{\sqrt{3}}\left[\begin{array}{c|c} 0[I_3] & 0[I_3] \\ \hline -L_m[W_3] & (l_2+L_m)[W_3]\end{array}\right]\left[\begin{array}{c}[i_s]\\ \hline [i_r]\end{array}\right] \qquad (A.16)$$

Which in brief is

$$[v] = [R][i] + [L]p[i] + [G]\theta[i]$$

In this case,

l_1, l_2 : leakage inductances of stator and rotor phases of Induction motor respectively.

$[v_s]$: stator voltage vector = $[v_{as}\ v_{bs}\ v_{cs}]^t$

$[v_r]$: rotor voltage vector = $[0\ \ 0\ \ 0]^t$

$[i_s]$: stator current vector = $[i_{as}\ i_{bs}\ i_{cs}]^t$

$[i_r]$: rotor current vector = $[i_{ar}\ i_{br}\ i_{cr}]^t$

$[I_3]$: 3x3 identity matrix

and $[W_3]$ is an weight matrix that represents

$$[W_3] = \begin{bmatrix} 0 & 1 & -1 \\ -1 & 0 & 1 \\ 1 & -1 & 0 \end{bmatrix}$$

Equation A.16 is same as eqn.7.1 and comparing these two equations one can evaluate the elements of all the matrices.

A3.2 Admittance Sub-matrices A_{ss}, A_{sp}, and A_{ps} are given in Fig A.3 and App in Fig. A.4

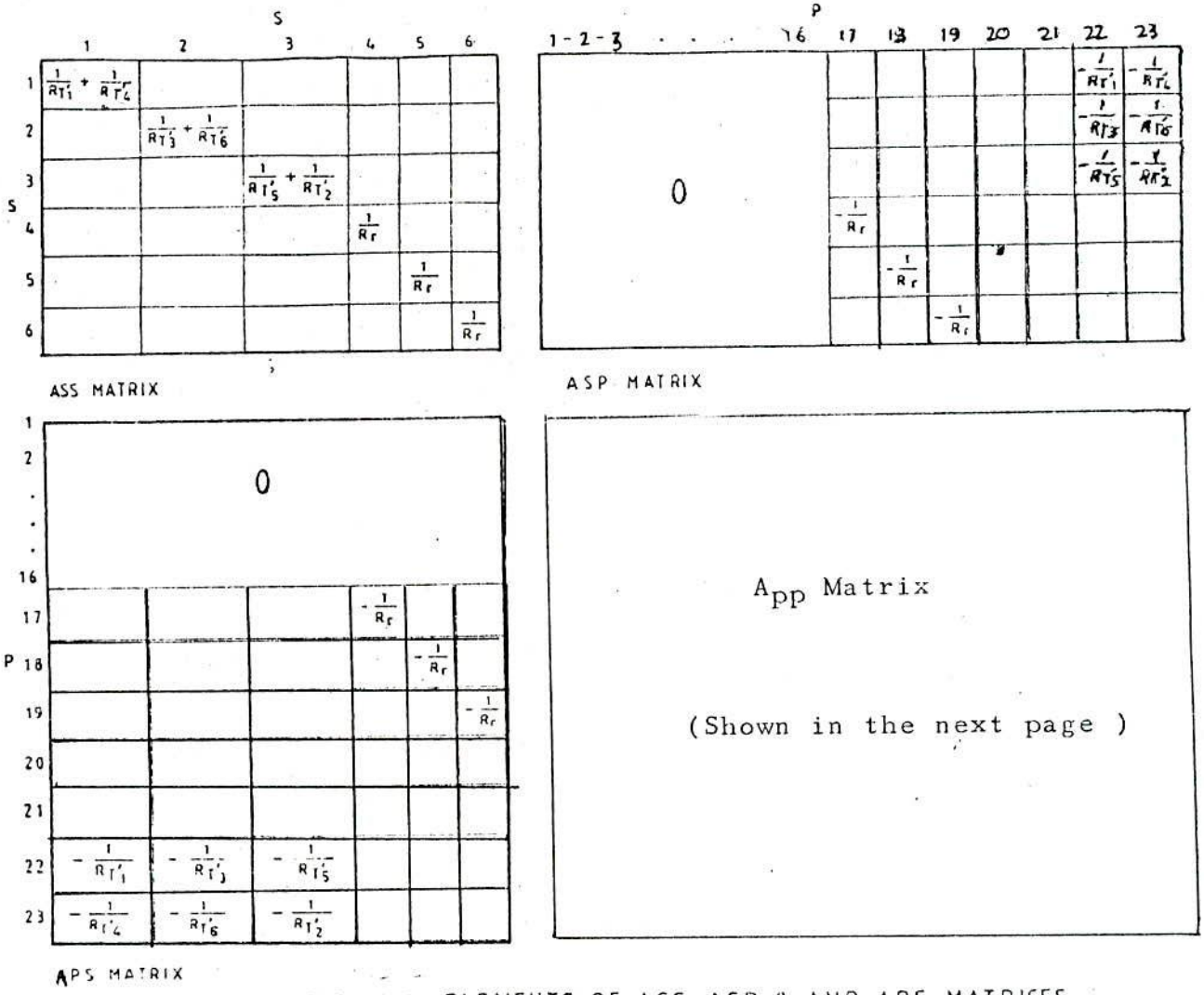

FIG. A.3 ELEMENTS OF ASS ASP & AND APS MATRICES.

A.3.3 Corrector current matrices $[i_p]_{n-1}$ and $[i_s]_{n-1}$

$$[i_p]_{n-1} = \begin{bmatrix} 1 & -i_{LF} \\ 2 & -i_{c1}+i_{c5} \\ 3 & -i_{c3}+i_{c1} \\ 4 & -i_{c5}+i_{c3} \\ 5 & 0.0 \\ 6 & 0.0 \\ 7 & 0.0 \\ 8 & -i_{c2}+i_{c4} \\ 9 & -i_{c4}+i_{c6} \\ 10 & -i_{c6}+i_{c2} \\ 11 & i_{as} \\ 12 & i_{bs} \\ 13 & i_{cs} \\ 14 & -i_{as}+i_{ar}+i_{am} \\ 15 & -i_{bs}+i_{br}+i_{bm} \\ 16 & -i_{cs}+i_{cr}+i_{cm} \\ 17 & -i_{ar} \\ 18 & -i_{br} \\ 19 & -i_{cr} \\ 20 & -(i_{am}+i_{bm}+i_{cm}) \\ 21 & i_{LF} \\ 22 & 0.0 \\ 23 & 0.0 \end{bmatrix}$$

$$[i_s]_{n-1} = \begin{bmatrix} 1 & 0.0 \\ 2 & 0.0 \\ 3 & 0.0 \\ 4 & 0.0 \\ 5 & 0.0 \\ 6 & 0.0 \end{bmatrix}$$

Fig. A.5 Corrector current matrices

APPENDIX - IV

Concept of observer and activated bonds

Bond graphs are equipped with the facility to observe effort or flow at a particular point in the same manner as we use sensors in an actual system. In mathematical form, an observer expresses effort or flow in terms of state variables and the software automatically derives that expression from the structure code. The bonds which are used as observers are represented with a full arrow and a symbol(**E** or **F**) indicating the type of activation. A **C**-element connected to a **S** junction with effort activated bond acts as a current observer and an **I**-element connected to a **P** junction with flow activated bond acts as an effort observer. These are represented in Fig. A. 6.

The observers introduce nothing into the system dynamics. For a flow observer effort activation is making the effort across the observer element zero. Similarly, for an effort observer flow through it is made zero by activation.

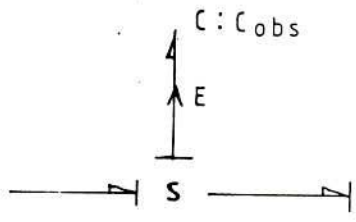

Fig. A. 6(a) Flow or current observer.

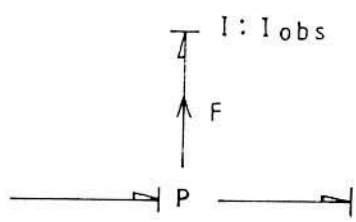

Fig. A. 6(b) Effort or voltage observer.

APPENDIX - V

Induction motor parameters and power circuit data for simulation model of Bond Graph Method

(i) The Parameters of an 18.6kw, 230v, 60Hz, 4-pole, 3-phase Y-connected induction motor are:

Stator resistance, R_s=0.0788Ω;

Rotor resistance, R_r=0.0408Ω;

Motor inductances L_s=0.0153H, L_r=0.0159H, L_m=0.0147H;

Inertia J=0.40kg m^2;

(ii)Parameters of CSI network

Commutating capacitors each 60.0μF;

Thyristor resistance, R_ts=0.05Ω(50kΩ) when it is ON (OFF);

Diode resistance, R_ds expressed as $v_d=0.06+0.04\times i_d$;

Resistance of dc link choke, R_f=0.10Ω;

Inductance of dc link choke=0.0146H;

REFERENCES

1. F. Blaschke, "The Principle of Field Orientation as Applied to the New Transvektor Closed Loop Control System for Rotating Field Machines", *Siemens Review,* 1972, vol.34, pp. 217- 220.
2. K. Hasse, "Zum dynamischen Verhalten der Asynchronmaschine bei Betrrieb mit variabler Staenderfrequenz und Staenderspannung"("On the Dynamic Behavior of Induction Machines driven by Variable Frequency and Voltage Source"), *ETZ-A,* Bd 89 H.4, 1968, pp. 77-81.
3. S. Yamamura, *AC Motors for High-frequency Applications : Analysis and Control,* Marcel Dekker, Inc., New York and Basel, 1986.
4. A. Nabae, K. Otsuka, H. Uchino, & R. Kurosawa, "An Approach to Flux Control of Induction Motor Operated with Variable Frequency Power Supply", *IEEE Trans, Ind. Appl.*, vol.IA-16, 1980, pp. 342-350.
5. T. Kume and T. Iwakane, "High Performance Vector Controlled AC Motor Drives : Applications and New Technologies", *IEEE Trans., Ind. Appl.*, vol. IA-23, 1987, pp. 172-180.
6. K. Jelassi, B. de Fornel and M. P-David, "Influence of the Numerical Quantization and Discretisation on the Performances of Field Oriented Asynchronous Drive", *Conference Record ICEM-90,* pp. 550 -555.
7. I. Boldea, I. Pfeiffer and A. L. Trica, "Modified Sliding Mode (MSM) Versus PI Speed Control of a Current Controlled Field Oriented Induction Motor Drive," *Electric Machines and Power Systems,* vol. 16, 1989, pp. 209-223.

8. R. Gabriel, W. Leonhard and C. J. Nordby, "Field Oriented Control of a Standard AC Motor Using Microprocessors", *IEEE Trans., Ind. Appl.*, vol. IA-16, 1980, pp 186-192.

9. K. Ohnishi, H. Suzuki, K. Miyachi and M. Terashima, "Decoupling Control of Secondary Flux and Secondary Current in Induction Motor Drive with Controlled Voltage Source and its Comparison with Volts/Hz Control", *IEEE Trans. Ind. Appl.*, vol.IA-21, 1985, pp. 241-246.

10. T. Ito, T. Yamaguchi, R. Ueda, T. Mochizuki and S. Takata, "Analysis of Field Orientation Control of Current Source Inverter Drive Induction Motor System", *IEEE Trans. Ind.Appl.*, vol. IA-19, 1983, pp. 206-209.

11. W. Leonhard, *Control of Electrical Drives,* Springer Verlag 1985.

12. H. Y. Zhong, H. P. Messinger and M. H. Rashid, "A New Micro-Computer Based Torque Control System for Three Phase Induction Motor", *IEEE-IAS Annual Meeting Record,* 1989, pp. 2322-2326.

13. K. S. Rajashekara, J. Vithayathil, W. Hofman and R. Schonfeld, "Current Impressed Voltage Source Inverter Fed Induction Motor Control by Field Orientation", *Can. Elec. Engg.Journal*, vol. 8, 1983, pp. 135-141.

14. F. Harashima, S. Kondo, K. Ohnishi, M. Kajita and M. Susono, "Multimicroprocessor-based Control System for Quick Response Induction Motor Drive", *IEEE Trans. Ind. Appl.*, vol. IA-21, 1985, pp 602-608.

15. J. Zhang, V. Thiagarajan, T.Grant and T.H. Barton, "New Approach to Field Orientation Control of CSI Induction Motor Drive", *IEE Proc.*, vol. 135, Pt B, 1988, pp. 1-7.

16 S. K. Biswas, "Vector Decoupled Control of Current fed Induction Motor", *Journal IE(I)*, vol. 72, Pt EL 2, 1991, pp. 48-53.

17. J. Zhang and T.H. Barton, "Microprocessor-Based Primary Current Control for a Cage Induction Motor Drive", *IEEE Trans. Power Electron.* vol.4, 1989, pp. 73-81.

18. E. Y. Y. Ho and P. C. Sen, "Decoupling Control of Induction Motor Drives", *IEEE Trans. Ind. Electron.*, vol 35, 1988, pp. 253-262.

19. Y-Y. Tzou and H-J. Wu, "Multimicroprocessor-based Robust Control of an AC Induction Servo Motor", *IEEE Trans. Ind. Appl.*, vol.26, 1990, pp. 441-449.

20. X. Xu and D.W. Novotny, "Selecting the Flux Reference for Induction Machine Drives in the Field Weakening Region", *Research Report* 91-7, Wisconsin Electric Machines and Power Electronics Consortium, The College of Engineering Univeristy of Wisconsin Madison.

21. K. H. Bayer and F. Blashke, "Stability Problems with the Control of Induction Machines Using the Method of Field Orientation", *Siemens Review*, vol. 34, 1972, pp 483-492.

22. D. S. Zinger, F. Profumo, T. A. Lipo, D. W. Novotny, "A Direct Field-Oriented Controller for Induction Motor Drives, using Tapped Stator Windings", *IEEE Trans. Power Electronics*, vol.5, 1990, pp. 446-453.

23. Y. Hori and T. Umeno, "Implementation of Robust Flux Observer Based field Orientation (FOFO) Controller for Induction Machines", *IEEE Conf.Rec.*, IAS 1989, pp. 523-528.

24. T. Umeno, Y. Hori and H. Suzuki, "Design of the Flux Observer-based Vector Control System of Induction Machines Taking

into Consideration Robust Stability", *Journal of Elect. Engg. in Japan*, vol. 110, 1990, pp. 53-65.

25. W.L. Erdman and R.G. Hoft, "Induction Machine Field Orientation along Air Gap and Stator Flux", *IEEE Trans. Energy Conv.*, vol.5, 1990, pp. 115-121.

26. E. Bassi, F. Benzi, S. Bolognani, amd G.S. Buja, "A Field Orientation Scheme for Current-Fed Induction Motor Drives Based on the Torque Angle Closed-loop Control," *IEEE Conf.Record IAS*, 1989, pp. 384-389.

27. Z. K. Wu and E. G. Strangas, "Feedforward Field Orientation Control of an Induction Motor Using a PWM Voltage Source Inverter and Stgandarized Single-Board Computers", *IEEE Trans. Ind. Electron,* vol.35, 1988, pp. 75-79.

28. G. K. Dubey, S. R. Doradala, A. Joshi and R. M. K. Sinha, *Thyristorised Power Controllers,* Wiley Eastern Limited, First Reprint, 1987.

29. M.P. Kazmierkowski and H-J. Kopcke, "A Simple Control System for Current Source Inverter-Fed Induction Motor Drives, *IEEE Trans, Ind. Appl.*, vol. IA-21, 1985, pp 617-623.

30. R. Prakash, S. Vittal Rao and F. J. Kern, "Robust Control of a CSI-Fed Induction Motor Drive System" *IEEE Trans. Ind. Appl.*, IA-23, 1987, pp. 610-615.

31. S. Bolognani and G. S. Buja, "DC Link Current Control for High-Performance CSIM Drives", *IEEE Trans. Ind. Appl.*, vol. IA-23, 1987, pp 1043-1047.

32. H. Kubota, K. Matsuse, and T. Fukao, "Indirect Field Oriented Control of CSI-Fed Induction Motor with State Observer", *Conf. Rec., IEEE IAS,* 1987, pp. 138 - 143.

33. C-H. Liu, C-C. Hwu and Y-F. Feng," Modeling and Implementation of a Microprocessor-based CSI-Fed Induction Motor Drive using Field Oriented Control", *IEEE Trans.,Ind.Appl.,* vol.25, 1989, pp 588-597.

34. T. Tsuji, J. Sakakibara and S. Naka, "CSI Drive Induction Motor by Vector Approximation", *IEEE Conf. Rec., IAS,* 1990, pp 513-517.

35. I. Boldea, I. Pfeiffer and A. Trica, "Modified, Sliding Mode (MSM) Versus PI Speed Control of a Current-Controlled Field-Oriented Induction Motor Drive", *Journal of Electric Machines and Powet Systems,* vol. 16, 1989, pp. 203-223.

36. J. W. Finch, P. P. Acarnley and D. J. Atkinson, "Field Oriented Induction Motor Drives : A Practical Implementation Facility", *Conf.Record, ICEM-90,* pp. 1272 - 1277

37. C. C. Chan, W. S. Leung and C. W. Ng, "Adaptive Decupling Control of Induction Motor Drives" , *IEEE Trans., Ind. Electron.,* vol. 37, 1990, pp 41-47.

38. A. Kumamoto, S. Tada, and Y. Hirane, " Speed Regulation of an Induction Motor Using Model Reference Adaptive Control", *IEEE SICE,* 1986, pp.25-29.

39. T. Murata, T. Tsuchiya and I. Takeda, "Vector control for Induction Machine on the Application of Optimal Control Theory," *IEEE Trans., Ind.Electronics,* vol.37, 1990, pp 283-290.

40. D. I. Kim, I. J. Ha and M. S. Ko, "Control of Induction Motors Via Feedback Linearization with input-output Decoupling", *Int. Journal of Control,* vol. 51, 1990, pp 863-883.

41. S. Yamamura, T. Nakagawa, and A. Kawamura, "Equivalent Circuit of Induction Motor as Servomotor of Quick Response", *Conference Record IPEC Tokoyo -83*, pp. 732 - 743.

42. S. Sathikumar and J. Vithayathil, " Digital Simulation of Field - Oriented Control of Induction Motors", *IEEE Trans., Ind. Electron.*, vol. IE-31, 1984, pp. 141-148.

43. E. Y. Y. Ho and P. C. Sen, "A Microcontroller-based Induction Motor Drive System Using Variable Structure Strategy with Decoupling", *IEEE Trans., Ind. Electronics*, vol. 37, 1990, pp. 227-235.

44. I. Boldea and S. A. Nasar, "Torque Vector Control (TVC) - A Class of Fast and Robust Torque-Speed and Position Digital Controllers for Electric Drives", *Electric Machines and Power Systems*, vol. 15, 1988, pp. 135-147.

45. M. Koyama, M. Yano, I. Kamiyama and S. Yano, "Microprocessor-based Vector Control System for Induction Motor Drives with Rotor Time Constant Identification Function," *IEEE Trans., Ind. Appl.*, vol. IA-22, 1986, pp. 453-459.

46. R. Krishnan and F. C. Doran, " Study of Parameter Sensitivity in High Performance Inverter-fed Induction Motor Drive Systems", *IEEE Trans., Ind. Appl.*, vol. IA-23, 1987, pp. 623-635.

47. K. B. Nordin, D. W. Novotny and D. S. Zinger, "The Influence of Motor Parameter Deviations in Feedforward Field Orientation Drive Systems", *IEEE Trans.,Ind. Appl.*, vol. IA-21, 1985, pp. 1009-1015.

48. P. Vas and M. Alakula, "Field Oriented Control of Saturated Induction Machines", *IEEE Trans., Energy Conv.*, vol.5, pp. 218-224.

49. O. Ojo and M. Vipin, "Steady State Performance Evaluation of Saturated Field Oriented Induction Motor", *Conf. Rec., IEEE-IAS*, 1990, pp 52-60.

50. F. Khater, R. D. Lorenz, D. N. Novotny and K. Tang, "Selection of Flux Level in Field Oriented Induction Machine Controllers with Consideration of Magnetic Saturation Effect", *IEEE Trans., Ind. Appl.*, vol. IA-23, 1987, pp. 276-281.

51 D. Y. Ohm, "Simulation of a Vector-Controlled Induction Motor Includes Magnetic Saturation of Effects", *Intelligent Motion*, 1989, PC/M ,pp. 64-79.

52. E. Levi and V. Vuckovic, "Field Oriented Control of Induction Machines in the Presence of Magnetic Saturation", *Electric Machines and Power Systems*, vol. 16, 1989, pp. 133-147.

53. L. J. Garces, "Parameter Adaptation for the Speed Controlled Static AC Drive with Squirrel Cage Induction Motor," *IEEE Trans., Ind. Appl.*, vol. IA-16, 1980, pp. 173-178.

54. D. Y. Ohm, Y. Khersonsky and J. R. Kimzey, "Rotor Time Constant Adaptation Method for Induction Motors Using DC Link Power Measurement," *Conf. Rec., IEEE-IAS*, 1989, pp. 588-593.

55. T. M. Rowan, R. J. Kerkman and D. Leggate, "A Simple On-line Adaptation for Indirect Field Orientation of an Induction Machine", *IEEE Conf. Rec., IAS*-89, pp. 579-587.

56. M. Koyama, H. Sugimoto, M. Mimura and K. Kawasaki, "Effects of Parameter Change on Coordinate Control System of Induction Motor", *Conf. Rec., Proc. IPEC-Tokyo*-83, pp. 684-695.

57. T. Okuyama, N. Fujimoto and H. Fujii, "A Simplified Vector Control System without Speed and Voltage Sensors-Effect of Setting Errors of Control Parameters and Their Compensation", *Journal of Elect. Engg. in Japan,* vol. 110, 1990, pp. 129-137.

58. C. Wang, D. W. Novotny, and T. A. Lipo, "An Automated Rotor Time Constant Measurement System for Indirect Field-Oriented Drives", *IEEE Trans.,Ind. Appl.,*vol. IA-24, 1988, pp. 151-159.

59. R. D. Lorenz and D. W. Novotny, "Saturation Effects in Field-Oriented Induction Machines", *IEEE Trans. Ind. Appl.* Vol.26, 1990 pp. 283-289.

60. D. S. Kirschen, D. W. Novotny and W. Suwanwisoot, "Minimizing Induction Motor Losses by Excitation Control in Variable Frequency Drives, "*IEEE Trans., Ind. Appl.*, vol. IA-20, 1984, pp. 1244-1250.

61. R. D. Lorenz and D. B. Lawson, "Flux and Torque Decoupling Control for Field-Weakened Operation of Field-Oriented Induction Machines", *IEEE Trans., Ind. Appl.*, vol. IA-26, 1990, pp. ??.

62. T. Saitoh, T. Okuyama and T. Matsui, "An Automated Secondary Resistance Identification Scheme in Vector Controlled Induction Motor Drives", *IEEE Conf Rec., IAS-89,* pp. 594-600.

63. T. Matsuo and T. A. Lipo, "A Rotor Parameter Identification Scheme for Vector Controlled Induction Motor Drives", *IEEE Trans., Ind. Appl.*, vol. IA-21, 1985, pp. 624-632.

64. H. Sugimoto and S. Tamai, "Secondary Resistance Identification of an Induction-Motor Applied Model Reference Adoptation System and its Characteristics", *IEEE Trans., Ind. Appl.*, IA-23, 1987, pp. 296-303.

65. A. M. Khambadkone and J. Holtz, "Vector-Controlled Induction Motor Drive with a Self-Commissioning Scheme", *IEEE Trans., Ind. Electron.*, vol. 38, 1991, pp 322-327.

66. M. V. Reyes, K. Minami and G. C. Verghese, "Recursive Speed and Parameter Estimation for Induction Machines", *IEEE Conf. Rec., IAS*-89, pp. 607-611.

67. S. K. Sul, "A Novel Technique of Rotor Resistance Estimation Considering Variation of Mutual Inductance", *IEEE Trans., Ind. Appl.*, vol. IA-25, 1989, pp. 578-587.

68. R. D. Lorenz and D. B. Lawson, "A Simplified Approach to Continuous On-line Tuning of Field-Oriented Induction Motor Drives", *IEEE Trans., Ind. Appl.*, vol. IA-26, 1990, pp. 420-424.

69. D. Dalal and R. Krishnan, "Parameter Compensation of Indirect Vector Controlled Induction Motor Drive Using Estimated Airgap Power," *IEEE IAS*, Atlanta, 1987, pp. 170-176.

70. W. Farrer and J. D. Miskin, "Quasi-sine-wave fully regenerative converter", *IEE Proc.*, vol. 120, 1973, pp. 969-976.

71. A. Joshi and S. B. Dewan, "Modified Steady-state Analysis of the Current Source Inverter and Squirrel Cage Motor Drive", *IEEE Trans., Ind. Appl.*, vol. IA-17, 1981, pp.50-58.

72. T. A. Lipo, "Hybrid Computer Simulation of an ASCI Current Source Inverter", *Electric Machines and Power Systems*, vol. 8, 1983, pp.1-15.

73. W. McMurray, "Hybrid Computer Simulation of a Controlled-Current Inverter Under Normal and Fault Conditions", *IEEE Trans. Ind. Appl.*, vol. IA-19, 1983, pp.268-280.

74. A. Consoli and A. Abela, "Digital Simulation of a Current Source Inverter Feeding an Induction Motor", *Electric Machines and Power Systems*, 1984, pp.251-268.

75. E. P. Cornell and T. A. Lipo, "Modelling and Design of Controlled Current Induction Motor Drive Systems", *IEEE Trans., Ind. Appl.*, 1977, vol. IA-13, pp.321-330.

76. A. K. Chattopadhyay and N. Meher, "A Generalized Approach to Steady-State Analysis of a Current Source Inverter with Induction Motor load Including Commutation Overlap", *IEEE Trans., Ind. Appl.*, vol. IA-35, 1988, pp.434-441.

77. R. C. Rosenberg and D. C. Carnopp, *Introduction to Physical System Dynamics,* McGraw Hill Book Company, 1983.

78. J. U. Thoma, "Simulation, Realistic(Engineering)", *Encyclopedia of Physical Science and Technology*, 1987, pp. 680-698.

79. J. J. Beaman and R. C. Rosenberg, "Constitutive and Modulation Structure in Bond Graph Modelling", *ASME Journal of DynamicsSystems Measurement and Control*, vol. 110, 1988, pp.395-402.

80. D. Sahm, "A Two-axis Bond Graph Model of the Dynamics of Synchronous Electrical Machines",*Journal, Franklin Institute*, vol. 308, 1979, pp. 205-218.

81. K. Sirivadhna et. al., "The Application of Bond Graphs to Electrical Machinery and Power Engineering", *IEEE Trans., PAS*, vol. 102, 1983, pp. 1176-1184.

82. X. Xu, R. K. Doncker and D. W. Novotny, "Stator Flux Orientation Control of Induction Machines in the Field Weakening Region", *IEEE-IAS, Annual Meeting Record,* 1988, pp. 437-443.

83. R. Krishnan and P. Pillay, "Sensitivity Analysis and Comparison of Parameter Compensation Schemes in Vector Controlled Induction Motor Drives," *IEEE IAS*, 1986, pp. 155-161.

84. R. Krishnan and A. S. Bharadwaj, "A Review of Parameter Sensitivity and Adaptation in Indirect Vector Controlled Induction Motor Drive Systems", *Conf.Rec, IEEE-PESC*, 1990.

85. C. Wang, D. W. Novotny and T. A. Lipo, "An Automated Rotor Time Constant Measurement System for Indirect Field-Oriented Drive," *IEEE Trans., Ind.Appl.*, vol.24, 1988, pp 151-159.

86. R. D. Lorenz, "Tuning of Field-Oriented Induction Motors for High Performance Applications", *IEEE Trans., Ind. Appl.*, vol. IA-22, 1986, pp. 293 - 297.

87. B. C. Ghosh and S. N. Bhadra, "A Simple Indirect Method for Decoupling Control of Current-fed Induction Motor and a Compensation Scheme for Rotor Resistance Variation", *Pre-conference Proc.*, vol. 1, IEEE TENCON, 1991, pp. 24-28.

88. B. C. Ghosh and S. N. Bhadra, "DC Link Voltage-Based Rotor Resistance Adaptation Scheme of a Field Oriented CSI-IM Drive System", *Conference rec., Electrical Rotating Machines*-ELROMA-92, pp. II-A-15-22.

89. H. Harashima et. al., "Synchronous Watt Torque Feedback Control of Induction Motor Drive", *IEEE IAS Annual Meeting*, 1987, pp. 156-162.

90. V. L. Kharitonov, "Asymptotic Stability of an Equilibrium Position of a Family of Linear Differential Equations", *Differential Uravnen.*, vol.14, 1978, pp. 2086-2088.

91. K. S. Yeung and S. S. Wang, "A Simple Proof of Kharitonov's Theorem", *IEEE Trans Aut. Contr.*, vol. AC-32, 1987, pp. 822-823.

92. H. Chapellat and S. P. Bhattacharyya, "An Alternative Proof of Kharitonov's Theorem", *IEEE Trans, Aut. Contr.*, vol. AC-34, 1989, pp. 448-450.

93. B. R. Barmish, "A Generalization of Kharitonov's four polynomial Concept for Robust Stability Problems with Linearly Dependent Coefficient Perturbations",*Proc.* 1988 ACC, GA, pp. 1857-1862.

94. H. Chapellat and S. P. Bhattacharyya, "A Generalization of Kharitonov's Robust Stability of Interval Plants", *IEEE Trans.,Aut. Contr.*, vol. AC-34, 1989, pp. 306-311.

95. M. J. Grimble and M. A. Johnson, "H_∞ Robust Control Design - A Tutorial Review", *Journal of Computing & Control Engineering,* Nov. 1991, pp. 275-282.

96. C. V. Hollot, D. P. Looze and A. C. Bartlett, "Parametric Uncertainty and Unmodeled Dynamics Analysis via Parameter Space Methods",*Automatica,* vol. 26, 1990, pp 269-282.

97. H. Chapellat, M. Dahleh and S.P. Bhattacharyya, "Robust Stability Under Structured and Unstructured Perturbations", *IEEE Trans., Aut. Contr.*, vol. 35, 1990, pp 1100-1107.

98. B. C. Ghosh, S. N. Bhadra and K. B. Datta, "Controller Design and Robust Stability Study of a CSI-Fed Induction Motor Under Indirect Field Orientation Control", *National Systems Conference,* NSC-91, Roorkee, 1992, pp.225-229.

99. T. Ohmae, T. Matsuda, K. Kamiyama and M. Tachikawa, "A Microprocessor-Controlled High-Accuracy Wide-Range Speed Regulator

for Motor Drives", *IEEE Trans., Ind. Electron.*, vol. IE-29, 1982, pp. 207-211.

100. N. Chaudhuri, S. Ghosh and A. M. Ghosh, "Wide-Range Precision Speed Measurement with Adaptive Optimization Using Microcomputer", *IEEE Trans., Ind. Electron.*, vol. IE-30, 1983, pp. 369-373.

101. K. Saito, K. Kamiyama, T. Ohmae and T. Matsuda, " A Microprocessor-Controlled Speed Regulator with Instantaneous Speed Estimation for Motor Drives", *IEEE Trans. Ind. Electron.* vol. IE-35, 1988, pp. 95-99.

102. S. K. Pillai, *A First Course in Electrical Drives*, Wiley Eastern Limited, New Delhi, (Revised), 1983.

103. K. P. Philips, "Current-Source Converter for ac Motor Drives", *IEEE Trans. Ind. Appl.*, vol. IA-8, 1972, pp. 679-683.

104. M. L. MacDonald and P. C. Sen, "Control Loop Study of InductionMotor Drives Using DQ Model", *IEEE Trans. Ind. Electron. and Control Inst.*, vol. IECI-26, 1979, pp. 237-243.

105. J. Hindmarsh, *Electrical Machines and Drives - Worked Examples*, Pergamon Press, (2nd edition), 1985.

106. G. Kron, *Tensor Analysis of Electrical Networks*, John Willey and Sons, New York, 1937.

107. K. Czernek, W. Koczsa and Z. Szule, "Construction of Induction Motors Mathematical Model on the basis of Nominal Parameters", *Proc. 2nd. International Symp. on Modelling and Simulation of Electrical Machines and Power Systems*, Quebec, Canada, 1987, pp. 185-196.

108. S. Bolognani and G. S. Buja, "Control System Design of a Current Inverter Induction Motor Drive", IEEE Trans. Ind. Appl., vol. IA-21, 1985, pp. 1145-1153.

109. *Continuous System Modelling Program*, COSMO-CAD, IIT Kharagpur, India.

110. S. H. Birkett and P. H. Roe, "The Mathematical Foundations of Bond graphs-III, Matroid Theory", *J. Franklin Institute*, vol. 327, 1990, pp. 87-108.

111. J. Barreto and J. Lefevre, "R-fields in the solution of Implicit Equations", *J. Franklin Institute*, vol. 319, 1985, pp. 227-236.

112. S. H. Birkett and P. H. Roe, "The Mathematical Foundations of Bond graphs-I, Algebraic Theory", *J. Franklin Institute*, vol. 326, 1989, pp. 329-350.

113. S. H. Birkett and P. H. Roe, "The Mathematical Foundations of Bond graphs-I, Duality", *J. Franklin Institute*, vol. 326, 1990, pp. 691-708.

114. A. M. Bos and P. C. Breedveld, "1985 Update of The Bond Graph Bibliography", *J. Franklin Inst.* vol. 319, 1985, pp. 269-285.

115. A. J. Blundell, *Bond Graphs for Modelling Engineering Systems*, Ellis Horwood Ltd., 1983.

116. N. N. Hancock, *Matrix Analysis of Electrical Machinery*, Pergamon Press Ltd., London, 1984.

117. R. Krishnan and F. C. Doran, "A Method of Sensing Line Voltages for Parameter Adaptation of Inverter-fed Induction Motor Drives," *IEEE Trans. on Ind. Appl.* vol. IA-23, 1987, pp 617-682.

118. S. N. Bhadra, "A Direct Method to Predict Instantaneous Saturation Curve from rms Saturation Curve", *IEEE Trans., Magnetics,* vol. MAG-18, 1982, pp. 1867-1869.

119. K. Ogata, *Modern Control Engineering,* Eastern Economy Edition, Prentice- Hall of India Pvt. Ltd., New Delhi, 1988.

120. D. F. Stout and M. Kaufman, *Handbook of Operational Amplifier Design,* McGraw- Hill Book Company, New York, 1976.

121. G. R. Slemon, "Modelling of Induction Machines for Electric Drives", *Conference Record, IEEE-IAS Annual Meeting,* 1988, pp. 111-115.

122. B. A. Francis, *Lecture Notes in H_∞-Optimal Control Theory,* Springer Verlag, 1987.

123. S. M. Islam and C. B. Somuah, "An Efficient Higfh Performance Voltage Decoupled Induction Motor Drive with Excitation Control", *IEEE Trans. Energy Conv.*, vol. 4, 1989, pp 109-117.

124. H. Matsumoto, H. Takami and R. Takase, "Vector Control Scheme for an Induction Motor Controlled by a Voltage Model Operation with Current Control Loop", *Conference Rec. IEEE IAS Annual Meeting,* 1989, pp. 368 - 374.

125. B. C. Ghosh and S. N. Bhadra, "Bond Graph Simulation of a Current Source Inverter Driven Induction Motor (CSI-IM) System", *accepted for publication in Electric Machines and Power Systems.*